UNIVERSITY OF OKLAHOMA

GRADUATE COLLEGE

MULTISCALE, MULTIPHYSICS MODELING OF SUBSURFACE ENGINEERING APPLICATIONS

A DISSERTATION

SUBMITTED TO THE GRADUATE FACULTY

in partial fulfillment of the requirements for the

Degree of

DOCTOR OF PHILOSOPHY

By
YULIANA M ZAPATA ARBOLEDA
Norman, Oklahoma
2020

MULTISCALE, MULTIPHYSICS MODELING OF SUBSURFACE ENGINEERING APPLICATIONS

A DISSERTATION APPROVED FOR THE

MEWBOURNE SCHOOL OF PETROLEUM AND GEOLOGICAL ENGINEERING

BY THE COMMITTEE CONSISTING OF

Dr. Zulfiquar Reza, Chair

Dr. Richard Elmore

Dr. Benjamin Shiau

Dr. Catalin Teodoriu

Dr. Hamidreza Karami

Dedicated to Ana, Jaime, and Laura

Acknowledgments

I would like to express my deepest gratitude and appreciation to my advisor Dr. Zulfiquar Reza for his expertise, motivation, and continuous support. His guidance helped me throughout the research. To the committee members, Dr. Richard Elmore, Dr. Benjamin Shiau, Dr. Catalin Teodoriu, and Dr. Hamidreza Karami, I am incredibly grateful to you for being part of my committee and for your valuable feedback, advice, and encouragement.

I wish to extend my gratitude to my coauthors Morten Kristensen, Nick Huerta, Chris Brown, and Shah Kabir, for their contribution and insights. Besides, I would like to thank Katie Garret, Tien Phan, and Javier Tellez for their inputs at different stages of my research. And to the Mewbourne School of Petroleum and Geological Engineering staff for their valuable assistance and support.

To my Mom, Dad and Sister, thank you for always being my biggest fans, for the love and support, and all the videocalls that made me feel like they were next to me. Special thanks to Nubia, Gladys, Eugenia, Karen, Isabel, Hernando, William, and John; I genuinely appreciate their encouragement and support. To Saurabh Sinha, thank you for being the best partner for this journey, for being my first reviewer, and for the coffee. Finally, I would like to thank my friends for always being there, Andres, Ricardo, and Natalia. Thanks to my Norman family, Any, Laura and Ruben, Michael and Estefania, Andrea and Felipe.

Abstract

Fluid flow, particle transport, and chemical reactions in porous media play a vital role in various disciplines, including hydrology, medicine, and engineering. In particular, in the petroleum industry, subsurface engineering applications involving injection or production of fluids are associated with physical and chemical processes at the pore-scale (nano/microscale). These processes encompass fluid-rock interactions that can determine and alter the fluid behavior and rock properties at reservoir scales (macroscale). Developing engineering tools to probe and link pore-scale processes to reservoir-scale remains a fundamental research challenge to enhance our understanding and our ability to predict the observed phenomena in the subsurface

In this work, I explored various subsurface engineering applications of multiphysics, multiscale modeling paradigms including pore-scale network models, experimental data, and reservoir scale simulation to investigate the role of physical and chemical interactions on the evolution of rock properties and fluid behavior. Three such applications were studied: (1) formation damage due to particle plugging during hydraulic fracturing as a result of proppant crushing and fluid invasion, (2) the evolution of migration pathways due to chemical diagenesis in unconventional reservoirs, and (3) plume characterization, storage mechanisms, and well-based monitoring during CO_2 sequestration in saline aquifers.

First, I employed a particle plugging simulator that integrates pore-scale phenomena with hydraulic fracturing simulation at the reservoir-scale to examine the effects of fracturing fluid invasion and proppant crushing on the formation permeability damage at the matrix-fracture interface. The model is based on the generation of 3D pore networks that capture the pore space topology and serve as the frame for fluid flow and particle transport simulations. The pore networks are coupled with a commercial reservoir-scale fracture simulator that provides the

fracturing process macroscale characteristics to compute the particles' retention and their effect on the formation permeability. This integrated model aims to enhance the design and modeling of hydraulic-fracturing operations in unconventional shale reservoirs by considering the pore-scale dynamics at the matrix-fracture interface.

Next, I incorporated a modeling workflow that integrates mineralogical, petrophysical, and chemical data to delve into the influence of chemical diagenesis on macroscopic properties from a pore-scale perspective. The pore-scale model proposed has two main components. The first component involves examining the depositional environment, mineralogy, and pore structure characteristics to identify diagenetic controls on the reservoir quality. The second component comprises the generation of hybrid pore network models representing the pore space, followed by the numerical simulation of fluid transport and mineral reactions related to relevant diagenetic events. The model aims to improve our understanding of the influence of diagenetic events on the migration pathways' evolution.

Finally, I investigated the geological sequestration of CO_2 in saline aquifers to characterize and monitor the temporal and spatial evolution of the CO_2 plume. The integrated modeling framework used provides the means to ascertain the relative influence of multiple parameters on the plume characteristics and the contributing trapping mechanisms. The selected parameters involve facies distribution, aquifer-water composition, heterogeneity and anisotropy of petrophysical properties, transport physics, and operational variables like injection rate and bottomhole pressure. Several well-based fluid variables are monitored to assess the plume evolution and identify behavior correlations between the near-wellbore and plume region properties.

Table of Contents

List of Tables

List of Figures

Chapter 1. Introduction

1.1. Motivation and Objectives

This dissertation investigates multiscale physical and chemical processes that govern the fluid-rock interactions associated with fluid flow, injection, or production during subsurface engineering operations. The main objective is to enhance our understanding and ability to predict fluid dynamics and rock properties by linking pore- to reservoir-scale numerical simulation of various engineering applications. The processes explored include (1) formation damage due to particle plugging during hydraulic fracturing, (2) the evolution of migration pathways due to chemical diagenesis, and (3) CO_2 sequestration in saline aquifers. Bearing this objective in mind, I introduce distinct integrated modeling frameworks that facilitate capturing the pore space characteristics and fluid-rock interaction, providing the necessary tools to address relevant questions associated with the engineering applications explored.

In the case of formation damage due to particle plugging during hydraulic fracturing, the multiscale modeling approach aims to identify: How is the permeability affected by the retention of fines at the matrix-fracture interface? What is the relationship of proppant disintegration with closure stress and particle size? What hydraulic-fracture design variables appear to have the most considerable impact on fracture conductivity and the resulting particle retention?

To examine the evolution of migration pathways due to chemical diagenesis, the integrated pore-scale model presented intends to determine: What is the relationship of mineralogical composition and rock fabric, with pore space characteristics such as pore type, size, and abundance? How are porosity and permeability affected by precipitation and dissolution processes? What is the role of transport mechanisms such as advection and diffusion on the evolution of the main migration pathways?

In terms of the study of the subsurface dynamics of the CO_2 sequestration in saline aquifers, the purpose of the modeling framework is to tackle several aspects of the process: How are the plume dimensions evolving due to continuous long-term CO_2 injection? Can we monitor the geometric/spatial characteristics of the CO_2 plumes? What is the storage efficiency of different trapping mechanisms? Which plume features could we monitor using well-based variables? And What are the influences of uncertain variables on the various response attributes of trapped CO_2 and the plume dynamics?

1.2. Literature Review

A concise review of the main numerical approaches and modeling paradigms available to study physical and chemical phenomena associated with the rock-fluid interactions underground is summarized in this section. The methodologies presented are related to particle migration and retention during fluid injection, reactive transport due to chemical diagenesis, and the transportation and storage of CO_2 in geological formations.

1.2.1. Particle Transport and Retention Simulation in Porous Media

In general, particle transport studies in porous media aim to understand better the phenomena responsible for changes in permeability, dispersion coefficients, and concentration profiles due to the interaction between particles, fluid, and the porous space. Early research approaches at the macroscale followed classical filtration theory based on the continuum conservation equation (Eq. 1) combined with kinetic rate laws that relate particle retention rate with particle concentration (Eq. 2) and Darcy's law (Eq. 3) (Herzig, et al., 1970; Payatakes, et al., 1973). These first studies that consist of trajectory analysis or semi-empirical models required experimental determination of time and space-dependent filtration coefficients (λ) for specific suspensions and porous medium. Moreover, these studies overlooked the pore space characteristics such as the pore size

distribution, pore connectivity, and the pore surface structure that greatly influence the particle behavior.

$$\phi \frac{\partial c(x,t)}{\partial t} + \frac{\partial \sigma(x,t)}{\partial t} = -U \frac{\partial c(x,t)}{\partial x} \quad (1)$$

$$\frac{\partial \sigma(x,t)}{\partial t} = \lambda(\sigma) c(x,t) U \quad (2)$$

$$U = -\frac{k_0 k(\sigma)}{\mu} \frac{\partial p}{\partial x} \quad (3)$$

Where x and t are length and time, $c(x,t)$ is the concentration of suspended particles, $\sigma(x,t)$ is the concentration of deposited or captured particles, ϕ is the porosity, U is the velocity, $\lambda(x,t)$ is the filtration coefficient that represents the particle trapping capacity of the porous rock, k_0 is the initial permeability, $k(\sigma)$ is the formation damage factor that accounts for permeability reduction due to particle deposition, μ is the viscosity, and p is the pressure.

Subsequent modeling studies included stochastic and probabilistic approaches and the implementation of pore-network models at the microscale and mesoscale (i.e., pore-scale) to account for the pore/particle interactions and to incorporate relevant pore-space properties. Pore-network models represent the pore-space, considering the pore size distribution and connectivity to capture the porous medium's transport properties. These theoretical pore-networks have evolved with time, from models consisting of bundle-of-tubes, regular lattices, and sphere packing to image-based models and acyclic pore models (Purcell, 1949; Fatt, 1956; Bryant et al., 1993; Blunt et al., 2013; Sakhaee-Pour and Bryant, 2015).

One of the first studies that included a pore-network formulation on the particle transport model was by Donaldson et al. in 1977. The authors examined particle transport in sandstones based on

a theoretical pore network consisting of a bundle of parallel tubes with distributed pore sizes. Their work included experimental injection of an aqueous suspension of sand particles in sandstone cores at constant flow rates, monitoring pressures, and collecting effluent particles. In addition to having pore networks, another critical aspect of their investigations resides in their use of random statistical processes to select the particle size and model the particle movement through the system, assuming that the probability of a particle traveling into a capillary is proportional to the flow.

Later on, in 1984 Todd, et al. investigated the permeability impairment at the pore-scale due to particle transport and retention by computing the number of particles trapped considering various trapping mechanisms in their analysis, in contrast to only modeling straining as in previous studies. The mechanisms included random capture, straining, settling, inertia, and hydrodynamic action. The authors' network model consisted of a regular lattice of capillaries that considered the connectivity among the pore tubes (unlike Donaldson's model). Additionally, a random walk technique was used to characterize particles' transport inside the network by generating random numbers to determine the particle's path. The authors applied their model formulation to study the effects of formation damage in water injectivity due to suspended solids in the injected fluid. However, their random walk technique alone failed to capture the flow field's impact on the particle path selection, which is reflected in the lack of agreement between their predictions and quantitative data.

In 1987, Sharma and Yortsos formulated a mathematical model to calculate permeability reduction due to the transport of particulate suspensions in porous media based on effective medium theory to determine the fluid flow distribution in pore networks. The authors considered a physical system that accounted for particles trapped by mechanical straining and particles attached to pore surfaces due to the interaction forces (deposition on pore walls). They developed population balance

equations to provide the concentration and size distribution profiles for each species (trapped and attached), concluding that particle dispersion and retention in the pore-space is dependent on particle size and time. However, their model can only be applied assuming homogeneous transport properties, which do not represent porous media's nature in general.

Following investigations delve into filtration's stochastic nature and included more robust two-dimensional (2D) and three-dimensional (3D) representations of the porous media. For instance, Rege and Fogler (1987) implemented the concept of "flow-biased probability" to track the particle path through the network. The flow-biased probability includes both the stochastic nature of filtration (probability) and the flow field's role (flow-biased) in the particle path selection. Based on this concept, the authors described formation damage by pore plugging due to mechanical straining using a 2D regular lattice as their pore-network model. Their results indicated that particle plugging generated by straining could significantly reduce the system permeability, particularly in the region near the entry face of the flow simulations, in agreement with experimental observations in core samples. In 1991, Imdakm and Sahimi employed three-dimensional pore networks combined with a Monte-Carlo simulation method to model the effect of transport of fines in porous medium on permeability. Flow field calculations and particle path selection follow the same principles as Rege and Fogler's (1987) model. In this case, besides considering particle trapping due to straining, the proposed model includes deposition and adsorption onto the pore surface. The attractive forces considered in the model involve Electrical Double-Layer and London forces interaction with the surface, including also surface roughness and protrusions that dictate the particle attachment. The authors validated their model, capturing permeability changes due to bentonite and kaolinite injection in experimental data from Ottawa sandpacks.

Building on previous studies, a wide range of disciplines implemented more robust numerical models. These models provided insights on processes such as fines migration due to water injection in rock formations (Bedrikovetsky et al., 2003; Idowu, 2009; Ochi and Vernoux, 1995), or microbial transport and drug delivery through the vascular system (Bauer et al., 2008; Tufenkji, 2007). For instance, Ochi and Vernoux (1995) used a stochastic model to simulate permeability impairment during brine injection at high flow rates. The authors used 2D regular-lattice pore networks integrated with microscopic first-order kinetic laws of detachment and retention to determine particle concentration changes with time. The mechanisms included in the trapping analysis were straining, interception, and diffusion. Their objective was to assess the influence of the release coefficient, critical velocity, and initial concentration on the permeability reduction. Bedrikovetsky et al. (2003) developed a pore-level stochastic model for deep bed filtration of water during injection in waterflood projects to analyze injectivity reduction. Their model is a modified version of the classic filtration theory that includes a population balance of both suspended and trapped particles equation and kinetic expressions for particle capture and plugging. Accessibility factors and the velocity reduction effect are incorporated into the analysis to account for the limited access of injected particles to certain pores as a function of particle size. Nonetheless, the model has limitations on capturing the pore structure as pore connectivity is not accounted for. Also, average pore and particle sizes are assumed, and model coefficients have to be calculated from coreflood experiments for specific case scenarios.

Following the advancement of deep bed filtration theory in the 1970s-1980s, and particle transport studies at the pore-scale during 1990s-early 2000s using pore network models, starting in the late 2000s, several modeling approaches were developed to investigate the particle movement through porous media at multiple levels integrating phenomena from pore- to reservoir-scale. Rhodes et al.

(2008) suggested that the analysis of particle transport in porous media should incorporate the solution of governing equations at the macro- or micro-scales but should be approached at different scales from pore to core, grid-block to field. They introduced a model that simulates particle movement at the pore scale based on advective-diffusive equations, coupled with random molecular diffusion. The authors then developed a multiscale upscaling methodology to simulate transport at larger scales and validated their results at different scales by predicting experimental breakthrough curves in sandpack data. Their main contribution is the analysis of the impact of heterogeneity at the pore scale on particle-transport processes at the field level and how all scales of observations are linked.

Shapiro and Bedrikovetsky (2010) presented a mathematical model based on classical filtration theory incorporating microscale characteristics such as the pore and particle size distributions into the macroscopic formulation. In this model, three main components are identified: the particle transport system of equations, the system of hydrodynamic equations, and the numerical solution of the resultant set of equations. The particle transport equations proposed by the authors are stochastic, consider the distribution of particle and pore sizes, and account for particle capture due to straining. This model's main limitation is the semi-micro scale treatment of the particle transport phenomena, which does not fully address the morphology of the pore space and does not capture the physics of flow and particle capture at the pore level.

More recent research considers multi-scale, multi-physics approaches to simulate the transport and retention of particles. French (2015) developed a particle plugging model considering trapping by straining and using concurrent coupling to allow communication between a 3D pore network model and a reservoir scale model at each timestep. In this approach, particle transport physics is solved at the pore-scale involving changes in permeability, dispersion, and retention coefficients,

which are later on provided to the reservoir simulator. This set up allowed the authors to examine the pore structure's role on continuum-scale parameters, such as the effect of injecting multiple particle species on dispersion and retention coefficients.

Other 3D pore network representations to simulate particle retention and permeability reduction include Yang and Balhoff's (2017) and Meng and Yang's (2019) work. Yang and Balhoff (2017) examined the effects of various forces acting over the particles at the pore -scale (i.e., gravity, electrostatic, Van der Waals, drag, and Brownian motion), and the role of pore throat geometry in the filtration coefficient prediction by comparing capillary tubes and converging-diverging pore throats. Their model provided insights on the dependence of damage factors on the volume of particles injected and the uniformity of deposition. On the other hand, Meng and Yang (2019) used pore network representations to study the effect of variable pore space heterogeneity, flow conditions, and particle size on particle dispersion. Their formulation is based on coupling a particle tracking method based on random walk algorithms with a pore-network model. The authors observed that the dispersion coefficients are highly dependent on particle size when the medium is homogenous. In contrast, for heterogeneous media, the pore throat size plays a more critical role.

A compilation of the particle transport theory's advancement, including some of the most relevant studies from the origins of deep bed filtration theory to current multi-scale, multi-physics numerical models, is presented in Table 1. The summary includes a brief description of the approach, model characteristics, applications, and limitations.

Table 1. Review of particle transport models in porous media.

Authors	Model scale and approach	Network type	Trapping mechanisms	Model characteristics	Model limitations
Herzig et al., 1970	Macroscale, Phenomenological model	-	Deposition	Continuum mass balance of particles, the kinetic equation for trapping mechanisms, empirical relations for relevant parameters. Basis of classical bed filtration theory	Derivation of empirical coefficients requires experimental data for specific porous media and particles. Does not provide insights into the effects of pore space characteristics
Donaldson et al., 1977	Pore-scale, Statistical network model	2D, bundle of tubes	Straining	Particle path selection proportional to flow, validation of results based on injection experiments. Applied to particle transport and retention in sandstones	Simple network depiction limits the effects of pore connectivity on fluid flow and particle transport
Tien and Payatakes, 1979	Macroscale, Trajectory models	-	Deposition given by forces acting upon particles	Trajectory analysis to estimate particle deposition rate based on forces acting upon particles, pore space represented as an assembly of collectors. Basis of deep filtration theory	Representation of the pore space does not account for pore space morphology and other characteristics defining the interaction between the particles and the pore surface
Todd et al., 1984	Pore-scale, Statistical network model	2D, regular lattice	Straining, random capture, settling, inertia, hydrodynamic	Imposed a variety of particle captured mechanisms and used a random walk method for particle path selection. Applied to formation damage during water injection	The model does not include the role of advection-diffusion in the fluid flow calculations and particle path selection. Results do not capture experimental data
Sharma and Yortsos, 1987	Hybrid, Mathematical model	Network of interconnected pores	Straining and wall deposition	Used continuum population balance equations to model rates of deposition and release and effective medium theory for flow field calculations at the pore-scale. More realistic depiction of the pore space. Applied to deep bed filtration	Effective medium theory fails to describe permeability reduction when the medium is not homogeneous because it assumes a mean velocity
Rege and Fogler, 1987	Pore-scale, Statistical network model	2D, triangular network	Straining	Developed the concept of "flow-biased probability" for path selection. Implemented simultaneous entry of particles. Applied to formation damage	Limited trapping mechanisms that explain the effects of pore surface interaction with the particles are accounted for in the model
Imdakm and Sahimi, 1991	Pore-scale, Statistical network model	3D, regular network	Straining, deposition, and adsorption	Monte-Carlo simulation model. Employed a more realistic representation of the pore space by including more trapping mechanisms. Applied to fines migration in porous media	The model is limited to the pore-scale domain. Additional work on coupling with macroscale properties could be implemented

Table 1 Continued

Authors	Model scale and approach	Network type	Trapping mechanisms	Model characteristics	Model limitations
Meloy et al., 1991	Pore-scale, Statistical network model	2D, regular lattice	Straining	Monte-Carlo simulation model. Investigated different pore size distribution types: Rayleigh, Lognormal, Gauss, and Exponential. Examined permeability reduction due to particle movement in porous media	More complex networks that account for the connectivity and the pore space morphology are necessary to analyze the effects of the pore-throat size distribution in particle trapping.
Ochi and Vernoux, 1995	Pore-scale, Statistical network, and phenomenological model	2D, regular lattice	Straining, interception, and diffusion	Proposed first-order kinetic laws of detachment and retention at the pore scale, combined with the stochastic determination of permeability. Studied the effects of network size, critical velocity, diffusion, and initial concentration. Applied to permeability impairment during brine injection	The model does not take into account advective transport of particles between pores and flow biased dispersion of particles
Bedrikovetsky et al., 2003	Pore-scale, Stochastic model	-	Straining	Modified classical filtration theory model, including a velocity reduction and particle accessibility coefficient to represent the effects of the pore-space structure on transport. Applied the model to injectivity reduction during waterflooding	The coefficients implemented to describe the interaction of particle and pore size distributions still fail to capture the topology of the pore space by not including the effects of connectivity and tortuosity, as well as the stochastic character of the particle transport in porous media
Salehi Mojarad and Settari, 2007	Macroscale, Numerical model	-	Deposition	Coupled flow and formation damage at reservoir scale, based on modified filtration theory by including a formation damage factor to characterize injectivity decline	The reservoir scale model does not consider the physics role at the pore level in the formation damage calculations. Furthermore, it does not account for the pore structure features
Rhodes et al., 2008	Multiscale, Statistical network model	2D, diamond lattice	-	Multiscale study of transport from pore to core, grid block to field scale. Based on advection-diffusive equations coupled with random molecular diffusion. Implemented upscaling technique to analyze transport at all scales	Particle retention mechanisms could be included to study the effect of trapping. The model could also be improved by extending its application to 3D networks and evaluating different geometries for pores and throats to capture the pore space's nature.

Table 1 Continued

Authors	Model scale and approach	Network type	Trapping mechanisms	Model characteristics	Model limitations
Bauer et al., 2008	Pore-scale, Statistical network model	2D, triangular network	Straining	Random walk model for particle tracking defined different transport types based on percolation theory, calculated dispersion coefficients, and particle concentration as a function of particle size. Applied to biology and drug delivery through the vascular system	Resultant dispersion and particle concentrations could be used to upscale the results and couple them with macroscopic properties. The model could be broadened to include more extensive networks with 3D components that consider the topology of the system
Shapiro and Bedrikovetsky, 2010	Hybrid, Stochastic model	-	Deposition	The model is based on continuum filtration theory, incorporating microscale characteristics such as pore size distribution and particle motion's random nature. Calculated retention profiles	Does not include physics of flow at micro-level, neglecting pore structure characteristics such as connectivity
French, 2015	Multiscale, Statistical network model	3D, from microtomography images	Straining	Concurrent coupling model to link pore and reservoir scale. With reservoir properties being transmitted to the pore model, and vice-versa. Predicted permeability reduction, filtration coefficients, and effluent concentrations. Applied to particle migration in petroleum reservoirs	Implementing additional physics at the pore-scale to complement the particle trapping mechanisms could improve the pore-space representation and therefore make the coupling with macroscopic reservoir properties better
Yang and Balhoff, 2017	Pore-scale, Statistical network model	2D, regular network	Hydraulic drag, gravity, electrostatic, Van der Waals, and Brownian motion	Physically robust particle tracking method. Included geometry of the throats into their analysis by implementing converging-diverging throats. The models predicted effluent concentrations and filtration coefficients for particle retention in porous media	The model could be improved to be more representative of the pore space nature by using 3D networks that bring into the simulations the topology and connectivity, as well as the effects of tortuosity and dispersion
Meng and Yang, 2019	Pore-scale, Statistical network model	2D, diamond network	Straining	Random walk particle tracking method. Studied the effect of straining and pore space heterogeneity on dispersion coefficient under various flow conditions. Applied to particle dispersion in porous media	Additional physics that capture attachment of particles to the surface could be included to observe their effect on particle dispersion, as well as more complex networks that represent better the topology of the pore system

1.2.2. Modeling Diagenesis and Reactive Transport in Porous Media

Early approaches to explore diagenetic processes in sedimentary rocks were based on petrographic observations using microscopic techniques. In the 1970s, the use of scanning electron microscopic significantly advanced the examination of chemical diagenesis (Berner and Holdren, 1977). But the need for additional mathematical tools to predict the impact of diagenetic processes in the rock properties evolution became evident. Berner (1980b) proposed one of the first theoretical models for chemical diagenesis based on the balance of solute mass in a small box of sediments. The model aims to describe the change in concentration with time for both the solid and liquid phases at a macroscopic scale. To illustrate the three major processes affecting sediments' concentration, Berner (1980b) considered two types of fluxes: advective and diffusive, then included a reaction component to account for the rock-fluid reactions (Eq. 4). The resulting equation is the basis of reactive transport modeling, in this case, applied to diagenetic processes.

$$\frac{\partial C_i}{\partial t} = \frac{\partial}{\partial x}\left(D\frac{\partial C_i}{\partial x}\right) - \frac{\partial v C_i}{\partial x} + \sum R_i \qquad (4)$$

Where $C_i$is the concentration of component i, D is the diffusion coefficient, v is the flow velocity, and R_i is the reaction rate of every diagenetic event affecting the component i.

Reactive transport models began to be implemented to explore various processes and phenomena in porous media from a macroscale perspective (Le Gallo et al., 1998; Walsh et al., 1984). One of the first reactive transport models was developed by Walsh et al.(1984) to reproduce the genetic mineralization features of sandstone uranium deposits based on reactive transport. The model accounted for advection and assumed local thermodynamic equilibrium. The model also included the dissolution and precipitation of nine common minerals in a uranium depositional system, namely: iron, uranium, sulfur, selenium, molybdenum, arsenic, carbon, hydrogen, and oxygen. Le

Gallo et al. (1998) proposed a model to evaluate reservoir quality, predicting diagenesis's effects on porosity and permeability of sandstone reservoirs in the Dunbar field (North Sea). Their methodology coupled transport of chemical species accounting for diffusion and dispersion, with equilibrium and kinetic reactions at the reservoir scale. The chemical model was composed of selected diagenetic events involving kaolinite and k-feldspar transformation into illite and quartz and dissolution of kaolinite, albite, and k-feldspar.

Macroscopic models of reactive transport offered an excellent first approach to study the rock's behavior. However, these models did not consider the impact of the pore structure, heterogeneity, and reactivity of minerals at the microscale on the evolution of the continuum-scale reservoir properties. Thus, subsequent reactive transport simulation incorporated microscopic and pore-network models to simulate diagenetic alterations in sandstones (Li et al., 2006, 2007; Xiao and Jones, 2006; Kim et al., 2011; Yuan et al., 2017) and carbonate rocks (Algive et al., 2009; Algive et al., 2012; De Boever et al., 2012). Øren and Bakke (2002) presented a statistical model to reconstruct a sandstone structure at the microscale level accounting for different forming processes. The authors used petrographical information from 2D thin section images to obtain the grain size distribution and mineralogy. Different algorithms were implemented to simulate grains' sedimentation (successive deposition of individual grains), compaction (vertical stress reduces porosity), and diagenesis. In the latter, the diagenetic events modeled were quartz overgrowth and precipitation of clays on the free surface.

Li et al. (2006, 2007) employed 3D pore networks and geochemical models to investigate the effect of scaling on reaction rates of anorthite and kaolinite dissolution and precipitation in the presence of CO_2 in sandstones. The model has four main components: a theoretical pore network, a transport model that considers both advection and diffusion, a reaction model that includes the

calculation of reaction rate laws for the minerals of interest, and the analysis of reaction rates of the network (averaging at the continuum scale). The authors' simulations indicated that under conditions of high heterogeneity and reactivity, scaling becomes important and geochemical modeling should incorporate the pore-scale characteristics. In 2011, Kim et al. improved the previous model by implementing pore networks extracted from computed tomography maps to capture the rock samples' mineral distribution. In this case, an additional dependency of the reaction rates on the flow rate at the pore scale was observed.

In carbonates, the evolution of porosity and permeability has been generally examined during cycles of dissolution and precipitation as a function of two dimensionless numbers that characterize the flow and reaction regimes: Peclet and Damköhler (Algive et al., 2012). These models included correlations between relevant dimensionless numbers and the distribution of dissolved and precipitated material that allows for a simplified reactive model. The authors revised the dynamics of the flow field interaction with the reactive model. Their observations account for the effects of high flow rates that facilitate dissolution in the main flow pathways and low flow rates that can increase permeabilities when the dissolution rate is lower than the precipitation rate.

Nogues et al. (2013) applied a different pore-scale model approach to capture dissolution and precipitation in carbonates. This reactive model evaluated porosity and permeability evolution in an oolithic dolostone analyzing the effects of various chemical, flow, and mixing conditions in the presence of CO_2. The transport and chemical models followed the simulations of Li et al. (2006). Besides, variations to the pore structure due to mineral reactions were incorporated by relating changes in the pore volume with pore conductivity changes. The authors observed that slow flow conditions created non-unique porosity-permeability relations, while fast flow produced uniform changes across the domain and, therefore, a unique porosity-permeability relationship.

Reactive transport in shale formations at the pore-scale entails additional challenges given the fracture-rock system's multiscale nature. Models at a macroscopic scale have been used to analyze the seal integrity and investigate shale weathering and mineralogical controls on formation water (Cai et al., 2018; Heidari et al., 2017). For instance, Wang and Battiato (2020) presented a multiscale model to capture microcracks' alteration in a shale formation due to the precipitation of minerals. The authors developed a patch-based algorithm where microscale simulations are performed in sample regions. A more realistic model that overcomes the pore-scale physics limitations of this approach could include pore-network models.

Additional applications of pore-scale models coupled with reactive transport involve the assessment of changes in the pore structure due to injection of acids in the context of improved oil recovery for matrix acidization (Budek and Szymczak, 2012; Tansey and Balhoff, 2016) or to investigate the impact of geological CO_2 sequestration (Mehmani et al., 2012; Steefel et al., 2013). Matrix dissolution models besides the classical reactive transport physics (advection, diffusion, and reaction) included pore merging criteria to capture the effects of channeling and wormholing on the pore-space and permeability of the rock. On the other hand, developed models for CO_2 sequestration investigate how the injected CO_2 alters the equilibrium at the pore level, resulting in precipitation and dissolution of rock minerals and trapping of CO_2 as mineralized carbonates or dissolved in the formation fluids. For instance, Mehmani et al. (2012) modeled calcite precipitation and permeability reduction during CO_2 injection and employed a coupling approach to upscale pressure, concentration, and fluxes to the macroscopic scale. Their model predicted cementation and disconnection of flow paths with lower flow rates, whereas high permeability pathways persisted in all regimes.

Current diagenetic models not only considered chemical diagenesis but incorporate the effect of mechanical processes. Roded et al. (2018) proposed a model for permeability evolution in porous media undergoing dissolution of the matrix and compaction at the pore-scale. The reactive model considers the enlargement of pores due to dissolution and the resulting loss of pore volume due to the rock's weakening (impact of stress). The sequential coupling of these processes was evaluated using mass conservation of the aqueous phase (pressures and fluxes) and conservation of solute mass (fluid composition and reaction rates). Then, the stress distribution and pore deformation were computed from force balance, and the transport and mechanical properties were updated due to the combined effects of dissolution and compaction. Their results indicated significant inhibition of permeability by stress, and those changes are dependent on the dissolution regime. Table 2 condenses the different reactive transport model formulations investigated, their characteristics, and their limitations.

Table 2. Reactive transport formulations in porous media.

Authors	Model scale	Network type	Model characteristics	Model limitations
Berner, 1980	Macroscale	-	Proposed general diagenetic equation, including advection, diffusion, and reaction terms	The author presents a theoretical approach at the macroscopic scale. It does not include a description of the kinetic reaction formulation or the coupling of the different processes
Walsh et al., 1984	Macroscale	-	Modeled reactive transport considering advection and thermodynamic equilibrium to model precipitation and dissolution of minerals related to uranium deposition in sandstones	The model's main limitation is that it does not consider the effects of molecular diffusion on the transport. Also, the reaction of minerals in the geochemical system is not kinetically modeled
Le Gallo et al., 1998	Macroscale	-	Coupled mass transport and water-rock reactions at the reservoir scale to predict reservoir quality changes due to chemical diagenesis. The reactions included are illitization, dissolution of kaolinite, k-feldspar, and albite. Permeability and volume-fraction content of illite were predicted.	The reservoir model does not take into account the role of physics at the pore scale. Assumes a homogeneous pore system, where diagenetic events coincide in the whole domain

Table 2 Continued

Authors	Model scale	Network type	Model characteristics	Model limitations
Oren and Bakke, 2002	Microscale	3D network based on spherical grain deposition	Reconstructed sandstone features considering sedimentation, compaction, and diagenetic processes such as quartz overgrowth and clay precipitation. Considered transport by advection, and mineral growth correlations as grain coats. The porous media structure was modeled in terms of grains, not pores	The statistical model does not consider diffusion for the fluid transport and does not include kinetic modeling of the diagenetic reactions, which in turn are modeled based on homogeneous mineral growth around the grains as a function of the direction of growth
Li et al., 2006, 2007	Multiscale	3D regular lattice	Investigated the effects of scaling of reaction rate laws. Transport model (advection and diffusion), coupled with a reaction model of kaolinite and anorthite precipitation and dissolution in the presence of CO_2	The pore network model is not representative of the pore space. Changes in the pore structure are not taken into account when precipitation of minerals occurs in the network.
Kim et al., 2011	Multiscale	3D lattice extracted from X-ray micro-tomography	Improved Li et al. model including representative pore networks and calculating initial mineral concentrations. Investigated the relationship between reaction rates and flow rates	The domain size limits the model. The effect of mineral precipitation on the pore size and conductivity is not considered
Algive, et al., 2009, 2012	Pore-scale	3D lattice	Investigated the impact of dissolution and precipitation cycles on the porosity and permeability of carbonate rocks. Implemented the use of dimensionless numbers that correlate to the geochemical dynamics	The simplified chemical model based on dimensionless numbers that characterize the reaction regimes does not fully describe physical and chemical parameters. It does not allow simulation of precipitation and dissolution processes simultaneously
De Boever et al., 2012	Pore-scale	3D lattice extracted from computer tomography	Combined classical diagenetic analysis (petrography and imaging) with a geochemical simulation to model precipitation and dissolution of dolomite, calcite, and anhydrite, and its impact on the pore space	The model is limited to either precipitation or dissolution simulation, considering both could improve the reactive component. Applications to scenarios that include heterogeneous case studies could also be implemented
Budek and Szymczak, 2012	Pore-scale	2D random and regular	Captured matrix dissolution due to injection of acids. The network is allowed to change dynamically, allowing pore merging. Dissolution patterns are characterized based on the Damköhler number. Also, the authors investigated optimum flow rates for maximum dissolution	The domain dimensions, size, and homogeneous character limit their prediction of the correlation between the flow rates and the optimum Damköhler numbers
Mehmani et al., 2012	Multiscale	-	Simulated the effects of CO_2 injection at the pore level on pore structure, including the reduction of throat conductivities resulting from mineral precipitation. Implemented a coupling methodology to upscale concentrations, pressures, and fluxes. Preferential cementation regions related to lower flow rates were identified	The model does not include molecular diffusion on transport and reactivity of the minerals at the pore-scale. The model is also limited to low Damköhler numbers due to the assumption of the slow reaction of calcite compared to advection
Raoof et al., 2013	Pore-scale	3D random structure	Developed a simulator that couples complex pore networks and a reactive transport model with multiple applications, including porosity changes due to dissolution of calcite	The model does not consider realistic initial mineral compositions at the pore scale, which results in a simplified chemical system that is not representative of the rocks studied

Table 2 Continued

Authors	Model scale	Network type	Model characteristics	Model limitations
Nogues et al., 2013	Pore-scale	3D stochastic	Examined the evolution of porosity and permeability in carbonate rocks during CO_2 injection. Different flow, chemical, and mixing conditions are studied. Transport includes advection and diffusion, and the reactions are kinetically modeled	The model is limited by the size and lower complexity of the networks implemented to improve computation time. Using more realistic networks could add insights into the phenomena studied, as well as coupling rock properties at larger scales
Tansey and Balhof, 2016	Pore-scale	3D lattice, based on computed tomography	Modeled dissolution regimes during matrix acidizing. Incorporated a pore merging criterion that allowed for analysis of permeability changes due to channeling and wormholing. The reaction model assumes a mass-transfer limited regime	The model does not consider the impact of reaction-rate limited regimes that could result from variations of the mineralogical composition of the grains and the pore space topology
Heidari et al., 2017	Macroscale	-	Modeled shale weathering based on 1D reactive transport. The chemical model includes the dissolution of pyrite, chlorite, and precipitation of iron hydroxides	The model is a simplified representation of weathering and does not account for many weathering aspects, like volume change, and does not include the organic matter in the mineral composition
Roded et al., 2018	Pore-scale	2D regular lattice	Studied the interplay of dissolution and compaction and how the permeability evolves. Both chemical and mechanical diagenetic processes are modeled based on reactive transport and calculation of the stress distribution. Increasing stress inhibits permeability as a function of the dissolution regime.	A simple chemical model is implemented considering a single reactive component that does not account for the rock's mineralogical composition or the fluid/rock interaction.
Wang and Battiato, 2020	Multiscale	-	Developed a patch-based algorithm that performs microscale simulation of flow and reactive transport in small sample regions of a fractured shale system. The other regions of the domain are evaluated by interpolation. The model considers precipitation and the evolution of permeability in the microcracks	A more realistic model that overcomes the pore-scale physics limitations of this approach could include the use of pore-network models

1.2.3. Numerical Modeling of Geological Storage of CO_2 in Saline Aquifers

Numerical modeling of CO_2 injection and storage can provide numerous means of evaluating the capacity, behavior, and performance of injection sites. Typical modeling approaches involve finite-difference or streamline models to study multiphase flow, simulate different trapping mechanisms, and capture the behavior and evolution of the CO_2 plume. Table offers a selection of various reservoir scale simulations performed to analyze various aspects of CO_2 injection in saline

aquifers. The general approach, model characteristics, injection times, and limitations are presented.

Early research on CO_2 disposal in saline aquifers included simulation studies based on petroleum reservoir modeling of aquifers or depleted gas/oil reservoirs, as well as the development of criteria for site selection and evaluation of the storage capacity (Bachu et al., 1994; Gunter et al., 1998; Holloway, 1997; Weir et al., 1996). For instance, Pruess et al. (2001) examined the CO_2 storage capacity of homogeneous aquifers implementing 2D multiphase transport simulations, considering different CO_2 phases (supercritical and aqueous) and realistic PVT fluid properties. The chemical and transport models, however not coupled, provided insights on the relevance of different trapping mechanisms and the potential of various minerals to react with the injected CO_2. Basbug et al. (2005) used 3D models to capture the role of different trapping mechanisms, namely structural, solubility, and mineral trapping, but neglected changes in porosity and permeability as a result of its mineralization. Also, the authors evaluated the effects of initial pressure, permeability anisotropy salinity, and injection rates on the CO_2 saturation. According to their findings permeability anisotropy played the most dominant role on the CO_2 saturation profiles. Their model however failed to capture the role of salinity on the CO_2 dissolution, as the salts precipitation and interaction with CO_2 were not accounted.

Another relevant modeling concept used to ensure understanding of geochemical processes occurring at various time and spatial scales during injection of CO_2 is the numerical simulation based on reactive transport models can capture the complexities of the reactions and the solute transport (Ding et al., 2018; Jin et al., 2016; Lagneau et al., 2005; White et al., 2005; Xu et al., 2011). Lagneau et al. (2005) used a single-phase, 2D reactive transport simulator to model the behavior of CO_2 dissolved in the water, taking into account the mineralogical composition of the

aquifer formations and the reactivity of the host rock with the dissolved CO_2. Despite the model limitations in terms of multiphase flow and the plume evolution, the authors captured the behavior of the CO_2 dissolved in the brine and illustrated the use of reactive transport for storage studies.

Numerous studies have examined the effects of variations in reservoir properties, brine characteristics, and operational parameters on CO_2 storage and trapping. Flett et al. (2007) assessed the role of reservoir quality and heterogeneous properties on trapping mechanisms and concluded that the degree of heterogeneity significantly affects migration and containment of CO_2. Hurter et al. (2007) employed pre-injection studies to determine how brine salinity changes affected the CO_2 injectivity. The authors used a compositional simulator that captured CO_2 and water's mutual solubility and salts' speciation in the aqueous phase. Zhao et al. (2010) performed a sensitivity analysis on CO_2 injection into a homogeneous reservoir varying salinity and residual phase saturations to examine the consequent changes in the amount of CO_2 dissolved in water. Other aspects investigated in terms of the impact of main geological, petrophysical and operational parameters include the geological depositional environment (Okwen et al., 2014), permeability ratios (Basbug et al., 2005), pressure conditions (Birkholzer et al., 2009), the hysteresis of relative permeability curves (Juanes et al., 2006), the reservoir wettability (Al-Khdheeawi et al., 2017), injection schemes (Baz et al., 2016), and the caprock integrity (Raza et al., 2016).

Sensitivity and uncertainty characterization studies have also been performed to incorporate parameter distributions and variability into the models. For instance, Lengler et al. (2010) analyzed the impact of unknown spatial variability of petrophysical properties on the saturation distribution, arrival time of the plume, and injectivity. Deng et al. (2012) assessed the reservoir and caprock heterogeneity influence on storage capacity, injectivity, and leakage. Sarkarfarshi et al. (2014) presented a sensitivity analysis that considered the impact of different physical and constitutive

relationships on the CO_2 plume evolution in a homogeneous reservoir. The authors concluded that porosity, residual saturation, entry capillary pressure, and the CO_2 relative permeability curves' endpoints are the most influential parameters on the average plume radius, maximum radius, and the overall plume spread.

More recent numerical simulations are based on robust models of CO_2 injection that account for multiphase and multicomponent flow, integrating realistic geological features. Diao et al. (2020) used 3D seismic attributes and well-log data to capture and validate the plume evolution observations from vertical seismic profile monitoring. Cao et al. (2020) used distance correlation and machine learning support vector regression to analyze the role of geomechanical and hydrogeological parameters, predicting the formation response, including pressure change and formation deformation. Nonetheless, these models have been limited to the integral role of the pore structure. Additional physics that affect the flow and transport of CO_2 in porous media, such as molecular diffusion, have not been fully considered. Future research efforts should emphasize the study of CO_2 processes at different scales, linking pore- to reservoir phenomena and behavior (Newell and Ilgen, 2019), aiming to include the heterogeneity of the porous medium, and to couple multiphase fluid flow, thermal, chemical and stress gradients in the simulations.

Table 3. Numerical simulation formulations of CO_2 injection in porous media.

Authors	Modeling approach	Model characteristics	Injection time	Model limitations
Pruess et al., 2001	2D, Reservoir-scale, Multiphase flow simulator, Batch reaction model	Studied the storage capacity in different phases (supercritical, dissolved) in aquifers with different compositions. Reported the trapping capacity of different minerals based on batch reaction models	30 years	The transport model and the geochemical model are not coupled. Predictions on trapping in the supercritical and aqueous phases are modeled based on homogeneous systems
Lagneau et al. 2005	2D - Reservoir-scale, Reactive transport, Operator splitting algorithm, Single phase	CO_2 injection in different aquifer formations considering mineral composition, coupled transport, and chemical reactions. Studied CO_2 dissolution and precipitation in carbonated and sandstone aquifers	Massive instantaneous injection	The model only considers the CO_2 dissolved in water and does not capture the plume evolution nor multiphase flow. Incorporating pore-scale physics can be improved by incorporating the reactivity of the minerals

Table 3 Continued

Authors	Modeling approach	Model characteristics	Injection time	Model limitations
Babus et al., 2005	3D, Reservoir-scale, Compositional simulator	CO_2 injection in a sandstone aquifer using two injector wells. Brine production from 6 wells. Structural, solubility, and mineral trapping considered. Studied injection rate effects, initial reservoir pressure, vertical permeability anisotropy, and salinity (around 30 different cases)	30 years, 170 years post-injection	The model did not consider changes in permeability and porosity due to mineralization or the pore structure's role. The salts precipitation and their role on CO_2 dissolution was not captured
Flett et al., 2007	3D, Reservoir-scale, Multiphase simulator	Studied the plume evolution with time, varying the degree of heterogeneity of the systems	50 years, 950 years post-injection	The model does not consider the brine and rock composition. Trapping due to mineralization processes is not included as well.
Hunter et al., 2007	3D, Reservoir-scale, Compositional simulator	Modeled injection of different brine salinities and evaluated the effects on CO_2 trapping mechanisms	Two years	Limitations related to the duration of the simulation and the neglected effects of post-injection interactions.
Taku Ide et al., 2007	2D, Reservoir scale, Multiphase simulator	Studied the effects of gravity, viscous, and capillary forces, as well as different injection schemes. Implemented homogeneous and heterogeneous models. Observed that residual trapping is positively affected by the gravity number	Ten years	Compositional characteristics of the brine and the rock are not included. Limitations related to the model dimensions (2D).
Birkholser et al., 2009	2D, Reservoir-scale, Multiphase simulator	CO_2 injection in a multilayer aquifers (sandstone) system and aquitards (shale) with homogeneous properties. Estimated pressure perturbation and brine migration. Evaluated the impact of CO_2 injection on groundwater systems	30 years, 70 years post-injection	Limitations related to neglecting the interaction and speciation of the aqueous components. Mineral trapping, including precipitation and dissolution of minerals, is not considered (the reactivity of between CO_2 and the rock)
Zhao et al., 2010	3D, Reservoir-scale, Multiphase simulator	CO_2 injection into homogeneous formations with realistic PVT properties. Performed sensitivity analysis on salinity, residual phase saturations, and permeability ratio	30 years	The model does not consider representative geological features. The evolution of the plume and the CO_2 dissolved are not studied after the injection period
Gasda et al., 2012	3D, Reservoir-scale, Vertically integrated model, Multiphase	Used a simplified numerical model to studied residual trapping, local capillary fringe effects, and convective mixing effects on CO_2 solubility. Evaluated CO_2 migration, plume footprint, and final distribution of trapped CO_2	50 years, 2000 years post-injection	The simplified model does not account for relevant physical and chemical phenomena occurring underground, neglecting, for example, diffusion, and the kinetics of the CO_2-brine-rock interaction
Okwen et al., 2014	3D, Reservoir-scale, Multiphase simulator	Modeled various geo-cellular structures to represent different depositional environments and capture their effects on CO_2 storage efficiency.	20 years	The model does not take into account the effects of capillary forces or diffusive flow. The chemical interactions among CO_2-brine-rock are also neglected

Table 3 Continued

Authors	Modeling approach	Model characteristics	Injection time	Model limitations
Sarkarfarshi et al., 2014	3D, Reservoir - scale, Multiphase simulator	Proposed a homogeneous reservoir model to evaluate the uncertainty of different physical and constitutive relationships on the plume evolution. A total of 14 other parameters where considered	One year	The short simulation time does not allow for a proper study of the plume evolution, the role of different trapping mechanisms, and the CO_2-brine interaction. The speciation inside the brine is not considered.
Baz et al., 2016	3D, Reservoir - scale, Multiphase simulator	Investigated the optimization of residual and solubility trapping in 3D geological representative models. Studied different injection configurations including horizontal wells, water-gas alternated injection, and simultaneous water-gas injection	40 years, 100 years post-injection	The model does not consider diffusive flow and capillary forces. The chemical interactions among CO_2-brine-rock are also neglected
Al-Khdheeawi et al., 2017	3D, Reservoir-scale, Multicomponent, Multiphase simulator	Evaluated the impact of reservoir wettability on plume behavior and trapping mechanisms. Strongly water-wet reservoirs have higher CO_2 storage in the form of residual trapping	Ten years	The simulation time limits the plume evolution observations, as later on, the relative contributions of different trapping mechanisms may change. Also, the mineral composition of the rocks is not considered, and how the interaction mineral-CO_2-brine can affect the CO_2 storage
Diao et al., 2020	3D, Reservoir-scale, Compositional simulation	Captured CO_2 plume migration in a heterogeneous, low permeability reservoir. Accounting for realistic geological features and validating vertical seismic profiles of the plume	Four years	The model does not integrate the pore level physics that could be relevant to the trapping processes. Additional geochemical considerations could be included to improve the characterization of the CO_2 behavior

1.3. Dissertation Outline

Numerical simulation of physical and chemical phenomena occurring at pore- and reservoir-scales constitutes the best tool to comprehend the fluid-rock interactions associated with the injection or extraction of fluids in rock formations. After introducing the research objectives in terms of modeling of various subsurface engineering applications and presenting a brief literature review of the different modeling paradigms implemented to capture the processes of interest, we proceed to outline the rest of the dissertation as follows:

In Chapter 2, particle transport and trapping are studied by integrating modeling of pore-scale phenomena with hydraulic fracturing simulation at the reservoir-scale to investigate the effects of fracturing fluid invasion and proppant crushing on the formation permeability damage at the matrix-fracture interface. First, the critical physical phenomena related to particle transport and entrapment at the pore-scale is reviewed, identifying the forces acting upon solid particles and trapping mechanisms. Next, the particle plugging simulator is presented. The model's objective is to quantify the effect of particle trapping at the pore-scale on the system permeability. The resulting pore-scale model is coupled with a commercial reservoir-scale fracture simulator to capture particles' transport and retention derived from proppant disintegration. The simulator is then applied to a case study in the Wolfcamp Shale.

In Chapter 3, the influence of chemical diagenesis on macroscopic properties from a pore-scale perspective is examined. Initially, chemical diagenetic processes related to precipitation and dissolution processes are revised, including standard geochemical systems encountered and reservoir quality changes. Then, the modeling workflow that integrates mineralogical, petrophysical, and chemical data to capture diagenesis's role in migration pathways' evolution is presented. The pore-scale model used has a two-pronged approach that combines the diagenetic analysis with reactive transport simulation. The first component involves examining the depositional environment, mineralogy, and pore structure characteristics of the formation to identify possible diagenetic controls on reservoir quality. The second component comprises the representation of the pore-space features based on the observations from diagenetic analysis and numerical simulation of fluid transport and mineral reactions related to relevant diagenetic events, considering advection, diffusion, and reactive transport. The workflow developed is then applied

to critically analyze diagenetic signatures in the Woodford Shale, focusing on rock-fluid interactions that cause precipitation and dissolution.

Chapter 4 comprises the investigation of geological sequestration of CO_2 in saline aquifers to undertake questions associated with the CO_2 plume characterization and monitoring. Essential aspects of the sequestration process are reviewed, including the CO_2-fluid-rock interactions, trapping mechanisms, and monitoring and verification techniques used to track the evolution of the CO_2 plume. Then, the integrated modeling framework is introduced. The framework is employed to evaluate the CO_2 storage during long-term injection and post-injection periods incorporating hydrogeological, petrophysical, and operational characteristics of the process. The model provides the means to ascertain the relative influence of selected parameters on the plume characteristics and the CO_2 storage via different trapping mechanisms, including the impact of heterogeneity and anisotropy in the formation properties, the litho-facies dependencies, the aquifer fluid composition, and the role of various transport mechanisms such as molecular diffusion. Besides, analytic and diagnostic tools are presented. These tools aim to monitor several well-based fluid variables, explore the plume's temporal and spatial evolution, and determine how representative the near-wellbore properties contrast with the entire plume body.

To conclude, in Chapter 5, the contribution of the research work performed is discussed for each of the subsurface applications reviewed during this investigation.

Chapter 2. Formation Damage at the Matrix-Fracture Interface During Hydraulic-Fracturing: A Multiscale Model of Particle Transport and Plugging

2.1. Introduction

Recent commercial exploitation of unconventional reservoirs was enabled by the development of horizontal drilling and hydraulic fracturing technologies. During hydraulic fracturing operations, large quantities of fluids at high pressures are injected into the formations to create fractures that enhanced permeability by increasing the contact area between the well and the reservoir (King, 2012). Successful operations result from maximizing the conductivity of the created fractures while reducing formation damage effects. Therefore, the recovery efficiency of hydraulically fractured wells is influenced by formation damage, and understanding the matrix-fracture interaction becomes vital to determine the impact on the conductivity and productivity. Several damage mechanisms that affect the conductivity can be identified during or after the hydraulic fracturing operations, including fracturing fluid invasion, proppant embedment, proppant crushing, gel filter cake residue at the fracture face, and the fracturing fluid residue in the proppant packs (Gdanski et al., 2005; Reinicke et al., 2010). Out of the possible damage mechanisms, the fluid invasion is considered to have one of the most harmful effects on the conductivity, resulting in chemical interaction with the in-situ fluids and rock minerals and facilitating proppant embedment and fines migration.

Our understanding of various characteristics of the fracturing process associated with damage is based on extensive research on hydraulic fracturing, from laboratory tests to numerical modeling. Several numerical models have been developed to predict the properties and performance of hydraulic fractures. Over the years, these models have become more complex involving multiple

processes to optimize the treatment design, including multiphase flow, fracture propagation, heat transfer, mechanical deformation, and the interaction with natural fractures (Hossain and Rahman, 2008; Ji et al., 2009; Li et al., 2012; Marongiu-Porcu and Economides, 2008; Rocha et al., 2017; Sun et al., 2014). These studies have helped the design and performance prediction at the reservoir scale. However, to improve the reservoir models, it is imperative to integrate different aspects of the damage mechanisms at the pore level to consider pore space characteristics such as its heterogeneity and interaction with fluids and particles.

This chapter explores damage mechanisms at the matrix fracture interface related to the hydraulic fracturing process using a combined approach of pore- and reservoir-scale simulation. First, a review of crucial physical phenomena related to particle transport and entrapment at the pore-scale is presented, identifying the forces acting upon solid particles and associated trapping mechanisms. The particle plugging simulator is then introduced, integrating pore-scale phenomena with the hydraulic fracturing process at the reservoir-scale. The objective is to improve the comprehension of fracturing fluid invasion and proppant crushing effects on the formation's conductivity at the matrix-fracture interface. The pore-scale model is coupled with a commercial reservoir-scale fracture simulator to capture particles' transport and retention derived from proppant disintegration. Finally, the hydraulic fracturing operation impact on the matrix-fracture interface permeability in a case study on the Wolfcamp Shale is reported.

2.2. Forces Acting upon Solid Particles at the Pore-Scale

In porous media, the migration of suspended solids can lead to changes in the pore-space structure and alter fluid flow properties due to particle retention. As the fine particles move along the preferential migration pathways, they can be captured, retained, and deposited within the porous matrix. The grain surface interacts with both the fluid and solid particles through various forces

that can be classified into three categories: (1) forces related to transport, (2) forces related to attachment, and (3) forces related to detachment mechanisms (Ives, 1985; Zamani and Maini, 2009). Figure 1 shows a schematic representation of the forces acting upon particles traveling through a pore.

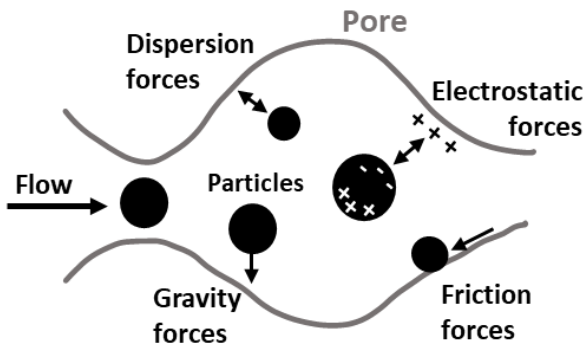

Figure 1. Forces acting upon particles inside a pore, including gravity forces (related to transport), dispersion, electrostatic and friction forces (related to attachment and detachment mechanisms). Modified from (Nunes et al., 2010).

The forces related to transport are responsible for particle migration. These forces include inertia, gravity, diffusion, and hydrodynamic forces (Ives, 1985). Inertia influences the particles to maintain motion in a straight line. While gravity forces result from the density difference between the particle and the fluid promoting movement in the gravity direction following Stoke's law. Diffusion forces are related to the particles' thermal motion that tends to move in the concentration gradient direction towards a more homogeneous concentration. And hydrodynamic forces consider the fluid shearing and the pressure forces that cause the particle motion along with the fluid flow (Bedrikovetsky et al., 2010; Civan, 2007; Herzig et al., 1970).

The forces related to attachment and detachment act on the particles when they are near the grain surface. Attractive forces include surface forces such as London- van der Waals and friction-drag. The London dispersion forces rise from the electromagnetic waves generated by the electronic characteristics of atoms and molecules. The friction-drag results from the flow resistance

experienced at the surface. On the other hand, detachment mechanisms comprise shearing and electrostatic forces. In terms of shearing forces, the detachment occurs when the shearing force created by the shear stress of the liquid is greater than the forces attaching the particles to the surface the particles can be detached and mobilized. The other mechanisms related to electrostatic forces created due to ionic conditions (such as electrostatic double-layer forces) cause detachment from the repulsive forces originated when the grain and the particles carry similar electrostatic charges (Civan, 2007; You et al., 2015).

2.3. Particle Trapping Mechanisms

The forces acting upon solid particles described in the previous section determine particle deposition and release rates and influence the type of retention mechanisms that limit the particle migration. The first studies on particle transport in porous media gave origin to what is known as filtration theory or deep filtration theory founded by the research of Herzig et al. (1970), Ison and Ives (1969), and Ives (1985). In 1986, McDowell-Boyer et al., based on the previous work on filtration, defined three main mechanisms of particle trapping: (1) surface filtration, (2) straining filtration, and (3) physicochemical filtration. These mechanisms can entrap particles in the pore space, each associated with the relation between the particle size and the porous media pore size. A brief description of these mechanisms is presented below.

Surface filtration occurs when particles are too large to enter the pore system and form a permeable filter cake that can affect the system's fluid flow characteristics (i.e., locally reduce the system's permeability at the entrance). For instance, at a macroscopic scale, surface filtration has been commonly used to minimize the mud loss into the formation during drilling operations and contribute to wellbore stabilization (Ezeakacha et al., 2017). Figure 2a shows a sketch of surface filtration, with the solid particle being retaining at the entrance of the porous medium

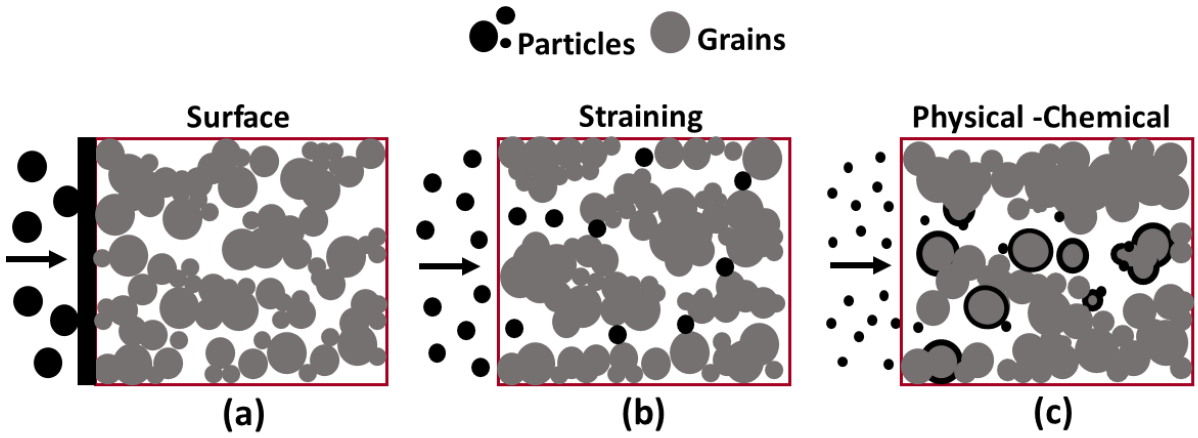

Figure 2. Main particle trapping mechanisms at the pore-scale. (a) surface, (b) straining, and (c) physicochemical filtration. The prevalence of a given filtration mechanism is related to the size of the particles traveling through the system, with surface filtration occurring for larger particles and physicochemical filtration playing a dominant role in the retention of fine particles (McDowell-Boyer et al., 1986).

On the other hand, straining filtration occurs when particles are small enough to enter the porous media but are trapped in smaller pore spaces such as the pore-throats. This process is considered the dominant mechanism for permeability reduction (Imdakm and Sahimi, 1987). Early studies based on experimental data on particle capture by Sakthivadivel (1969) indicated that a critical factor determining straining is the ratio of the media's pore diameter to the particle diameter (d_m/d_p), with a permeability reduction up to a factor of 7-15 for ratios between 10 and 20. Figure 2b shows the basics of straining.

The remaining mechanism, physicochemical filtration, can retain particles much smaller than the median pore size due to attractive forces between the pore surface and the particles, such as electrostatic and gravity forces and other sorption phenomena due to the pore surface roughness (Babakhani et al., 2017). Figure 2c illustrates this mechanism.

2.4. Formation Damage Related to Hydraulic Fracturing

The formation damage generated during hydraulic fracturing operations has a significant role in the fractured wells' recovery efficiency. Therefore, the conductivity and productivity of

hydraulically fractured wells are affected by the matrix-fracture interaction and the fracture face damage (Gdanski et al., 2005). Several damage mechanisms have been identified during the fracturing operations, namely fracturing fluid invasion, proppant embedment, proppant crushing, gel filter cake residue at the fracture face, and the fracturing fluid residue in the proppant packs (Reinicke et al., 2010). As a consequence of formation damage, various permeabilities can be encounter in the region near the fracture. Figure 3 illustrates these permeability zones, including the reservoir permeability (k_i), the permeability of the altered fracture face (k_s) that extends into the reservoir a distance (W_s), and proppant pack permeability or fracture permeability (k_f) in the area given by the fracture width (W_f) and the fracture length ($2X_f$).

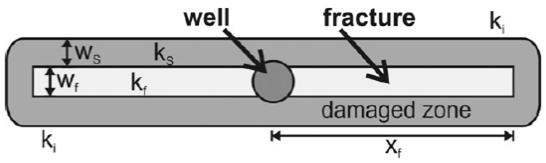

Figure 3. Depiction of various permeability regions found in a hydraulically fractured reservoir with damage in the matrix-fracture interface (Reinicke et al., 2010).

Out of the formation damage mechanisms related to fracking operations, fracturing fluid invasion is considered one of the most destructive processes. The fracturing fluid flow into the matrix can reduce the permeability through different processes, such as clay swelling, chemical adsorption, formation dissolution, solid precipitation, and wettability alterations. Various experimental and numerical studies have been performed to explore the fracturing fluid's interaction, the formation fluid, and the rock matrix (Bazin et al., 2010; Cramer, 2005; Eveline et al., 2017; Farah et al., 2015; Wu et al., 2019). For instance, Cramer (2005) correlated fracture skin with fluid loss and water blockage by integrating production and pressure buildup data analysis. Bazin et al. (2010) used core experiments to evaluate fracture-face damage by fracturing fluid leak-off, concluding that the formation's water sensitivity is responsible for significant permeability reductions. And

Eveline et al. (2017) developed a numerical simulator to understand the clay-water interaction, swelling mechanisms, and their impact on permeability, representing the shale matrix as a multi-scale porosity medium with an altered zone.

Proppant embedment on the fracture face is also related to the invasion of the fracturing fluid. Both fluid leak-off and the formation closure stress facilitate proppant penetration into soft formations during hydraulic fracturing. Furthermore, the rock's mechanical properties, such as Young's modulus, appear to be affected by the fracturing fluids entering the formation, ultimately enabling the proppant embedment and altering the fracture conductivity. Laboratory studies conducted in shales have shown that a reduction in Young's modulus due to contact with fracturing fluids influences the embedment process and can cause a reduction in the fracture conductivity (Akrad et al., 2011). Further studies are focus on the prediction of the conductivity loss in the fractures as a result of proppant embedment at different closure pressures based on analytical models, proppant embedment tests, and computational fluid dynamics (Alramahi and Sundberg, 2012; Zhang et al., 2015)

Other processes associated with the fracture conductivity loss are the migration of fines into the proppant pack and the generation of fines derived from proppant crushing. The closure stress in the fracture is the main factor influencing the proppant's mechanical degradation and can rapidly affect the permeability in the matrix-fracture interface and the pack's conductivity (Terracina et al., 2010; Weaver et al., 1999). Coupled fluid flow and geomechanical numerical models have been used to identify the proppant crushing region and quantify the pack damage severity (Han et al., 2016). Besides mechanical degradation, another mechanism reported is chemical degradation or proppant diagenesis. In this case, diagenesis refers to dissolution and precipitation reactions that can reduce the pack's porosity, permeability, and strength (Osholake et al., 2011). Various

investigations have examined the role of the proppant composition, the formation mineralogy temperature, and closure stress to optimize the proppant performance (Duenckel et al., 2011; Weaver et al., 2007).

2.5. Model Formulation: Particle Plugging Simulator

In this section, the pore-scale particle plugging simulator proposed is introduced. The model is based on a 3D pore network that captures the pore space topology and serves as the frame for fluid flow and particle transport simulations. The simulator computes the particle retention due to mechanical straining and the changes in porosity and permeability caused by the trapping process. The pore-scale simulator is coupled with a reservoir-scale simulation of the hydraulic fracturing operation that provides the required input for the particle transport/retention model, comprising: the diameters and concentration of the fines migrating into the system, the leak-off rate (inlet velocity), and fracture closure pressures. A description of the pore network generation, the flow field's calculation, and the transport and retention model are presented below.

2.5.1. Pore Network Model

3D pore networks represent the porous medium structure, where the pore space is divided into pore-bodies and pore-throats. The pore-bodies are the broader regions that account for the pore volume. In contrast, the pore-throats are the narrowest regions connecting neighboring pore-bodies and acting as flow constrictions that have a dominant effect on the fluid displacement. The pore size distributions of bodies and throats included in the network generation were modeled based on Weibull distributions, with shape and scale parameters selected for the characteristic throat and body size distributions and the radii ranges established by characteristics of the porous media of interest.

The pore-body connectivity is defined by the coordination number, which indicates how many throats are associated with a single pore. Coordination numbers typically varying from 0 to 14, with a mean between 3 and 4 in sandstones (Raoof and Majid Hassanizadeh, 2010). Cylindrical ducts with various cross-sectional geometries were considered (circular, triangular, and square) to capture different pore shapes in the pore space. The location, coordination number, and cross-sectional geometry of each pore-body and -throat were assigned stochastically. Figure 4. shows a sketch of the pore network generated for flow simulation. Pore-bodies are represented as spheres and pore-throats as cylinders, with the spheres' size and color reflecting the pore-body radius. Additional relevant parameters such as pore volume, cross-sectional area, and shape factor (ratio between the cross-sectional area and squared perimeter) were calculated for each pore-body and throat based on the pore sizes and geometry.

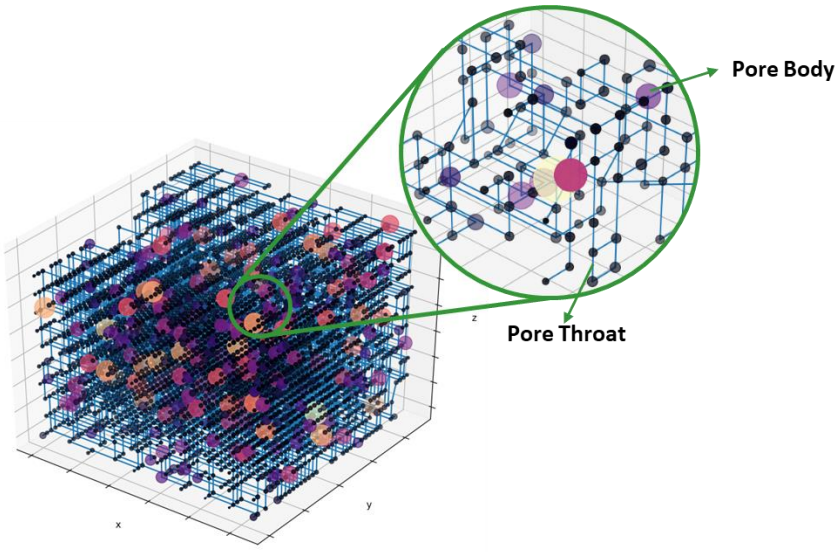

Figure 4. Pore network sketch. Pore-bodies are represented as spheres with color and sphere sizes given by the pore radius. While and pore-throats are represented as cylinders without any association in color or size with the original throat radius.

Then, the system's initial porosity was obtained by adding the volumes of pores and throats and dividing by the total volume of the model. It is necessary to identify boundary throats, dead-ends, and isolated pores' clusters to prepare the network for the flow simulation. These pore-bodies and

-throats should be removed from the flow simulations to ensure no-flow boundary conditions on the faces that do not correspond to the inlet or outlet and avoid singularities in the matrix solution.

2.5.2. Calculation of the Flow Field

After the pore network and the particle size distributions are defined, the network's flow field is established by setting a pressure difference in the flow direction. The faces perpendicular to the flow are identified as inlet and outlet, and all other boundaries are treated as no-flow boundaries. Mass conservation is imposed in each pore, i.e., the sum of discharges into and out of the pore must be zero to solve the flow field. For single-phase, steady-state, incompressible flow, the continuity equation for a given pore i is given by Eq. 5.

$$\sum_{j} q_{ij} = 0 \tag{5}$$

Where, q_{ij} is the volumetric flow rate through the throat that connects pore i with a neighbor pore j. The volumetric flow rate through a throat is derived from the simplification of the Navier-Stokes equation for laminar flow, which relates the flow rate and pressure drop (Poiseuille law) as shown in Eq. 6 (Thompson and Fogler, 1997).

$$q_{ij} = \frac{g_{ij}}{l_{ij}}(p_j - p_i) \tag{6}$$

Where, g_{ij} is the hydraulic conductance of the throat, l_{ij} is the distance between two-pore centers, p_i and p_j are the pressures in pores i and j, respectively. The hydraulic conductance of the throat is a function of its geometry and shape factor. A unit flow channel is defined to calculate the conductance, involving pore i, its neighbor j, and the throat ij connecting them, as shown in Figure 5. And the overall conductance is calculated as the harmonic mean of the elements' conductance in the unit flow channels, as shown in Eq. 7.

$$\frac{l_{ij}}{g_{ij}} = \frac{l_t}{g_t} + \frac{1}{2}\left(\frac{l_i}{g_i} + \frac{l_j}{g_j}\right) \tag{7}$$

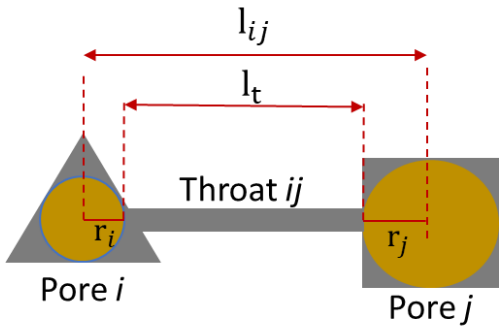

Figure 5. Elements of a unit flow channel including pore i, j and the throat connecting them. The hydraulic conductance of the throat is calculated, considering the unit flow channel defined for each throat. Based on (Patzek 2001)

Individual hydraulic conductance of the pores and throats were computed based on the dimensionless hydraulic conductance expressions derived by Patzek and Silin (2001) for different duct cross-sections as shown in Eq. 8 to 10 for triangular, square, and circular geometries. Where g is the hydraulic conductance, μ is the fluid viscosity, A is the cross-sectional area, and G is the shape factor.

$$\frac{g\mu}{A^2} = (0.5)G \tag{8}$$

$$\frac{g\mu}{A^2} = \left(\frac{3}{5}\right)G \tag{9}$$

$$\frac{g\mu}{A^2} = (0.5623)G \tag{10}$$

The system of linear equations that characterize single-phase flow in the network was obtained by substituting Eqs. 6 to 10 into Eq. 5 for each pore in the network. The boundary conditions employed to solve the system of equations included a constant inlet flow rate (Q) that represents the sum of the flow rates overall inlet pores (Eq. 11), and an outlet pressure reference value (p_{outlet}) meaning that for the outlet pores, the sum of all flow rates (Q_{out}) will have an unknown

but non-trivial value (Eq. 12) (Øren et al., 1998). Successful setup of the model equations should ensure that inlet and outlet flow rates are equal, given the system's conditions.

$$Q = \sum_{j=inlet} \left[(p_{inlet} - p_i) \frac{g_{ij}}{l_{ij}} \right] \tag{11}$$

$$Q_{out} = \sum_{j} \left[(p_j - p_{outlet}) \frac{g_{ij}}{l_{ij}} \right] \tag{12}$$

2.5.3. Particle Transport and Retention Model

The transport and retention model's purpose is to keep track of the particles' movement and plugging throughout the network. The injected particles' behavior is affected not only by the fluid flow but also by the particle interaction with the pore space structure. As previously indicated, particles traveling inside the porous media are subjected to physical trapping mechanisms such as straining, gravity segregation, and electrical attraction. Out of these mechanisms, straining or size exclusion has the highest impact on permeability reduction and alteration of the migration pathways. Thus, the model considers particle retention based on the relationship between the particle size and the size of pore-bodies or throats that they travel through. Figure 6 presents a flowchart with the main components of the particle transport model implemented for the pore networks previously generated and considering particle retention due to straining.

First, the boundary conditions specified in the flow field calculation are set for the inlet and outlet faces. The fractional flow into each inlet pore was then calculated from the total inlet flow rate into the network. Once the fractional flow into each inlet pore is defined, the particle path is computed. As previously mentioned, the filtration process in porous media is governed by the system's flow characteristics, but a stochastic component influences it. The path selection of a given particle from inlet to outlet throughout the network is computed using the flow-bias

probability concept developed by Rege and Fogler (1987) to account for the nature of filtration. When a particle enters a pore, it has a choice of exit paths. According to the flow-rate probability concept, the exit channel should be selected randomly, but with a bias toward the routes with larger flow rates. The higher the fractional flow into a pore-body or -throat, the greater the probability of selecting that pore as the entrance.

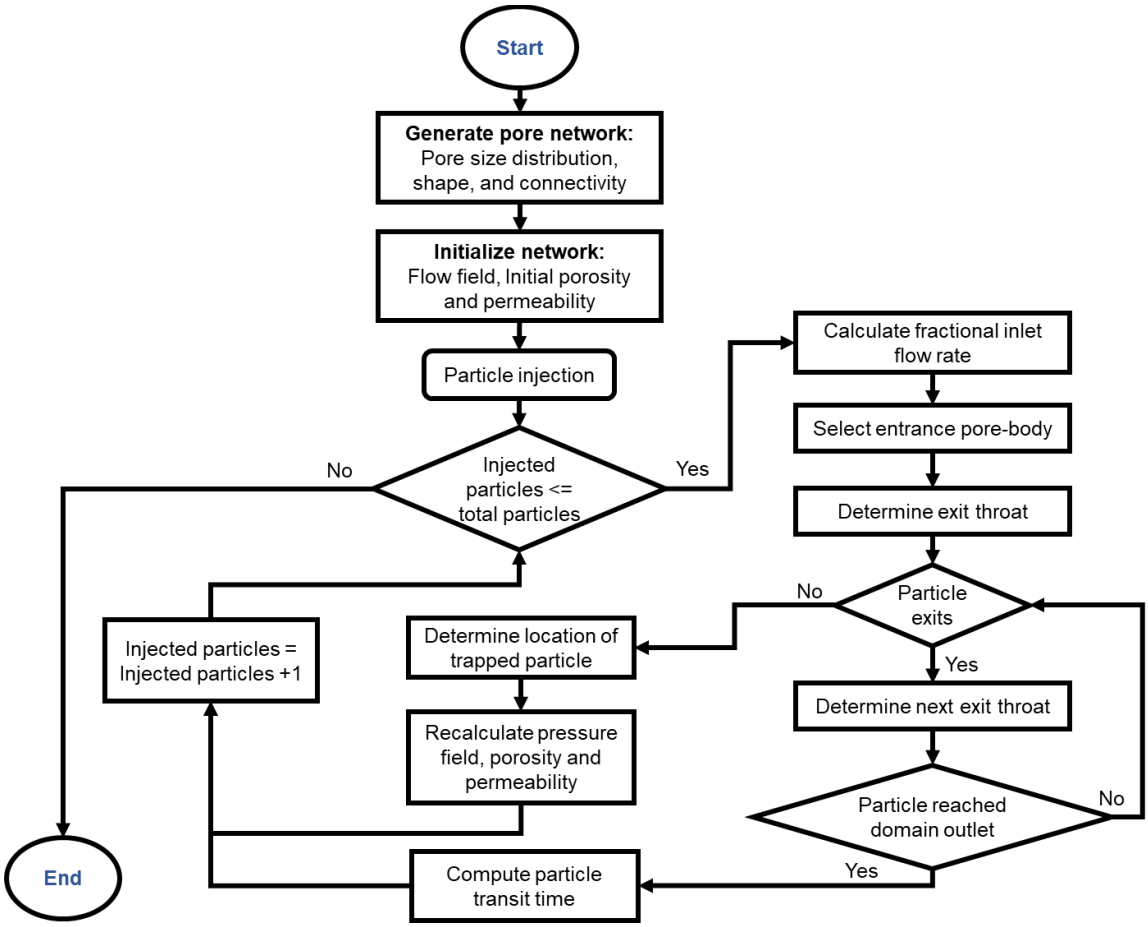

Figure 6. Diagram of the particle transport simulator considerin straining as the primary trapping mechanism causing permeability damage.

Thus, a probability range is assigned to each path related to the fractional flow rate, and a random number between 0 and 1 is generated for each particle exiting a given pore. If the random number falls inside the range for one of the possible exit throats, the particle will travel through it. Figure 7 shows a representation of the path selection scheme. A particle travels into the pore and has three

possible exit paths A, B, and C. A probability range is assigned to each exit based on the possibility of a particle traveling through it related to each path's flow rates. For instance, in the figure, the range for path A is 0 to 0.3, for B is 0.3 to 0.8 and for C is 0.8 to 1. If the random number generated is 0.5, the particle will travel through path B.

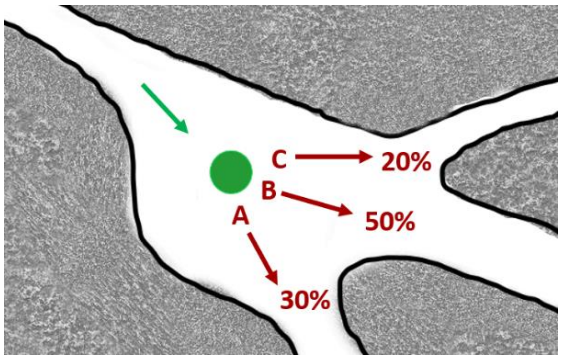

Figure 7. Path selection for particle transport in porous media based on flow-biased probability (Rege and Fogler, 1987). The path selected preserves its stochastic nature while considering the effect of the flow rate in the process.

Next, particles are injected one after another into the network, their paths and travel times recorded individually. If a particle is larger than the pore throat it travels through, it will be trapped. When a particle is trapped, it reduces the throat's hydraulic conductivity, the volume of the pore, and the probability of another particle selecting that path. Consequently, the pressure, porosity, and permeability of the network model are affected. Particle trapping also alters the migration pathways by modifying the pore volume and decreasing the pores' connections. The flow field is recalculated every time a particle is trapped, and the final spatial location of the trapped particles is recorded. If the particle exits the network, the transit time is computed. The latter is the amount of time that it takes for the fluid transporting the particle to flow across the network model from inlet to outlet.

2.5.4. Particle Size Distribution from Proppant Crushing – Population Balance

The distribution of particle sizes coming into the network also plays a role in the particle interactions with the pore space. It is necessary to determine the size distribution and its evolution as a function of time and stress to investigate the migration and retention of fines generated by proppant crushing and fluid invasion during hydraulic fracturing. The concept of population balance has been applied to study different phenomena from particulate suspensions in porous media (Sharma and Yortsos 1987) to proppant size changes due to crushing during hydraulic fracturing (Zhang et al., 2015).

Here, a population balance model is implemented to capture the particle size reduction and describe the population density change per unit application of stress. The balance facilitates the description of changes in the particles' pore size distribution migrating into the formation. Figure 8 shows the algorithm's description to calculate the particle size distribution changes with stress based on the population balance equations previously defined by Zhang et al. (2015).

The particle population balance has two main components: a selection function, $S(x)$, and a breakage function, $B(y,x)$. The selection function $S(x)$ described in Eq. 13, represents the number of particles that will experience size reduction from a given size (x) per unit stress (σ). While the breakage function $B(y,x)$ characterizes the number of particles that experienced size reduction from larger sizes (y) into the specific size interval (x) as shown in Eq. 14. In these equations, $P(x,\sigma)$ refers to the cumulative mass fraction of the particles smaller than size x at stress σ.

$$S(x) = -\frac{\frac{\partial}{\partial\sigma}\left[\frac{\partial P(x,\sigma)}{\partial x}\right]}{\frac{\partial P(x,\sigma)}{\partial x}} \tag{13}$$

$$B(y,x) = -\frac{\frac{\partial P(x,\sigma)}{\partial \sigma}}{\frac{\partial}{\partial \sigma}\left[\frac{\partial P(y,\sigma)}{\partial y}\right]}, \quad 0 \le x \le y \tag{14}$$

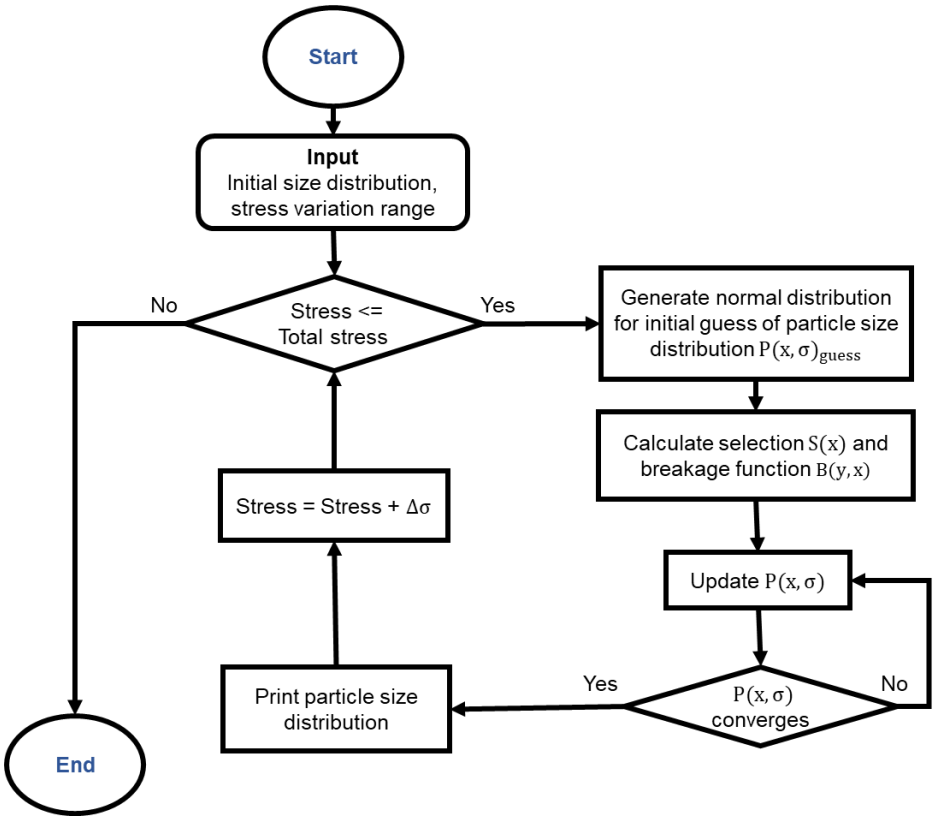

Figure 8. Population balance algorithm for particle size distribution changes with stress.

The integrodifferential equation for size reduction is shown in Eq. (15). It is assumed that the particles can only be crushed into smaller sizes, and there are no additional "sources" of particles. The selection function, Eq. (16), and breakage function, Eq. (17), that were chosen for this analysis are the expressions given by Austin (1999).

$$\frac{\partial}{\partial x}\left[\frac{\partial P(x,\sigma)}{\partial \sigma}\right] = -S(x)\frac{\partial P(x,\sigma)}{\partial x} + \int_{y=x}^{x_{max}} \frac{\partial B(y,x)}{\partial x}\frac{\partial P(y,\sigma)}{\partial y} S(y)dy \tag{15}$$

$$S(x) = a_1 x^{a_2} \tag{16}$$

$$B(y,x) = a_3\left(\frac{x}{y}\right)^{a_4} + (1-a_3)\left(\frac{x}{y}\right)^{a_5}, 0 \le x \le y \tag{17}$$

The empirical coefficients a_1 to a_5 were determined by Zhang et al. (2015), from experimental data from Gardner and Austin (1962). The values assigned to the coefficients are: a_1= 3e-4, a_2= 0.565, a_3= 0.65, a_4 = 1.25, and a_5 = 4.5. The initial particle size distributions, $P_0(x,\sigma)$ must be obtained from available data on the particles of interest, as input for the balance equation.

2.5.5. Numerical Solution

The particle transport and plugging model described requires the solution of two different sets of equations. First, the population balance equation has to be solved to determine the particle size distribution changes with stress. The particle size distribution obtained is provided as input for the pore-scale transport simulation. A finite difference method is used to solve the discretized population balance equation (Eq. 18) using the selection and breakage function approximations defined in Eq. (16) and Eq. (17).

$$P_i^{n+1} = -S_i^{n+1}(P_i^{n+1} - P_{i+1}^n)\Delta\sigma + \sum \overline{S_j^n}\left(P_j^{n+1} - P_{j+1}^n\right)\left(B_{j,i}^{n+1} - B_{j,i+1}^n\right)\Delta\sigma + (P_{i+1}^{n+1} - P_{i+1}^n) + P_i^n \tag{18}$$

Where n is the time counter, i,j are the particle size range counters, the first term on the right represents the selection function, and the second term the breakage function.

After every variable and parameter required as input for the transport model has been calculated, the flow equation for each pore can be defined (Eq. 4). The set of equations obtained represents a linear system that can be solved for the pressure distribution using an iterative technique appropriate for large and banded matrices. Every time a particle is trapped, the pressure field and the total flow rate are recalculated, and the change in the system permeability is computed using

Darcy's law. Properties such as porosity and permeability can be upscaled for particle transport simulation at the macroscale by coupling the pore-network model with a continuum scale model for fluid flow and particle transport.

2.5.6. Coupling with a Hydraulic Fracture Simulator at the Reservoir-Scale

In this study, we coupled a particle transport and retention simulator (at the pore-scale) with a fracture simulator (at the macroscopic scale) to model and investigate multiple pore-scale phenomena and understand their effects at larger scales, in particular at the matrix-fracture interface. The coupling consists of connecting the pore-scale model to a continuum scale region at the boundary (matrix-fracture interface). It implies matching the boundary conditions at the interface of both scales (Balhoff et al., 2007).

The fracture simulator used is a commercial simulator with fully coupled fluid/solid transport modules to model planar geometry hydraulic fractures at the reservoir scale in the shale formation of interest (Barree and Associates LLC, 2017). The simulator predicts the geometry and properties of the hydraulic fracture. Three main inputs are required for the simulation: a 3D static model that captures the petrophysical properties of the formation, well log data to fully describe the rock's mechanical behavior, and the fracture design parameters.

We performed a sensitivity analysis on the fracturing process's operational constraints such as proppant type, the volume of fluid injected, proppant volume, and injection rate. Table 4 shows the design variables used and the appropriate ranges considered for the analysis. A total of 40 scenarios were generated using the Plackett-Burman design of experiments to screen the extreme values of the factors involved. Besides, the objective function formulated provides the optimal fracture conductivity for the cases investigated. Various response variables required for the

coupling with the pore-scale simulator were examined, such as leak-off and proppant concentration (see the complete list in Table 5). Then, three scenarios were selected from all the cases studied. The selection is based on ranking the most pessimistic, the most probable, and the most promising fracturing conductivity results: P10, P50, and P90.

Table 4. Factor treatment parameters and range values considered for sensitivity analysis on the hydraulic fracturing simulation

Design Parameters	Ranges
Fluid type	Slick water High Concentration Friction Reducer (HCFR)
Proppant type	Sand 12/20 Sand 40/70
Fluid Volume (gal)	40,000 - 80,000
Proppant Concentration (ppa)	1 - 3 1 - 4 2 - 3 2 - 4
Proppant Volume (lb)	60,000 - 180,000
Injection rate (bbl/m)	50 90

Table 5. Response variables investigated during the hydraulic fracturing simulation.

Response Variables	Response ranges
Net pressure (psi)	690 – 1,060
Leak-off (gal)	0.009 - 0.153
Proppant concentration (ppg)	0.3 - 1.5
Fracture conductivity (mD-ft)	7.7 - 75.8
Fracture width (in)	0.14 - 0.24
Pressure (psi)	6,580 – 7,275
Closure stress (psi)	5,820 – 6,230

After the sensitivity analysis is performed, the representative fracture-treatment scenarios obtained are provided to the pore-scale simulator to investigate the matrix-fracture interface's mechanical behavior. The pore-scale simulator receives the fracture parameters as input to determine the retention and transport of fines derived from the proppant degradation during the fracturing process

and the changes in permeability and porosity in the fracture face. Figure 9 shows a summary of the workflow that describes the relationship between both simulators.

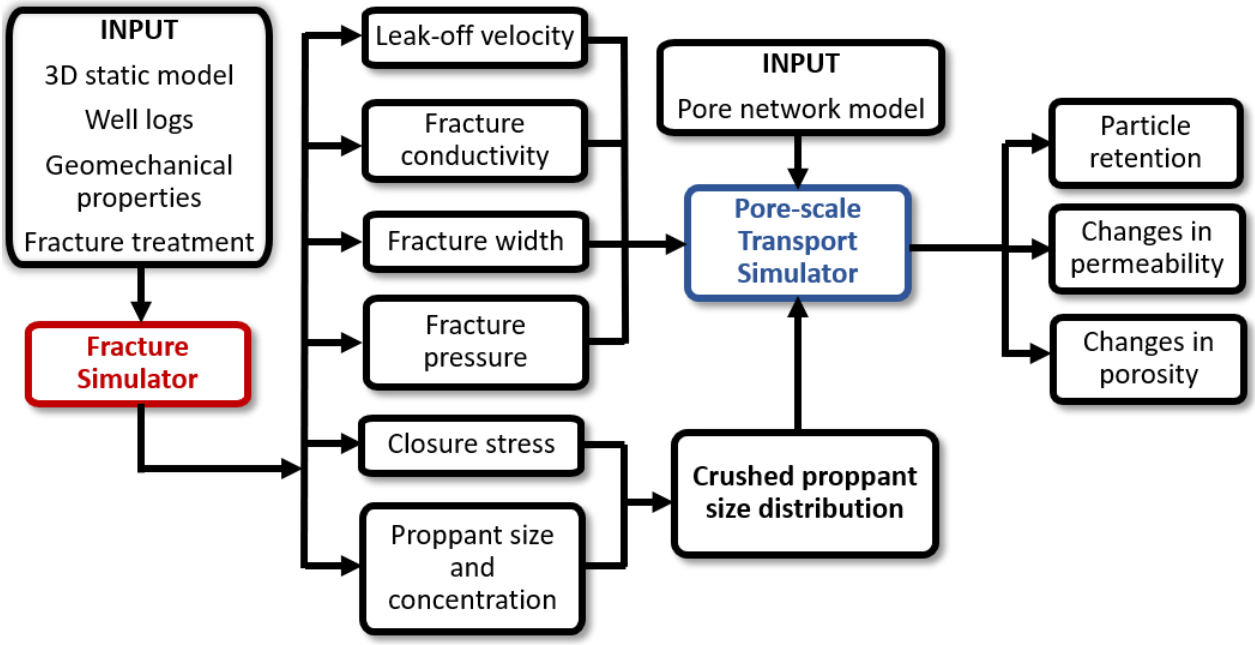

Figure 9. Workflow for coupling the fracture and pore-scale transport simulators.

2.6. Results

This study's primary purpose was to understand the role of particle-plugging processes at the pore-scale on the fracture conductivity at larger scales during hydraulic-fracturing operations. The coupled model presented accounts for the pore structure's influence and the pore space's heterogeneous nature while modeling hydraulic fracturing operations at the reservoir scale, specifically in the region comprising the matrix-fracture interface. To illustrate the application of the particle plugging model and the reservoir scale hydraulic fracturing simulator, we present the results from the numerical simulations of a hydraulic fracture in a shale reservoir. In this case, the Wolfcamp shale.

The 3D static model used in the simulations captures the geological and petrophysical characteristics of the Wolfcamp shale, built from available petrophysical measurements and well

log data for ten wells in Howard County within the Midland basin (Phan et al., 2018). The sensitivity simulations for various hydraulic fracture operations previously established were performed on the 3D static model. Figure 10 shows an example of the multi-stage hydraulic fractures created from one of the sensitivity runs.

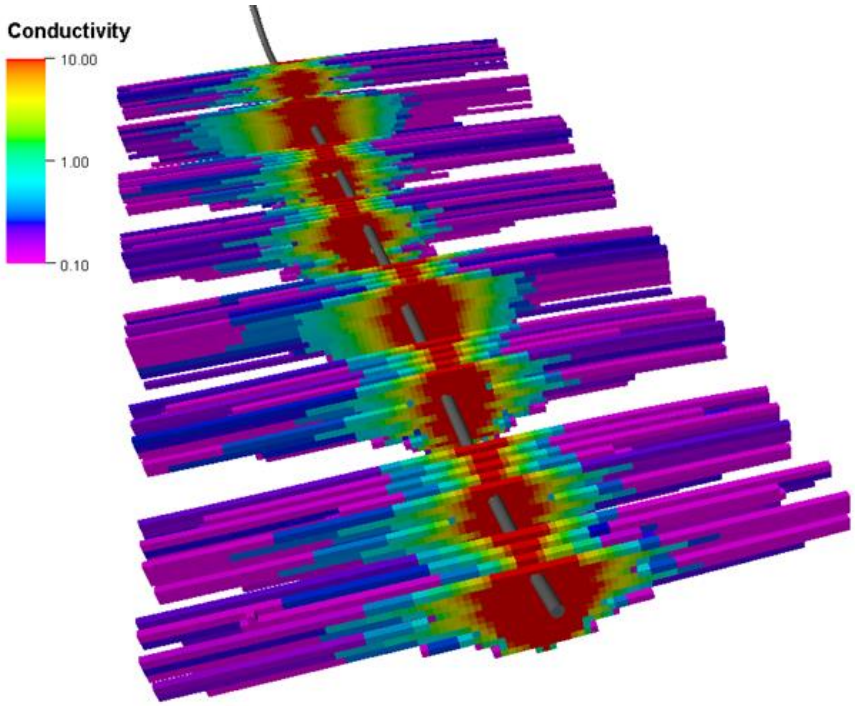

Figure 10. Example of a multi-stage hydraulic fracture scenario. This scenario was selected from the sensitivity analysis based on Plackett-Burman design.

From the 40 cases simulated during the sensitivity analysis, three representative scenarios from the hydraulic fracturing operation depicting P10, P50, and P90 cases were selected to account for different fracture treatment design aspects that optimize the fracture conductivity. The main characteristics and response variables of the selected scenarios are summarized in Table 6. The chosen cases' fracture conductivity varies from 8.7 to 62.8 $mD \cdot ft$ (P10 and P90, respectively). Moreover, Case P90 exhibits the highest leak-off and the lowest closure stress, while Case P10 has the lowest leak-off and the highest closure stress.

Table 6. Selected scenarios P10, P50, and P90 for the hydraulic fracturing operation to optimize the fracture conductivity

	Fracturing Operation Scenarios		
Parameters	**Case P10**	**Case P50**	**Case P90**
Proppant size	40/70	12/20	12/20
Net Pressure(psi)	1,057	1,055	979
Leak-off (gal)	0.0099	0.0103	0.0138
Proppant concentration (ppg)	0.387	0.342	0.441
Fracture conductivity (mD*ft)	8.7	49.8	62.8
Fracture width (in)	0.237	0.237	0.2
Fracture Pressure (psi)	7,250	7,247	7,022
Closure stress (psi)	6,200	6,192	6,043

Once the fracture scenarios were defined, we generated different pore network models to represent the pore space characteristics of the Wolfcamp shale for each one of the sensitivity cases shown in Table 6. The size of the pore networks generated is around 0.5 x 0.5 x 0.5 cm^3. The number of pore bodies and throats, the initial permeability, and porosity for the selected cases are shown in Table 7.

Table 7. Pore network characteristics for P10, P50, and P90.

Case	**P10**	**P50**	**P90**
Porosity (%)	8	7	8
Permeability (nD)	493	455	378
Number of nodes	11,500	11,500	11,500
Number of throats	22,492	19,311	18,641

The calculated porosity and permeability values agree with available petrophysical properties for the Wolfcamp shale (Mohan et al., 2013). The pore body and throat distributions for the networks were generated using a Weibull distribution function based on size distribution measurements for Wolfcamp shales from NMR and mercury injection capillary pressure (MICP) (Ojha et al., 2017; Rafatian et al., 2014). The Weibull distribution function is constrained by maximum and minimum

radii and the characteristic shape and scale parameters. The computed distributions are shown in Figure 11. An example of the 3D pore network generated for Case P10 is shown in Figure 12.

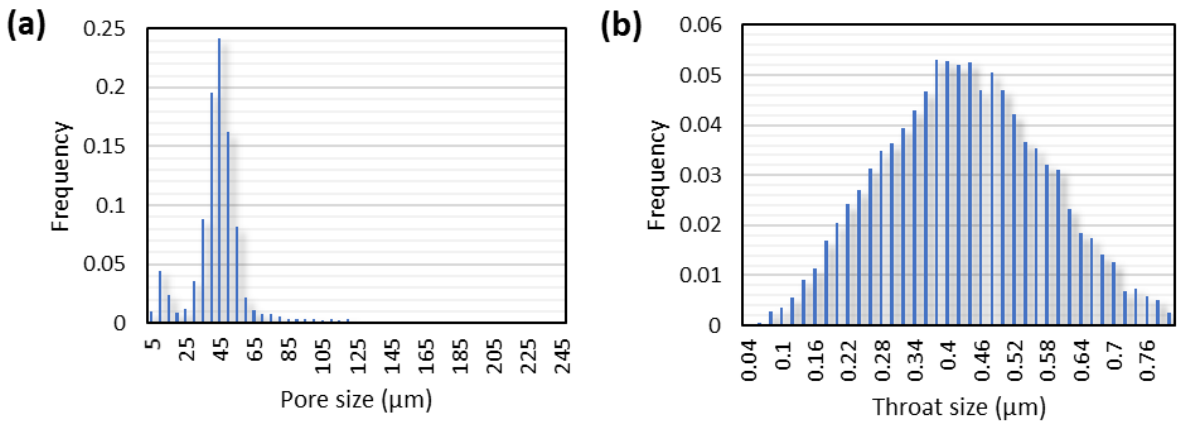

Figure 11. Pore size distribution for the case scenarios studied (a) Pore-body size distribution, (b) Pore-throat size distribution. Both distributions are generated stochastically based on the Weibull distribution function, following the distributions given for Wolfcamp (Ojha et al., 2017; Rafatian et al., 2014).

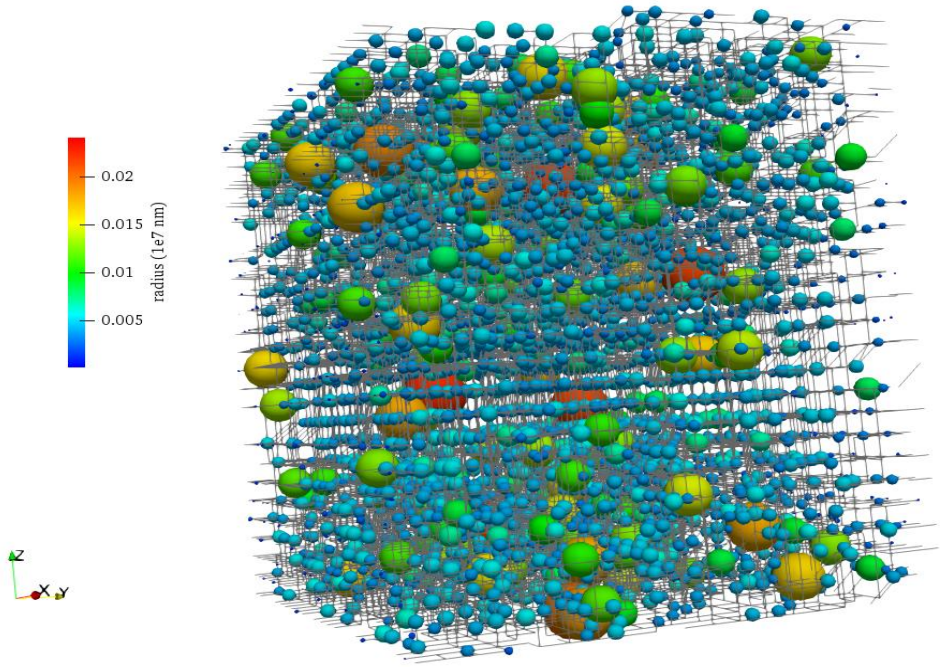

Figure 12. 3D pore network for Case P10. The spheres represent pore bodies colored by its radius, and the pore throats are represented as gray lines. The pore network represents a portion of the matrix-fracture interface at the pore-scale level to study the behavior of fines generated from proppant crushing.

Next, we used the proppant type defined for each scenario's sensitivity analysis and the obtained closure pressures to determine the percentage of fines generated from proppant crushing using the

population balance equation solution. The initial proppant-size distributions used for the analysis ($P_0\ (x, \sigma)$), were obtained from available literature on sieve distribution measurements (Dees and Coulter, 1986; Kothamasu et al., 2012) for the specific proppant sizes used to evaluate the sensitivity analysis in the fracture simulator (sand 12/20 and sand 40/70).

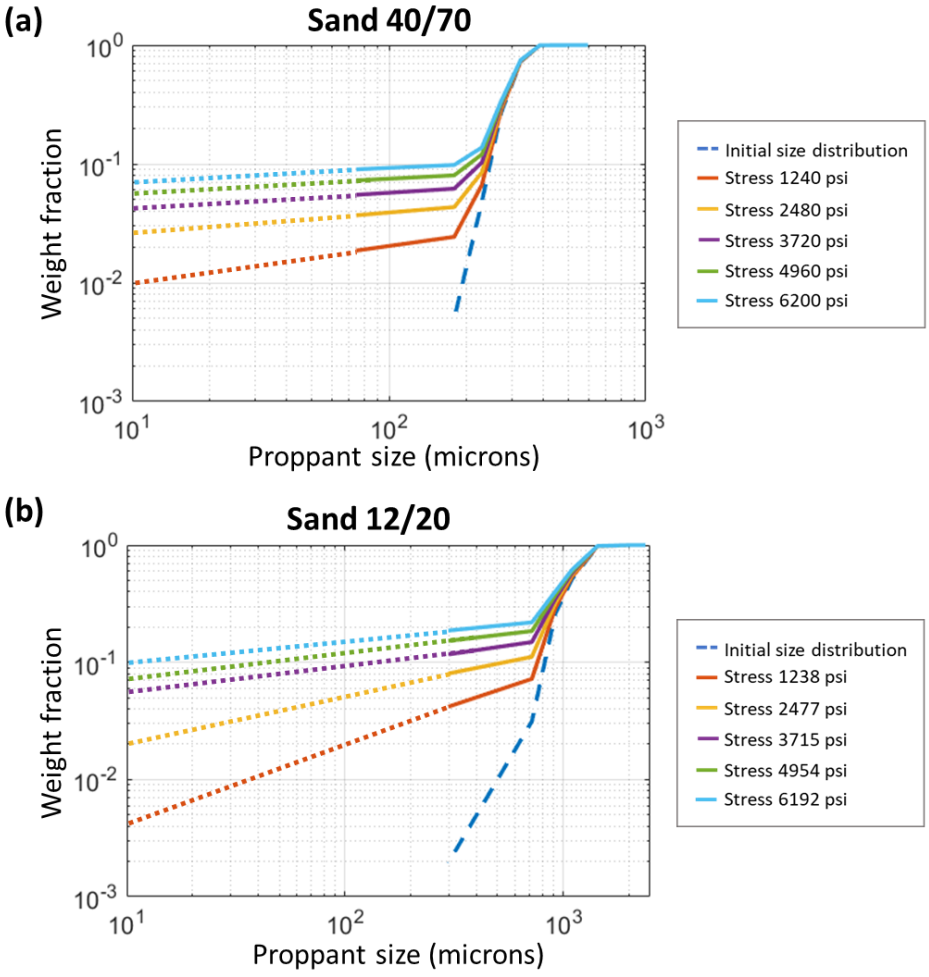

Figure 13. Proppant size distribution changes for increasing closure stress in the fracture for (a) sand 40/70 as in Case P10, and (b) sand 12/20 as in Cases P50 and P90. As the stress increases, the particle size distribution moves to the upper right, showing that the proppant size decreases. We can see how the fine particles are equivalent to 10% or more of the proppant size distribution for each case's largest closure pressure.

The fines distribution for the two types of proppant evaluated in the selected scenarios (sand 40/70 and sand 12/20) are illustrated in Figure 13. The fine particles' size range that results from crushing calculated for sand 40/70 (0 to 75 microns) is less than for sand 12/20 (0 to 297 microns). This is

not only because the closure pressure is higher for P10 where sand 40/70 is used, but also because the original size of the proppant particles is smaller than sand 12/20. We assumed that the concentration of fines carried by the leak-off fluid into the matrix is given by the percentage of crushed particles available and the leak-off volumes. Figure 13 shows that the size fraction of the fines from the crushed proppant for cases P10, P50, and P90 are 0.09, 0.19, and 0.18, respectively. Flow simulations were conducted in the y-direction with a constant flow boundary condition given by the leak-off rates obtained from the fracture simulator as inlet flow rates. The fluid viscosity used for the fracturing fluids was 0.01 g/cm-s. We investigated the flow of particles into the network, considering both the fraction of fines generated from crushing and the crushed proppant distribution's sizes.

The size of the particles coming into the network varies from 0.15 to 0.45 microns. For each scenario, the batch of particles studied contained single species of uniform size. Particles larger than the maximum throat size value will not enter the pore space and stay in the fracture creating a region of reduced permeability in the face of the fracture or reducing the fracture conductivity while occupying space between the proppant grains. Depending on the particle size, the particles may enter the pore network and travel through it, possibly being trapped later due to straining or reaching the network outlet.

Besides the particle size, another parameter that affects the plugging process inside the pore space is the number of particles entering the network. We estimated these numbers as a function of the crushed proppant fraction in the finest size interval, the leak-off rate, and the network size. For each sensitivity case, the number of particles injected varied from 800 to 1800. For single species of uniform size after a given number of particles inside the network, the porous medium can reach a point where it is completely plugged or where the fines are no longer retained as only the more

permeable paths are available for flow. These two conditions are dependent on the relation between the particle size and the throat size distribution.

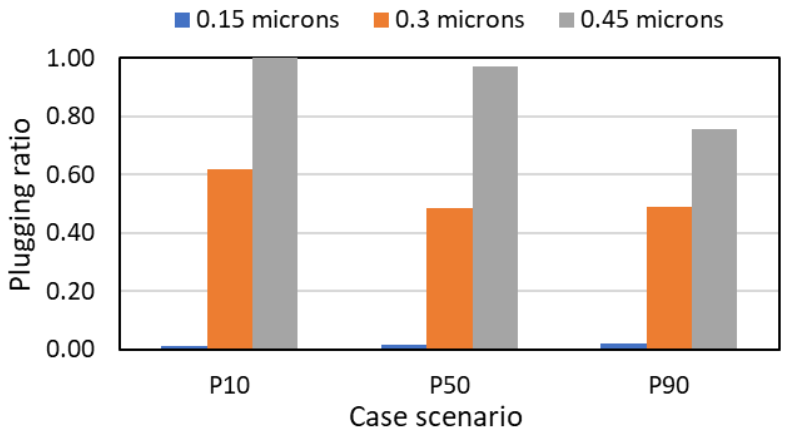

Figure 14. Plugging ratio as a function of particle size and the number of particles traveling through the network

The simulation outputs encompass the changes in pressure and permeability inside the network, the location of the particles trapped, and the paths followed by the particles that travel through it. The calculated plugging ratio for the various case scenarios as a function of both the particle size and the total number of particles traveling into the pore network is presented in Figure 14. As expected, larger particle sizes result in a higher trapping ratio for all case scenarios. Case P10 with the lowest leak-off rate exhibits a higher trapping ratio than other case scenarios as the particle size increases. This is related to a higher concentration of proppant and higher closure pressure, resulting in a larger fraction of fines migrating into the network carried by the leak-off fluid.

Figure 15 shows the trapped particles' location for the case scenarios investigated and various particle sizes traveling through the network, including 0.15, 0.3, and 0.45 microns. As the particle size increases, the trapped particles' location is closer to the inlet face in all cases. Besides, it is observed that the amount of particles trapped for both 0.3 and 0.45 microns is significantly higher than for 0.15 microns. This is related to the average throat size in the network, which is larger than

0.15 microns in this case (See Figure 11b). Moreover, for 0.3 microns, the trapped particles are spread around the network model, while for 0.45 microns, the particles are trapped at the entrance. This indicates that 0.45 microns particle size is above the average throat size, blocking more conduits at the inlet as the fluid flows through the network.

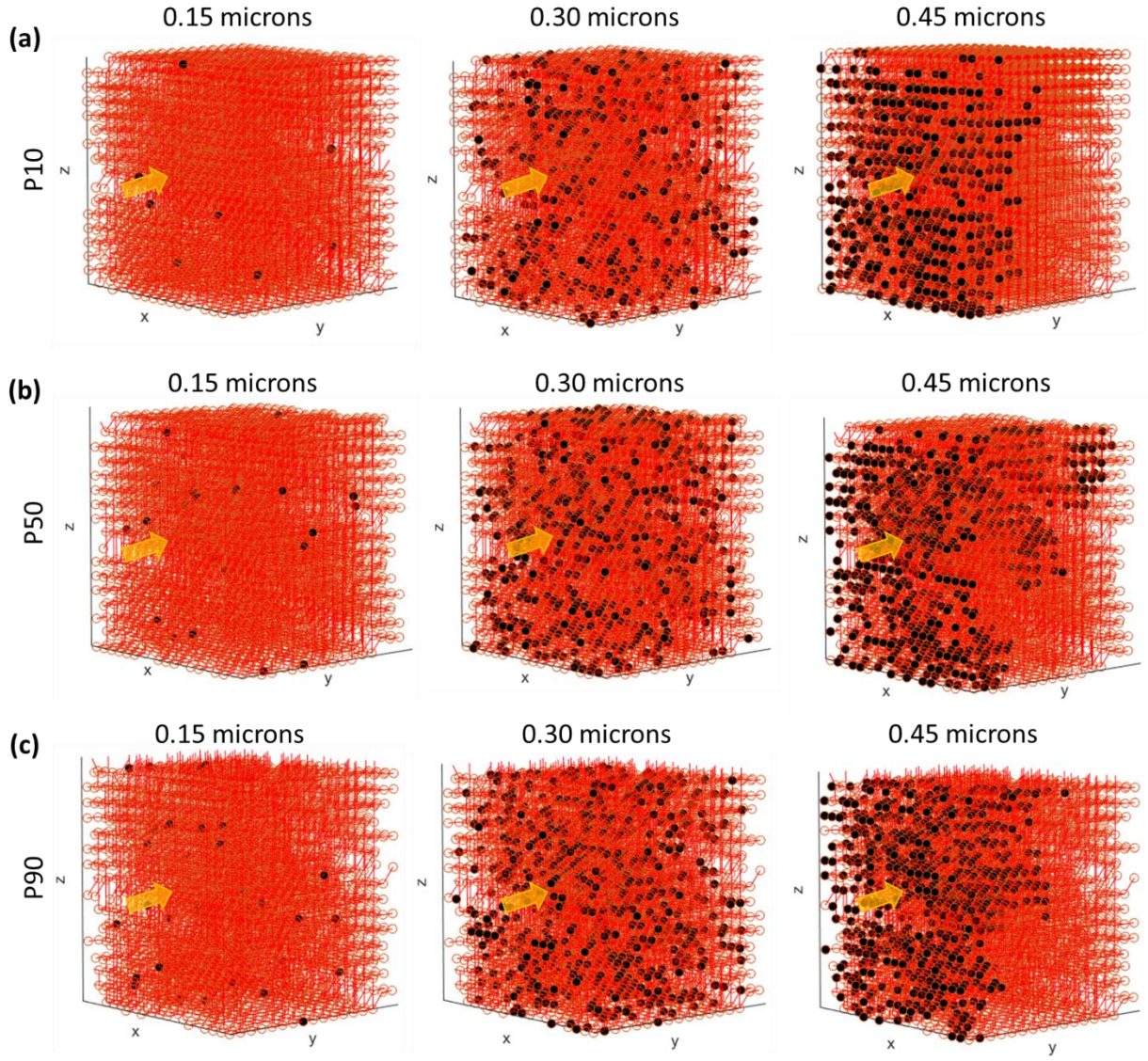

Figure 15. Trapped particles location for (a) case P10, (b) case P50, (c) case P90. The yellow arrow indicates the flow direction of the leak-off fluid. As the particle size increases, the retention occurs closer to the entrance, blocking the flow channels in the interface matrix-fracture

Due to the particle trapping patterns observed above, the flow capacity of the network changes. The greater the throat plugging, the more extensive the pore space damage in the region of interest.

There is a point at which all the pluggable throats will be blocked, and the permeability will not change anymore, or it will become zero, and there will not be any flow. Figure 16 shows the permeability changes as a function of the number of particles traveling into the network and its size for the cases studied. The permeability change is expressed as a fraction of the damaged permeability (k_s) and the original permeability (k_o). The number of particles present in the network is normalized by the total number of particles injected to compare the cases. From the figure, it is evident how the permeability reduction becomes steeper as the number of particles being trapped becomes larger, especially for 0.45 microns particles above the network's average throat size.

In particular, for Cases P10 and P90, we observed a steeper reduction in the permeability for the largest particle size investigated. This is possibly due to a larger proppant concentration and generation of fines due to crushing in comparison with Case 50. On the other hand, Case 50 shows stabilization of the permeability reduction after around half of the total particles injected is inside the network. This behavior indicates that the throats with sizes below the average particle size injected have been plugged. The flow and particle transport occur now through the main migration pathways constituted by the largest throat sizes.

P90 is the scenario representing an optimistic combination of operational constraints for the fracturing design, exhibiting the most considerable fracture conductivity. However, the results obtained here indicate that despite the fracture conductivity, the permeability in the matrix-fracture interface can be vastly affected due to the fines migration. Therefore, it is essential to analyze the effect of the particle plugging in the interface region, considering the number of particles coming into the network, their size, and the particle size relation with the throat size distribution.

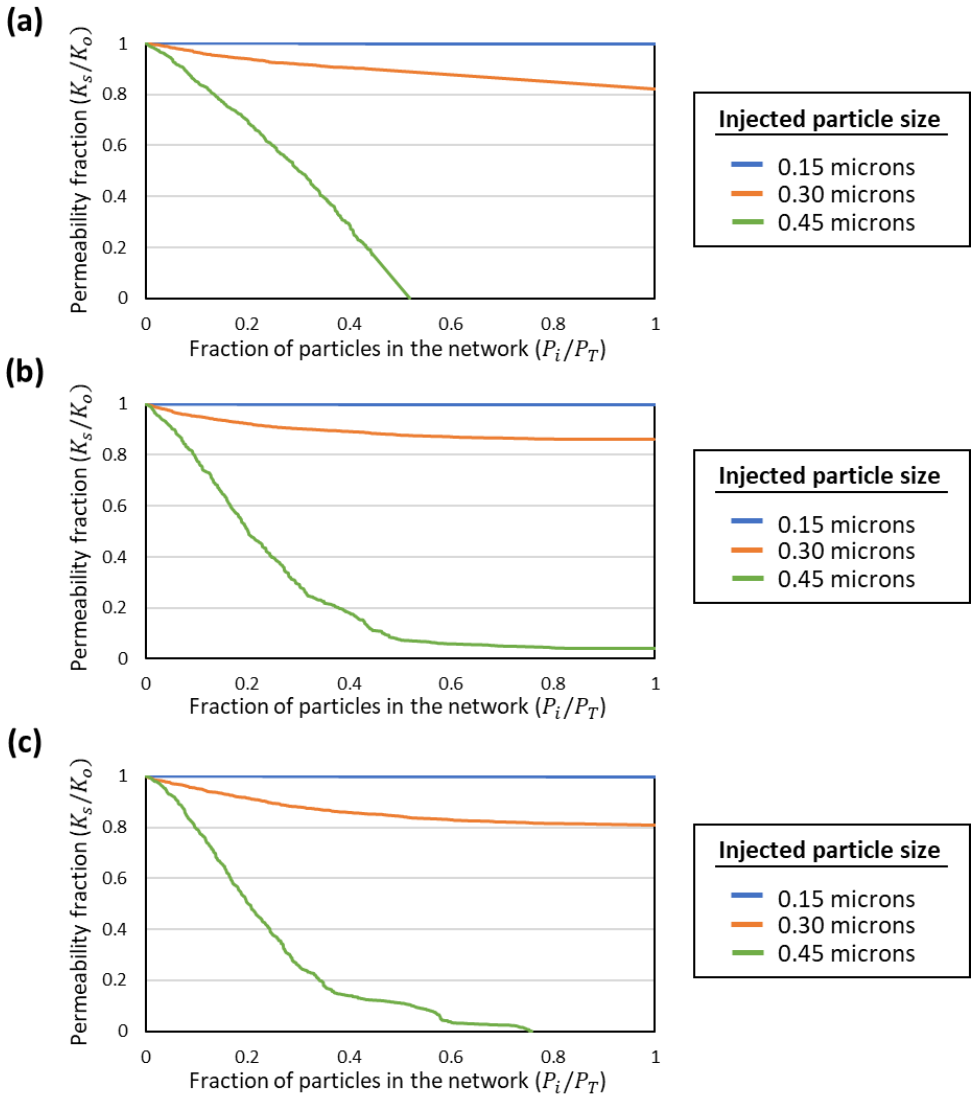

Figure 16. Permeability change due to trapping of fines in the fracture face for scenario (a) P10, (b) P50, and (c) P90. As the number and size of fines increases in the network, the permeability reduction is more considerable in all cases.

2.7. Discussion: Model Advantages and Limitations

The methodology discussed presents a practical way to understand the particle-plugging process in the matrix-fracture interface during hydraulic fracturing operations due to the migration of fines facilitated by fracturing fluid invasion and proppant crushing. The coupled model considers heterogeneity at the pore scale to account for the pore structure's role on particle transport while studying the process at the reservoir scale, accounting for various operational and design characteristics of the hydraulic fracturing process.

The pore-scale model implemented in the simulator presents an improvement to the conventional macroscopic modeling of particle transport that fails to capture the pore space's features such as pore-size distribution, the topology of the interconnected pores, and heterogeneity. Besides, the model facilitates the analysis of the migration pathways evolution and the tortuosity of the system. Simulations based on flow and transport in pore networks consider all these characteristics and incorporate the forces and physics at the pore scale that affect the particle-surface interaction. The pore-scale model considers both the stochastic nature of the pore space and the physics that describe the behavior of the particles transported, including advection, dispersion, and trapping mechanisms.

In addition, the pore network models used for the simulations allow for the characterization of larger domains with much less computational effort given the simplified representations of the pore structure. Flow properties can be computed and implemented to estimate macroscopic properties such as permeability or dispersion coefficients that would have otherwise require experimental work. However, using pore networks can result in the resolution loss of the more complex structures. In the case of highly heterogeneous porous media, the pore network may not represent the whole system. Therefore, some uncertainty is related to the construction of the networks, and multiple realizations are required to overcome these drawbacks. More reliable representations of the pore space obtained from microtomographic images could also help reduce the network representation's uncertainty.

A critical limitation of the model is the physical and chemical processes considered for particle plugging simulation. In this case, the retention of particles is measured only by size exclusion or mechanical straining. Even though this is the mechanism with the most considerable effect on the

permeability reduction, in some cases, it may be relevant to account for other processes to extend the predictive capabilities capturing, for instance, the role of electrostatic forces.

Coupling the pore-scale model with the commercial fracture simulator used for the hydraulic fracture design allowed us to capture different treatment variables' effects on the matrix-fracture interface's resulting formation damage. Note that the interface's behavior is limited by the parameters selected for the sensitivity analysis at the reservoir-scale. That is, it is limited by the fracturing treatment design variables such as the proppant size and type, the concentration, and the injection rate. Moreover, the sequential coupling used to link the simulators at different scales (pore-scale and fracture simulator) also constrains the results obtained because the evolution of the parameters with time cannot be predicted considering the processes at both scales. Instead, the processes were solved independently at the pore-scale and continuum-scale models. Considering alternative coupling techniques such as boundary coupling or concurrent coupling could help to overcome these restrictions.

2.8. Conclusions

This chapter introduced the multi-physics particle plugging simulator that connects pore-scale phenomena with those occurring at the reservoir scale during a hydraulic fracturing operation. The integrated model aimed to improve the design and modeling of hydraulic-fracturing operations in unconventional shale reservoirs by considering the effects of additional damage mechanisms in the fracture face.

The pore-scale particle-plugging simulator used 3-D pore-network models derived from petrophysical measurements to compute the transport and retention of particles and the resultant changes in petrophysical properties. These parameters were interfaced with a fracture simulator that provided pressure, leak-off rate, proppant size, and concentration to the pore-network model.

Furthermore, the parameters are representative of typical multi-stage hydraulic-fracturing operations. The fracture simulator also provided the fracture-geometry and fracture-conductivity.

The sensitivity analysis performed for different hydraulic-fracturing operational constraints and fluid properties like proppant size and concentration facilitated examining the effects of design treatment variables on the matrix-fracture permeability impairment at the pore-scale. The selected cases for the pore-scale flow simulations were based on the computed fracture conductivities ranging from pessimistic to optimistic scenarios. Higher conductivities were observed for larger proppant sizes, with lower fracture pressures and closure stress

The population balance methodology proposed allowed us to model the proppant degradation due to proppant crushing as a function of the original proppant size and considering the role of the closure pressure. We captured the proppant size distribution changes for increasing closure stress in the fracture for different proppant sizes. The resulting distributions show that fine particles with the potential to travel into the pore space are equivalent to 10% or more of the proppant size distribution for large closure pressures independently of the proppant size.

We also captured the transport and retention of particles derived from proppant crushing and transported by fluid invasion at the pore-scale level. We assessed the location of the trapped particles and their effect on permeability. Both the particle concentration and size govern the resulting trapping. Moreover, the relationship between the size of the fines migrating into the pore space and the pore throat size appears to influence the spatial distribution of the trapped particles significantly. The permeability variation calculated exhibits a steeper reduction for extreme cases (P10 and P90). In particular, for Case P90, the scenario representing an optimistic combination of operational constraints for the fracturing design exhibiting the most considerable fracture conductivity, the permeability in the matrix-fracture interface was highly affected due to the fines

migration. This emphasizes the importance of analyzing the effects of formation damage at the interface, as fracture designs displaying high conductivities could result in underperformance due to restrictions on the fracture communication with the matrix.

Using this modeling workflow in conjunction with other hydraulic-fracturing modeling techniques, one can improve the decision-making process for proppant selection. Matrix-fracture permeability alteration during the production phase can also be addressed using the proposed modeling framework. Furthermore, the workflow can be applied in similar scenarios involving fines or particle deposition due to fluid injection or production in water-disposal operations or asphaltene-deposition processes. The computed pressures, fluxes, and changes in the petrophysical properties at the pore space can be upscaled by coupling the pore networks with reservoir scale simulators and incorporating appropriate physics to predict changes at larger scales in the porous media.

Chapter 3. Modeling Chemical Diagenesis at the Pore-Scale: A Study of the Evolution of Migration Pathways in Unconventional Reservoirs

3.1. Introduction

Diagenesis in sedimentary rocks refers to the collection of physical and chemical processes occurring after deposition and before metamorphism that modify the rock structure at local and reservoir scales. Several variables and conditions determine the complex interplay of diagenetic processes that result in the rock's alteration. These parameters include temperature, pressure, the open or closed nature of the system, fluid composition, biological activity, tectonics, and burial. Also, rock characteristics, such as its origin, mineralogy, and organic content, play a vital role (Chilingarian and Wolf, 1988).

As new minerals are formed or dissolved, rock properties are modified, and ultimately, the rock's reservoir quality is affected. The alteration level will depend on the degree to which diagenetic processes influenced the rock structure, including features such as pore and throat size distributions, pore abundance, and pore connectivity. To understand the history and evolution of the rocks, it becomes necessary to establish the sequence of events as a function of time, temperature, and pressure. This sequence of events is known as the paragenetic sequence or paragenesis. The construction of the paragenetic sequence is based on the use of multiple diagenetic techniques, such as the detailed examination of thin sections, fluid inclusions, and other microscopic images, to identify phases and recognize diagnostic features (Craig and Vaughan, 1994).

In this chapter, we delved into chemical diagenetic processes from a pore-scale perspective to improve our understanding of their influence on the evolution of macroscale properties such as

permeability and porosity. First, chemical diagenetic processes were examined considering various rock types, geochemical reactions, and their relationship with reservoir quality. Then, we proposed a pore-scale modeling workflow, combining petrographic and paragenetic analysis and numerical simulation to capture the migration pathways' evolution and its impact on reservoir quality. Later, the workflow developed was applied to assess diagenetic signatures in the Woodford Shale, focusing on rock-fluid interactions that cause precipitation and dissolution.

3.2. Chemical Diagenesis

Two main types of diagenetic processes can be identified: physical and chemical. Physical diagenesis is related to compaction of the pore space due to pressure application. It can be classified into four main mechanisms: grain rearrangement, plastic deformation, brittle fracturing, and pressure solution, known as chemical compaction (Wilson and Stanton, 1994). On the other hand, chemical diagenesis results from the interaction of fluids and minerals through precipitation (cementation) and dissolution processes that involve the formation, replacement, or breakup of minerals in the pore space. Precipitation and dissolution process can involve one or more minerals, occurring independently or alongside, and can vary over several orders of magnitude from the pore- to the basin scale (Wood, 1994). A brief description of mineral precipitation and dissolution is presented next, including characteristic processes in different lithologies and their effects on the pore space properties evolution.

3.2.1. Mineral Precipitation, Cementation and Replacement

Cementation involves the growth or formation of minerals in the pore network, while mineral replacement is the substitution of pre-existing grains. Precipitation processes are generally associated with a decrease in pore volume as pore spaces are occupied by new minerals, and therefore the void space size can be reduced. Besides occluding the pore space, the presence of

cement can provide rigidity and influence the pore's resistance to collapse during compaction and burial, ultimately favoring porosity preservation (Katsube and Williamson, 1994). Moreover, cementation can impact effective porosity at local scales, affecting permeabilities, resulting in petrophysical properties variation over broad ranges, increasing the heterogeneous character of the formations.

The mineralogy of the precipitated components is correlated with the original grain mineralogy and the composition of the fluids that fill the pore spaces. In sandstones, cementation and replacement are essential diagenetic processes. Common mineral precipitations include quartz overgrowths, chalcedony, carbonate cement (calcite, dolomite, siderite), clay coats (chlorite, kaolinite, and smectite), and hematite (Hayes, 1979; Worden and Burley, 2003). Two main types of cement in sandstones are studied, rim and occluding cements. Rim cement exhibits preferred relationships to the grain, occurring as relatively even coats on the grain surfaces. For example, clay rims like chlorite.

Conversely, occluding cement fills the pores with no evident preference for the grain surface. It can be classified into three groups based on the crystals' size that fill the pore space: macrocrystalline, microcrystalline, and cryptocrystalline (Wilson and Stanton, 1994). Figure 17 shows different types of rim and occluding cement in sandstones and the extended division of rim cements into low surface area and high surface area.

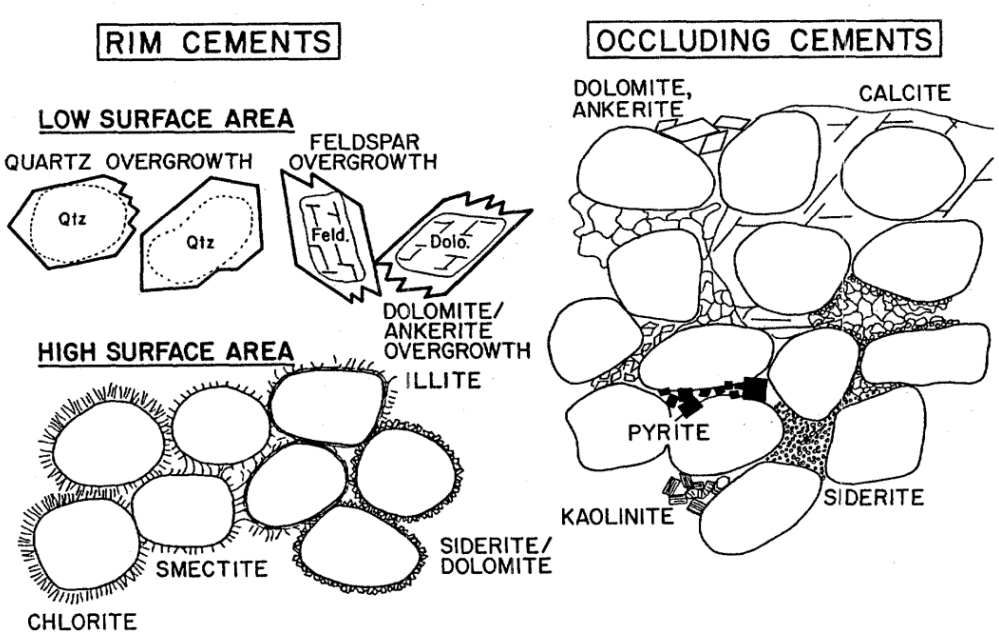

Figure 17. Types of cement in sandstones. Rim cement grows around the grain surfaces, like grain coats. They can be classified as low and high surface area cement. While occluding cement fills up the pore space and can be classified according to the crystal size as macrocrystalline, microcrystalline, and cryptocrystalline. From Wilson and Stanton (1994).

In carbonates, cementation can occur within the depositional environment as skeletal grains or precipitates that require an enormous input of $CaCO_3$ and efficient fluid flow mechanisms. The precipitation process of carbonates is highly influenced by pH, CO_2 activity, and the timing relative to hydrocarbon generation (Harris et al., 1985). Typical mineralogy of carbonate cement involves aragonite, High-Mg calcite, Low-Mg calcite, and dolomite. Furthermore, according to the morphology and arrangement of the precipitated crystals in carbonates, the cement can be classified as cement consisting of crystals growing from a free substrate into the pore space (i.e., fibrous, botryoidal, and bladed), pendant cement (meniscus), pore-filling cement (drusy, granular and blocky) and micritic cement (Flügel, 2013). Figure 18 presents the typical cement morphology in carbonate rocks.

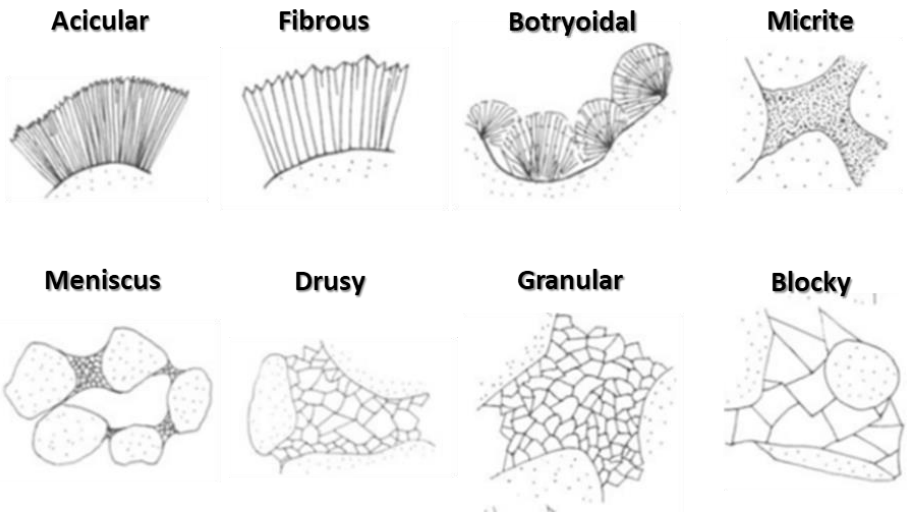

Figure 18. Common carbonate cement types. Differentiation of cement is based on the morphology and arrangement of cement crystals. This cement can be formed in meteoric, marine, or burial diagenetic environments (Flügel, 2013).

Mudrocks undergo similar cementation processes as sandstones and carbonates, in addition to grain replacement and fracture filling. Thus, precipitated minerals in mudrocks can fill intraparticle, interparticle pores, and fractures. For instance, authigenic quartz can be found in mudrocks replacing grains or filling fractures, characterizing the rock's mechanical properties (Milliken and Day-Stirrat, 2013). Various types of mineral precipitation can be identified at different stages of diagenesis in mudrocks. Early diagenetic precipitation includes carbonate, pyrite, and phosphate minerals, commonly forming concretions and hardgrounds (localized mineral segregations). Late mineral precipitation involves clay, cement overgrowths of quartz, carbonate, and feldspar (Loucks et al., 2012). Middle and late diagenesis in different shale formations in North America are characterized by fracture mineralization, with various fracture habits and complex paragenesis. Common minerals observed in fractures are calcite, ferroan calcite, dolomite, ferroan dolomite, quartz, barite, celestine, sphalerite, and anhydrite (Elmore et al., 2016)

3.2.2. Mineral Dissolution and Secondary Porosity

Chemically unstable solid minerals are dissociated, and their resultant components (ions) are dispersed in the fluid filling the pores. The rocks lose a high percentage of their primary porosity due to consolidation, compaction, and cementation processes after deposition. However, dissolution processes can result in the creation of secondary porosity that can significantly affect reservoir quality. Dissolution of framework grains can cause an increment in the system porosity, whereas the dissolution of cement can increase both the porosity and the permeability. The level of dissolution is a function of the rock's composition. In general, minerals such as carbonates (i.e., calcite, dolomite, siderite) and feldspars are more susceptible to dissolution, while clays and quartz appear resistant (Giles and Marshall, 1986). It is noteworthy that the creation of new porosity has been related to diagenesis in open systems given the large volume of water required for grain o cement dissolution reactions (Schmidt and Mcdonald, 1979b).

It is necessary to categorize the distinct types of porosity generated to evaluate the relevance of secondary porosity created during diagenesis in open systems. In 1979, Pittman grouped pore types in sandstones into four categories based on textural relations: intergranular (among detrital sand grains), dissolution pores, microporosity, and fractures, as shown in Figure 19a. Pittman's classification system was complemented by the scheme proposed by Schmidt and Mcdonald (1979a), which aimed to correlate the pore types encountered in sandstones with a given diagenetic process, as shown in Figure 19b. Thus, the pore types were associated with fracturing and shrinkage, dissolution of grains or cement, and those formed by the replacement minerals.

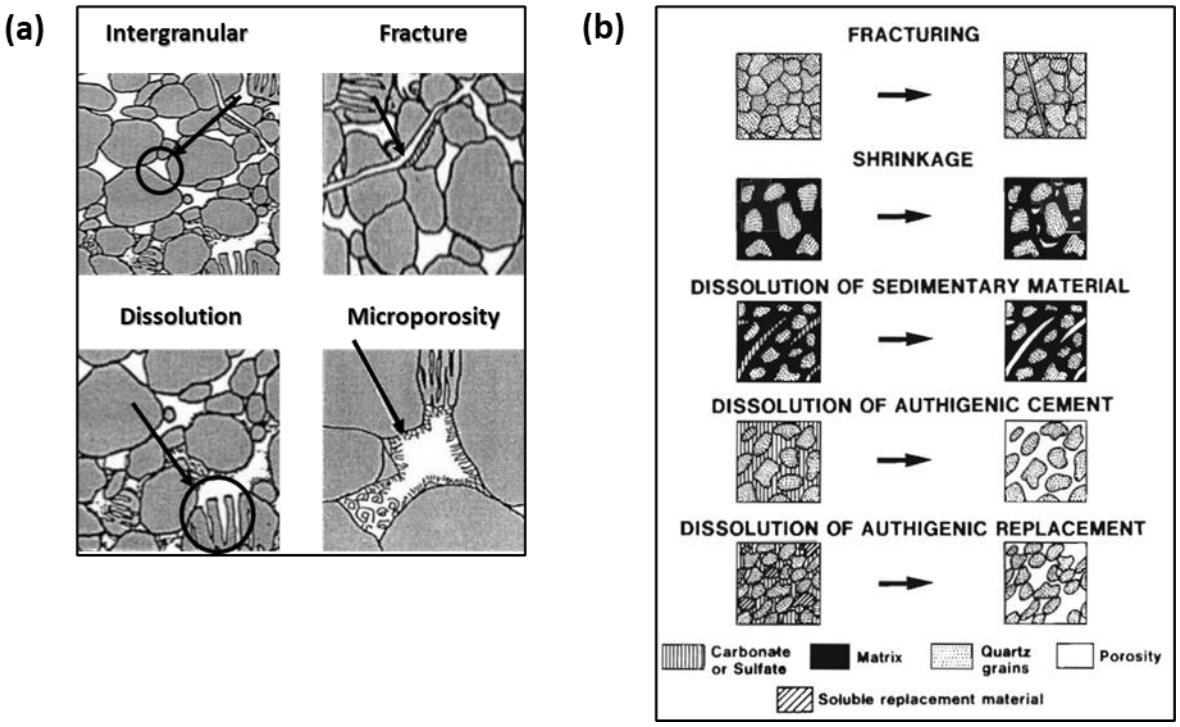

Figure 19. Sandstone pore types (a) based on textural characteristics (Pittman, 1979), (b) secondary porosity based on diagenetic processes (Schmidt and Mcdonald, 1979a).

Other classification systems were proposed for different rock types, including carbonates and mudrocks. Three main processes for carbonate rocks are considered responsible for secondary porosity: dissolution, dolomitization, and fracturing. Choquette and Pray (1970) classified carbonates' porosity into two major groups: fabric selective and nonfabric selective, as shown in Figure 20. Fabric selective pores are commonly related to primary porosity as the pore boundaries and location are dependent on the fabric elements, for example, in interparticle and intraparticle pores. Intraparticle depositional porosity is one of the fundamental differences between carbonate and clastic porosity. The living chambers of various organisms present in carbonates provide significant internal porosity. Conversely, for secondary porosity, the pore classification considers both fabric or nonfabric selective types, including moldic, intercrystal, and fracture pores.

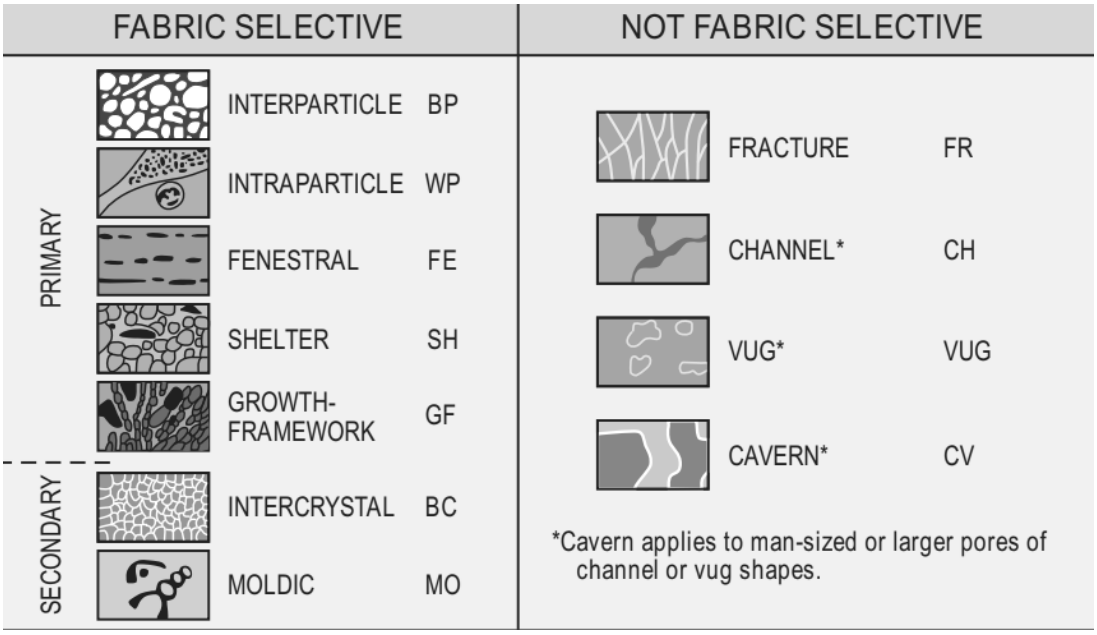

Figure 20. Carbonate pore types based on Choquette and Pray classification (Moore and Wade, 2013b).

For mudrocks (mudstones and shale), Loucks et al. (2012) presented a classification scheme for pore types related to the rock's matrix (Figure 21). The mineral matrix pores are grouped as interparticle (pores found between particles and crystals) and intraparticle pores (pores located within particles). A third category is associated with organic matter pores. The mudrock pore types are related to the age and depth at which the rock was deposited. Young shallow-buried muds contain interparticle and intraparticle pores that are reduced as compaction and burial increase. With burial, organic matter pores are created during hydrocarbon maturation, and additional intrapores may be developed due to dissolution by the acid fluids generated during the decarboxylation of kerogen. The creation of secondary porosity is highly intertwined with the diagenetic sequence of mudrocks, with an additional impact of organic matter processes that do not play the same role in sandstone or carbonate rocks.

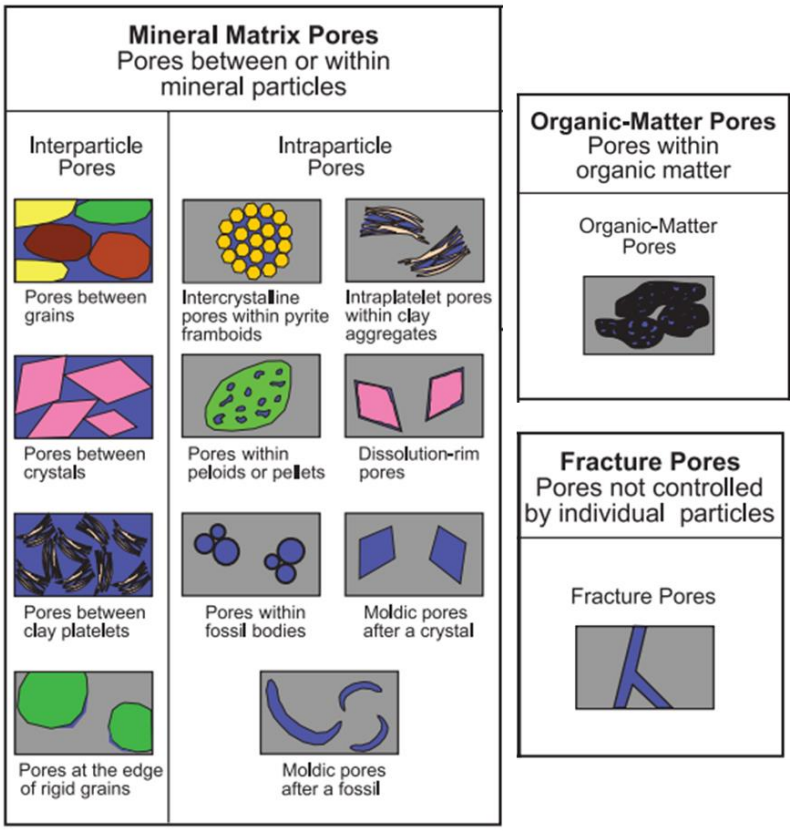

Figure 21. Pore types in mudrocks from Loucks et al. (2012). Pores are grouped based on their relationship to the particle. Intraparticle and interparticle are related to the mineral matrix, while organic-matter pores are associated with organic matter.

3.3. Geochemical Reactions

Minerals react through water-rock interactions driven by changes in the pore-fluid chemistry, temperature, and pressure. These reactions are fluid mediated, involving the transfer of material into or out of the aqueous solution, highly temperature-dependent, and classified as either dissolution or precipitation reactions (Blatt, 1979). Moreover, diagenetic reactions can be divided into stages following the rock's paragenesis and considering time, temperature, and pressure increment. These stages include: early, middle, and late diagenesis. Early diagenesis encompasses the reactions occurring during deposition and shallow burial. Middle diagenesis is characterized by reactions during intermediate burial and early hydrocarbon generation window, while late diagenesis comprises the late hydrocarbon generation window and deep burial reactions (Curtis,

1983). Figure 22 presents microscopic images with examples of diagenetic reactions resulting in dissolution, precipitation, or mineral replacement in different rock types.

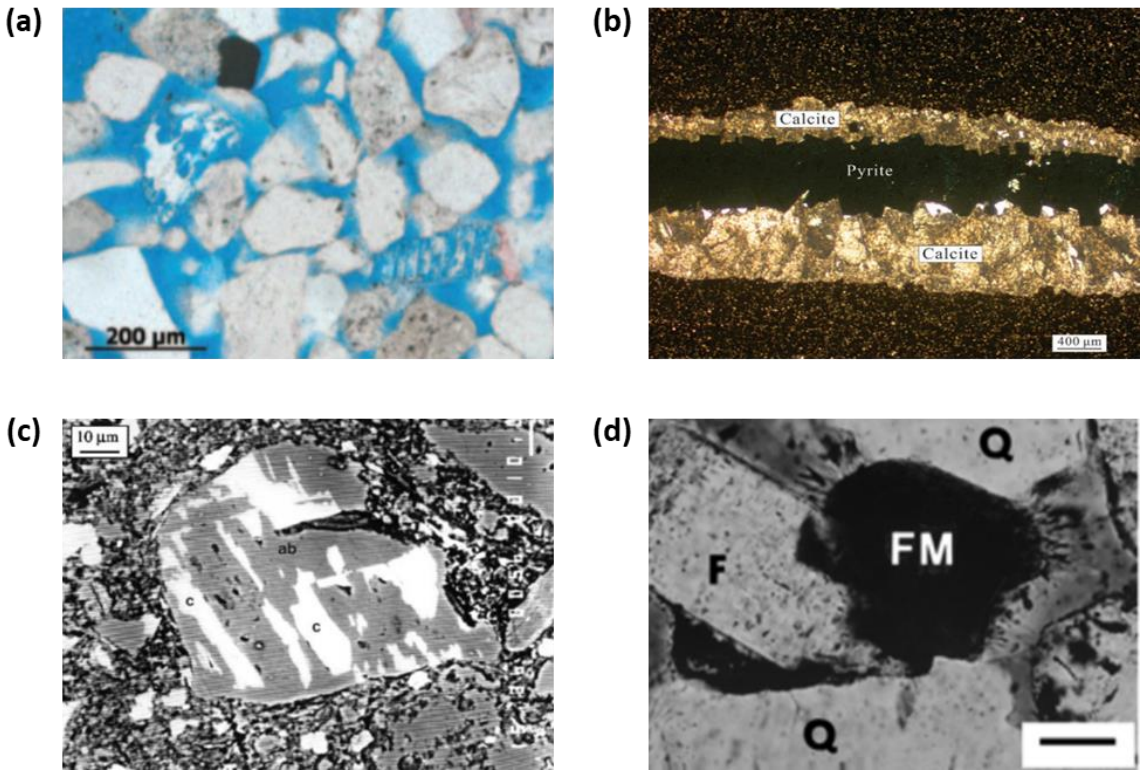

Figure 22. Examples of diagenetic events (a) Feldspar dissolution in sandstone (Taylor et al., 2010), (b) Precipitation of calcite and pyrite filling up a fracture in shale (J. Zhao et al., 2017), (c) Calcite replacing albite grain in shale (Milliken, 2003) (d) grain-coating smectite around ferromagnesian grain but absent in quartz (80 μm) (Worden and Burley, 2003).

The types of reactions occurring in a given geochemical system depend not only on the composition of the sedimentary rock undergoing diagenesis but also on characteristics of the pore fluid such as its aqueous composition, the ions solubility, and activity. Reactions occurring between the fluid and rock minerals are known as heterogeneous reactions or mineral reactions. Mineral reactions are slow processes where kinetic controls on reactions (related to the rate of product formation) tend to override thermodynamic controls (related to the products' relative stability). Likewise, chemical equilibrium in the bulk material is not achieved. This means that the local equilibrium between authigenic phases (in-situ minerals) and the aqueous phase can be

reached on a transient basis but will not tend to coincide in the bulk rock (Berner, 1980a). Additionally, homogeneous reactions such as dissociation of salts and acids occur inside the pore fluid (Clark, 2015). These ion interactions inside the aqueous phase are faster than the fluid-rock reactions, can be modeled based on thermodynamic equilibrium, and are considered instantaneous (Lichtner, 1996).

Table 8 shows selected key diagenetic reactions that can occur on sandstones, carbonates, and mudrocks. Examples of early diagenetic reactions in sandstones include precipitation of k-feldspars and carbonates and overgrowths of quartz and chlorite. Common late diagenetic reactions are the conversion of smectite to illite, albitization, quartz cementation, and conversion of kaolinite and k-feldspar to illite and quartz (Worden and Burley, 2003). Late diagenetic processes in sandstones are related to reactivity and diagenesis in mudrocks, mostly influenced by organic matter's maturation. Additional acids and diagenetic fluids are generated in mudrocks during clay reactions, thermal maturation of organic matter, and the hydrocarbon generating window, resulting in the interaction between fluids and minerals and initiating more diagenetic processes (Surdam et al., 1985).

In carbonate rocks, common diagenetic reactions comprise precipitation of cement such as calcite, aragonite, micritization (carbonate mud, recent micrite is composed of aragonite needles, ancient of equant calcite), dolomitization, and dedolomitization (dissolution of dolomite and precipitation of calcite) (Moore and Wade, 2013a). Carbonate diagenesis can take place in many settings: the marine environment during the deposition of the sediment, in freshwaters near the surface, in a subaerial setting produced by a sea-level fall, in a mixing zone between waters of varying chemistries, or in the subsurface brines (Harris et al., 1985).

Table 8. Main diagenetic reactions in different rocks including sandstones, mudrocks and carbonates (Berger et al., 1997; Curtis, 1985; Milliken, 2003; Moore and Wade, 2013a)

Process	Reaction	Temperature (°C)
Quartz precipitation	$H_4SiO_4 \rightarrow SiO_2 + 2H_2O$	>80
Calcite precipitation	$Ca^{2+} + CO_2 + H_2O \rightarrow CaCO_3 + 2H^+$	100-160
Albitization	$Na^+ + 3H_4SiO_4 + Al^{3+} \rightarrow NaAlSi_3O_8 + 4H^+ + 4H_2O$ $KAlSi_3O_8 + Na^+ \rightarrow K^+ NaAlSi_3O_8$	75-200+
Pyrite precipitation	$Fe^{2+} + 2H_2S \rightarrow FeS_2 + 4H^+$	-
K-feldspar and Kaolinite conversion	$KAlSi_3O_8 + Al_2Si_2O_5(OH)_4 \rightarrow muscovite/illite + 2SiO_2 + H_2O$	50-120
Organic matter	$CH_2O + H_2O \rightarrow CO_2 + 4H^+$	40-100
Smectite to illite conversion	$smectite + Al^{3+} + K^+ \rightarrow illite + Si^{+4}$	60-100
K-feldspar dissolution	$KAlSi_3O_8 + 4H^+ + 4H_2O \rightarrow K^+ + Al^{3+} + 3H_4SiO_4$	80-160
Carbonate dissolution	$CaCO_3 + H^+ \rightarrow Ca^{2+} + HCO_3^-$	>60
Dolomite dissolution	$CaMg(CO_3)_2 + 2H^+ \rightarrow Ca^{2+} + Mg^{2+} + 2HCO_3^-$	25-150
Dedolomitization	$CaMg(CO_3)_2 + CaSO_4 \rightarrow 2CaCO_3 + MgSO_4$	<50
Dolomitization	$2CaCO_3 + Mg^{2+} \rightarrow CaMg(CO_3)_2 + Ca^+$	70-110

The major diagenetic reactions involved in the mudrock pore structure's evolution include during early diagenesis cementation of carbonate, pyrite, and phosphates. Late diagenesis is characterized by the transformation of smectite to illite and the dissolution of carbonates (Loucks et al., 2012). Diagenetic reactions on the fractures present in mudrocks are also common. For instance, studies on the Woodford Shale suggest there is evidence of hydrothermal alteration, multiple hydrothermal minerals present in fractures might indicate at least one fluid migration event. Roberts and Elmore (2018) showed that the Woodford Shale evolved into an open system to external fluids during middle to late diagenesis when minerals such as saddle dolomite, magnesite, and sphalerite precipitated in the fractures.

The precipitation rate of the minerals can be controlled by transport processes, surface reactions, or both. These controls emerge from the stages of growth of a crystal, which are first the transport of ions to the mineral surface, then the surface reaction, and finally the removal of the reaction products (Berner, 1980a). At homogeneous macroscopic scales, mineral reactions can be considered surface-reaction controlled. This means that the reactions are limited by the attachment and detachment rates of ions from the mineral surface (i.e., limited by the surface reactions). However, at pore-scales, where heterogeneity of the mineral composition and concentrations are taken into account, reactions can be considered controlled by transport processes (Steefel, 2008).

Dimensionless numbers such as Péclet and Damköhler can be used to determine the importance of reactive kinetics relative to the transport rates in a given system. Two Damköhler numbers (Eq. 19 and 20) can be defined to compare the characteristic times for reaction-advective and reaction-diffusive transport. The Péclet number (Eq. 21) can be determined to evaluate the relative importance of advective and diffusive transport. Zones with lower Péclet numbers can be higher reactivity zones given that molecular diffusion dominates the transport (Steefel et al., 2013).

$$D_{aI} = \frac{t_A}{t_R} = \frac{kl}{|u|} \tag{19}$$

$$D_{aII} = \frac{t_D}{t_R} = \frac{kl^2}{D} \tag{20}$$

$$Pe = \frac{|u|l}{D} \tag{21}$$

Where k is the reaction rate constant, l is the characteristic length of the scale of interest, u is the fluid velocity, and D is the diffusion coefficient.

3.4. Reservoir Quality and Diagenesis

Diagenetic processes play a crucial role in the evolution of petrophysical properties in reservoir rocks. Primary porosity and permeability are highly influenced by the depositional environment, geothermal gradient, and sediment characteristics. However, after deposition and during burial, diagenesis significantly affects the pore space structure, including mechanisms that can reduce the primary porosity or generate new porosity (secondary porosity) in the system (Slatt, 2013). Loucks et al. (1984) investigated the effects of variations in diagenetic processes on the reservoir quality trends in the Lower Tertiary sandstones along the Texas Gulf Coast. The authors correlated porosity and permeability reductions with the increment of compaction and cementation activity with depth. They also noted the trend changes due to the creation of secondary porosity through dissolution in the deeper subsurface.

Later studies focused on establishing porosity-permeability relationships based on processes that affect the pore space during diagenesis (i.e., plastic compaction, elastic and brittle compaction, microcracking, and chemical diagenesis). For instance, Bernabé et al. (2003) interpreted the evolution of permeability and porosity impact in creating/destroying effective and non-effective porosity and analyzed different trends in porosity-permeability curves for sandstone and shale formations. Taylor et al. (2010) evaluated reservoir quality enhancement due to secondary porosity in sandstones by studying the fluids that drive chemical reactions and generate porosity, including the impact of CO_2 and organic acids by decarboxylation organic matter, as well as the hydrocarbon effect on preservation.

Diagenetic studies in the Middle Bakken shale (Williston Basin, North Dakota) have shown that diagenetic calcite cement has a detrimental impact on reservoir quality as it highly reduces the storage capacity of the pore space (Brennan, 2016). In contrast, changes in the pore structure due

to dissolution of carbonates or feldspars may increase secondary porosity and can be related to the presence of fluids associated with decarboxylation of kerogen or other processes that result in the generation of diagenetic fluids, such as the transformation smectite-illite.

Additional studies have examined the controls of pore systems and diagenetic pathways on the reservoir quality. Zhao et al. (2017) analyzed diagenetic events on the Longmaxi Shale. They concluded that shale-gas systems' primary porosity is mainly controlled by burial diagenesis and thermal maturation of organic matter, with porosity trends exhibiting a positive correlation with Total Organic Content (TOC) and quartz content. Therefore, the mineral types and organic matter pores play an essential role in the resultant diagenetic pathways and reservoir quality.

3.5. Model Formulation: Diagenetic Analysis and Reactive Transport

In this study, we proposed a multi-disciplinary framework that integrates mineralogical, petrophysical, and chemical data to investigate the role of chemical diagenesis on the pore structure's evolution. The pore-scale model has two main components: the diagenetic analysis and the reactive transport simulator. The first component involves examining the depositional environment, mineralogy, and pore structure characteristics of the formation of interest to identify possible diagenetic controls on reservoir quality. The second component comprises the representation of the pore-space features based on the observations from the diagenetic analysis and the numerical simulation of fluid transport and mineral reactions related to relevant diagenetic events, considering advection, diffusion, and reactive transport. Figure 23 illustrates the model formulation's workflow to couple the diagenetic analysis and the pore-scale simulator for reactive transport.

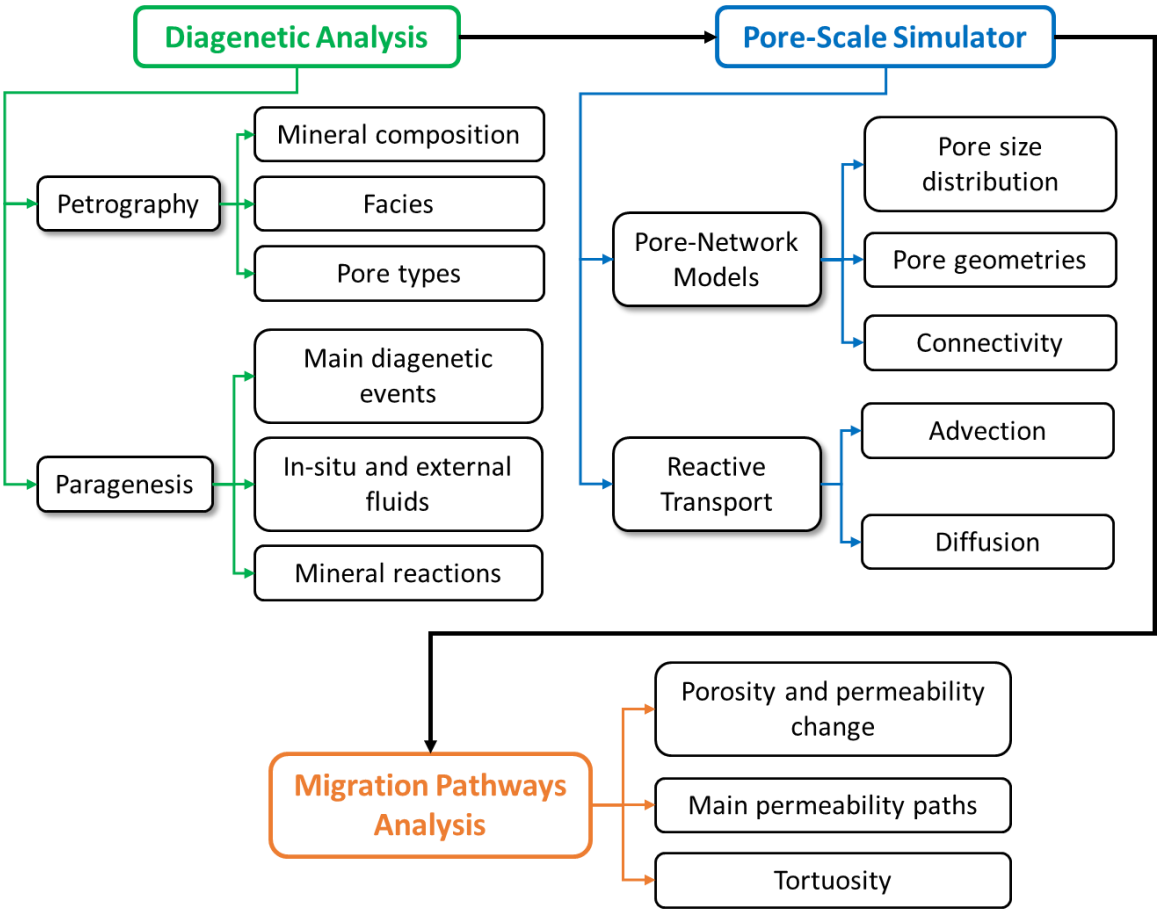

Figure 23. Workflow for diagenetic analysis and reactive transport at the pore-scale

3.5.1. Diagenetic Analysis

Understanding the impact of the depositional environment and diagenetic processes on the rock's petrophysical properties is essential to quantify the pore structure evolution and predict reservoir quality. Integrating information about the geological setting, textural features, mineralogy, pore size distribution, and main diagenetic events provides the foundation to establish pore network models representing the rock structure. Traditional techniques used to reconstruct the processes that characterize the alteration history of the rock include petrographic studies, XRD (X-ray diffraction) and XRF (X-ray fluorescence) analyses, SEM imaging (Scanning Electron Microscopy), among others (Burley et al., 1985). The purpose of the analysis is to develop a

paragenetic sequence that reflects the pore space's evolution as a function of mineralogy, pore fluids, and diagenetic events from available thin sections, core samples, outcrops, or well-log data. For this study, we used a petrographic microscope with transmitted and reflected light capabilities for a broad analysis of the thin sections. Additionally, we used a FEI Quanta 250 Scanning Electron Microscope fitted with two detectors. A Bruker XFlash 61100 energy dispersive spectroscopy (EDS) was used to identify various chemical components and sample variations. Also, a secondary electron detector (SE) was used to observe topographic changes. The system was operated at an acceleration voltage between 20kV and 25kV with a spot size of 5 and a working distance between 5 and 10mm.

3.5.2. Pore Network Model and Flow Field

To represent the pore structure, we generated 3D pore-networks based on idealized representations of the porous media. In this case, the pore-body and -throat size distributions and connectivity used for the model were generated after experimental size data taken from petrographic analysis of available rock samples. Besides the size, the pore types investigated are captured by assigning mineralogical compositions and geometrical shapes that follow the distributions observed in the samples. The geometries of the pore-bodies and -throats considered include circular, triangular, and rectangular cross-sections. The mineralogical composition is represented as a percentage of the pore surface area occupied by each mineral. Other properties such as location and coordination number are assigned stochastically. Additional parameters like pore volume and shape factor are computed from the pore dimensions. The hydraulic conductivity of the throats (g) is calculated as a function of the shape factor (G), the cross-sectional area (A), and the fluid viscosity (μ), based on the expressions for dimensionless hydraulic conductance of a duct given by (Patzek and Silin, 2001).

The network's initial porosity is calculated as the ratio of the void space volume given by pore-bodies and -throats and the model's total volume. Before performing flow simulations, it is necessary to identify isolated clusters and dead-end structures of pores and throats that are not connected to the main flow channels and remove them from the network to avoid singularities in the flow solution model. Besides, no-flow boundary conditions should be ensured in faces that do not correspond to the inlet or outlet faces. The initial permeability is calculated from Darcy's law, using the pressure field solution for steady-state flow. The resulting network porosity and permeability can be additionally constraint by macroscopic porosity and permeability data reported in the literature.

After the network characteristics are defined, the flow field for steady-state is computed by solving the system of linear equations that characterize single-phase flow through a pore network. Each equation in the system represents the volumetric flow-rate balance for a given pore-body (see Eq. 4). The flow rate is a function of the pressure at pore i (p_i), the pressures of the neighboring pores j (p_j), and the fluid conductivity in the throats ($g_{i,j}$) connecting pore i to pores j. Eq. 22 represents the net volumetric flow (Q_{net}) for a given pore i connected to neighboring pores j.The boundary conditions employed to solve the system are a constant inlet flow rate (Q) that represents the sum of the rates overall inlet pores, and an outlet pressure reference value (p_{outlet}).

$$Q_{\text{net}} = 0 = \sum_j \left[(p_j - p_i) g_{i,j} \right] \tag{22}$$

3.5.3. Reactive Transport Model

Reactions among the rock minerals, in-situ fluid, and external fluids (if the system is open) can change the composition and the structure of the pore space. To evaluate chemical diagenesis at the pore scale, we defined a solute mass transport model that reflects the concentration variations of

all the components in each pore as shown in Eq. 21 (Berner, 1980b). Relevant physical and chemical processes between the rock minerals and the aqueous phase filling the pore space should be considered. A discretized form of the conservation of solute mass balance equation for a given pore i and chemical component k (Steefel et al. 2005) is presented in Eq. 23. The left-hand side represents the accumulation term. The first three terms on the right side characterize the transport by advection (inflow and outflow) and diffusion. The last term on the right describes the effect of the mineral/fluid reactions on concentration. For species transport between pores, perfect mixing, or the mixed cell method (MCM) can be assumed for each pore. This means that the concentration in each pore is considered uniform (Tansey and Balhoff, 2016).

$$V_i \frac{\partial C_{k,i}}{\partial t} = \sum_{j=1}^{c_n} Q_{ij} C_{k,j} + \sum_{j=1}^{c_n} Q_{ij} C_{k,i} + \sum_{j=1}^{c_n} D_{k,ij} A_{ij} \frac{C_{k,j} - C_{k,i}}{l_{ij}} + \sum_{m=1}^{N_m} A_{m,i} R_{m,i} \qquad (23)$$

$$(\mathrm{q}_{ij} > 0) \qquad (\mathrm{q}_{ij} < 0)$$

where V_i is the volume of pore i, $C_{k,i}$ is the molar concentration of component k in pore i, t is time, c_n is the coordination number of pore i, j are the pore connected to pore i, Q_{ij} is the flow rate between pore i and j, $D_{k,ij}$ is the diffusion coefficient of component k between pores i and j, A_{ij} is the cross-sectional area of the throat connecting pores i and j, l_{ij} is the length of the throat connecting pores i and j, $A_{m,i}$ is the surface area in pore i of mineral m available for reaction, and $R_{m,i}$ is the reaction rate of the mineral ($\mathrm{mol\ cm^{-2}s^{-1}}$).

The diffusion term in Eq. 23 captures the solute transport due to molecular diffusion as conveyed from Fick's First Law. The diffusive flux is considered proportional to the concentration of the species in solution (Eq. 24). The proportionality is given by the diffusion coefficients of the species analyzed. These coefficients are obtained from available data for anions and cations at 25℃ and

converted to the system's temperature using the Stokes-Einstein Relation (Kim et al., 2011). After the chemical system is defined, the lumped components' effective diffusion coefficients are determined as a weighted average of the diffusion coefficients of the species present weighted by their concentration differences.

$$J_k^{diff} = -D_k \nabla c_k \tag{24}$$

Where k is the chemical component, J^{diff} is the diffusive flux, D_k is the diffusion coefficient of the component k, and c_k is the concentration of component k.

The solute mass balance equation is solved for every k component included in the chemical system, which incorporates all the species present in the reactions between the rock minerals and the aqueous phase (heterogeneous reactions) and the reactions within the aqueous phase (homogeneous reactions). The reactions occurring within the fluid (aqueous phase) can be described by local equilibrium conditions and are considered to be instantaneous. In contrast, the heterogeneous reactions between the fluid and rock minerals are considered to be slower and kinetically controlled. The latter category involves the mineral dissolution, and precipitation reactions that should be accounted for in the reaction term showed in Eq. 23.

The precipitation/dissolution reactions to be modeled are defined by the diagenetic processes observed in the paragenetic sequence that depend on both the mineral and fluid composition. In general, geochemical systems are highly complex due to the presence of various minerals, the heterogeneous nature of the pore space, and the intricate interactions among multiple minerals and fluids with time. The solute mass balance equation should be solved for every species present in the reactions included in the analysis. Therefore, to simplify the number of equations to be solved,

only the diagenetic reactions that appear to have a larger impact on the pore structure should be considered to describe the mineralogical evolution.

To further simplified the chemical system, the species that constitute the reactions of interest can be grouped into subsets of chemical species. These lumped species can then be identified as the components characterizing the system, and the solute mass balance equation will be solved for each group and not for each species. The component groups are designed so that all the species can be written as a combination of the smaller set. The selection of these lumped components is based on the tableau method that establishes the rules to set the species combinations and provides the resultant relations among species and components (Li et al., 2006; Nogues et al., 2013).

3.5.4. Geochemical System: Homogeneous and Heterogeneous Reactions

The reactions within the aqueous phase are faster than the reactions occurring between the fluid and the rock and the advective flow's relative times. Thus, these reactions can be considered in equilibrium and are represented by the mass action equations (Steefel and MacQuarrie, 1996). Eq. 25 and 26 show the mass action equations for the lumped components in terms of the primary components and the secondary species present in the aqueous phase. Primary components are those independent species that are the basis to express all other species (secondary species) in the system as a linear combination.

$$[c_T] = [c_p] + \sum_{s=1}^{Nr} v_{stoi}[c_s] \tag{25}$$

$$[c_s] = \frac{1}{K_s \gamma_s} \prod_{s=1}^{N_c} (\gamma_p [c_p])^{v_{stoi}} \tag{26}$$

Where $[c_T]$ is the concentration of the lumped component, $[c_p]$ is the concentration of the primary components, $[c_s]$ is the concentration of secondary species, N_r is the number of linearly

independent reactions, v_{stoi} is the stoichiometric reaction coefficient, K_s is the equilibrium constant, and N_c is the number of components.

Table 9 summarizes the chemical interactions included in the system and the corresponding equilibrium constants at 50℃. Reactions 1 to 4 are kinetically modeled and represent the dissolution and precipitation of dolomite, kaolinite, albite, and anorthite. While reactions 5 to 14 are considered instantaneous and in equilibrium at all times. A total of 18 species can be present in the aqueous phase from the reactions shown. Including H_2O, H^+, OH^-, Ca^+, Na^+, Cl^-, Mg^{2+}, H_2CO_3, HCO_3^-, CO_3^{-2}, H_4SiO_4, $H_3SiO_4^-$, $H_2SiO_4^{2-}$, Al^{3+}, $Al(OH)^{2+}$, $Al(OH)_2^+$, $Al(OH)_3$, and $Al(OH)_4^-$. To simplify further the chemical system, we used the tableau method. From this formulation, eight components were designed to represent the sodium, chloride, magnesium, hydrogen, calcium, carbon, silica, and aluminum bearing species. The chemical component lumping scheme is shown in the Appendix (Table A 1).

Besides considering the thermodynamic equilibrium in the aqueous phase for primary and secondary species, it is necessary to account for the species' effective concentrations (ions). The effective concentration is used to describe the behavior of a “real” solution, where the tendency of the ions for electrostatic interactions limits their ability to react, differing from “ideal” solution formulations. The effective concentration or activity is proportional to the actual concentration and a proportionality constant, or correction factor called the activity coefficient (γ).

Table 9. Kinetic and equilibrium reactions included in the chemical system, and their equilibrium reaction constants at 50 ºC (Morel and Hering, 1993)

Type		Reaction	Equilibrium constant ($\log K_{eq}$)
Kinetic	1	$CaMg(CO_3)_2(s) + 2H^+ \leftrightarrow Ca^{2+} + 2HCO_3^- + Mg^{2+}$	1.63
	2	$Al_2Si_2O_5(OH)_4\,(s) + 6H^+ \leftrightarrow 2Al^{3+} + 2H_4SiO_4 + H_2O$	3.8
	3	$NaAlSi_3O_8(s) + 8H_2O \leftrightarrow Na^+ + Al(OH)_4^- + 3H_4SiO_4$	-1.67
	4	$CaAl_2Si_2O_8(s) + 8H^+ \leftrightarrow Ca^{2+} + 2Al^{3+} + 2H_4SiO_4$	21.7
Equilibrium	5	$H_2O \leftrightarrow H^+ + OH^-$	-13.26
	6	$H_2CO_3 \leftrightarrow H^+ + HCO_3^-$	-6.15
	7	$HCO_3^- \leftrightarrow H^+ + CO_3^{-2}$	-10
	8	$CaCO_3(s)\ + H^+ \leftrightarrow Ca^{2+} + HCO_3^-$	-8.22
	9	$H_4SiO_4 \leftrightarrow H^+ + H_3SiO_4^-$	-9.2
	10	$H_3SiO_4^- \leftrightarrow H^+ + H_2SiO_4^{2-}$	-12.4
	11	$Al^{3+} + OH^- \leftrightarrow Al(OH)^{2+}$	-8.76
	12	$Al^{3+} + 2OH^- \leftrightarrow Al(OH)_2^+$	-18.9
	13	$Al^{3+} + 3OH^- \leftrightarrow Al(OH)_3$	-27.3
	14	$Al^{3+} + 4OH^- \leftrightarrow Al(OH)_4^-$	-33.2

Several models have been proposed to determine the activity coefficients of the species present in the aqueous solution, with different models being appropriate for solutions in a given ionic strength range. In this study we used, the Davies Equation (Eq. 27) to determine these coefficients given that the ionic strength (Eq. 28) of the subsurface fluids is generally larger than 0.1 M (Fitts, 2002). The activity coefficients are assumed to be constant with time and are determined for the initial concentrations of the aqueous phase in place.

$$\log \gamma = -Az^2 \left(\frac{I^{1/2}}{1 + I^{1/2}} - bI \right) \tag{27}$$

$$I = 0.5 \sum_{i=1}^{n} [c_i] z_i^2 \tag{28}$$

Where γ is the activity coefficient, A is a constant that depends on the dielectric constant and the absolute temperature, I is the ionic strength, b is an empirical parameter in the range 0.2 to 0.3, and z is the ion charge.

Next, the reactions between minerals and fluid are modeled kinetically (heterogeneous reactions). Changes in concentration due to kinetic reactions enclosed in the chemical system are considered reaction-limited, constrained by the surface area of the mineral available for reaction and the reaction rate, as shown in the reaction term in Eq. 23. The reaction-rate term for the lumped components in each pore (i) is the sum of the rates of all the involved kinetic reactions. In other words, these rates correlate the change in concentration of the species present in the aqueous phase with the mineral dissolution and precipitation. Eq. 29 shows the general form of the rate law implemented in the model based on transition state theory (TST) for dissolution and precipitation reactions treated as reversible (Lasaga, 2014; Steefel et al., 2013). Eq. 30 shows the saturation state function used, which introduces the dependency of the reaction rate on the saturation state of the system as a function of the Gibbs free energy change:

$$R = k \prod_{s} \{s\}^{n_s} f(\Delta G) \tag{29}$$

$$f(\Delta G) = 1 - \Omega^m \tag{30}$$

where R is the reaction rate ($\mathrm{mol\ cm^{-2}s^{-1}}$), k is the rate constant, s incorporates the activities of other species that have catalytic or inhibitory effects on the precipitation or dissolution rate, n_s is the degree of dependence on $\{s\}$, and $f(\Delta G)$ is the saturation state function. There are various forms for the $f(\Delta G)$ function. In this study, the selected form is a function of the saturation ratio (Ω). This ratio provides information about how far from equilibrium is the reaction, and it is formulated in terms of the equilibrium constant and the ion activity product. For instance, based on Eqs. 29 and 30, expressions for the general reaction rate law and the saturation ratios for the kinetic reactions of dolomite and kaolinite are shown in Eq. 31 to 33 (L. Li et al., 2006).

$$R_{mineral,i} = \left(\kappa_{OH^-}\{OH^-\}_i^{n_{OH}} + \kappa_{H^+}\{H^+\}_i^{n_H} + \kappa_{H_2O}\{H_2O\}_i^{n_{H_2O}}\right)(1 - \Omega_{mineral,i}) \quad (31)$$

$$\Omega_{dol,i} = \frac{\{\mathrm{Ca}^{2+}\}_i\{\mathrm{HCO}_3^-\}_i^2\{Mg^{2+}\}_i}{\{H^+\}_i^2 K_{eq,dol}} \quad (32)$$

$$\Omega_{kaol,i} = \frac{\{Al^{3+}\}_i^2\ \{\mathrm{H_4SiO_4}\}_i^2}{\{H^+\}_i^6 K_{eq,kaol}} \quad (33)$$

Where $R_{m,\mathrm{i}}$ is the reaction rates of mineral m in pore i (mol $\mathrm{cm}^{-2}\mathrm{s}^{-1}$), κ_{OH^-}, κ_{H^+}, κ_{H2O} are the temperature-dependent reaction rate constants, $\{OH^-\}$, $\{H^+\}$, and $\{H_2O\}$ are the activities, n_{OH^-}, n_H, n_{H2O} describe the degree of dependence on the ion, $\Omega_{dol,\mathrm{i}}$ and $\Omega_{kaol,i}$ are the dolomite and kaolinite saturation ratios in pore i, K_{eq} is the equilibrium constants, and $\{\mathrm{x}\}_i$ is the activity coefficient of ion x in pore i. The kinetic parameters for Eqs. 31 to 33 are grouped and shown in the Appendix (Table A 2). The total reaction rate for the lumped components formulated is different for each element. Given that the species involved in the component definition vary, the resulting reactions participating differ as well. The resulting reaction terms for the lumped components as a function of the various reactions involved in each case are shown in the Appendix (Table A 3).

3.5.5. Evolution of Pore Size

Mineral precipitation reduces the size of the pores, while dissolution increases it. The changes in the solid phase volume are calculated to determine the changes in the pore structure due to the phase changes of the minerals present. Those changes in pore volume ultimately represent changes in the network's porosity and permeability; consequently, it embodies changes in the reservoir quality. The mass changes for each mineral in each pore i (i.e., the changes in concentration) are converted into volume changes using the mineral molar volumes, followed by a conversion to

mineral volume fractions. The pore volume is reduced or increased for each pore according to the volume of minerals precipitated or dissolved.

Furthermore, the conductivity in the pore throats is recalculated with the volume change in the connected pore. Based on the assumption that changes in the throats' conductivity are related to changes in pore volume (Nogues et al., 2013). An expression for the updated throat diameter is given in Eq. 34

$$d_{ij}^{new} = d_{ij}^{prior} + d_{ij}^{prior}\left[\frac{V_i^{new} - V_i^{prior}}{V_i^{prior}} + \frac{V_j^{new} - V_j^{prior}}{V_j^{prior}}\right] \quad (34)$$

Where d_{ij}^{new} and d_{ij}^{prior} are the new and prior throat diameter connecting pores i and j. The evolution of the pore surface area assigned to each mineral is calculated as a function of the change in pore volume and following a similar procedure as for the throat diameter.

3.5.6. Numerical Formulation and Simulation Conditions

The solute mass balance equation for each pore's species concentration in the network results in a system of non-linear equations. An operator splitting approach with a sequential iteration is implemented to solve this system. The operator splitting approach consists of solving the concentration, including only transport terms, then solving the reaction term. In other words, a single time step involves a transport step followed by a reaction step using the concentrations after transport. Then, the concentrations for transport and reaction in every pore are solved in the network until convergence is achieved. Mathematically, the method can be depicted as a two-step sequential process involving a transport step (Eq. 35) and a reaction step (Eq. 36) (Steefel et al., 2015).

$$\frac{\left(c_k^{transp} - c_k^n\right)}{\Delta t} = L(c_k)^n, (k = 1, \dots, N_{tot}) \quad (35)$$

$$\frac{\left(c_k^{n+1} - c_k^{transp}\right)}{\Delta t} = R_k^{n+1}, (k = 1, \dots, N_{tot}) \quad (36)$$

Where c_k is the concentration of the component k , L is the spatial operator, and Δt is the time step. The Courant number criterion can be implemented to determine the time step size (Eq. 37). If the Courant number is 1, then the entire contents of the pore are transferred to the next one downstream (mixing cell model).

$$CFL = \frac{v\Delta t}{\Delta x} \quad (37)$$

The solute mass balance equation (Eq. 23) is solved for the lumped components in each iteration using the operator splitting approach. The concentration of individual species is calculated from the equilibrium computation of the instantaneous reactions. Besides the pore network characteristics and the diagenetic events selected to establish the chemical system, it is necessary to determine the initial system conditions, including the diagenetic stage, the in-situ fluid composition, temperature, and pressure. Moreover, boundary conditions related to the composition and pH of any external fluids coming into the network should be assigned to solve the system of equations.

3.6. Case Study: Woodford Shale

To illustrate the application of the pore-scale model formulation described above, an example case study is presented here. We investigated the diagenetic signatures in the Woodford Shale, focusing on rock-fluid interactions to assess their impact on reservoir quality and the evolution of migration pathways. The analysis performed is based on outcropped samples from the southeastern Anadarko

Basin. The location of the main outcrops studied, and the Arbuckle mountains' geology is shown in Figure 24.

The Woodford Shale was deposited in the Oklahoma Basin during the Late Devonian-Early Mississippian, primarily under anoxic conditions at slow sedimentation rates that favored organic material preservation (Kirkland et al., 1992). In the Late Mississippian-Early Permian, the Ouachita Orogeny deformed the rocks in southern Oklahoma, forming the Arbuckle Uplift and the Ouachita Mountains resulting in the Anadarko, Ardmore, and Arkoma Basins. In the Anadarko Basin, the Woodford unconformably overlies carbonate rocks of the Hunton Group and conformably underlies the Osage Lime (Johnson, 1989). Based on geological, paleontological, geochemical, and electrical variations, the Woodford has been subdivided into the lower, middle, and upper sections (Cardott, 2013; Comer, 2008). The Woodford shale is broadly classified as a siliceous black shale interbedded with light-colored shale, siltstone, sandstone, dolostone, and chert (Miceli-Romero and Philp, 2012; Slatt et al., 2011).

Diagenetic events on shale formations have been extensively investigated in active and previous research. Studies of shale diagenesis include the characterization of pore systems (Chalmers, Bustin, and Power, 2012), thermal maturity based on vitrinite reflectance (Cardott, 2012), and integrated geochemical and petrologic analysis to determine critical mechanisms that control oil and natural gas generation, expulsion, migration, and retention in producing unconventional reservoirs (Laughrey and Purrazzella, 2016). In particular, in the Woodford Shale, previous studies suggest there is evidence of hydrothermal alteration. Roberts and Elmore (2018) proposed that the Woodford Shale evolved into an open system to external fluids during middle to late diagenesis when multiple hydrothermal minerals precipitated in the fractures. The authors affirm the most likely mechanism for this influx of hydrothermal fluids is through fault-related activity.

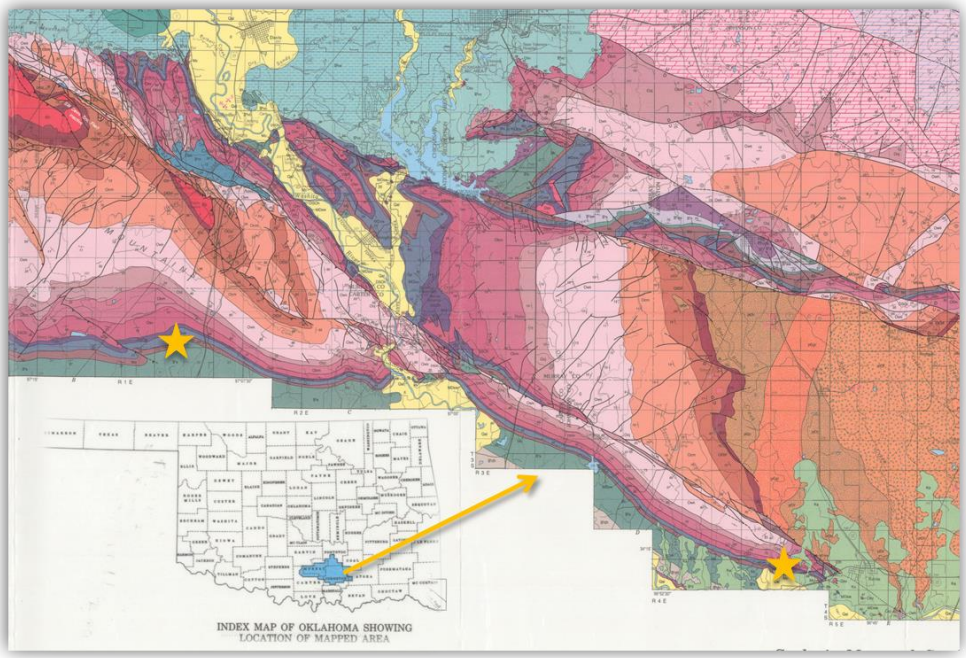

Figure 24. Arbuckle mountains geology. The yellow stars mark the outcrops used for the diagenetic analysis. Modified from Oklahoma Geological Survey.

3.7. Results

As previously mentioned, the pore-scale model proposed aims to improve our understanding of the diagenetic influence on the migration pathways evolution of the Woodford shale at the pore level. In this section, we present the petrographic observations and diagenetic evidence of the pore space alteration. Followed by the geochemical system generated based on the diagenetic analysis and the pore networks models constructed to represent the various characteristics of the pore structure. Finally, we introduce the observed changes in the flow pathways due to the migration of external fluids that interact with both the in-situ fluid and the rock minerals.

3.7.1. Petrography and Paragenesis

The petrographic analysis was conducted on ten polished thin sections. Four main microfacies were identified in the sections analyzed, including siliceous mudstone, calcareous mudstone, dolomitic mudstone, and argillaceous mudstone, as shown in Figure 25. Radiolarians and

tasmanites are present in almost all the facies observed. Quartz, calcite, dolomite, and clay are the main minerals found in all samples, with pyrite and iron oxides as major accessory minerals. The siliceous mudstone facies exhibit an abundance of biogenic quartz and pyrite replacements (Figure 25a).

In contrast, the calcareous mudstone is characterized by an abundance of calcareous allochems, iron oxides, and pyrite replacements (Figure 25b). The dolomitic mudstone shows intercalated dolomitic and quartz-rich layers with abundant pyrite and hydrocarbon filling pores (Figure 25c). And the argillaceous mudstone is typified by high clay content, authigenic quartz, and pyrite replacements, as well as mineralized veins with multiple orientations (Figure 25d).

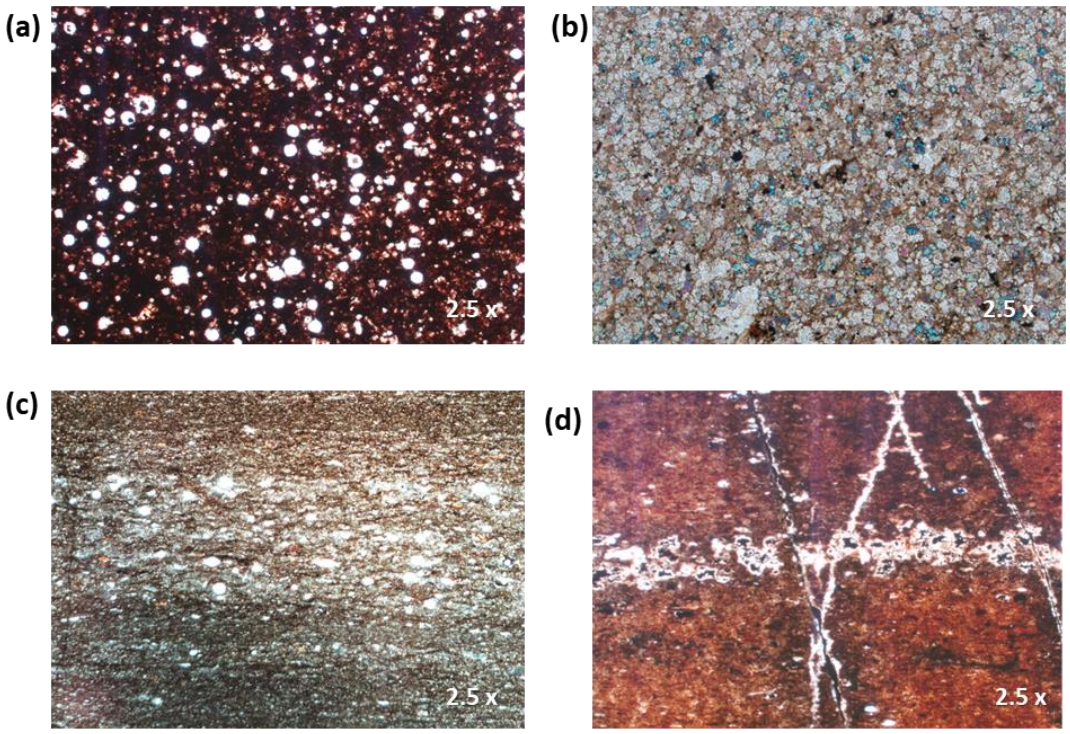

Figure 25. Petrographic characteristics of the microfacies observed in the Woodford shale samples (a) siliceous mudstone, (b) calcareous mudstone, (c) dolomitic mudstone, and (d) argillaceous mudstone.

The samples exhibit dissolution and precipitation events in the matrix and some presence of mineralized veins and fractures (see Figure 26). Quartz is found in multiple forms, including

detrital, biogenic, and authigenic filling pore space. Radiolarians and Tasmanites are common throughout the shale, often silicified by different forms of quartz. Pyrite is abundant and can be found as early pyrite framboids and late cubic pyrite replacing quartz, filling pores and veins. There is evidence of pyrite alteration to iron oxides. Dolomite and ferroan dolomite are also present exhibiting composition variations throughout the samples. Both dolomite and ferroan dolomite are considered early events.

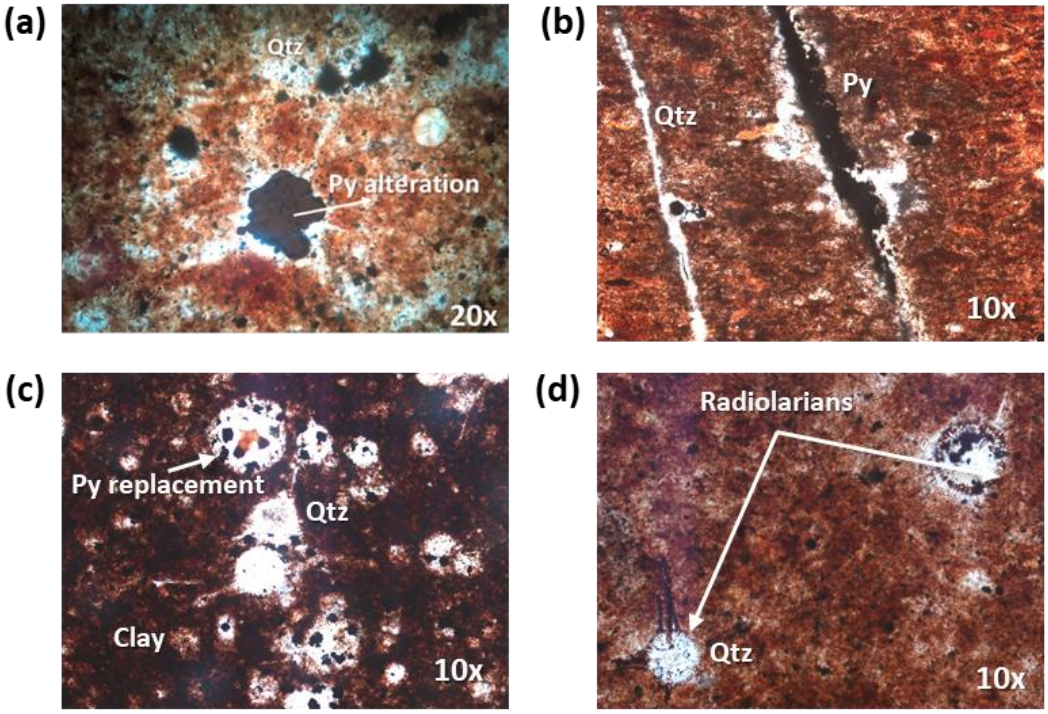

Figure 26. Diagenetic events evidence in the samples. (a) authigenic quartz, pyrite replacements and later pyrite alteration, (b) Mineralized veins with quartz and pyrite filling, (c) Pyrite replacement in radiolarians, (d) Quartz and pyrite replaced radiolarians in the clay matrix.

Examining selected samples under the SEM showed high variation in iron (Fe) content in the ferroan-dolomite present in the dolomitic facies. Figure 27 presents a line scan analysis performed in one of the thin sections that showed high-density variation (changes in color) for a single dolomite crystal. The components recorded in the spectrum include calcium, magnesium, and iron. From the line scan results, it is evident that the color variations are related to changes in Fe-content.

Darkest regions (Less dense) coincide with lower iron content (Fe) and higher magnesium (Mg). These variations in the dolomite composition are a common indicator of evolving fluid composition, as the availability of iron in the fluid changes while the dolomite is being precipitated.

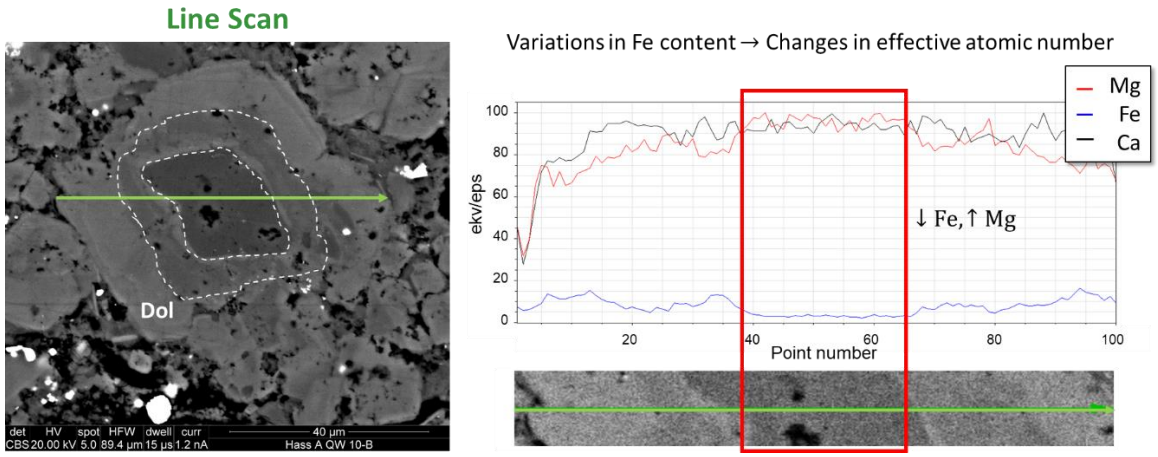

Figure 27. Line scan analysis of ferroan-dolomite composition. Variations in dolomite composition are an indicator of evolving fluid composition as the dolomite is being precipitated.

Further inspection using the SEM revealed additional accessory minerals present in the samples. Among the minerals observed are sphalerite (ZnS) and gorceixite ($BaAl_3(PO_4)(PO_3OH)(OH)_6$) identified from the compositional spectrum obtained with the energy dispersive spectroscopy (EDS). The EDS is used to detect elemental components and variation in samples, as shown in Figure 28. These sulfur and barium bearing minerals are associated with hydrothermal minerals, and they could be indicators of hydrothermal fluid presence in the Woodford. Diagenetic and paleomagnetic studies have previously suggested the presence of hydrothermal minerals around fractures in the Woodford Shale, as indicated by the analysis of core samples from the Anadarko and Ardmore basins (Roberts et al., 2019; Roberts and Elmore, 2018).

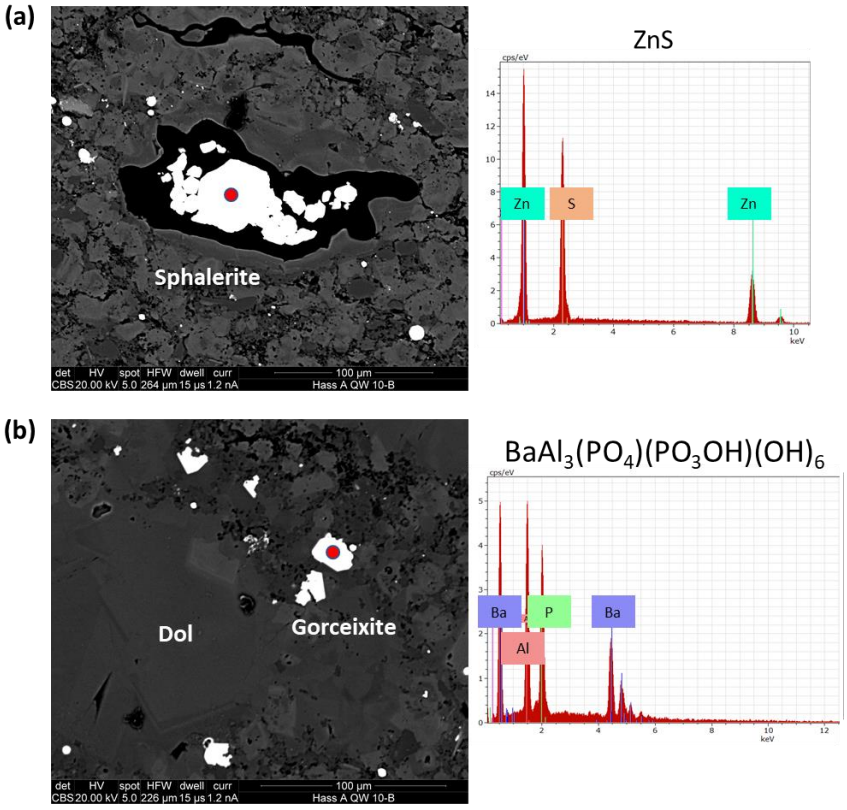

Figure 28. Additional minerals found in the matrix and their composition spectrum (a) sphalerite, (b) gorceixite. Both sphalerite and gorceixite can be associated with the presence of hydrothermal fluids.

A tentative paragenetic sequence based on observations obtained from the samples studied is shown in Figure 29. Diagenesis is dominated by compaction, dissolution, and precipitation events. Early diagenetic alteration of the matrix and allochems is dictated by precipitation of several authigenic phases: pyrite framboids, quartz overgrowths, dolomite, and ferroan-dolomite. There is evidence of late precipitation of hydrothermal minerals and hydrocarbon migration. Additional paramagnetic studies could be conducted to examine the presence of magnetite and hematite and their role in pyrite alteration. Previous research on core samples from the Woodford Shale in the Anadarko and Ardmore basins (Roberts et al., 2019; Roberts and Elmore, 2018) unveiled evidence of the complex paragenetic history and indicated the possibility of hydrothermal fluid migration through fractures, supporting the evidence encountered in this study.

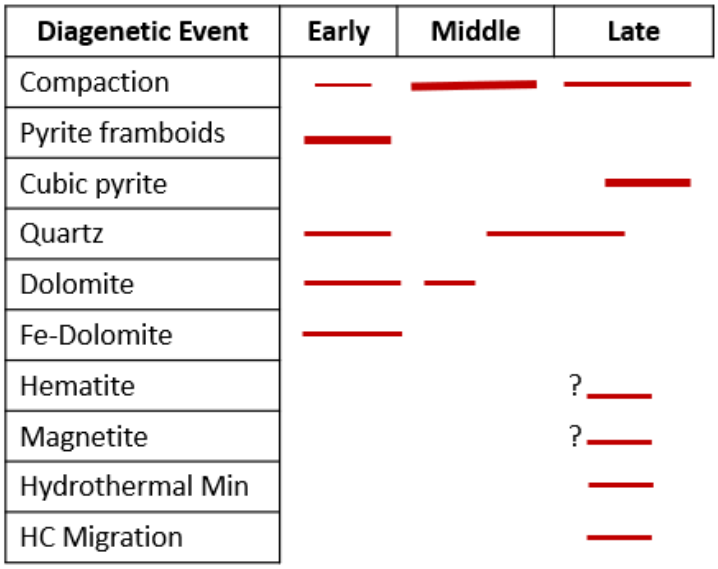

Figure 29. Paragenetic sequence. The events listed are the major occurrences observed. The timing is based on information from previous studies and the conclusions drawn from the thin sections analyzed.

3.7.2. Pore space: types, abundance, and distribution

The pore types observed in the Woodford Shale samples can be classified as intraparticle and interparticle (Loucks et al., 2012; Pommer and Milliken, 2015). Organic matter-hosted pores are also present but will not be addressed here, as additional studies with higher resolution image capabilities are required for their characterization. Initial observations indicate facies dependent relations with pore types, abundances, and distributions. Based on the quantity and variety of pore types encountered, two of the four microfacies identified were selected to be modeled in the next stage, namely, the dolomitic mudstone facies and the laminated argillaceous facies.

For the laminated argillaceous mudstone facies, interparticle pores occur between grain boundaries or clay sheet boundaries and are also abundant, showing a preferred orientation parallel to the laminations (Figure 30a). In the dolomitic mudstone facies, interparticle pores are common and abundant, occurring along crystal boundaries and crystal-authigenic component boundaries (Figure 30b). In laminated argillaceous facies, intraparticle pores are present primarily through moldic pores of dissolved tasmanites, radiolarians, and within the clay sheets. Interparticle pores

are abundant and range in sizes from 2 microns to 11 microns (Figure 30c). In contrast, intraparticle pores may appear larger in some cases by comparison to the interparticle pores but are in lower abundance. Intraparticle pores are also observed in the microfacies analyzed. In the case of dolomitic mudstone facies, intraparticle pores are found in radiolarians, pyrite framboids, and partially dissolved grains (Figure 30d).

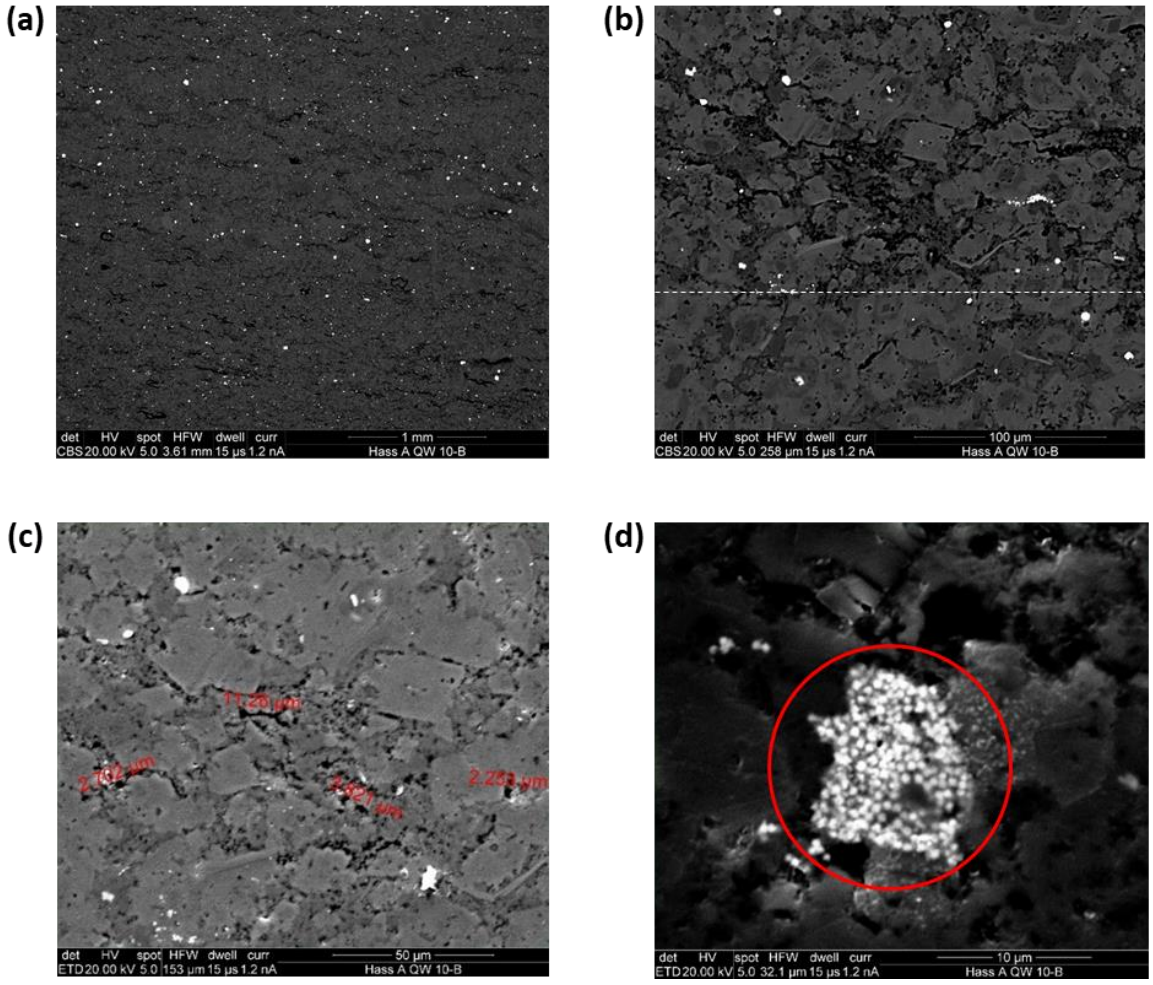

Figure 30. Pore space characteristics between facies (a) laminated argillaceous mudstone pores, (b) dolomitic mudstone pores, (c) interparticle pores including pore sizes and cross-sectional shapes, and (d) intraparticle pores in a pyrite framboid.

3.7.3. Geochemical system

The observations obtained from the petrographic and diagenetic analysis suggest a complex paragenetic sequence for the Woodford Shale. Based on these observations and pointing to model significant events with the most substantial influence on the pore structure alteration, we defined a geochemical system that considers early-middle diagenesis in the Woodford involving dissolution and precipitation events of dolomite and accessory minerals such as feldspars and clay. The system conditions of pressure and temperature were selected within the middle diagenetic window stage at 50 ℃ and 100 bar (1450 psi). A simplified mineralogical composition was implemented based on the XRD measurements (Abousleiman et al., 2007), shown in Table 10.

Table 10. XRD mineralogical composition Woodford Shale (Abousleiman et al., 2007).

Mineral	Composition
Quartz	4.2-90%
Clays	1.3-40%
Carbonates	13-94%
Pyrite	5-13%
K-Feldspar	2-6%
Other	1.4-4%
Kerogen	11-18%

The reactions selected to be kinetically modeled include the dissolution and precipitation of dolomite, albite, anorthite, and kaolinite. The calcite reactions are fast compared to the other mineral reactions and can be considered in equilibrium (Noiriel et al., 2012). Besides the mineral reactions, the system should incorporate the reactions inside the aqueous phase that comprise the ions' speciation and dissociation according to the mineral components. In this case, the speciation of carbon, silica, and aluminum bearing species.

The initial conditions of the fluid present in the pore space were assigned as follows. A pH of 7.5 was assumed, along with equilibrium between the fluid, quartz, and clay minerals present in the rock. The concentration of species involved in the aqueous phase reactions was derived from equilibrium calculations. The calcium ion concentration was determined from electroneutrality balance to satisfy the electronic conditions. The initial concentrations of the sodium and chloride ions were obtained from typical groundwater concentrations ([Na]=0.45 M,[Cl]=0.45 M), then used to determine the ionic strength and estimate the species activities. Also, it was assumed that there are no initial carbon-bearing species present in the aqueous phase.

The characteristics of the external-fluid coming into the pore network were assigned to capture the acidic diagenetic fluid properties. A pH of 2.9 was assumed, and initial concentration of carbon-bearing species was calculated at 100 bar and 50℃ (323 K) following the CO_2 solubility analysis by Duan and Sun (2003). Similar to the in-situ fluid, the sodium and chloride ions' initial concentrations were assumed to reflect typical groundwater concentrations, then used to determine the ionic strength and estimate the species activities. No initial aluminum and silica bearing species were included.

3.7.4. Hybrid Pore Networks

We generated two types of pore networks to capture the differences in structure discovered in the facies studied. The first network aims to capture the pore structure of laminated facies. In this case, we employed a higher percentage of pore geometries with a sheet-like, rectangular shape to represent the pores' structure seen, for example, in Figure 30b and Figure 30c**.** The second network type was designed to represent facies without lamination, as seen in Figure 30a for dolomitic mudstone facies. In this case, the geometry of the pores is dominated by triangular and circular

cross-sectional shapes. Table 11 summarizes the network properties, including size, number of pore bodies and throats, geometry percentages, porosity, and permeability.

Table 11. Hybrid-network properties for laminated and non-laminated facies.

Property	**Network 1 (Laminated)**	**Network 2 (Not laminated)**
Number of pore bodies	3200	2700
Number of pore throats	7763	4000
Cross-section geometry %	Rectangular 69.28% Circular 16.34% Triangular 14.37 %	Rectangular 20.37% Circular 49.30% Triangular 30.33 %
Porosity	2.31%	5.20%
Permeability (μD)	8.05	1.11

The network characteristics for laminated facies reflect the higher connectivity of the available pores with a higher number of throats and absolute permeability. In contrast, dolomitic mudstone facies' pore space is modeled with a lower number of throats and lower permeability, just as observed in the pore space analysis. However, although there is less connectivity in the dolomitic mudstone facies, there is still an abundance of interparticle pores with larger characteristic sizes than in other facies. This is reflected in the more extensive porosity built-in the network. An example of the pore-body and throat size distributions for Network 2 is shown in Figure 31**.** The size distributions used for the simulations are based on pore size measurements took during the SEM analysis at random locations and different magnifications to create representative distributions. Using the Weibull distribution function, we sampled the experimental distributions and generated the simulator's distributions to develop the 3D networks.

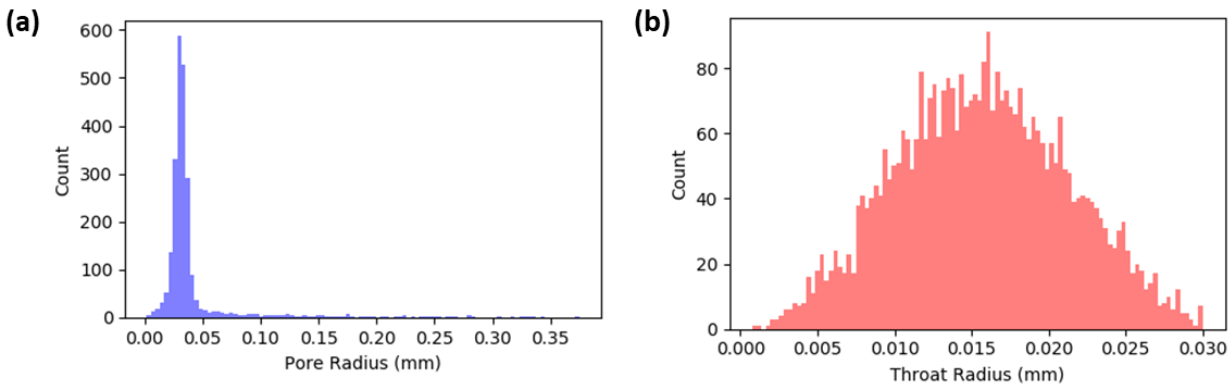

Figure 31. Size distributions for Network 2 (Not laminated) (a) Pore-body distribution and (b) Pore-throat distribution.

3.7.5. Flow pathways

After we defined the pore network properties and the boundary conditions, we performed the flow simulations. First, we initialized the network by computing the initial pressures and flow rates for all the pores saturated by the in-situ fluid. Then the external fluid is injected at the boundary. At this point, we record the concentration, velocity, and pressure changes to assess the evolution of the main flow paths.

The migration pathways are analyzed by identifying the paths with the highest flow rates at the simulations' initial conditions and after the reactive transport simulation is performed to detect changes in the migration pathways and their relationship with pore size, diffusion, and mineral reactivity. All possible migration pathways from inlet to outlet were mapped with the total number of potential paths in the networks ranging between 932,000 and 3,018,000. Next, we detected the main flow paths by tracking the highest flow rates across the pore structure emanating from the inlet pore nodes. Figure 32 shows the highest flow rate migration pathways observed for Network 2. The fraction of the main paths is roughly 2-5% per thousand of total ways. Pathways leading to dead pores are not accounted for in this analysis.

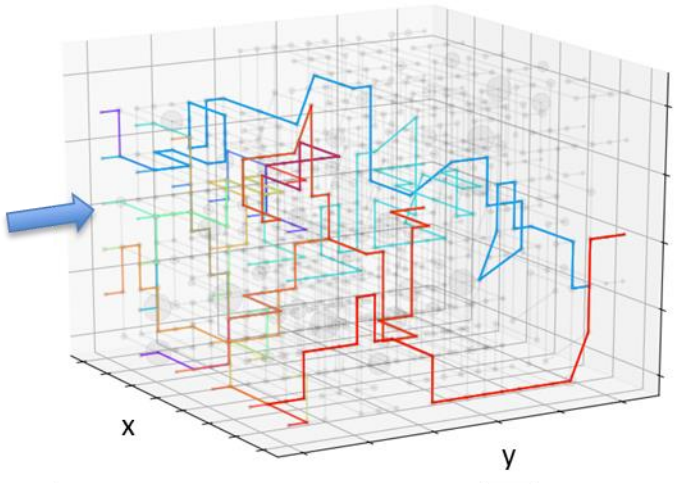

Figure 32. Sketch of the highest flow rate pathways in Network 2. All paths start from inlet pores and travel along the network, following neighbor pores with the highest flow rate at each possible exit throat. The blue arrow indicates the inlet face. The highlighted paths reflect the tortuous nature of the system.

Once the main pathways were identified, the tortuosity of the paths is calculated following Eq. 38 (Steefel et al., 2013). Tortuosity is a measurement of how far from a straight-line path is the actual pathway followed to cross the network. Figure 33 shows the tortuosity of the main flow migration pathways. It is observed that when only advection is considered in the simulation, the tortuosity values are in general higher than in the cases where both advection and diffusion are considered. This is an indicator of the role of diffusion on the transport of ions through the network that could increment the contact area of the grain surface with the solutes traveling in the fluid and eventually facilitate the reactions between the minerals and the fluid. Figure 34 presents tortuosity values for high flow rate migration pathways for advection and advection/diffusion transport. Higher tortuosity values are again observed when diffusion is not considered.

$$\tau = \left(\frac{L}{L_0}\right)^2 \tag{38}$$

Where τ is the tortuosity, L is the actual path length traveled through the network (through porous media) and L_0 is the path traveled in a straight line (the medium is not porous).

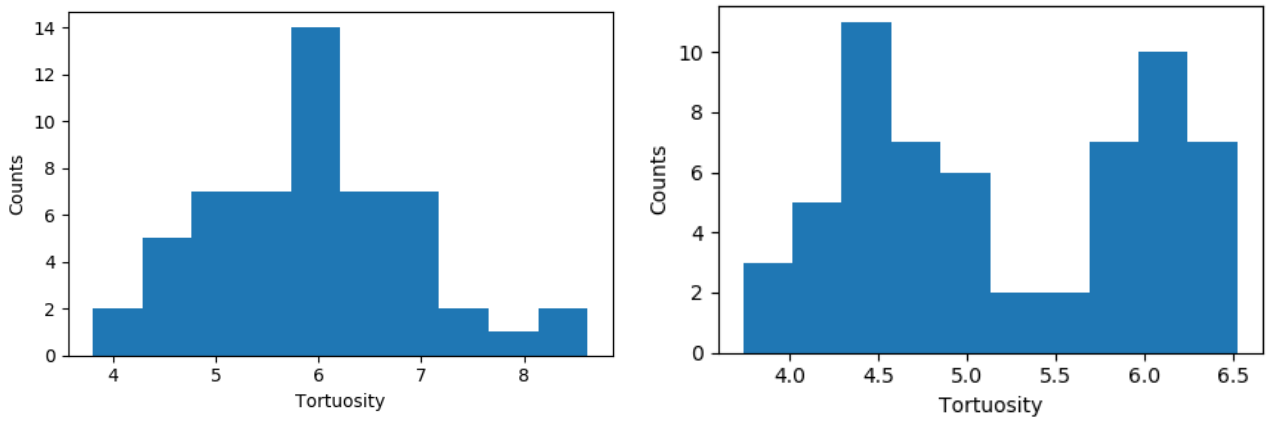

(a) **(b)**

Figure 33. Tortuosity of main migration pathways accounting for (a) advection transport and (b) advection and diffusion transport.

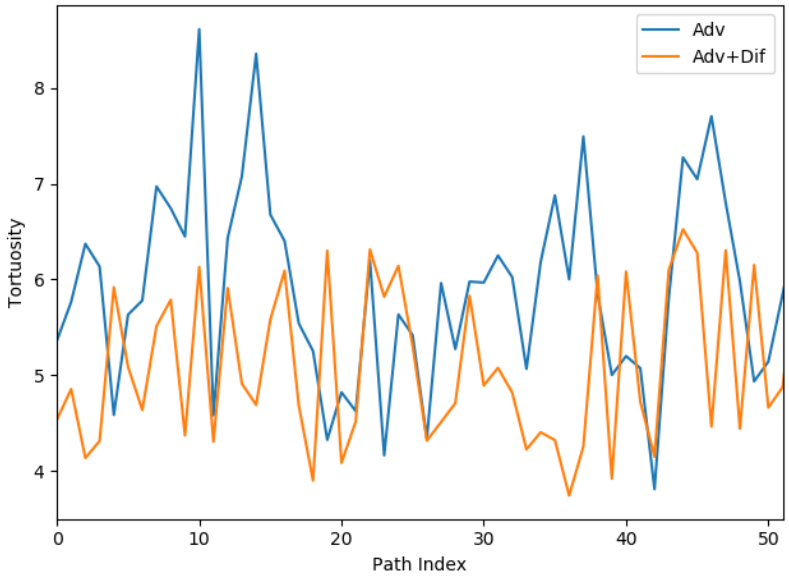

Figure 34. Tortuosity values for the main migration pathways, including only advection and advection/diffusion transport mechanisms.

Additionally, we studied the changes in pore structure characteristics and flow properties due to transport mechanisms such as advection and diffusion. Figure 35a and Figure 35b show the differences in flow rates when advection only or advection/diffusion are considered. When diffusion is included, a slight increment in flow rates is observed. This may be due to the higher interaction between species as their transport is also dependent on the changes in concentration,

leading to more contact with the minerals in the rock and more rapid dispersion. Figure 35c and Figure 35d show the differences in pore radius. Similarly, slight increments in pore radius are observed, which can be related to dissolution mechanisms. The contact with the surface is increased by more rapid interactions and transport of species. Figure 36 presents the changes in pore and throat volume for the different mechanisms investigated. As the main differences in volume are represented in the pore-bodies, we see an increment in the pore volume in advection and diffusion transport (Figure 36a and Figure 36b). In contrast, throat volumes do not exhibit significant changes (Figure 36c and Figure 36d).

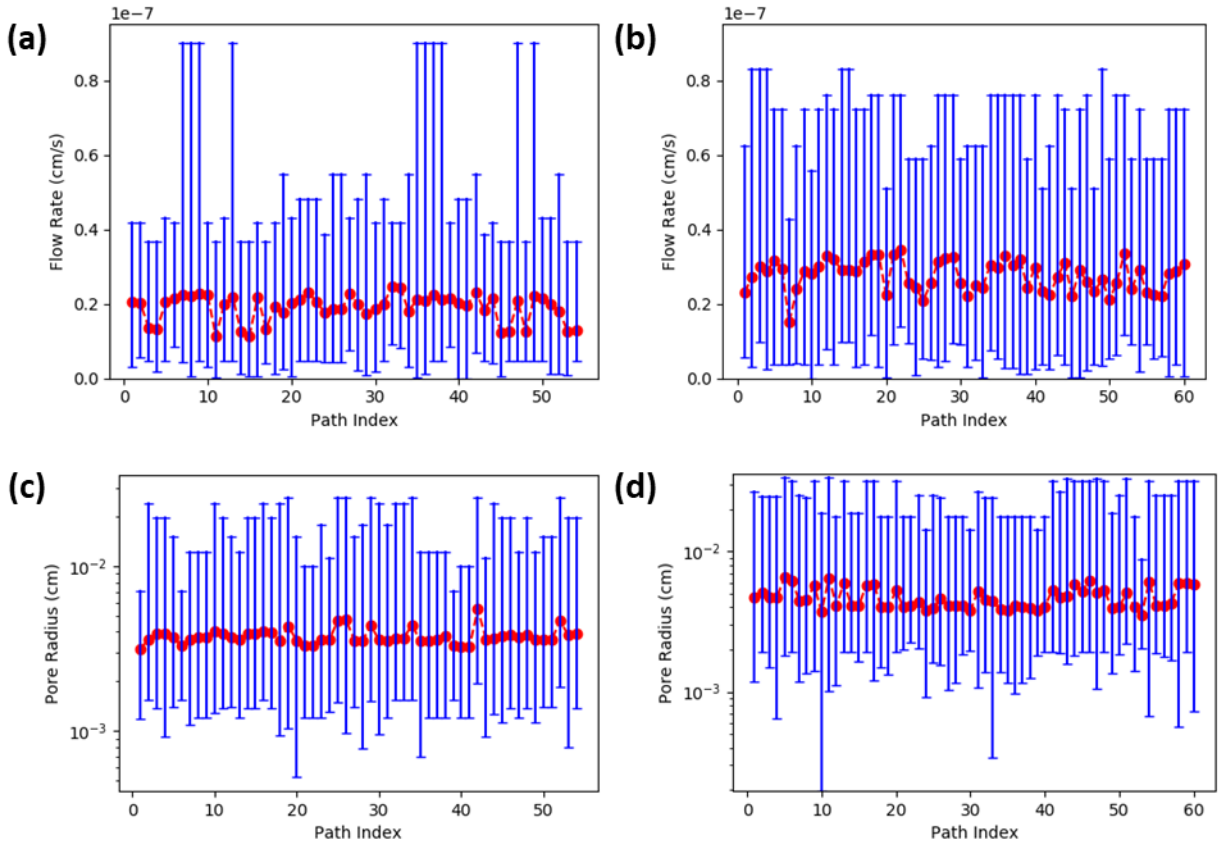

Figure 35. Changes in flow rate for the primary migration pathways simulation when (a) only advection is included, and (b) both advection and diffusion are included. Changes in pore radius for the main migration pathways as (c) only advection is considered, and (b) both advection and diffusion.

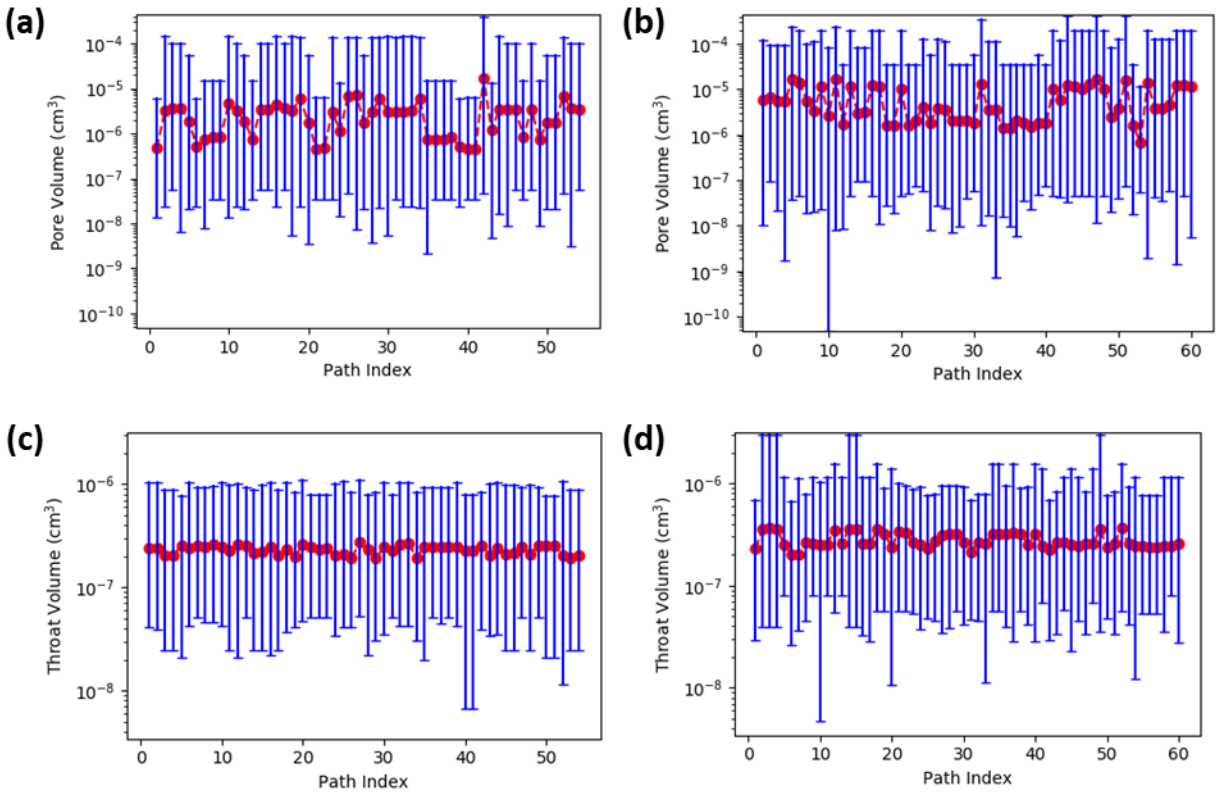

Figure 36. Changes in pore volume for the primary migration pathways simulation when (a) only advection is included, and (b) both advection and diffusion are included. Changes in throat volume for the main migration pathways as (c) only advection is considered, and (d) both advection and diffusion.

3.8. Discussion: Model Advantages and Limitations

Diagenetic alterations are responsible for the complex and heterogeneous pore space in sedimentary rocks. Thus, predictions of the pore system evolution should take into account the impact of diagenetic processes. Developing a model at the pore-scale that couples reactive transport with a pore network representation of the pore space is an excellent approach to capture the physical and chemical processes that the rock undergoes and integrate the effects of the rock structure and its heterogeneity into the characterization.

The methodology proposed here incorporates a 3D network model that represents the pore structure based on statistical distributions of the pore size and mineralogical composition. We coupled hybrid pore-networks to capture the pores' topology and geometry that characterize the

various microfacies identified from diagenetic analysis. The change in concentration of mineral components for each pore in the network is computed as a function of advection, diffusion, and kinetic reactions of the minerals and the aqueous phase present in the pore space. Furthermore, the model captures the pore space's evolution and the migration pathways, providing insights into the diffusive processes and tortuosity impact on solute transport.

The complexity of the chemical system is going to determine how accurately the chemical-diagenetic processes can be capture. A more robust chemical system that includes, for example, the interactions with the organic matter and the role of organic matter pores can result in a better approximation of the pore structure evolution but can imply higher computational costs. In this case, the model considers only the most relevant mineralogical components and their interaction with the aqueous phase (five minerals, four kinetic reactions), constituting a simple chemical representation but reducing computational costs.

The model's main limitation is related to the domain of the pore network and the upscaling of pressures, concentrations, and fluxes. Additional research is required to couple the observations at the pore-scale with reservoir and field representative quantities. Mechanical processes related to diageneses such as compaction and geomechanical effects should also be included to increase the accuracy of the predictions for reservoir quality and pore structure evolution. And the impact of the reaction component of the solute transport balance on porosity occlusion and permeability changes.

3.9. Conclusions

This chapter presented a pore-scale simulator that combines mineralogical, petrophysical, and chemical data to investigate chemical diagenesis's role in the migration pathways evolution. The model has two main components: diagenetic analysis and reactive transport simulation at the pore-

scale. The diagenetic analysis involves examining the depositional environment, mineralogy, and pore structure characteristics of the formation of interest to identify possible diagenetic controls and provide relevant structural and chemical properties of the system to the pore-scale model. The second component comprises the pore-space characteristics' representation based on the previous analysis and the numerical simulation of fluid transport and mineral interactions related to relevant diagenetic events. We employed multi-component coupled fluid-flow and reactive-transport to investigate these processes accounting for both advection and diffusion critically. To illustrate the application of the pore-scale model formulation described above, we explored the diagenetic signatures in the Woodford Shale, focusing on rock-fluid interactions to assess their impact on the evolution of migration pathways.

Petrographic analysis of the formation samples allowed us to characterize diagenetic processes. Diagenesis in the Woodford Shale is dominated by compaction, dissolution, and precipitation events. Early diagenetic alteration of the matrix and allochems is dictated by precipitation of several authigenic phases, including pyrite framboids, quartz overgrowths, dolomite, and ferroan-dolomite. In addition, there is evidence of evolving fluids, late precipitation of hydrothermal minerals, and hydrocarbon migration.

Four microfacies were identified in the samples analyzed, including siliceous mudstone, calcareous mudstone, dolomitic mudstone, and argillaceous mudstone. The main facies included in the analysis were the dolomitic mudstone facies and the laminated argillaceous facies. Initial observations showed pore types, abundances, and distributions to be facies dependent. The laminated argillaceous facies showed abundant interparticle pores between grain boundaries or clay sheet boundaries with preferred orientation parallel to the laminations. In contrast, dolomitic mudstone facies exhibited interparticle pores without preferential orientation and less connectivity.

We constructed hybrid 3D pore network models that represent the characteristic facies observed in the Woodford. The network characteristics for laminated facies reflect higher connectivity of the available pores with a larger number of throats and absolute permeability. While the pore space of dolomitic mudstone facies that were modeled with a lower number of throats and therefore a lower permeability just as observed in the pore space analysis.

The flow simulations showed that the migration pathways' tortuosity on paths with high flow rates is affected by the transport mechanisms included in the analysis. It was observed that when only advection is considered in the flow simulations, the tortuosity values are in general higher than in the cases where both advection and diffusion are considered. This is an indicator of the role of diffusion on the transport of ions through the network that could increment the contact area of the grain surface with the solutes traveling in the fluid and eventually facilitate the reactions between the minerals and the fluid. Higher flow rates and pore volume changes were observed when multiple transport processes were included, such as advection and diffusion. When diffusion is included, a slight increment in flow rates was observed. This may be due to the higher interaction between species as their transport is also dependent on the changes in concentration, leading to more contact with the minerals in the rock and more rapid dispersion.

Chapter 4. Geological Sequestration of CO_2 in Saline Aquifers: Critical Insights on Plume Dynamics, Storage Efficiency and Monitoring

4.1. Introduction

Carbon dioxide capture and storage (CCS) technologies have the potential to stabilize greenhouse gas concentrations in the atmosphere and contribute to climate change mitigation. The process consists of capturing CO_2 from industrial and energy-related sources, compressing it for transportation, and storing it in selected sites for long-term isolation. The captured CO_2 can either be utilized in industrial processes or sequestered into underground geological formations or the ocean. Sequestration in geological formations is currently the best option in terms of efficiency, environmental impact, cost, and understanding of the physical and chemical processes involved (Bachu, 2000). Furthermore, it is technically feasible on large scales, and the technology for deep injection of CO_2 has already been developed and employed in the petroleum industry.

Typical geological storage sites include deep saline aquifers, depleted hydrocarbon reservoirs, unmineable coal seams, salt caverns, and basalt formations. Out of these possible storage sites, deep saline aquifers represent a crucial alternative for CO_2 sequestration efficiency (Newell and Ilgen, 2019). Their geological, hydrodynamic, and geothermal conditions and promising large storage capacities and more accessibility to capture sites due to their broad geographical distribution make saline aquifers excellent candidates for storage operations (Intergovernmental Panel of Climate Change, 2005). Among the main characteristics of saline formations that are suitable for CO_2 storage are (1) sufficient porosity and permeability, (2) an overlying cap rock that acts as reservoir seal to avoid the leakage of the buoyant CO_2, and (3) injection depths located at 800 m to 3000 m to ensure pressures, temperatures, salinity and high CO_2 densities (Benson and Cook, 2005).

Numerous storage projects from pilot- to commercial-scale are under construction or are operational worldwide (Figure 37). The first commercial operation for CO_2 injection started in Norway in 1996, known as the Sleipner project, with an estimated storage capacity of 20 million tonnes (Mt) (Michael et al., 2010). Currently, the global capture and storage capacity of projects in operation or under construction stands at around 40 million tonnes per annum (Mtpa), with 260 Mt of CO_2 emissions from human activity already captured and stored (Global CCS Institute, 2019). Estimates from the IPCC (Intergovernmental Panel of Climate Change) indicate that to meet climate targets, up to 1,200 Gt of CO_2 would have to be stored by 2100. This means that the deployment rate of carbon capture and sequestration operations has to grow at a pace more than double the oil industry's growth during the last century (Mac Dowell et al., 2017).

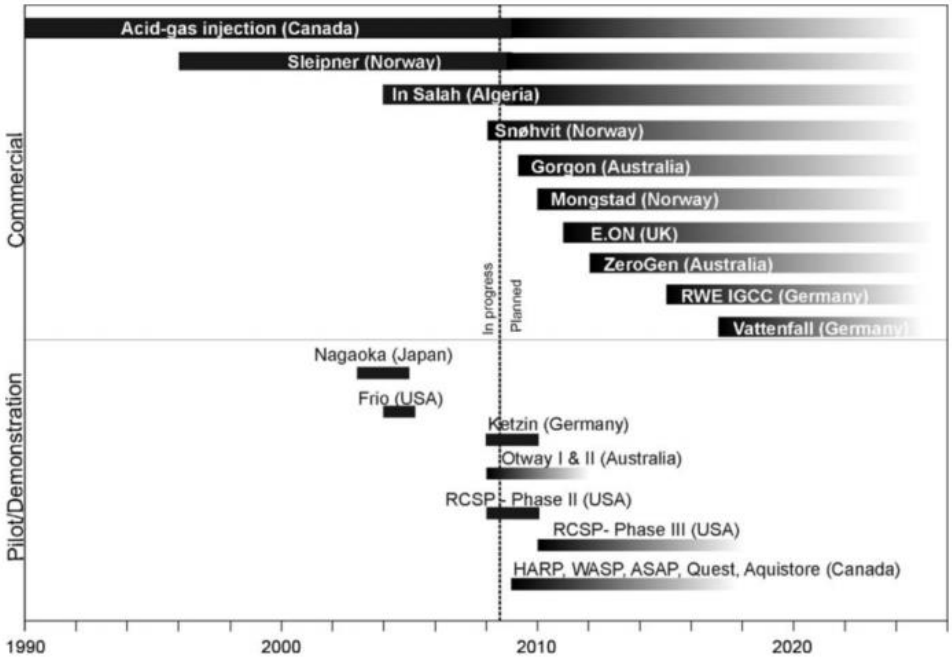

Figure 37. Timeline of selected commercial and pilot projects executed or in the planning phase as of 2010. (Michael et al., 2010). Before the first CO_2 sequestration project, the petroleum industry had already injected acid gas. The technologies used then transferred to CCS planning and operation.

Geological carbon sequestration projects are technically feasible, but several questions related to their development and long-term management are yet to be answered. Some of the main challenges

include assessing reservoir-specific storage capacities accounting for heterogeneities in the underlying properties, describing the role of different trapping mechanisms on the storage process, ensuring the security of the CO_2 sequestered, and understanding the evolution and extent of the CO_2 plume in the subsurface.

This chapter explores the plume characterization and monitoring during the geological sequestration of CO_2 in saline aquifers. First, we evaluated essential aspects of the sequestration process, including the CO_2-fluid-rock interactions, trapping mechanisms, storage capacity, and efficiency, as well as monitoring and verification techniques used to track the CO_2 plume. Then, we introduced our integrated modeling framework to appraise the CO_2 storage during long-term injection and post-injection periods, which includes uncertainty characterization and sensitivity analysis to investigate the impact and relative influence of selected parameters on the CO_2 storage process. The parameters analyzed comprise heterogeneity and anisotropy of formation properties, litho-facies dependencies, aquifer fluid composition, and the role of various transport mechanisms like molecular diffusion. Additionally, we delved into the plume's temporal and spatial evolution and how representative the near-wellbore properties are compared to the entire plume body by monitoring several well-based fluid variables.

4.2. Physico-Chemical Properties of CO_2

Carbon dioxide's physico-chemical properties play an essential role in terms of the physical state and interaction patterns of CO_2 encountered underground, ultimately reflecting on the storage efficiency and security. The physical state of CO_2 varies with pressure and temperature. At standard atmospheric conditions, CO_2 is a stable gas with a density of 1.872 kg/m^3. During injection, as pressure and temperature increase with depth, the CO_2 density increases rapidly, resulting in phase changes, as shown for two different temperature gradients in Figure 38a. A phase

diagram for CO_2 picturing phase behavior in terms of pressure and temperature is presented in Figure 38b.

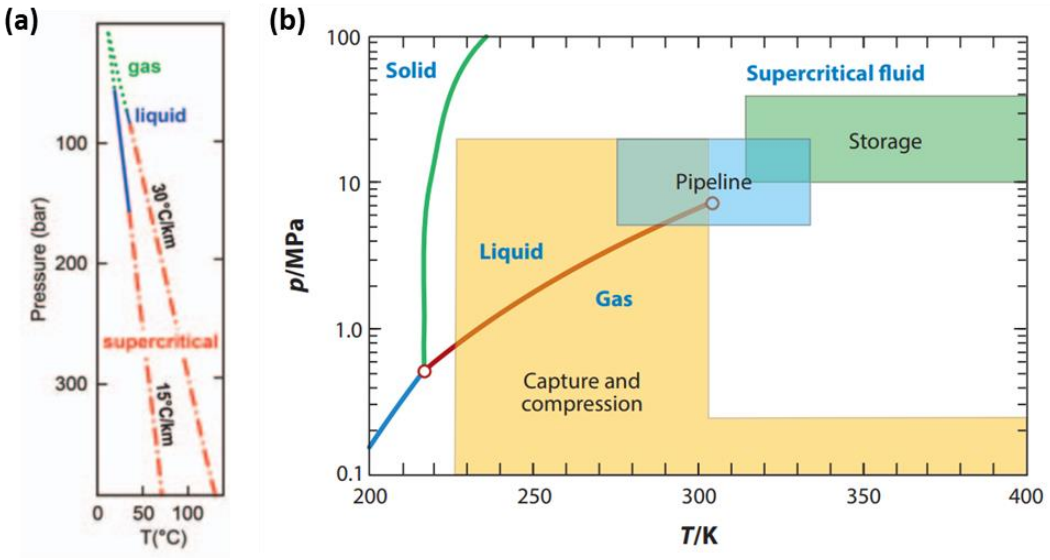

Figure 38. CO_2 behavior with pressure and temperature (a) phase changes with depth, (b) phase diagram for CO_2 (Benson and Cole, 2008; Trusler, 2017).

When the critical point is reached, which in the case of CO_2 is when the temperature and pressure exceed 31.1 ºC and 7.38 MPa, respectively, CO_2 becomes a supercritical fluid. Supercritical conditions indicate that CO_2 has a high liquid-like density but moves like a gas (i.e., gas-like viscosity). The supercritical CO_2 injected into the formation tends to form a free phase plume that rises to the sealing rock due to the difference in density with the in-situ fluid. These conditions are ideal for sequestration, given that they allow for larger amounts of CO_2 to be stored and provide longer residence times than gaseous CO_2 injection (Yang et al., 2010).

Injection of supercritical CO_2 into saline aquifers alters the porous media's chemical equilibrium, resulting in reactions among CO_2, formation brine, the host rock, and the overlying seal formations. Various types of reactions can occur within the host rock or with the caprock. The reaction's type and magnitude depend on the mineralogical composition of the rock, the formation

brine chemistry, in-situ pressures, temperature, and time. Temporal and spatial scales of the reactions are highly heterogeneous, adding complexity to the chemical system analysis (Rochelle et al., 2004). Furthermore, these interactions may help contain CO_2, either as a free phase, a dissolved phase, or precipitated minerals.

Nonetheless, the interactions can also result in reduced efficiency of CO_2 trapping if the pathways are blocked (due to mineral precipitation), making more difficult the CO_2 injection (reducing injectivity), or if additional paths that facilitate the CO_2 migration are created (decreasing storage security). The trapping processes initiated from the CO_2 interactions are strongly influenced by crucial thermophysical properties of the CO_2-brine system. These influential properties include solubility, diffusion coefficients that control the mass transfer between phases, interfacial tension that governs capillary forces, and properties essential for buoyancy and convective flows, i.e., density and viscosity (Trusler, 2017).

Initially, when CO_2 is injected into the aquifer, the free phase closer to the injection well dissolves into the pore fluid (brine). CO_2 dissolution then becomes the first reaction and the leading trigger for other pore space's geochemical interactions. Eq. 39 shows the chemical expression for the CO_2 dissolution in water to form aqueous CO_2, followed by Eq.40 that exhibits the equilibrium between the aqueous CO_2 and carbonic acid formed in the aqueous phase. In addition, the carbonic acid partially dissociates into bicarbonate ions (Eq. 41) and consequently carbonate ions (Eq. 42), in both cases increasing the concentration of H^+thus causing a pH drop on the formation brine (De Silva et al., 2015). The speciation of the dissolved CO_2 is highly dependent on pH. Aqueous CO_2 is the dominant component at lower pH values, but as pH increases, the amount of bicarbonate and, later on, carbonate ions increases. These chemical interactions representing the CO_2

dissolution process are faster than other fluid-mineral reactions, so for geochemical modeling, CO_2-brine equilibria (instantaneous reactions) can be assumed to simplify the chemical system.

$$CO_2(sc) \leftrightarrow CO_2(aq) \tag{39}$$

$$CO_2(g) + H_2O(l) \leftrightarrow H_2CO_3(aq) \tag{40}$$

$$H_2CO_3(aq) \leftrightarrow H^+(aq) + HCO_3^-(aq) \tag{41}$$

$$HCO_3^-(aq) \leftrightarrow H^+(aq) + CO_3^{2-}(aq) \tag{42}$$

Four main factors drive the dissolution kinetics described: the flow of supercritical CO_2 inside the reservoir, the convection of CO_2 saturated brine, dispersion during the flow, and molecular diffusion of CO_2 into the brine (Iglauer, 2011). Besides these drivers, the amount of CO_2 dissolved is also affected by pressure, temperature, and salinity, as shown in Figure 39a, where changes in CO_2 solubility in pure water with temperature and pressure are depicted. It is evident that the solubility increases with pressure and decreases with temperature. This behavior can be explained by the increasing pressure exerting a greater pushing force that increases the CO_2 solubility. While rising temperatures provide additional thermal energy that overcomes the bonding energy between CO_2 and water molecules, reducing the solubility (De Silva et al., 2015).

Moreover, the solubility is affected by the presence of other ions and molecules in the aqueous phase. Figure 39b presents the CO_2 solubility with total dissolved solids (TDS). It is observed that the solubility decreases as the TDS increases. This is also related to the salinity and the ionic strength of the brine. If the salinity or ionic strength increase, the solubility of CO_2 decreases. This phenomenon is known as the salting-out effect (Miri and Hellevang, 2016).

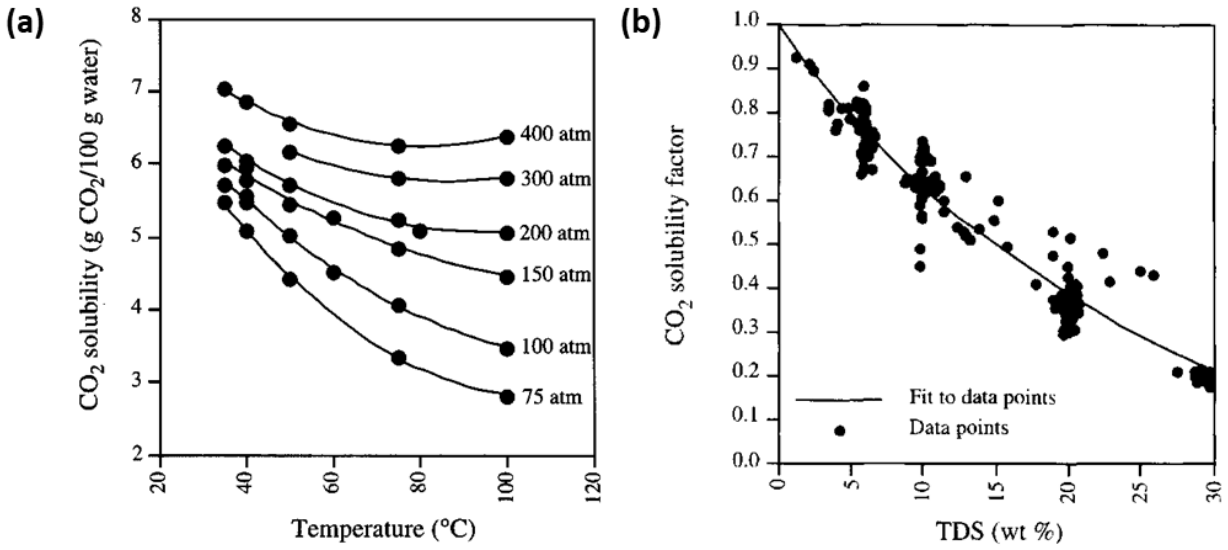

Figure 39. CO_2 solubility changes with pressure and temperature (a) in pure water, (b) as a function of the total dissolved solids (Rochelle et al., 2004).

4.3. CO_2-Water-Rock Interactions

The CO_2 dissolved in the brine promotes other reactions between the aqueous phase and the minerals present in the rock, such as precipitation and dissolution of salts, silicates, and carbonate minerals that can modify the pore structure. The pH reduction due to CO_2 dissolution results in acidic conditions that support interactions with carbonate minerals, which can dissolve and ultimately buffer the pH as Ca^{+} and Mg^{2+} ions are incorporated into the aqueous system (Eqs. 43 and 44). The pH-buffered reactions enhance the solubility trapping process through the formation of ions and complexes.

$$CaMg(CO_3)_2(s) + 2H^+ \rightarrow Ca^{2+} + 2HCO_3^- + Mg^{2+} \quad (43)$$

$$CaCO_3(s) + H^+ \rightarrow Ca^{2+} + HCO_3^- \quad (44)$$

Mineralogical reactions associated with the precipitation of minerals such as calcite, magnesite, dolomite, dawsonite, and siderite, have the potential to store a significant amount of CO_2 for very long periods. However, these are slow processes that can take hundreds to thousands of years and

are strongly dependent on the rock composition. Among common mineral alterations in sandstone formations that could have a significant role in mineral trapping are the transformation of albite to dawsonite (Eq. 45), the alteration of chlorite to form siderite and dolomite (Eq. 46), and the precipitation of anhydrite and magnesite (Eq. 47 and 48) (De Silva et al., 2015; Gaus, 2010). Besides sandstone, mafic rocks such as basalt, which mainly consist of Ca, Mg silicate minerals, are also formations of interest for CO_2 sequestration. Given their composition, basalts have a high acid neutralization capacity by providing alkaline earth elements that react with the carbonate minerals, increasing their geochemical trapping potential (Goldberg et al., 2008; Matter et al., 2007; McGrail et al., 2006; Schwartz, 2020).

$$NaAlSi_3O_8 + CO_2 + H_2O \rightarrow NaAlCO_3(OH)_2 + SiO_2 \quad (45)$$

$$Fe_{2.5}Mg_{2.5}Al_2Si_3O_{10}(OH)_8 + 2.5CaCO_3 + 5CO_2 \rightarrow \rightarrow 2.5FeCO_3 + 2.5MgCa(CO_3)_2 + Al_2Si_2O_5(OH)_4 + SiO_2 + 2H_2O \quad (46)$$

$$Ca^{2+} + SO_4^{2-} \rightarrow \ CaSO_4 \quad (47)$$

$$Mg^{2+} + CO_3^{2-} \rightarrow MgCO_3 \quad (48)$$

4.4. Trapping Mechanisms

Different trapping mechanisms arise from the interaction of CO_2 with the aquifer, the host rock, and the seal. The storage potential of a given formation depends on the trapping efficiency and security of these mechanisms. Their relative importance changes with time due to their occurrence at various time and spatial scales. Four CO_2 trapping mechanisms are typically considered during sequestration in saline aquifers, including structural and stratigraphic, residual, solubility, and mineral trapping (Friedmann, 2007). In the structural or stratigraphic trapping, also known as physical trapping, the free phase or supercritical CO_2 is confined as a buoyant immiscible phase that initially represents the dominant trapping mechanism. Figure 40a presents a sketch of physical

trapping. CO_2 in free-phase migrates into a structural trap below a caprock where it stays confined. With time the CO_2 may be gradually dispersed as a result of dissolution geochemical reactions. Whereas in residual trapping, also called capillary trapping, CO_2 is trapped at the pore-level inside the smaller pores as the CO_2 displaces water from the pore space on its way up. Once injection stops, the water is drawn into the pores again by capillary imbibition. Figure 40b shows the CO_2 molecules trapped in the pore space. This trapping mechanism becomes very important in dipping formations that do not have a structural closure (Burnside and Naylor, 2014; Taku Ide et al., 2007).

The other two trapping mechanisms result from the chemical interaction of CO_2 with the aqueous phase and the rock minerals. Solubility trapping comes from the reaction with the brine. In this case, the CO_2 is dissolved and trapped in the aqueous phase (Figure 40c). This mechanism is safer than structural trapping, where a higher chance of leakage exists due to buoyant CO_2 flow. The amount of CO_2 that can be dissolved is a function of the brine composition, pressure, and temperature. For instance, solubility trapping may be enhanced by the formation of bicarbonate and other ionic complexes, causing additional ionic trapping (Rackley, 2010). Finally, mineral trapping involves the trapping of CO_2 by precipitation of carbonate minerals such as calcite, dolomite, and siderite (Figure 40d). The mineralization process depends on the rock-brine-CO_2 interaction and the kinetics of dissolution and precipitation. Mineral trapping is a long-term, slow mechanism, but it is considered the most permanent trapping option to store CO_2 in subsurface formations (Gaus et al., 2008).

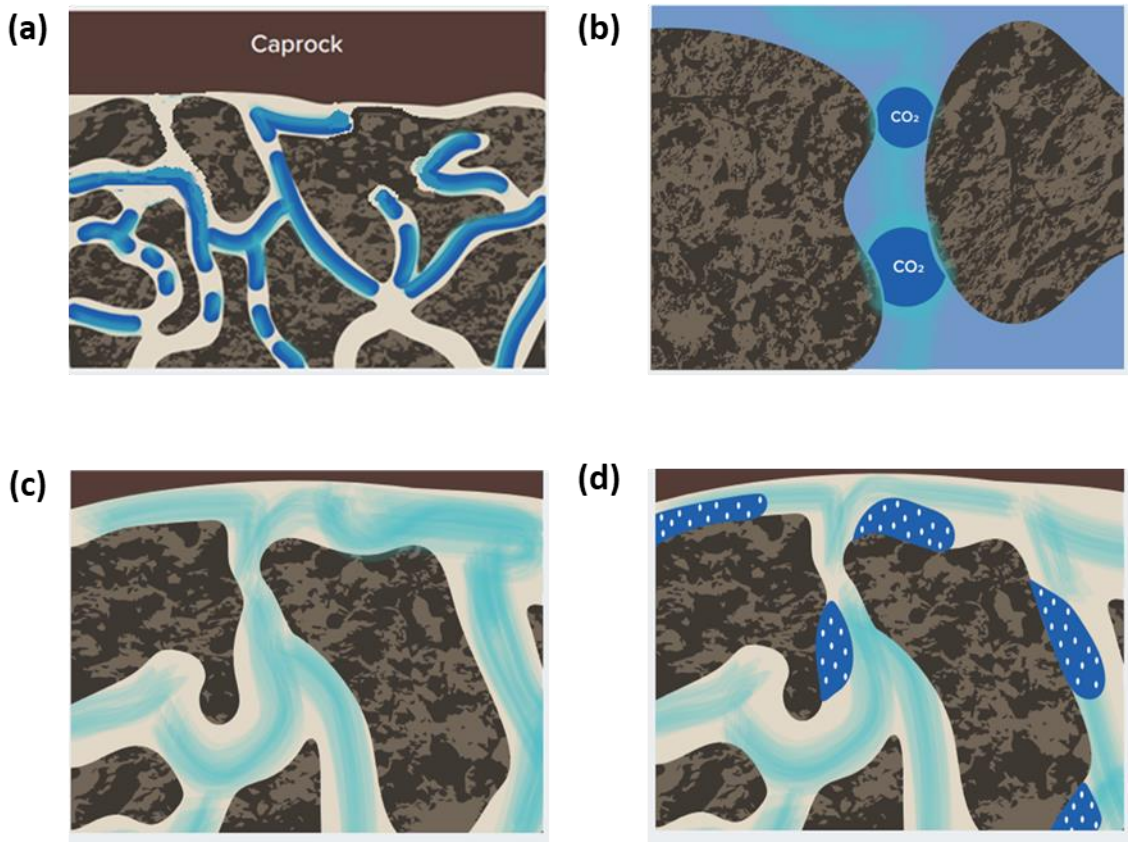

Figure 40. Trapping mechanism in CO2 sequestration in saline aquifers (a) structural or stratigraphic trapping (free phase), (b) residual trapping, (c) dissolution trapping, and (d) mineral trapping (Global CCS Institute, 2019).

The relative contribution to the total storage of CO_2 for each mechanism changes with time. Figure 41a presents the contribution of selected trapping mechanisms with time after injection and how much storage security they provide. Structural trapping represents the most important mechanism with time but exhibits very low security due to the possibility of leakage. On the other hand, mineral trapping represents a small fraction of the CO_2 trapped but appears to provide the highest storage security. It becomes evident that the presence of different trapping mechanisms and their time scales play essential roles and must be integrated to assess the storage capacity of a formation (Bradshaw et al., 2007). A different depiction of the time scales of the various trapping mechanisms is provided in Figure 41b, where the trapping mechanisms' role is presented

individually and as a function of time. Again structural and stratigraphic trapping appears to be the earliest forms of trapping, with solubility, residual, and mineral trapping occurring at later times.

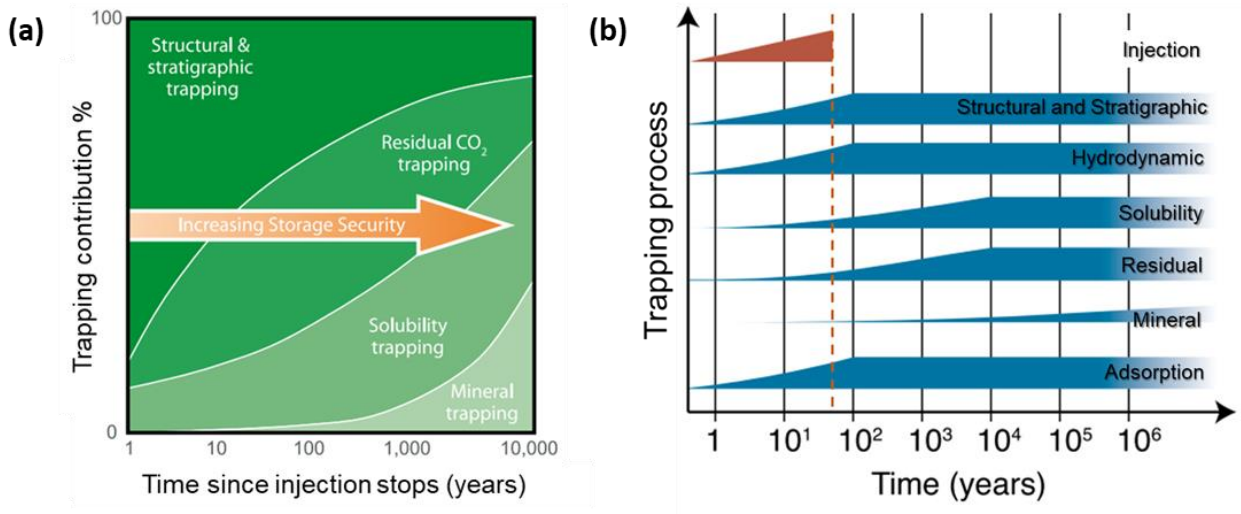

Figure 41. Trapping mechanisms contribution (a) percentage contribution of different mechanisms with time, (b) time-scale of trapping mechanisms (IPCC, 2005)

4.5. Storage Capacity and Efficiency

The storage potential of a saline aquifer is given not only by its capacity to store significant amounts of CO_2 but also by immobilizing CO_2 for a long time effectively. The system's storage capacity is defined by the amount of CO_2 that can be store through the different trapping mechanisms, and it is a function of the reservoir heterogeneity, pore-volume, the rock-fluid interaction parameters, and multiphase flow characteristics. Various methodologies are available to assess the storage capacity. Doughty et al. (2001) proposed a mathematical model to estimate the effective capacity of the Frio formation as a volume fraction of the reservoir available for CO_2 storage considering the intrinsic reservoir capacity that depends on relative permeability to CO_2 and the viscosity ratio; the geometric capacity factor which is a function of the reservoir shape, permeability anisotropy, and density ratio; and the heterogeneity capacity coefficients. In 2007, Bachu et al. developed a volumetric model to determine the storage capacity for different trapping

mechanisms in a saline aquifer with structural and stratigraphic trapping considered the only suitable traps for CO_2 storage. The amount of CO_2 in terms of mass is calculated, as shown in Eq. 49. Soon after, the US-DOE (Goodman et al., 2011) presented a different methodology for storage capacity calculations in saline aquifers that considered structural and hydrodynamic tapping as dominant trapping mechanisms, neglecting the effects of solubility and mineral trapping. Eq. 50 presents the model equation, which includes an alternative efficiency coefficient that implicitly reflects the fraction of the total pore volume occupied by the injected CO_2.

$$M_{CO_2} = C_c \, \rho_{CO_2,av} \, A_{av} \, H_{av} \, \phi_{av}(1 - S_{wirr}) \tag{49}$$

$$M_{CO_2} = E_{saline} \, \rho_{CO_2,av} \, A_{av} \, H_{av} \, \phi_{av} \tag{50}$$

Where C_c is an efficiency coefficient that incorporates effects such as heterogeneity, and CO_2 buoyancy and mobility; E_{saline} is another efficiency storage factor;A is the aquifer area; H is the thickness; ϕ is the porosity; the subscript av represents average values; and S_{wirr} is the irreducible water saturation.

Kopp et al. (2009a, 2009b) also investigated the storage capacity but from a different approach, based on dimensionless analysis of the forces driving the CO_2 flow. Namely, the ratio of gravitational-to-viscous forces, capillary-to-viscous, and mobility ratios as shown in Eqs. 51 and 52. The authors concluded that higher storage capacities are related to the dominance of viscous forces with respect to gravitational forces and the presence of high capillary forces. They proposed a qualitative ranking system using the gravitational number and the capillary number to evaluate the plume evolution behavior. Besides, they modified the Doughty model to include the effects of relative permeabilities and capillary pressure on the storage capacity calculations.

$$Ca_n = \frac{capillary \; forces}{viscous \; forces} = \frac{k \, p_{cr}}{\mu_{CO_2} \, v_{cr} \, l_{cr}} \tag{51}$$

$$Gr_n = \frac{gravitational\ forces}{viscous\ forces} = \frac{\left(\rho_w - \rho_{CO_2}\right) g\ k}{\mu_{CO_2}\ v_{cr}} \quad (52)$$

Where, Ca_n is the capillary number, k is the absolute permeability, $p_{cr}$is the characteristic pressure, μ_{CO_2} is the CO_2 viscosity, v_{cr} is the characteristic Darcy velocity, l_{cr} is the characteristic length, ρ_w and ρ_{CO_2} are the water and CO_2 densities, and g is the gravity constant.

The efficiency of CO_2 storage is determined by the ratio of the volume occupied by CO_2 to the pore volume of the porous medium where it was injected. The efficiency is both spatial and temporal dependent, primarily affected by factors grouped in four categories comprising: characteristics of the storage aquifer (in-situ conditions, displacement characteristics, lithology, heterogeneity, etc.), attributes of the confining rock seal (permeability and capillary entry pressure), aspects of the storage operation (injection rate, injection duration, number of injection wells, and others), and the regulatory constraints and definitions for a given project (Bachu, 2015). The storage efficiency coefficient can be calculated from the US-DOE methodology (Eq. 53) that included geological characteristics such as area, thickness, and porosity, and implemented elements from enhanced oil recovery studies in the petroleum industry to define the displacement efficiency components (Goodman et al., 2011). The displacement efficiency considers the macroscopic and microscopic displacement. The former comprises the fraction of the planar area surrounding a vertical injection well that CO_2 will contact. It is a function of the aquifer heterogeneity and dip, the fraction of the vertical aquifer cross-section contracted by the injected CO_2 through a single vertical well (that depends on the layering, dip, and CO_2 buoyancy), and the density and viscosity contrast between CO_2 and the brine. The microscopic displacement accounts for water-saturated pore volume fraction that can be replaced by CO_2.

$$E = E_{An/At}\, E_{Hn/Hg}\, E_{\phi e/\phi t}\, E_A\, E_v\, E_g\, E_d \quad (53)$$

Where $E_{An/At}$ is the ratio of net to total area (fraction of aquifer suitable for storage), $E_{Hn/Hg}$ is the ratio of the net-to-gross thickness (fraction of the formation in the vertical dimension that meets the requirements of porosity and permeability for injection and storage), $E_{\phi e/\phi t}$ is the ratio of effective to total porosity, E_A is the areal displacement efficiency, E_v the vertical displacement efficiency, E_g is the gravity displacement efficiency, E_d is the microscopic efficiency.

4.6. Monitoring and Verification

A critical component of a CO_2 storage project's management strategy is the ability to track the movement of the injected CO_2 underground. This includes tracking CO_2-plume migration (plume monitoring) and assessment of leakage risk (assurance monitoring). Another key function of the monitoring activities is their role in the validation and revision of modeling tools to improve plume behavior prediction. A wide range of physical, chemical, and biological parameters are measured continuously or at timely intervals have been implemented, based on techniques borrowed from a variety of applications from different industries such as oil and gas, waste disposal, and groundwater (Benson et al., 2005). Monitoring, verification, and accounting (MVA) activities associated with CO_2 sequestration vary from site characterization to plume tracking, leak detection, caprock integrity, and long-term post-injection monitoring (Plasynski et al., 2011). Table 12 presents the recommended tools for monitoring at different stages of project development.

These monitoring techniques can be divided into deep focused and shallow focused. Shallow-focused tools are used for assurance monitoring to study the atmosphere, ocean, and surface, providing a direct measurement of site leakage, for example, atmospheric-CO_2 monitoring and CO_2-flux monitoring (Beaubien et al., 2013; Fessenden et al., 2010; Jones et al., 2011). While

deep-focused tools are used mainly for plume monitoring but can also be applied for assurance monitoring purposes, examples include seismic methods and well-testing (Hannis, 2013; Jenkins et al., 2015). Of particular interest are deep-focused subsurface monitoring techniques used to track the plume evolution. These techniques can be grouped into three main categories: geophysical monitoring, well-based monitoring, and geochemical monitoring.

Table 12. Monitoring tools used in different stages of the CO_2 sequestration project, including additional tools for improved analysis. Modified from (Benson et al., 2005)

Stage	Basic Monitoring Tools	Additional Monitoring Tools
Pre-operational	Well logs Wellhead pressure Formation pressure Injection- and production-rate testing Seismic survey Atmospheric-CO_2 monitoring	Gravity survey Electromagnetic survey CO_2-flux monitoring Pressure and water quality above the storage formation
Operational	Wellhead pressure Injection and production rates Wellhead atmospheric-CO_2 monitoring Microseismicity Seismic surveys	Well logs Gravity survey Electromagnetic survey CO_2-flux monitoring Pressure and water quality above the storage formation
Closure	Seismic survey	Gravity survey Electromagnetic survey CO_2-flux monitoring Pressure and water quality above the storage formation Wellhead pressure monitoring

4.6.1. Geophysical Monitoring

Geophysical monitoring provides useful tools to identify and map fluid migration, given the high imaging potential of seismic techniques that can detect changes caused by CO_2 in compressional wave velocity and attenuation. The most common tools are time-lapse seismic monitoring (4D, 3D, and 2D seismic), vertical seismic profiling, and cross-well imaging. Additional tools include microseismic, gravity, and electromagnetic surveys (Rackley, 2010). Time-lapse seismic data is

acquired over the full volume of the reservoir and overburden. Direct quantification of the amount of CO_2 is obtained from detecting contrasts in acoustic impedance between the CO_2 and the formation water in the seismic volume (Figure 42). Vertical seismic profiling (VSP) provides higher resolution data around the wellbore, with velocity and signal attenuation measurements. It is helpful, for instance, to detect early CO_2 migration outside de casing. Cross-well imaging is employed to map the velocities and attenuation changes between two wells, and the resulting high-resolution images can be used to calibrate 3D seismic data. Seismic methods have been successfully implemented to track the CO_2 plume movement in pilot and commercial-scale projects (Chadwick et al., 2009; Hovorka et al., 2006; Karstens et al., 2017). For instance, in the Sleipner sequestration project in Norway, the primary plume monitoring technique is 4D seismic, calibrated with vertical seismic profiling techniques.

4.6.2. Well-Based Monitoring

Well-based monitoring techniques include permanently deployed downhole sensors and specific time-lapse downhole surveys such as wireline logging (Freifeld et al., 2009; Würdemann et al., 2010; Xue et al., 2006). Permanent downhole sensors are essential for pressure and temperature monitoring, widely recognized as critical parameters to ensure the operation's integrity and to detect leakage (Park et al., 2013; Sun et al., 2016). For example, leakage detection at the Cranfield project in Mississippi, USA, has been assessed using pressure pulse tests to identify the response of leak versus non-leak cases (Sun et al., 2016). In Ketzin, a CO_2 storage site in Germany, distributed temperature sensors (DTS) have been employed to record the formation's thermal conductivity based on temperature variations using heat-pulse methods. The thermal conductivity analysis allows for the estimation of CO_2 saturation (Martens et al., 2015).

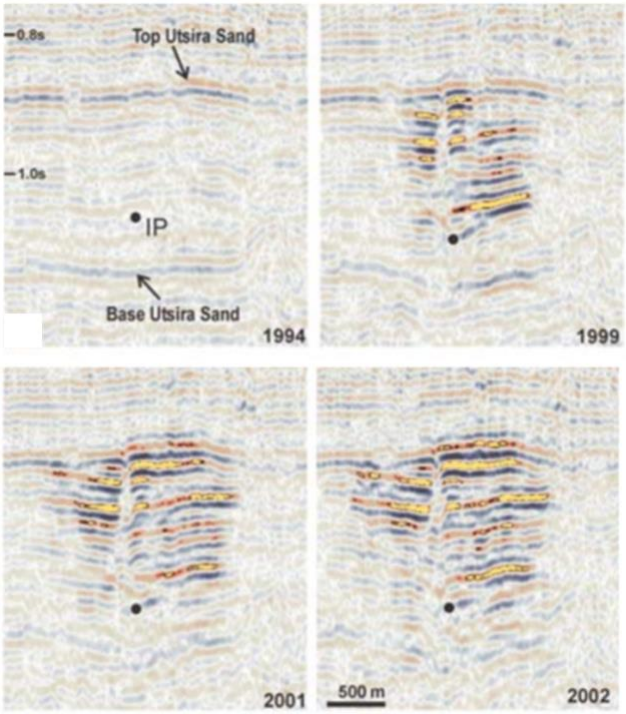

Figure 42. Time-lapse seismic images of the CO_2 plume from the Sleipner project. The bright spots on the amplitude display indicate the presence of CO_2 and show its evolution with time from 1994 (before injection) to 2002 (Chadwick et al., 2009).

Various pilot studies have implemented standard oilfield tools to characterize the distribution and saturation of CO_2. Well-logs cover an additional extensive array of measurements, including gamma-ray density, formation resistivity, acoustic velocity, and self-potential. Wireline tools are also utilized to collect sample fluid and perform geochemical analysis (Freifeld et al., 2009). In both the Nagaoka and Frio projects, in Japan and USA respectively, estimates of CO_2 saturation were obtained from the analysis of variations in sonic velocity and resistivity, and implementation of log tools such as the Reservoir Saturation Tool (RST), which can determine brine saturation changes (Hovorka et al., 2006; Xue et al., 2006)

4.6.3. Geochemical Monitoring

Geochemical monitoring is used to evaluate the CO_2-brine-rock interactions and account for its impact on the safe storage of CO_2. The collection of fluid samples from observation wells is the

most common approach to investigate variations in brine and gas composition, the presence of tracers, and pH measurements (Benson and Cole, 2008; Freifeld et al., 2009; Hannis, 2013; Roberts et al., 2017). Out of these, pH is the most important diagnostic indicator of the brine-CO_2 interaction. Specific downhole fluid geochemical methods have been developed to assess CO_2 storage sites, including the Gas Membrane Sensor (GMS) and the U tube fluid sampling system, which have been used, for example, at Ketzin and The Frio Pilot sites (Freifeld et al., 2005; Martens et al., 2015). The former is utilized to separate the gases dissolved in the fluid and push them up to the surface to measure dissolved CO_2 concentrations downhole. The U tube takes samples of the fluid itself and measures density, pH, alkalinity, and gas composition, then sends the samples to the surface.

One of the main areas of interest concerning the monitoring and simulation of CO_2 injection and storage in saline aquifers is understanding the CO_2-brine-rock interaction (Jayasekara et al., 2020). As massive amounts of CO_2 are injected underground, the chemical equilibrium of the system is disturbed, resulting in chemical reactions between the CO_2 and the aquifer fluid, as well as between the fluid and the rock minerals, as a function of the rock's mineralogy, brine composition, aquifer temperature, and pressure. These interactions are responsible for changes in the aquifer fluid properties such as pH and density, and trapping the injected CO_2 into different trapping mechanisms such as solubility and mineral trapping (Black et al., 2015; De Silva et al., 2015).

4.7. Model Formulation: CO_2 Storage and Transport at the Reservoir-Scale

The integrated modeling workflow for evaluation of long-term injection of CO_2 into saline aquifers is presented next. The employed model setup can be divided into six main stages. First, three-dimensional (3D) static models are constructed to represent the aquifer's nature incorporating structural, lithological, and petrophysical properties. The fluid and fluid-rock interactions are then

described, accounting for the fluid composition, temperature, pressure, and other thermophysical properties. Next, relevant transport physics and trapping mechanisms that govern the displacement and storage of CO_2 underground are incorporated. Once the modeling inputs and governing physics are identified, numerical simulation of the reservoir dynamics is performed, including the model initialization and design of experiments (DoE). The latter component allows for the generation of several case scenarios to assess the effects of variability of geological, petrophysical, and injection parameters on the simulation response observations. Finally, the CO_2 plume and aquifer interactions are studied to determine the plume characteristics, the storage through different trapping mechanisms, and to monitor fluid properties. Figure 43 shows a schematic representation of the workflow, followed by brief descriptions of the modeling approaches selected.

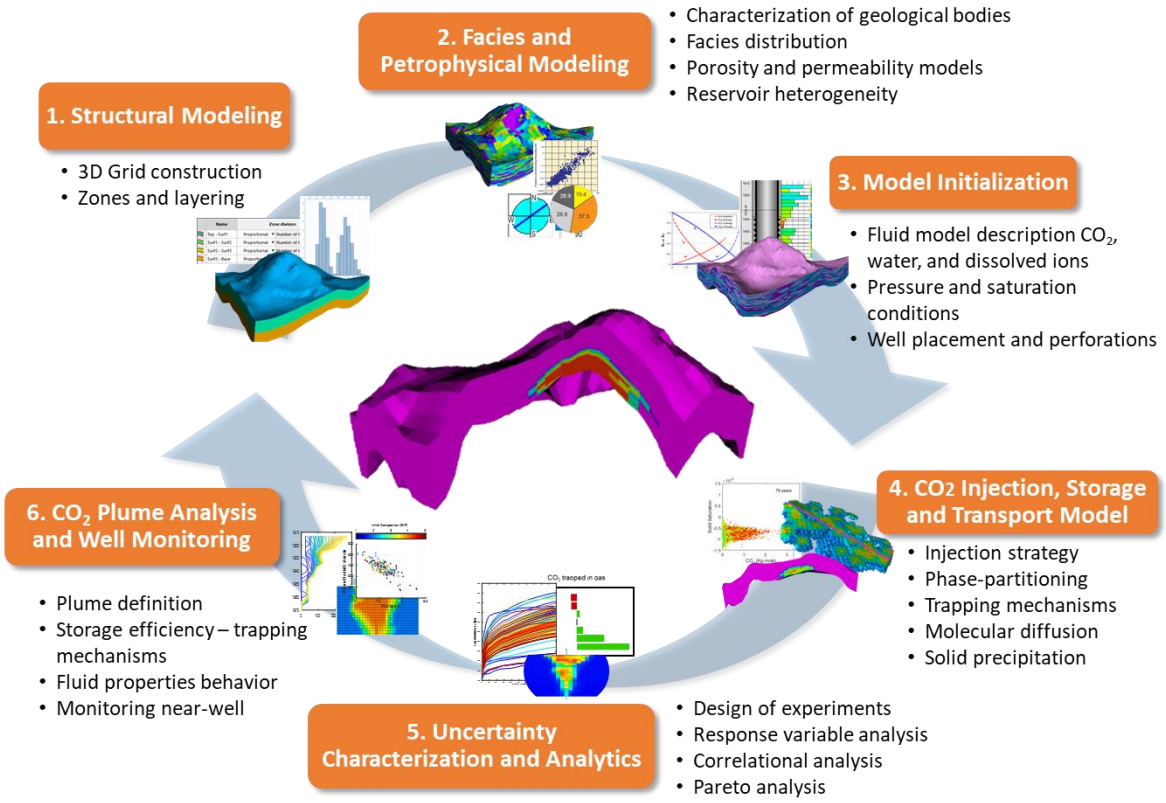

Figure 43. Schematic of the integrated workflow used to study the long-term injection of CO_2 into saline aquifers.

4.7.1. Structural Modeling

The deep saline aquifer structure where the CO_2 will be stored is represented by a 3D cartesian grid that delineates the subsurface geological formations and incorporates topological variations. The structural framework is discretized into 40 × 40 × 47 cells, with 75,200 grid cells. The areal extension of the grid is 3 km × 3 km, and the model thickness varies from 120 to 280 m with an average of 203 m. The lateral dimensions (i.e., X- and Y-axes) of the grid cells are 75 m, while the average thickness is 4.4 m per cell. Four zones constituted the structure, labeled as Overburden, Upper, Baffle, and Lower zones. The grid is divided into 47 layers, distributed into the four zones as 2, 22, 1, and 22 layers, respectively. Figure 44a shows the four geological formations modeled. Upper and Lower zones represent formations suitable for CO_2 injection. On the other hand, the Baffle zone, which separates the Upper and Lower permeable formations, acts as a flow baffle, and the Overburden zone represents the caprock comprising more than 90% shaly facies.

4.7.2. Facies and Petrophysical Modeling

Besides the structural framework, it is necessary to allocate geological and petrophysical properties to each grid cell in the model to capture the rock's main attributes. First, we characterized the stratigraphy and lithology of the geological zones modeled by identifying the principal lithofacies representing typical formations suitable for CO_2 injection. In this case, three fluvial lithofacies were selected, namely sand, shaly sand, and shale. Next, to populate and maintain these facies' paradigmatic distributions in the different geological zones, geostatistical modeling is required. Modeling techniques based on geostatistical concepts include Sequential Indicator Simulation (SIS) and Object-Based Modeling (OBM) (Deutsch and Journel, 1998). The SIS method uses two-point variograms that embody and describe the data's spatial continuity, allowing to extrapolate the facies around the reservoir domain. On the other hand, OBM assigns the facies based on

idealized objects and shapes that represent conventional geological features like channels, mouth bars, or point bars, using dimensions and characteristics according to a set of user-defined rules.

We used both modeling paradigms to capture the lithology of different zones in the model. More specifically, we used SIS to model the Overburden, Upper, and Baffle zones. The main parameters for each zone and facies in the base-case model are shown in the Appendix (Table A 4). Conversely, for the Lower Zone, we used the OBM technique considering various types of geological bodies involving sandstone channels and fine-sand deposits on the floodplain, with shale as the background facies. A critical component of the models described is the variograms implemented for each zone. We adapted the variograms to reproduce the natural spatial variability of the given facies. For example, shale facies are considered more spatially continuous than the sand; thus, the assigned major and minor direction correlation lengths (that is, the variogram ranges) are much more meaningful for shale than sandstone facies. Figure 44b shows the resultant facies model for all zones.

After lithological characteristics are assigned, properties that dictate the relationship dynamics between the rock and the fluid should be populated in the 3D grid. This refers to both porosity and permeability. The facies distribution controls petrophysical properties, given that they are a function of the pore structure and lithology characteristics, with permeability being also correlated with porosity. Consequently, the models generated are constrained by the previously assembled facies model.

Geostatistical modeling approaches are employed again, particularly Sequential Gaussian Simulation (SGS) (Deutsch and Journel, 1998), to populate the porosity and permeability models. Hence, the porosity model is generated using SGS, constrained by the facies model, and considering variations in each zone and facies separately. Overall, the model porosities range from

0.1 to 25%, with an average of 10%. While the permeability model is constructed using SGS, constrained by both the facies and porosity models, the latter based on co-kriging techniques. The modeled permeabilities range from 0.001 to 33.6 mD, with an average of 2.9 mD. The resulting porosity and permeability spatial distributions for the Base-case are shown in Figure 44c and Figure 44d, respectively. And a summary of the parameters used for porosity and permeability modeling.is presented in the Appendix (Table A 5 and Table A 6)

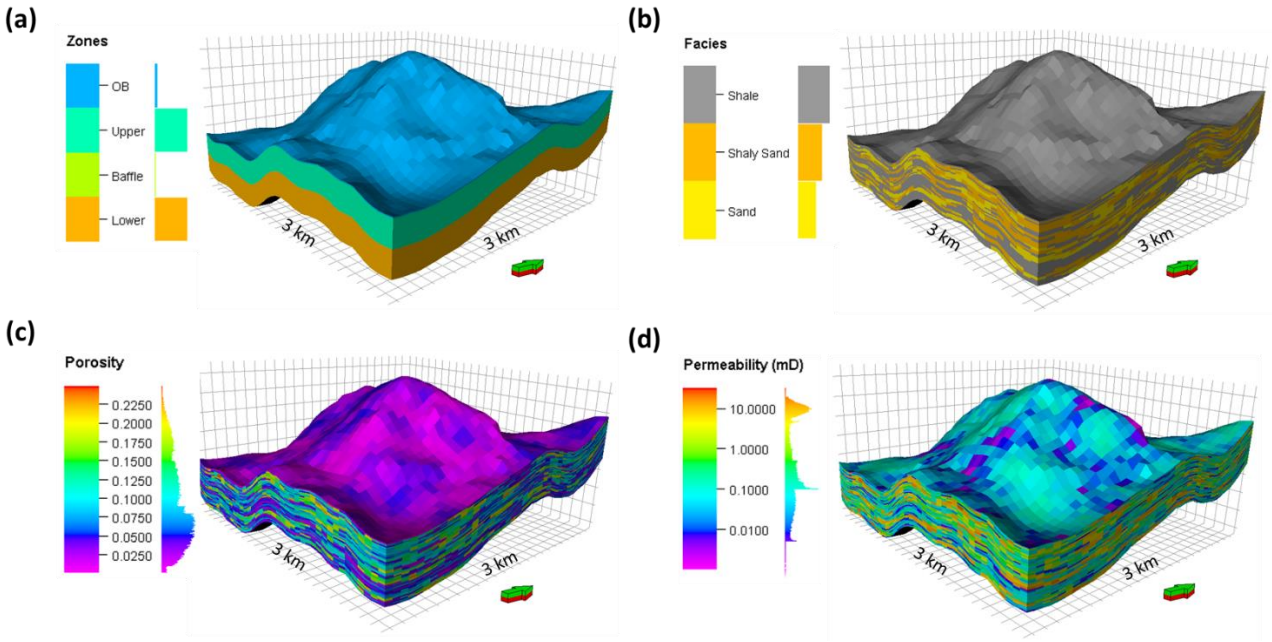

Figure 44. Main components of the static model (a) structural zones, (b) facies model, (c) porosity model, and (d) permeability model. A vertical exaggeration factor of 2 is used in the figures to show layering details. The lithological and petrophysical models are populated based on geostatistical conditional simulation. The lithofacies distribution biases petrophysical properties. In the case of the permeability model, it is additionally constrained by porosity.

4.7.3. CO_2 Storage and Transport Model

The core of the integrated framework presented here is the CO_2 storage and transport model used to examine the dynamic behavior of CO_2 in each zone while accounting for the CO_2-brine interaction and relevant transport physics (that is, convection, buoyancy, and diffusion). Here we

discuss the main components of the storage and transport model, involving the fluid components interaction, phase splitting, fluid properties, and two-phase flow dynamics and transport physics.

4.7.3.1. Fluid Model, Component Interaction and Phase Splitting

We defined a multicomponent fluid model involving five components, namely H_2O, CO_2, NaCl, $CaCl_2$, and $CaCO_3$. A total of three phases can coexist in the system, including a supercritical or free phase (this phase is CO_2-rich and it is characterized by gas-like viscosities and liquid-like densities), an aqueous phase (H_2O-rich, with the presence of CO_2 and dissolved salts), and solid components (salts and calcite) as shown in Figure 45. The supercritical fluid and solid components in the system (that is, CO_2, NaCl, $CaCl_2$, and $CaCO_3$) interact with water and can exist in the aqueous phase as ions. Moreover, salts and calcite can be present both in aqueous and solid phases.

Changes in solid saturation, i.e., precipitation and dissolution processes, can affect the system's porosity and permeability. To describe this interaction, we defined a system of equilibrium reactions occurring in the aqueous phase, as presented in Eqs. 54 to 59. The reactions modeled within the aqueous phase during flow simulations include CO_2 dissociation into bicarbonate and carbonate ions (HCO_3^- and CO_3^{-2}) and the dissociation of other ions such as $CaCl^+$. We also considered the reactions between solid components and the aqueous phase, namely dissolution and precipitation of sodium chloride (NaCl), calcium chloride ($CaCl_2$), and calcite ($CaCO_3$).

$$CO_2 + H_2O \leftrightarrow HCO_3^- + H^+ \quad (54)$$

$$HCO_3^- \leftrightarrow CO_3^{2-} + H^+ \quad (55)$$

$$NaCl(s) \leftrightarrow Na^+ + Cl^- \quad (56)$$

$$CaCl_2(s) \leftrightarrow CaCl^+ + Cl^- \quad (57)$$

$$CaCl^+ \leftrightarrow Ca^{2+} + Cl^- \quad (58)$$

$$CaCO_3(s) \leftrightarrow Ca^{2+} + CO_3^{2-} \quad (59)$$

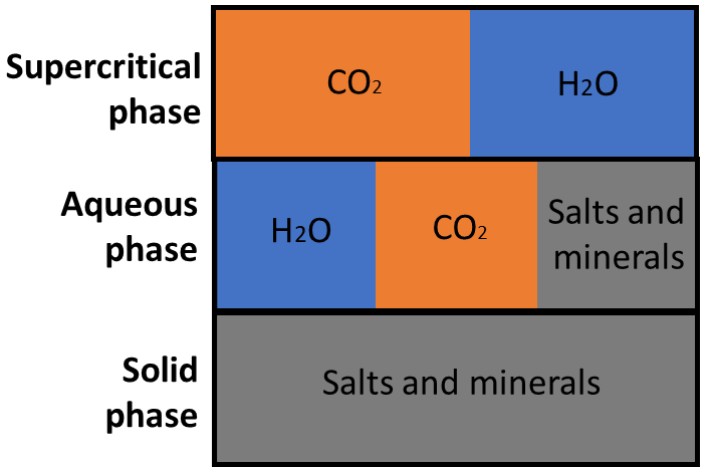

Figure 45. Phases and components included in the CO_2 storage and transport model.

Moreover, to characterize the species interaction between different phases, it is necessary to compute the species' mutual solubilities. Solubilities are controlled by temperature and pressure as well as the activities and fugacities of the species. We calculated these mutual solubilities between the supercritical CO_2 phase and the aqueous phase based on the solubility model formulated by Spycher and Pruess (2005) for a CO_2–H_2O system with the presence of salt (in this case NaCl, and $CaCl_2$). The solubility model accounts for the effects of dissolved salts by including a modified activity coefficient for aqueous carbon dioxide (γ_x') and a correction to the water activity (a_{H_2O}). The corrected activity coefficient for CO_2 is set on a mole fraction scale, and it becomes unity when no salts are present. The expressions for the water mole fraction in the CO_2 rich phase (y_{H_2O}), and the CO_2 mole fraction in the water rich phase (x_{CO_2}) are shown in Eqs. 60 to 63.

$$y_{H_2O} = \frac{(1-B)55.508}{(1/A - B)(vm_{salt} + 55.508) + vm_{salt}B} \tag{60}$$

$$x_{CO_2} = B(1 - y_{H_2O}) \tag{61}$$

$$A = \frac{K^0_{H_2O}}{\Phi_{H_2O}P_{tot}} exp\left(\frac{(P - P^0)\bar{V}_{H_2O}}{RT}\right) \tag{62}$$

$$B = \frac{\Phi_{CO_2}P_{tot}}{55.508\gamma_x' K^0_{CO_2(g)}} exp\left(-\frac{(P - P^0)\bar{V}_{CO_2}}{RT}\right) \tag{63}$$

Where P is total pressure, $\bar{V}$ is the average partial molar volume of each phase over the pressure range, Φ is the fugacity coefficient of each component in the gas phase, R is the gas constant, v is the stoichiometric number of ions contained in the dissolved salt, m_{salt} is the molality and γ'_x is the activity coefficient of CO_2 in the aqueous phase. $K^0$is the thermodynamic equilibrium constant at temperature T and pressure $P^0 = 1\ bar$, calculated for each component given the equilibrium reactions presented in Eqs. 64 and 65 (Spycher et al., 2003). f_{H_2O} and f_{CO_2} are the fugacities for gaseous water and CO_2 respectively, and a_{H_2O} and a_{CO_2} are the activities for liquid water and aqueous CO_2.

$$K_{H_2O} = f_{H_2O}/a_{H_2O(l)}\ \text{, reaction: } H_2O(l) \leftrightarrow\ H_2O(g) \tag{64}$$

$$K_{CO_2} = f_{CO_2}/a_{CO_2(g)}\ \text{, reaction: } CO_2(aq) \leftrightarrow\ CO_2(g) \tag{65}$$

The activities in a mole-fraction scale are given by $a_i = \gamma_i x_i$, while the fugacities are calculated as $f_i = \Phi_i y_i P$. Here i is the component in the mixture, γ_i is the activity coefficient, x_i and y_i are the mole fractions and Φ_i is the fugacity coefficient.

The fugacity coefficients are computed from the PVT properties of H_2O and CO_2 mixtures, using an equation of state in this case, the modified Redlich-Kwong equation (Eq. 71) described by Spycher et al. (2003), where the molecular attraction parameter (a) is modified to be temperature dependent (Eq. 72). In addition, the activity coefficients are calculated using the Margules expressions presented in Eqs. 66 and 67, and the Margules parameters as a function of temperature shown in Eqs. 68 and 69 (Spycher and Pruess, 2010). The CO_2 activity coefficient is modified to include the effect of the dissolved salts as previously mentioned (Eq. 70), following the (Rumpf et

al., 1994) that uses the Pitzer formulation yielding activity coefficients in the molality scale (Spycher and Pruess, 2005).

$$ln(\gamma_{H_2O}) = (A_M - 2A_M x_{H_2O}){x_{CO_2}}^2 \quad (66)$$

$$ln(\gamma_{CO_2}) = 2A_M x_{CO_2}{x_{H_2O}}^2 \quad (67)$$

$$A_M = 0 \text{ at } T \leq 100℃ \quad (68)$$

$$A_M = a(T_K - 373.15) + b(T_K - 373.15)^2 \text{ at } T > 100℃ \quad (69)$$

$$ln({\gamma_{CO_2}}') = 2m_{salt}B^0 + 3m_{salt}^2\Gamma \quad (70)$$

Where γ_{H_2O} and γ_{CO_2} are the activity coefficients, A_M is the Margules parameter, x_{H_2O} and x_{CO_2} are the mole fractions of each component, ${\gamma_{CO_2}}'$ is the modified activity coefficient for CO_2, m_{salt} is the salt molality, B^0 is given by $B^0 = 0.254 - 76.82 / T - 10{,}656 / T^2 + 6312x10^3 / T^3$ and Γ is – 0.0028.

In addition to the phase interactions, it is necessary to determine the different phases' fluid properties. In particular, thermophysical properties, such as density and viscosity, profoundly impact the aquifer's transport and storage capacity. For CO_2 in supercritical phase, the density is determined from the modified Redlich-Kwong equation of state (previously used to compute the fugacity coefficients) as shown in Eq. 71, recasting it as a general cubic equation in terms of volume. A modified temperature-dependent attraction parameter is implemented as shown in Eq. 72 Spycher et al., (2003).

$$P = \left(\frac{RT}{V - b_{mix}}\right) - \left(\frac{a_{mix}}{T^{0.5}V(V + b_{mix})}\right) \quad (71)$$

$$a = k_0 + k_1 T \quad (72)$$

Where parameters a_{mix} and b_{mix} represent measures of intermolecular attraction and repulsion of the mixture CO_2 - H_2O, respectively. V is the volume of the compressed gas phase at pressure P and temperature T, R is the gas constant and k_0 and k_1 are fitting parameters to available PVT data.

The CO_2 viscosity is calculated as a function of temperature and density following the methodology by Vesovic et al. (1990) and Fenghour et al. (1998). The viscosity is decomposed into three parts: the viscosity near the zero-density limit, the excess viscosity that represents the increment of viscosity at high densities compared to the diluted gas at the same temperature, and the critical viscosity that accounts for the increase in viscosity in the vicinity of the critical point (Eq. 73). The expressions for the viscosity in the zero-density limit are presented in Eqs. 74 and 75, and the excess viscosity, are shown in Eqs. 76 and 77. The coefficients for Eqs. 75 and 77 are listed in the Appendix (Table A 7).

$$\mu(\rho,T) = \mu_0(T) + \Delta\mu(\rho,T) + \Delta_c\mu(\rho,T) \tag{73}$$

$$\mu_0(T) = \frac{1.00697T^{0.5}}{\vartheta^*(T^*)} \tag{74}$$

$$\ln \vartheta^*(T^*) = \sum_{i=0}^{4} a_i (\ln T^*)^i \tag{75}$$

$$\Delta\mu(\rho,T) = \sum_{i=1}^{n} b_i(T)\rho^i \tag{76}$$

$$b_i = \sum_{j=1}^{m} d_{ij}/T^{*(j-i)} \tag{77}$$

Where μ is the viscosity, μ_0 is the zero-density limit viscosity, $\Delta\mu$ is the excess viscosity and $\Delta_c\mu$ is the viscosity in the critical region (μPa·s), T is the temperature in Kelvin, ρ is the density, $\vartheta^*(T^*)$is the reduced effective cross-section, T^* is the reduced temperature given by $T^* = kT/\varepsilon$,

$k/\varepsilon = 251.196\ K$ is the energy scaling parameter, a_i are the fitting coefficients for the reduced temperature, b_i are the density coefficients, and d_{ij} are coefficients determined by fitting experimental data for the excess viscosity.

The physical and chemical changes in the aqueous phase due to the injection of CO_2 are detailed by calculating, among other properties, density and pH changes as a function of pressure, temperature, and composition. The density estimation of the aqueous phase (including H_2O, CO_2, and salts) followed the modified Ezrokhi's method to include the effect of dissolved CO_2 and salts. The modified density is calculated as a function of pure water density, temperature, and empirical coefficients determined for the solution's electrolytes, as shown in Eqs. 78 and 79 (Zaytsev and Aseyev, 1992). The coefficients for the salts involved in this case study are shown in the Appendix (Table A 8).

$$log(\rho) = log(\rho_0) + \sum_i A_i c_i \tag{78}$$

$$A_i = b_{0i} + b_{1i}T + b_{2i}T^2 \tag{79}$$

Where ρ is the density of the multicomponent solution in kg/m^3, ρ_0 is the water density in kg/m^3, A_i, b_{0i}, b_{1i}, b_{2i} are the coefficients given for each electrolyte in solution, and c_i is the mass fraction of the component in weight percent (kg/kg).

4.7.3.2. Two-phase Displacement Properties

Once the mutual solubilities and the fluid properties of each phase have been processed, it is necessary to describe the displacement characteristics of those phases in relation to each other. The two-phase flow behavior of the fluids present in the system is governed by the relative permeability curves, wettability, and the saturation functions that reflect the effects of the capillary pressure.

Figure 46 shows the relative permeability curves obtained for a CO_2-brine system during drainage (non-wetting phase displaces the wetting phase) and imbibition (the wetting phase displaces the non-wetting phase) experiments performed in a core sample.

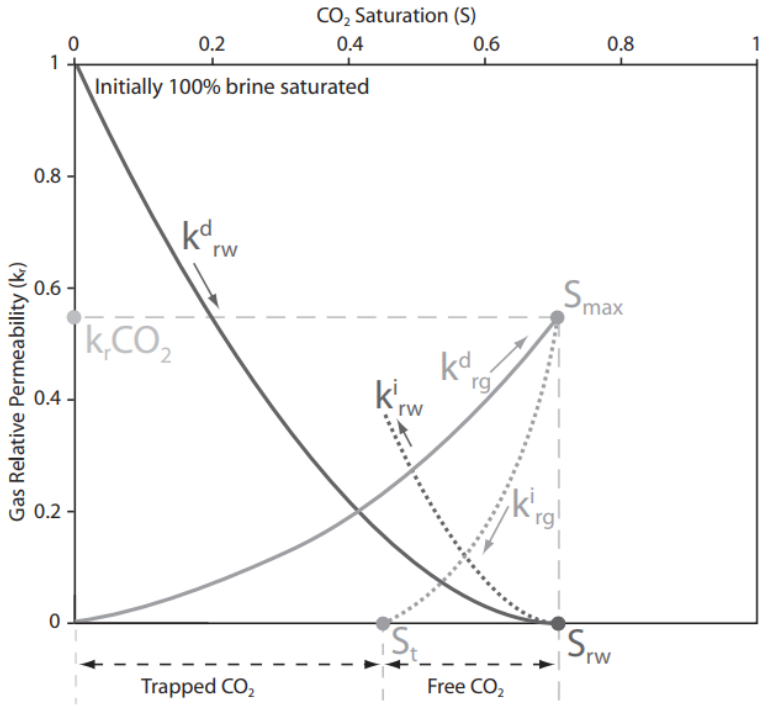

Figure 46. Experimental relative permeability curves for a CO_2-brine system (Burnside and Naylor, 2014).

Both drainage and imbibition are pertinent to the CO_2 sequestration process. First occurs drainage associated with the supercritical plume's movement through the aqueous phase on its way up, followed by the imbibition of water trailing the supercritical plume. Hysteresis is observed between the drainage and imbibition processes, and the residual saturation of the CO_2 trapped can be obtained as the difference between the gas curves saturations at zero relative permeability. Both relative permeability curves and capillary pressure employed in the model come from experimental studies or can be modeled after available correlations and formulations such as Brook-Corey and Van Genuchen (Juanes et al., 2006).

In particular, for this study, different sets of relative permeability and capillary pressure curves were assigned for each one of the facies included in the model. The objective is to consider the role of the facies type on the two-phase displacement simulation by having representative curves that reflect the observed interactions among the fluid, the mineralogy, and the rock's pore structure. Table 13 shows the primary saturation and relative permeability parameters for the Base-case model.

Table 13. Saturation and relative permeability parameters for the base-case model.

Parameters	Sandstone	Shaly Sand	Shale	Overburden shale
Irreducible water saturation	0.05	0.18	0.36	0.6
Critical saturation water	0.25	0.3	0.45	0.65
Maximum water relative permeability	0.65	0.5	0.25	0.2
Critical saturation CO_2 phase	0.03	0.04	0.05	0.06
Maximum supercritical CO_2 phase saturation	0.95	0.82	0.64	0.40
Maximum supercritical CO_2 phase relative permeability	0.9	0.8	0.65	0.5
Maximum CO_2 capillary entry pressure, Pa	5	25	50	240

4.7.3.3. Transport Physics: Molecular Diffusion

Various transport mechanisms play a role in the movement and displacement of CO_2 once injected into the saline aquifer. The CO_2 flow can be driven by advection, buoyancy, or molecular diffusion. In particular molecular diffusion, which is led by the chemical component concentration gradients, promotes diffusive flows in both supercritical and aqueous phases for each component and can significantly impact the transport of CO_2 in the subsurface, not usually accounted for in numerical models. Besides playing a role in the CO_2 transport, diffusion processes can affect the reactions between CO_2 and other components at the pore level, where heterogeneity of the mineral composition and concentrations can influence the reaction rates (Steefel, 2008).

In this model, in addition to considering transport driven by advection and buoyancy, the influence of diffusion in both the aqueous phase and the supercritical phase is investigated. In the aqueous

phase, we only modeled the diffusion of H_2O and CO_2. Diffusion of other components (NaCl, $CaCl_2$, and $CaCO_3$) is assumed to be negligible given that their diffusion rates are much lower than those for H_2O and CO_2.

To account for the diffusive flux of the mentioned components, it is essential to compute the diffusion coefficients. For H_2O, diffusion coefficients are determined from the temperature-dependent second-order polynomial correlation of Yoshida et al. (2008) is adopted. Then, the diffusion coefficients of CO_2 in the aqueous phase are calculated using the correlation derived with the Speedy–Angell power-law approach by Lu et al. (2013); Eq. 80 shows this relationship, which is valid for pressures up to 45 MPa and temperatures from 268 to 473 K (-5.15 to 200 °C).

$$D(\mathrm{CO_2}) = D_0 \left[\frac{T}{T_s} - 1\right]^{1.7094} \tag{80}$$

where D_0 is the diffusion coefficient (13.942e^{-9} m^2/s), at the reference temperature T_s (227°K).

The diffusion coefficients in the supercritical CO_2 phase are computed only for H_2O and CO_2 (given that the salts and calcite are not present in this phase). The methodology described by Hirschfelder et al. (1949), based on Chapman-Enskog's theory for gases, is employed. For each component present in the supercritical phase, binary diffusion coefficients for other species are computed given by Eq. 81 as a function of temperature, pressure, and composition.

$$D_{ij} = \frac{0.01607 * T^{\frac{3}{2}}}{p\sigma_{ij}^2\, \Omega} \left(\frac{1}{M_i} + \frac{1}{M_j}\right)^{\frac{1}{2}} \tag{81}$$

where D_{ij} is the binary diffusion coefficient in m^2⁄day, T is the absolute temperature in Kelvin, p is the pressure in atmospheres, M_i and M_j are the molecular weights, and σ_{ij} is the collision diameter in Angstroms. Ω is the collision integral of the Lennard-Jones potential, obtained from tabulated values as a function of the interaction energy between the components i and j.

4.7.3.4. Trapping Mechanisms: Trapped CO_2 Distribution

In section 4.4. we revised the various trapping mechanisms that arise from the interaction of CO_2 with the aquifer, the host rock, and the seal. Namely, structural and stratigraphic, residual, solubility, and mineral trapping. To understand the role of each of these trapping mechanisms and their relative contribution to the CO_2 stored, we monitored the CO_2 trapping distribution with time as ensues.

In structural and stratigraphic trapping, we keep track of the free-phase CO_2 that can be physically trapped in various structural or stratigraphic features of the formations, such as pinch-outs and dome structures. To calculate this CO_2 amount, we traced the free-phase flow rate (a vectorial sum of the directional flow rates) for each grid cell in the model. If this flow rate is less than a given threshold value (a minimal number), we consider the free-phase CO_2 is not mobile and is virtually trapped. Then, from the total amount of trapped free-phase CO_2, we subtract the residually trapped CO_2 (described below) to determine the structurally trapped CO_2. We first computed the normalized average flow rates encountered in the scenarios investigated to define the flow rate thresholds. We then chose a significantly small fraction of the average values, namely 0.001%, 0.01%, and 0.1% as the threshold values. These thresholds allowed us to compute the amount of CO_2 immobilized in the cells due to structural and stratigraphic constraints in the aquifer.

In terms of residual trapping, the amount of CO_2 trapped is directly dependent on the endpoint saturations (namely, the critical free-phase saturation) related to the relative permeability and capillary pressure curves. As indicated earlier, these endpoint saturation values implemented in this model are facies dependent. For example, shale-dominant facies will exhibit a higher critical saturation than sandy facies. Next, to determine the amount of CO_2 dissolved in water (Solubility trapping), which is governed by the CO_2 solubility and affected by pressure, temperature, and the

aqueous phase composition, we used the phase splitting model by Spycher and Pruess (2005), see section 4.7.3.1. for more information.

Lastly, mineral trapping that involves the trapping of CO_2 by carbonate mineral precipitation, such as calcite and dolomite, is not adequately captured with our model. Typically, this form of trapping is the slowest and also the most permanent. Naturally, to accurately determine the mineral trapping, the simulation time frame will have to be prohibitively long. This study considers a 100-year injection period and a 200-year post-injection period. Hence, the actual contribution of mineral trapping is under-estimated. More complex chemical systems that assume a robust set of minerals to represent the possible interactions on the subsurface should be used.

4.7.4. Uncertainty and Sensitivity Characterization

From the model description presented above, it becomes evident that the CO_2 storage and transport in geological formations are complex processes that depend on various parameters involving hydrogeological, petrophysical, and operational conditions. However, the complexity of the process is not only dependent on the number of parameters and their interactions, but it is also significantly influenced by the uncertainty associated with their measurement and estimation.

To account for the impact of uncertainty on the plume behavior, we investigated the nature and evolution of subsurface dynamics concerning CO_2 displacement under various scenarios by assigning ranges of variation to selected variables. In other words, we performed uncertainty characterization. We employed the statistical design of experiments (DoE) for this purpose, using two different approaches, namely the Plackett-Burman Design (Plackett and Burman, 1946) and the Latin Hypercube method. The former involves a more compact design matrix involving

extreme values of the uncertain variables (minimum and maximum values), while the latter is a space-filling design method. Based on these two methodologies, we simulated a total of 500 cases.

Table 14 presents a list of the input variables included in the analysis and the selected variation ranges. Some of the parameters examined are not single-valued but instead appear in tables; for example, the saturation tables, the fluid-mobility reduction due to solid adsorption on rock surfaces, and initial component mole fraction. For the relative permeabilities and capillary pressure, three different sets of curves were generated for each one of the facies modeled. Similarly, the fluid composition effect was studied by varying nine different sets of initial compositions, as shown in the Appendix (Table A 9). We also used three sets of fluid-mobility reduction due to solid adsorption on rock surfaces to investigate the effects of the solid phase saturation changes on permeability reduction due to precipitation and dissolution (shown in Table A 10 in the Appendix). Furthermore, we varied component diffusion coefficients in the water and supercritical CO_2 phases as functions of both the system's temperature and pressure.

Table 14. Variables and their range used for uncertainty and sensitivity analysis.

	Min	Base	Max
Percentage of sand channels	11	14	17
Percentage of shaly-sand bodies	15	18	20
Major direction of continuity in porosity variogram (sand facies), m	700	1,000	1,500
Minor direction of continuity in permeability variogram (shale facies), m	1,800	2,500	3,000
Porosity multiplier	0.5	1	2
Permeability in X-direction multiplier	0.1	1	10
Permeability vertical anisotropy	0.01	0.1	1
Permeability horizontal anisotropy	0.25	1	4
Caprock vertical permeability	0.01	0.1	1
Baffle vertical permeability multiplier	0.01	0.1	1
Initial reservoir pressure multiplier	0.83	1	1.17
Injection rate, t/day	30	65	100
Maximum bottom-hole pressure, MPa	51	55	60
Rock compressibility, 1/MPa	6×10^{-5}	1.2×10^{-4}	2.4×10^{-4}
Water and supercritical CO_2 phase saturation tables per rock facies	1	2	3
Fluid-mobility reduction due to solid adsorption (tables)	1	2	3
Initial composition (tables)	1	5	9

4.7.5. Numerical Simulation

The numerical simulations reported in this study were completed on the commercial reservoir simulator ECLIPSE (Schlumberger, 2020). In particular, the multicomponent carbon-storage module was used to model the long-term dynamics of CO_2 injection and storage in a saline aquifer centered on the investigation of the CO_2 plume evolution, storage efficiency as a function of different trapping mechanisms, and the well-monitoring options in terms of fluid property variation. In our model, CO_2 injection occurs through a single vertical well within a perforation interval of 3,635 m and 3,665 m in the Lower Zone of the geological model shown in Figure 44a. Each simulation scenario considered an injection period lasting 100 years and a post-injection period of 200 years, for a total of 300 years of analysis of the subsurface dynamics.

The main operational constraints for the Base-case included a target injection rate of 2,375 t/yr and a maximum limiting bottom-hole injection pressure of 55 MPa (to avoid injection-induced fracturing). We defined five regions based on the radial distance from the injection well to facilitate the analysis of the plume evolution and aquifer properties near and away from the wellbore. The innermost region to the wellbore, Region 1 (R1), comprises the space surrounding the well up to 150 m. Similarly, Regions 2 (R3), 3 (R3), 4 (R4), and 5 (R5) consist of the space surrounding the well from 150 to 300 m, 300 to 550 m, 500 to 800 m, and 800 m onwards, respectively. In addition to operational constraints, relevant reservoir parameters, such as aquifer depth, reservoir pressure, and facies distribution, appear in Table 15 for the Base-case model. The selected reservoir properties considered are based on typical characteristics of potential storage formations (Dana and Skoczylas, 2002; Krevor et al., 2012; Moosavi et al., 2014).

As previously mentioned, we employed multicomponent compositional simulation to explore the role of various salts and minerals on the interaction of CO_2 with the aqueous phase and the rock. This simulation approach helped to account for CO_2 trapping, not only due to structural and stratigraphic mechanisms but also due to residual and solubility trapping. The related fluid properties, such as the initial component composition, are shown in

Table 16. Likewise, to consider the role of additional transport mechanisms in the subsurface, we included diffusive transport, which occurs both in the aqueous phase and the supercritical phase.

Table 16 also provides the diffusion coefficients calculated for the reservoir pressure and temperature following the procedure described in Section 4.7.3.3.

Table 15. Reservoir parameters for the base-case model.

Parameters	Values
Reservoir temperature, ℃	71
Reservoir depth, m	3,650
Initial reservoir pressure, MPa	40
Aquifer brine saturation	1
Initial supercritical CO_2 saturation	0
Average permeability, mD	2.9
Average porosity, %	10
Facies fraction	Sand (32%), Fine sand (25%), Shale (43%)

Table 16. Fluid parameters for the base-case model.

Parameters	Values	
Initial aquifer composition	H_2O	0.96
	CO_2	0
	NaCl	0.025
	$CaCl_2$	0.007
	$CaCO_3$	0.008
Diffusion coefficients in aqueous phase, m^2/day	H_2O	5.0×10^{-4}
	CO_2	3.9×10^{-4}
Diffusion coefficients in supercritical phase, m^2/day	H_2O	3.0×10^{-3}
	CO_2	6.1×10^{-3}

4.8. Results

This study's main objective is to delve into the subsurface dynamics of the CO_2 plume during and after injection into a saline aquifer. This section addresses the questions raised concerning the investigation of multiple aspects of the storage and transport processes, namely the evolution of the plume characteristics, the storage efficiency of various trapping mechanisms, monitoring of fluid properties, and the analysis of the combined influence of uncertain parameters on the various response attributes of trapped CO_2 and the plume dynamics.

4.8.1. CO_2 Plume Definition

A key aspect of CO_2 storage in geological formations is determining the proportion of the formation around the injection well where changes are taking place due to CO_2 injection. In most studies, the volume of CO_2 present in supercritical state as a free phase is called the CO_2 plume. This plume is the most mobile form of the CO_2 present underground and could easily reach and escape to the upper or adjacent formations due to hydrodynamic flow and buoyancy effects.

Here, we expand this definition of the plume to characterize the presence of CO_2 underground. Consequently, we described the plume in terms of the pore volume of the aquifer where CO_2 resides in different forms (besides only the supercritical phase). We implemented several property-based metrics for a total of four plume categories. The property-based metrics used include (a) the extent of the aquifer where CO_2 is present in the aqueous phase (due to CO_2 dissolution in water), (b) the aquifer extent where pH change has taken place, (c) the aquifer volume where CO_2 is present in a supercritical state, and finally, (d) the size of the aquifer in which solid-phase saturation changes occurred due to dissolution or precipitation of minerals and salts.

Overall, the larger the plume volume, the larger the surface area of the CO_2-brine and CO_2-rock interaction. Although the larger contact area may lead to a more significant amount of trapped CO_2, this trend may not always hold. A larger plume volume may also indicate a higher risk for leakage of CO_2 into adjacent non-sealing formations.

Figure 47 shows the calculated plume volume based on the five dynamical metrics discussed above for all the case scenarios studied. It is evident from the figure that the CO_2 plume based on the presence of CO_2 in the aqueous phase (blue curves) represents the most substantial volume for all scenarios investigated, indicating that the CO_2 in the aqueous phase can reach deeper into the formation. The plume defined by CO_2 in the aqueous phase is followed by pH changes (orange curves) and the supercritical CO_2 (yellow curves).

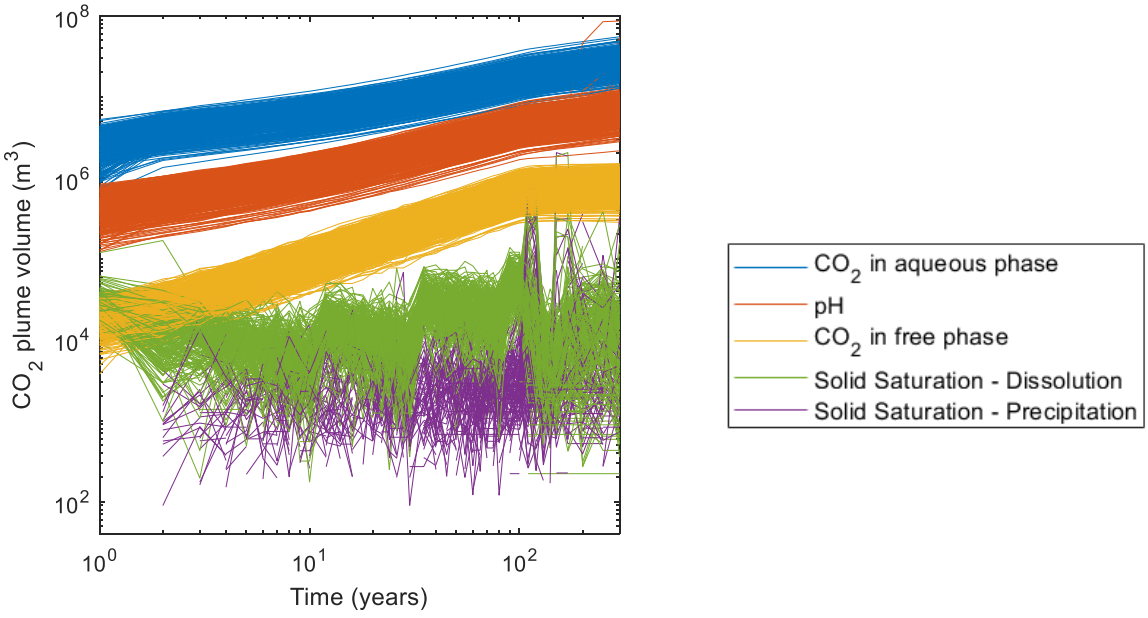

Figure 47. CO_2 plume volume for all the scenarios based on the property-change metrics (discussed), including CO_2 in the aqueous phase, changes in pH, supercritical free phase CO_2, and changes in solid saturation (precipitation and dissolution). Here, the plume volumes are in terms of the total pore volume of the plume.

The changes in solid saturation related to precipitation (purple) and dissolution (green) present a fluctuating behavior associated with both processes co-occurring in different parts of the reservoir.

Also, the behavior of the solid components considered in the simulation, including NaCl, $CaCl_2$, and $CaCO_3$, may differ at different stages of the injection process resulting in additional variations in the precipitation/dissolution region of influence. In general, dissolution appears to dominate during the injection period, with larger plume volumes; however, later on, a more considerable relevance of precipitation processes can be observed during the post-injection period. Out of the different plumes defined, the plumes given by the CO_2 in the aqueous and supercritical phases appear to capture with more detail the volumetric extent of CO_2 into the formation. They allow us to keep track not only of the free-phase with the higher risk of leakage but also of the interaction of CO_2 with water and the region extension where precipitation/dissolution can occur.

Figure 48 presents the plume volume (in terms of pore volume) based on both supercritical free phase and CO_2 in the aqueous phase as a function of the total CO_2 injected, with an average cumulative injection among all cases of 0.15 Mt. We observed a linear relationship (in the log-log space) between the cumulative injection and the plume volume for both the supercritical mole fraction and the aqueous mole fraction. When the injection stops, the pore-volume contact keeps growing due to the plume displacement due to transport processes such as buoyancy and molecular diffusion. Cases below the average line (orange) imply higher storage efficiency, as more CO_2 is stored in the contacted pore volume.

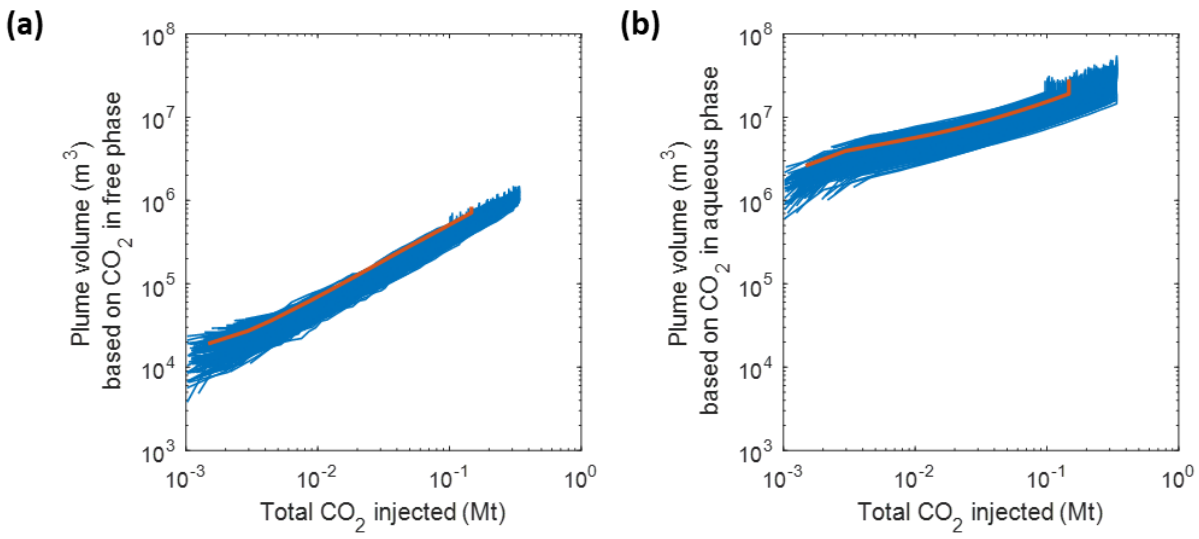

Figure 48. CO_2 Plume volume with total CO_2 injected for all the scenarios investigated based on the (a) CO_2 in free-phase and (b) CO_2 in the aqueous phase.

4.8.2. Plume Dynamics and Dimensions

We explored the plume dynamics identifying the differences in the CO_2 transport characteristics in the aqueous and supercritical phases and examining the plume shape and dimensions evolution with time. Figure 49 shows the plume radial extension variation with depth and time, based on the CO_2 dissolved in the aqueous phase and the CO_2 in the supercritical phase for three selected case scenarios. The plume front based on the CO_2 in aqueous phase grows mostly below the injection point and into the reservoir (left plots in Figure 49a, Figure 49b, and Figure 49c). This behavior can be related to both the structural characteristics and the convective mixing resulting from the increment of the brine density due to CO_2 diffusion. This phenomenon was also observed by Hassanzadeh et al. (2004), who studied convective flux and highlighted the role of convective instability in CO_2 solubility. Meanwhile, for CO_2 in supercritical phase, the plume is typically smaller than in the aqueous phase and grows mostly upwards (plots on the right in Figure 49a, Figure 49b, and Figure 49c). This is related to the upward movement of the CO_2 in supercritical phase governed by buoyancy and gravity effects. Some supercritical plume growth was also observed below the injection point, and it is explained by the structural and geological properties

of the cases studied. Case 253 exhibits large radial extension of the plume in both aqueous and supercritical phases, and it is characterized by high injection rates, high diffusion coefficients of CO_2 in aqueous phase, high salinity, and low solubility

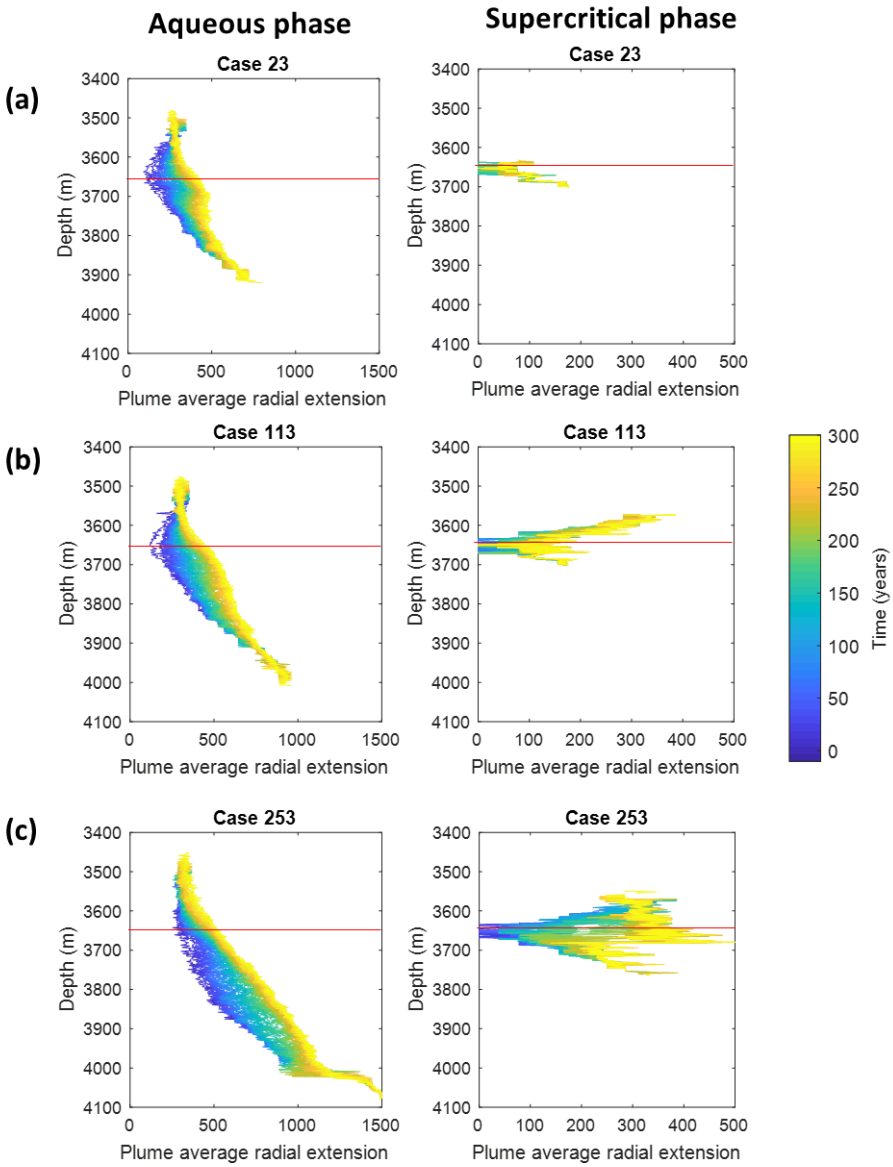

Figure 49. Plume radial extension gradient with time, based on CO_2 in aqueous phase (right) and supercritical phase (left) for selected case scenarios. (a) Case 23, (b) Case 113, and (c) Case 253. The red line indicates the injection depth.

Figure 50 presents 2D cross-sectional and 3D views of selected cases' plume shape after 300 years, including the injection and post-injection periods. For this analysis, the plume is delineated based

on the CO_2 present in the aqueous phase, considering as part of the plume the group of grid cells with a CO_2 aqueous mole-fraction larger than a threshold of 1×10^{-5}. We observed that plume growth is affected by the formation structure and layering. The baffle layer included in the grid structure exerts a significant influence on the vertical extension of the plume for all the cases analyzed, playing the seal's role. The narrow plumes observed, such as Case 195, are characterized by lower-CO_2 injection (0.23 Mt), a higher prevalence of CO_2 dissolved in water for mobile free phase, higher porosity values, as well as higher aspect ratios, compared to cases with more significant plumes, such as Case 377.

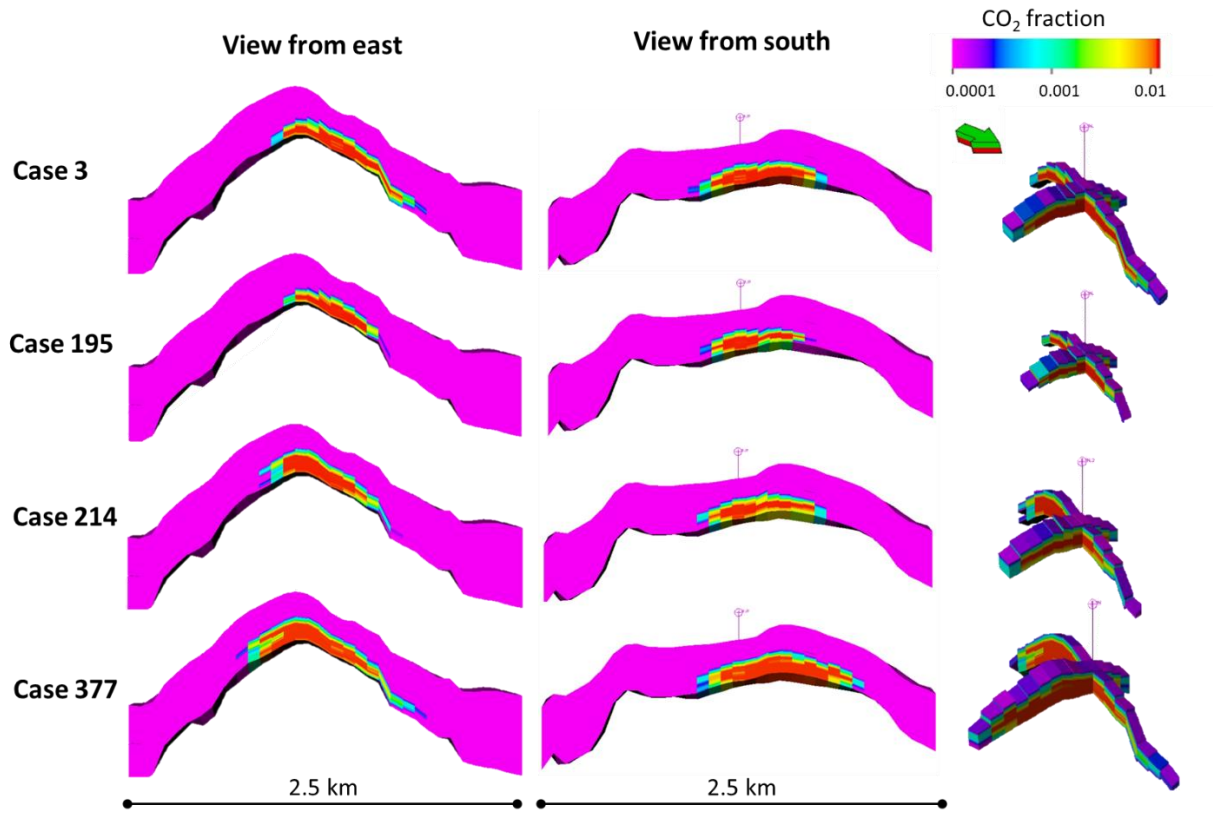

Figure 50. Plume geometry for selected cases, including cross-sectional views in *i* and *j* directions, and a 3D view of the plume growth after 100 years of injection and 200 years of post-injection (300 years). The Lower Zone is separated from the Upper by the Baffle indicated in the figures as a black line. For all cases, the Baffle played a vital role in containing the vertical growth of the plume. Each grid cell is 50 m × 50 m × 3 m. A vertical exaggeration of 2 is used in the displays.

Additional 3D views presenting the plume shape evolution at different time points for various cases are highlighted in Figure 51. For example, we observed that for Case 377, which shows one of the most sizeable plumes in terms of radial extension, the plume grows mostly via lateral expansion with vertical constraint in the Z-direction. The baffle zone's presence right on top of the formation where the CO_2 injection occurred aided this outcome. Also, the influence of the structure, stratigraphy, facies distribution, and permeability anisotropy becomes evident, given the plume's asymmetric growth in different directions. A lower percentage of CO_2 injected immobilized by residual or solubility trapping characterizes cases with larger plumes, in addition to lower porosity averages and higher permeabilities in the horizontal direction.

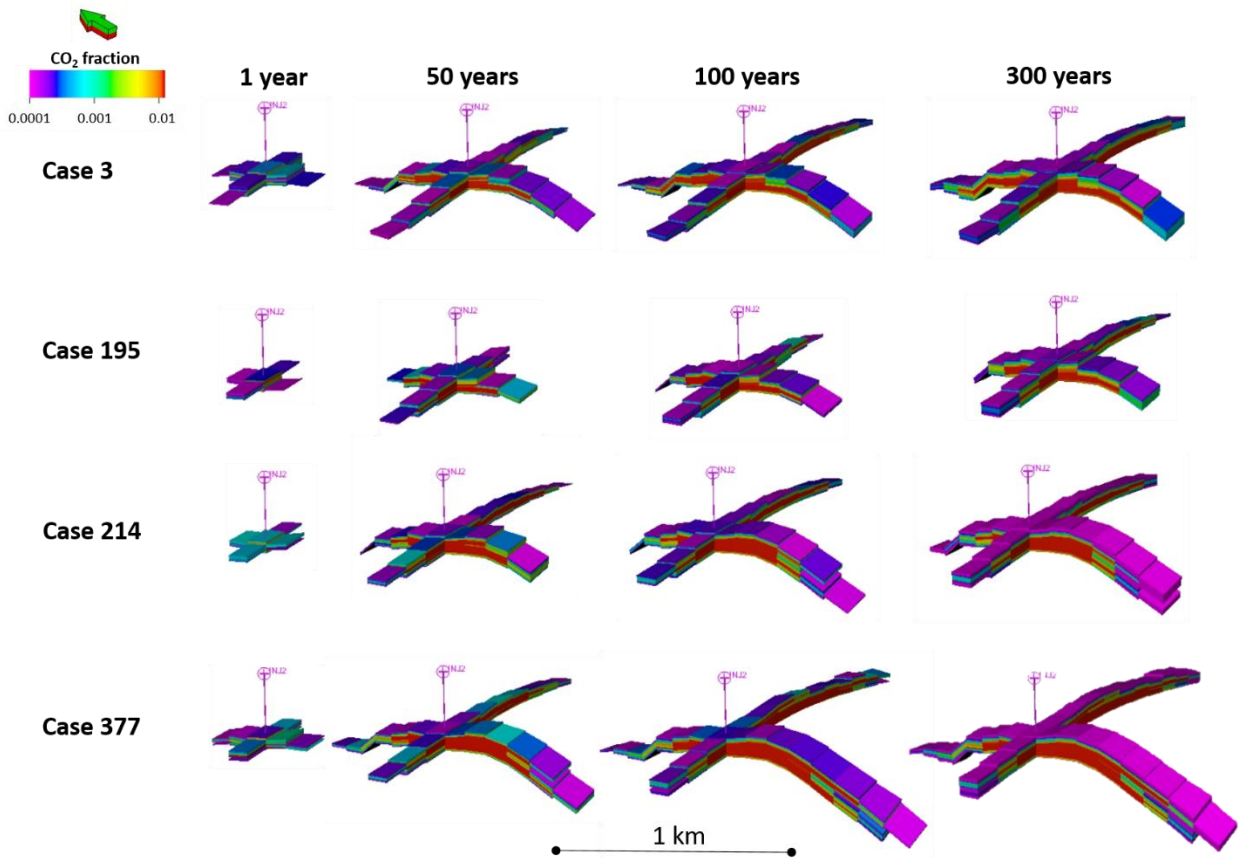

Figure 51. Plume evolution with time for selected cases. CO_2 mole fraction in the aqueous phase is shown at the end of 1, 50, 100, and 300 years. A vertical exaggeration factor of 2 is used in the displays.

Next, we move into a more detailed analysis of the plume dimensions variation with time for all the case scenarios. Figure 52 shows the changes inside the plume of the average radial extension, the average height, the aspect ratio, and the average pressure with time. The average lateral propagation of the plume appears more extensive than the vertical dispersion for all cases during the injection and post-injection periods, with rapid growth during injection in both directions. Although the vertical changes are less compared with the lateral, vertical growth is observed during injection and even in the post-injection period. This behavior is related to advection dominance during fluid injection that controls both vertical and lateral expansion.

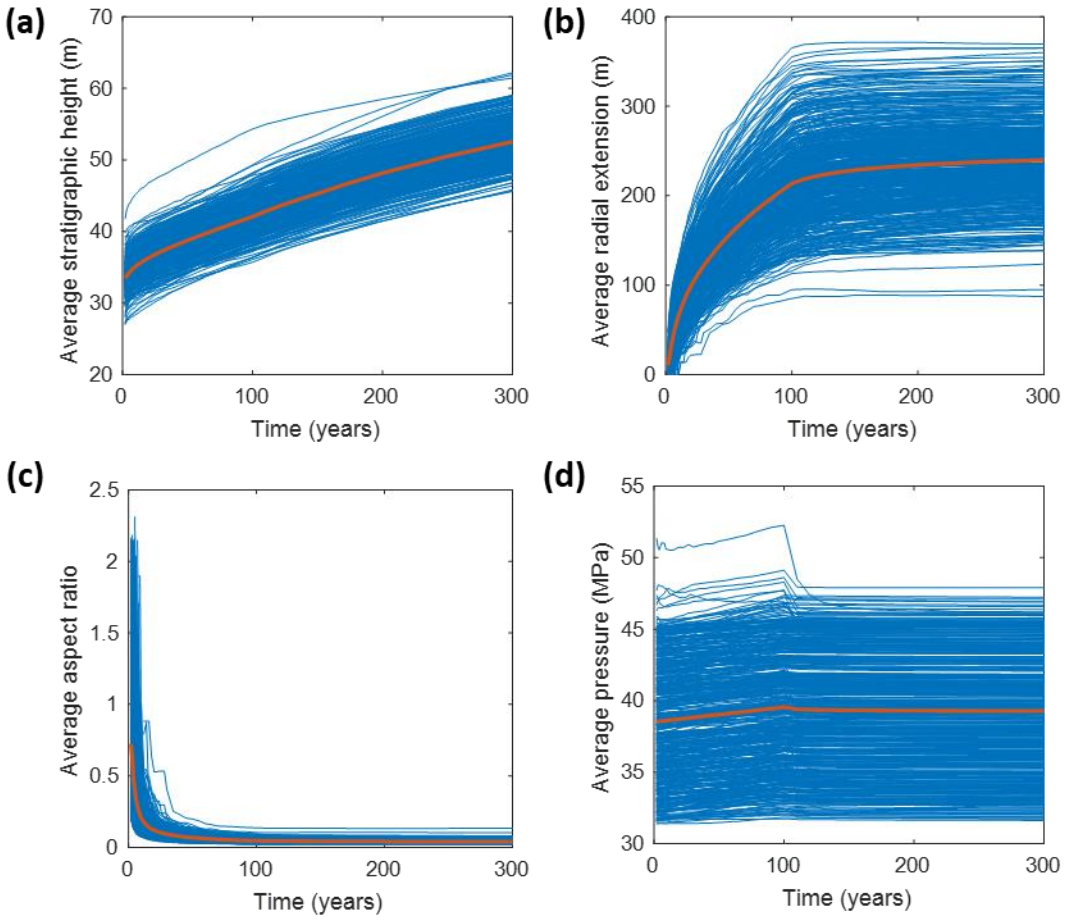

Figure 52. Variation of plume characteristics for all case scenarios (a) average height, (b) average radial extension, (c) aspect ratio, and (d) average pressure.

Despite the baffle zone's interference, buoyancy promotes the vertical plume movement even after the cessation of injection. Conversely, the aspect ratio over time varies from a factor of 2 to 0.04, underlining the initial preferential growth in the vertical direction, which later is eclipsed by the rapid lateral extension influenced by vertical and horizontal permeability characteristics. Figure 52d shows the pressure changes inside the plume with time, with cases with the most substantial initial pressures exhibiting a significant increment during injection, which equilibrates rapidly after injection. The distributions of the plume average radial extension, average height, and aspect ratio obtained for the 500 cases simulated after 300 years are shown in Figure 53. The average radial extension of the plumes spans from 100 m to 350 m.

In contrast, the height or vertical expansion varies from 46 m to 64 m, resulting in aspect ratios below 1 (aspect ratio defined as the relation height to twice the radial extension). In most cases, the lateral plume growth appears to be around 200 m to 300 m. Besides the aspect ratio, we explored the relationship between the plume height and lateral extension and the role of the total CO_2 injected.

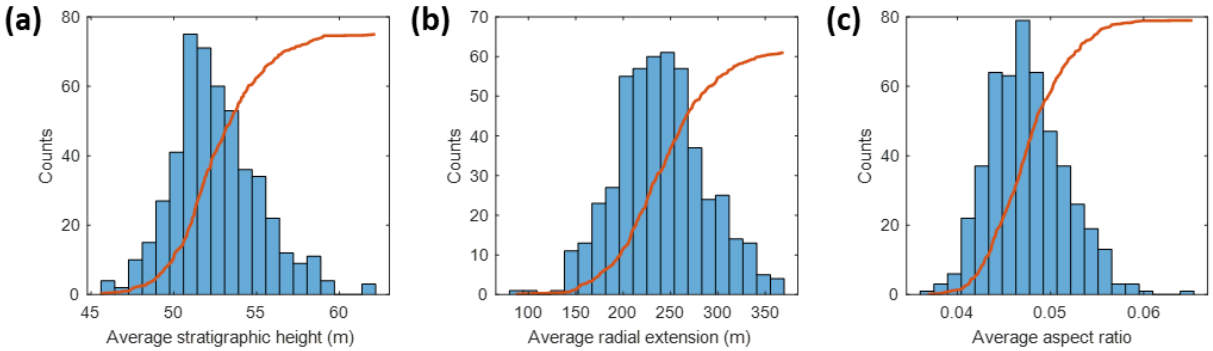

Figure 53. Histograms and cumulative distribution function after 300 years, for (a) average plume height, (b) average plume radial extension, and (c) average aspect ratio of the plume

We generated cross plots of the plume dimensions after 300 years to further investigate the plume geometry. Figure 54a shows the average plume height with average radial extension. Each marker represents a case scenario, and the color indicates the total amount injected for that case in specific.

A positive correlation is observed, with cases that have higher cumulative CO_2 injection exhibiting plumes of larger dimensions. While Figure 54b presents the average radial extension of the plume and the pore volume relationship for all cases, again colored by the total CO_2 injected. The observed relationship provides insights about the impact of pore volume or storage capacity on the plume growth. A negative correlation appeared, indicating that case scenarios with larger pore volumes result in plumes with shorter radial extensions as the formation's capacity becomes more significant. The trends are also related to the amount of CO_2 injected.

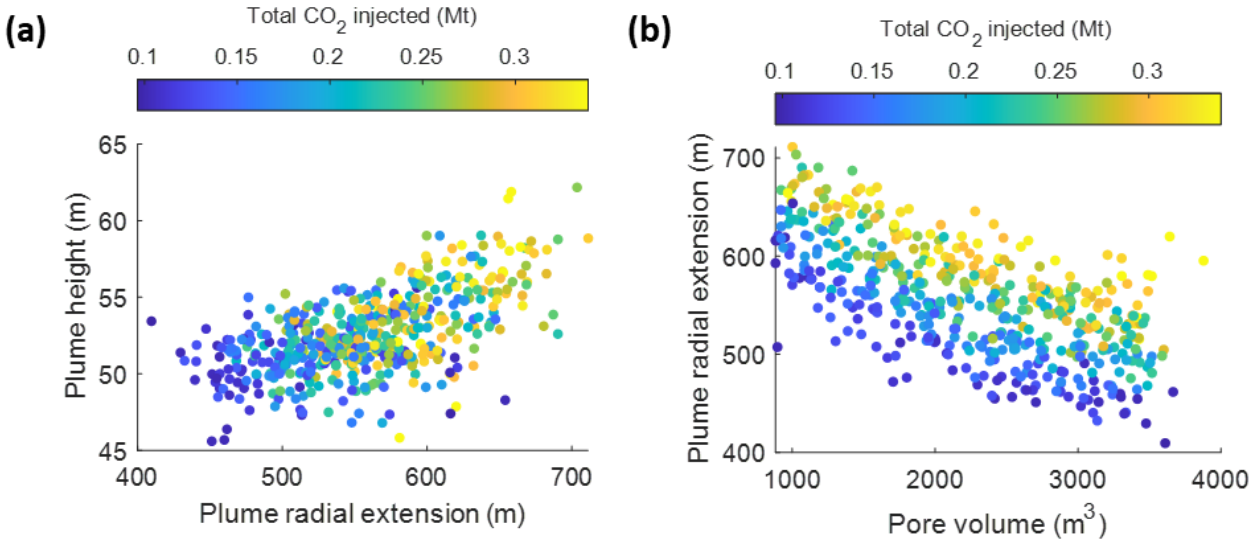

Figure 54. Plume dimensions and their relationship with pore volume for all cases at the end of the post-injection period (a) plume average height with average radial extension, and (b) relation between average plume radial extension and the pore volume. The plots are colored by the total amount of CO_2 injected.

4.8.3. Storage Efficiency

Here we address the relevance of different trapping mechanisms in terms of the total CO_2 immobilized, in other words, their storage efficiency. To this end, we tracked the amount of CO_2 stored as (1) mobile supercritical CO_2, (2) supercritical CO_2 immobilized via structural trapping, (3) supercritical CO_2 immobilized due to residual trapping, and (4) CO_2 dissolved in the aqueous phase by solubility trapping. To determine the CO_2 storage through the mechanisms mentioned, we implemented the methodology described previously in section 4.7.3.4.

We examined these different trapping mechanisms' storage efficiency by comparing the amount stored against the amount injected in both injection and post-injection periods up to 300 years. We defined different storage ratios for each trapping mechanism to measure the storage efficiency, as shown in Table 17. The resulting storage ratios for all the trapping mechanisms appear in Figure 55. The most considerable amount of CO_2 for all instances is stored as mobile CO_2 in the free phase. During the injection period, the mobile CO_2 ratio increases sharply; however, other trapping mechanisms' relevance increases, and the mobile CO_2 starts reducing when injection stops.

Table 17. Storage ratio definition for different trapping mechanisms.

Mechanism	Storage ratio
Mobile free phase CO_2	$\frac{\text{Mobile } CO_2 \text{ in supercritical phase (kg - mole)}}{\text{Injected } CO_2 \text{ (kg - mole)}}$
Structural trapping	$\frac{\text{Structurally trapped } CO_2 \text{ in supercritical phase (kg - mole)}}{\text{Injected } CO_2 \text{ (kg - mole)}}$
Residual trapping	$\frac{\text{Capillary trapped } CO_2 \text{ in supercritical phase (kg - mole)}}{\text{Injected } CO_2 \text{ (kg - mole)}}$
Solubility trapping	$\frac{\text{Dissolved } CO_2 \text{ in water (kg - mole)}}{\text{Injected } CO_2 \text{ (kg - mole)}}$

In Figure 55c and Figure 55d, both residual and solubility trapping exhibit large storage ratios as injection begins. This can be explained by the initial low amount of CO_2 injected, the early dissolution of CO_2, and the fact that the critical saturations required for displacement are not met yet. However, as injection continues, mobile CO_2 increases and both residual and solubility ratios are reduced. Note although the "relative" contribution of residual and solubility trapping mechanisms to the CO_2 trapping decreases during the injection period, the total amount of CO_2 trapped via both these mechanisms does not decrease. Once injection stops, and as a result of capillary forces and the CO_2 dissolution in water, these two mechanisms' contribution ratios increase again. On the contrary, the increment in the structural trapping ratio after injection stops

is subjected to the formation structure modeled in this study and the assumed thresholds to determine the CO_2 mobility.

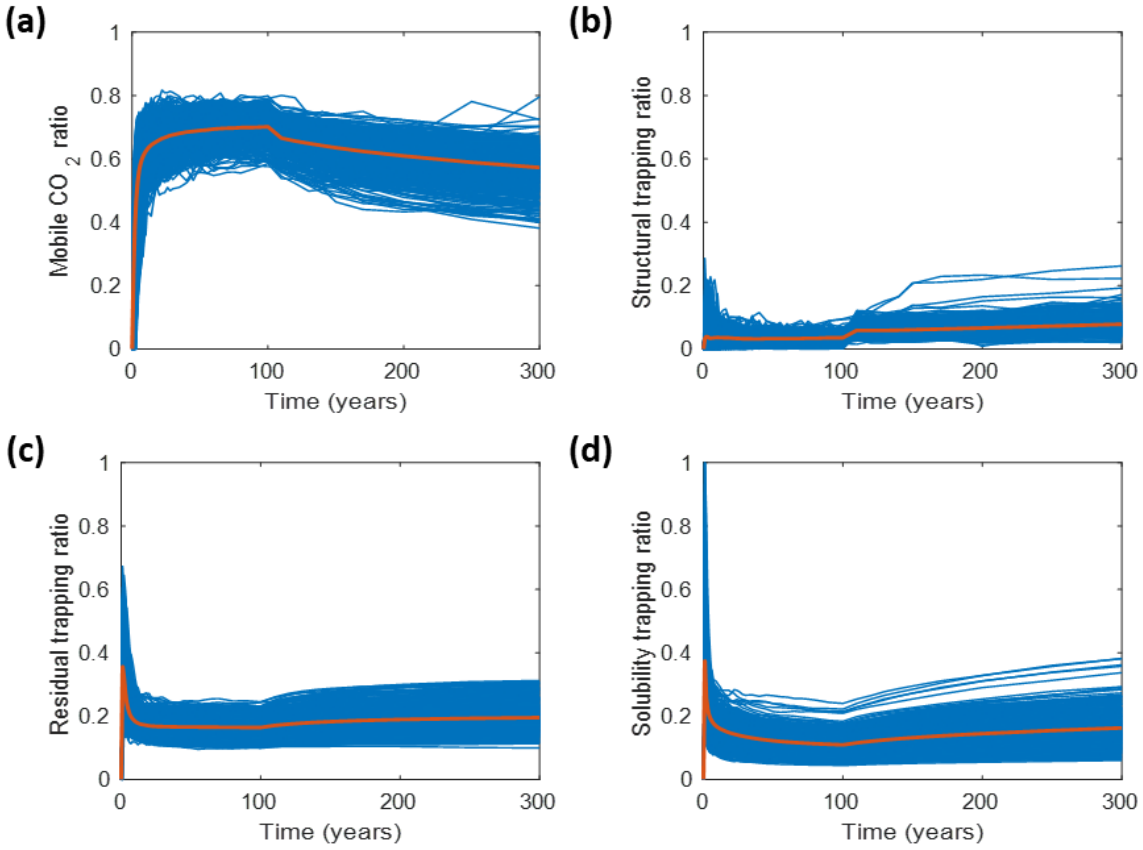

Figure 55. Storage ratio with time (a) mobile free phase CO_2 ratio (supercritical CO_2), (b) structural trapping ratio, (c) residual trapping ratio, and (c) solubility trapping. The orange line represents the average trapping ratio among all the cases.

Following, we determine the relative contributions of each trapping mechanism. We used the trapping storage ratios calculated for each case to represent the fractional contribution of all mechanisms with time. Figure 56 shows the obtained specific contributions for selected cases, and the total CO_2 injected. The collective contributions indicate that over the injection period, CO_2 is mostly stored as mobile CO_2 in the supercritical phase. In cases such as Case 377, mobile CO_2 can represent around 60% of the injected CO_2 when solubility trapping or other mechanisms cannot contribute to storage.

Nevertheless, in cases where different mechanisms can have significant roles in the CO_2 storage depending on geological, petrophysical, and hydrodynamic characteristics, the mobile CO_2 can be reduced. For instance, the trapping mechanisms contribution for Case 3 in Figure 56 point to structural trapping as a primary trapping option after injection stops. While Case 195 exhibits a significant contribution of solubility trapping even during the injection period, and Case 214 has a noteworthy contribution of residual trapping.

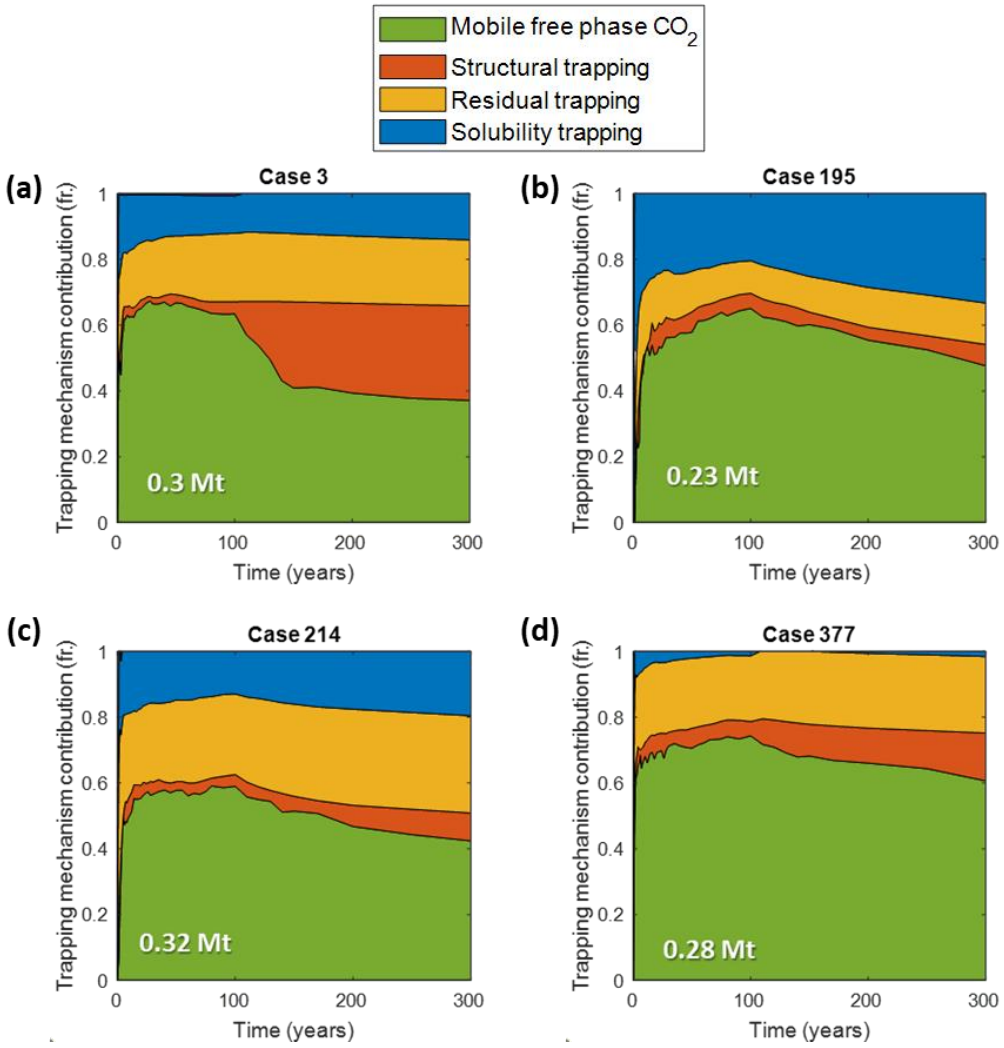

Figure 56. Trapping mechanisms contribution to CO_2 trapping for selected cases, including (a) Case 3, (b) Case 195, (c) Case 214, and (d) Case 377. The average contribution for all cases shows that most of the injected CO_2 can be found as free phase CO_2. Other mechanisms are predominant in specific instances, such as solubility trapping in Case 16 and residual trapping in Case 178.

Besides structural, residual, and solubility trapping, another relevant trapping mechanism is mineral trapping. Mineral trapping of CO_2 is related to the precipitation of carbonates, such as calcite ($CaCO_3$), and is a slow process that does not occur at significant rates in some rock-types (e.g., sandstones). The storage ratios obtained for all cases in Figure 56 showed insignificant to no contribution of other trapping forms. Given the simple chemical system included in this study and the time scale, accurately capturing the effects of mineral trapping became infeasible. However, to understand the dynamics of CO_2, salts, and $CaCO_3$ during the injection period, we recorded the solid saturation changes as CO_2 is injected according to the reactions included in the simulation, as shown in Figure 57.

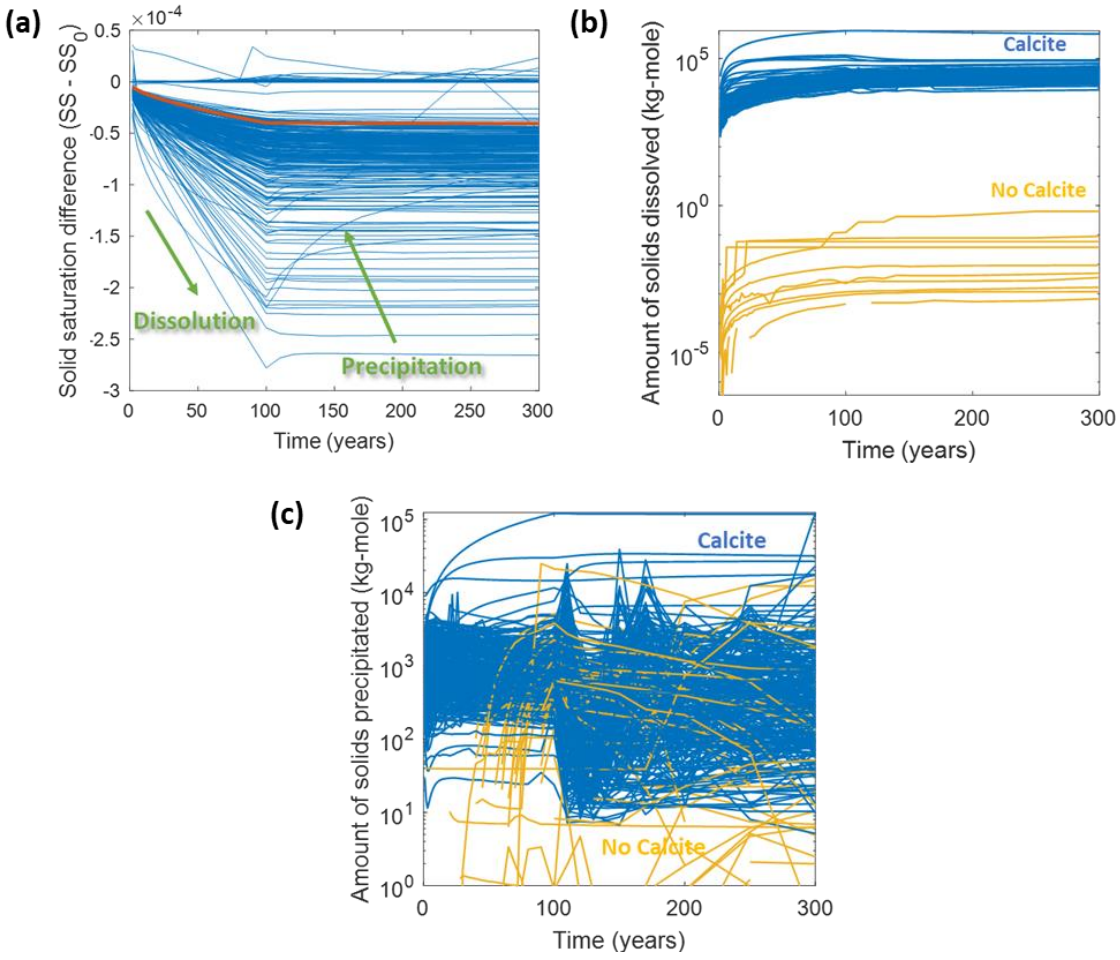

Figure 57. CO_2 interaction with solid components inside the plume region with time (a) average solid saturation changes, (b) amount of solids dissolved, and (c) amount of solids precipitated. The initial composition of the cases indicating the presence or absence of calcite is given by the blue and yellow colors, respectively.

The solid saturation in our models includes three solid-phase components: NaCl, $CaCl_2$, and $CaCO_3$. We observed a predominant dissolution period during CO_2 injection (Figure 57a), which can be related to the initial interaction of CO_2 with the aqueous phase, increasing the fluid acidity and therefore promoting calcite dissolution. As injection continues, CO_2 dissolution can also buffer the pH of the aqueous phase, resulting eventually in less dissolution, and solid saturation can then increase in some instances if precipitation events occur. It is important to note that these solid saturation changes (shown in the figures above) are averages upon the plume region. Also, note that precipitation and dissolution can co-occur and in different parts of the plume region. We also investigated the average amounts of solids deposited or dissolved to explore the dissolution and precipitation, as shown in Figure 57b and Figure 57c. As mentioned in the methodology, we considered various initial compositions, including cases with and without initial calcite in the aquifer. We observed that cases without initial calcite exhibited negligible dissolution and some solids precipitation that showed fluctuations with time. This behavior may arise from the precipitation and dissolution of salts at different stages. While for cases where calcite is initially present in the aquifer fluid, experience significant dissolution, especially during the injection period, and show highly variable precipitation behavior during and after CO_2 injection.

4.8.4. Monitoring Fluid Properties: Plume Temporal Evolution

The aquifer fluid properties evolve with CO_2 injection as a result of the interactions amongst the fluids. Chemical characteristics of the brine can enhance or impair the CO_2 dissolution and its reaction with other species present in the aqueous phase, resulting in more or less solubility and mineral trapping of CO_2. To understand the effects on the brine properties, we considered the changes of pH, density, and activity of species in the aqueous phase as a function of injected CO_2,

initial aquifer fluid composition, and plume dimensions. Our objective is to evaluate which of these properties would be good to monitor and use in inferring the characteristics of the CO_2 plumes.

With regards to pH, we investigated different aspects of the pH behavior, as presented in Figure 58. Each data point in the plots represents the pH of a given case scenario after 300 years (100 years of injection and 200 years of post-injection). First, we looked at the relationship between pH and the plume dimensions, as shown in Figure 58a and Figure 58b. Figure 58a plots pH against the plume radial extension with the total CO_2 injected as the ternary variable. Two clusters of pH values appear in this plot. This can be attributed to the presence or absence of initial calcite content in the aqueous phase. Cases with no initial calcite content exhibit lower pH compared to scenarios with initial calcite. This behavior can be explained by the buffering of the pH due to the CO_2 interaction with calcite. In both pH clusters, the plume radial extensions are governed by the total CO_2 injection, resulting in larger plumes with larger amounts of CO_2 injected and lower pH. We also examined the relative change of pH with the plume aspect ratio as a function of the total CO_2 injected in Figure 58b. smaller changes in pH are correlated with higher plume aspect ratios and low total CO_2 injected, which means shorter plumes in the vertical direction exhibit less relative changes in pH.

Figure 58c presents the variation of pH with the activity of aqueous CO_2 and the solubility trapping ratio. More considerable pH changes are related to higher aqueous CO_2 activity, while the solubility trapping ratio is observed to be higher for cases with lower pH changes. Figure 58d shows the relative changes in pH with the activity of HCO_3^{-1} ions. Again, two different clusters appear attributed to initial calcite content in the aqueous phase. Cases with initial calcite exhibit

higher HCO_3^{-1} activity with pH variation compared to cases without initial calcite. This behavior points to calcite playing a relevant role in the CO_2 interaction with the aqueous phase.

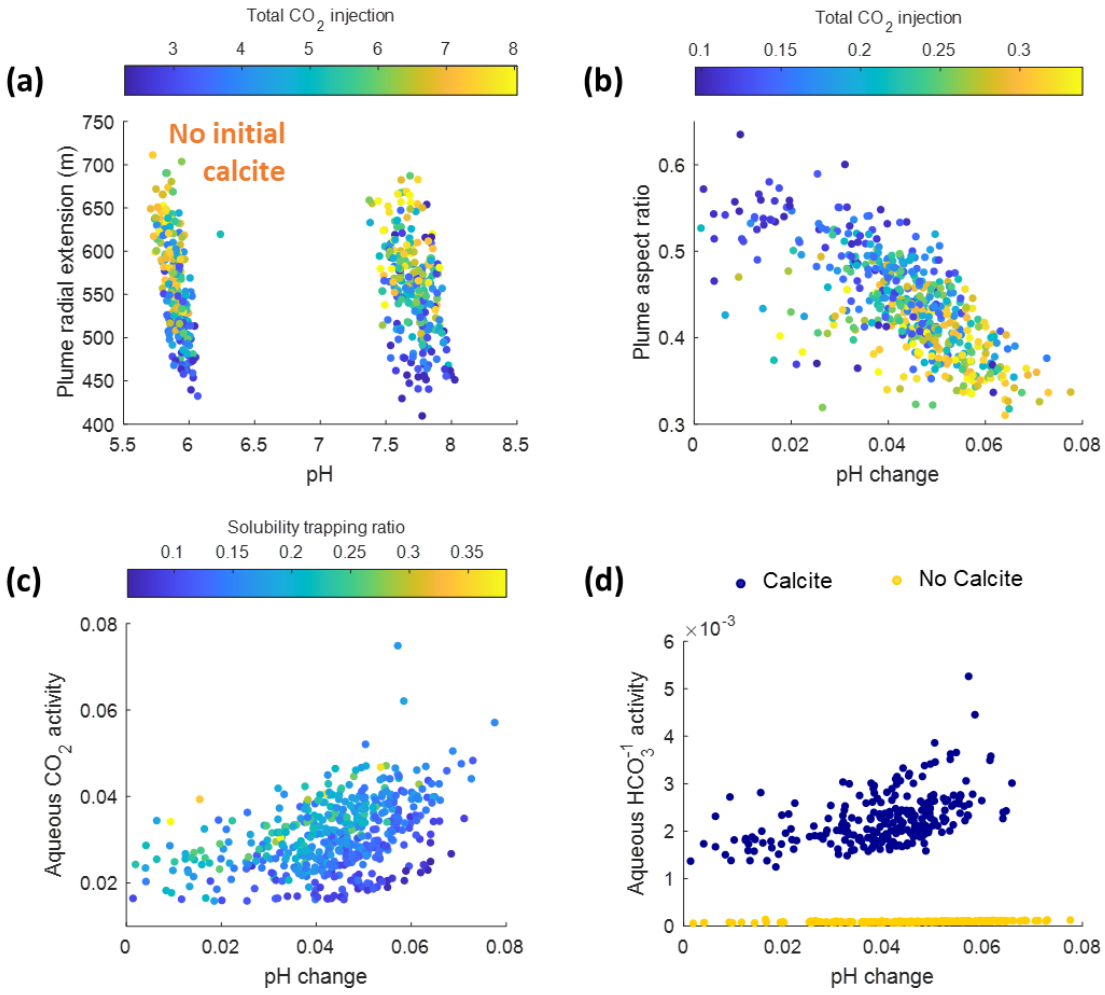

Figure 58. Aquifer fluid pH behavior for all case scenarios after 100 years of injection and 200 years of post-injection (a) pH with plume radial extension and total CO_2 injected, (b) pH change with plume aspect ratio and total CO_2 injected, (c) pH change and aqueous CO_2 activity with solubility trapping ratio, and (d) pH change and activity of HCO_3^{-2} behavior for cases with and without initial calcite content in the fluid.

Another aquifer fluid property of interest is the brine density. The initial fluid composition determines the fluid density and its relationship with the CO_2 solubility and the solid saturation. Figure 59a and Figure 59b show the brine density with aqueous CO_2 activity and bicarbonate ions (HCO_3^{-1}) activity. In both these figures, clusters appear due to the differences in the initial fluid composition. In Figure 59a, the CO_2 activity is negatively correlated to the brine density. CO_2 will

have higher activity in rarefied phase than denser phase. Two other trends are observed in Figure 59a, the brine density increases with salinity, and the CO_2 activity increases with continued CO_2 injection. Besides, cases without initial calcite and higher fluid density exhibit the lowest CO_2 activity in the aqueous phase, as indicated inside the orange circle in the plot. Similarly, in Figure 59b, the HCO_3^{-1} activity decreases with brine density only for the cases with initial calcite content in the aqueous phase. For cases without calcite, they exhibit negligible variations of the bicarbonate ion activity.

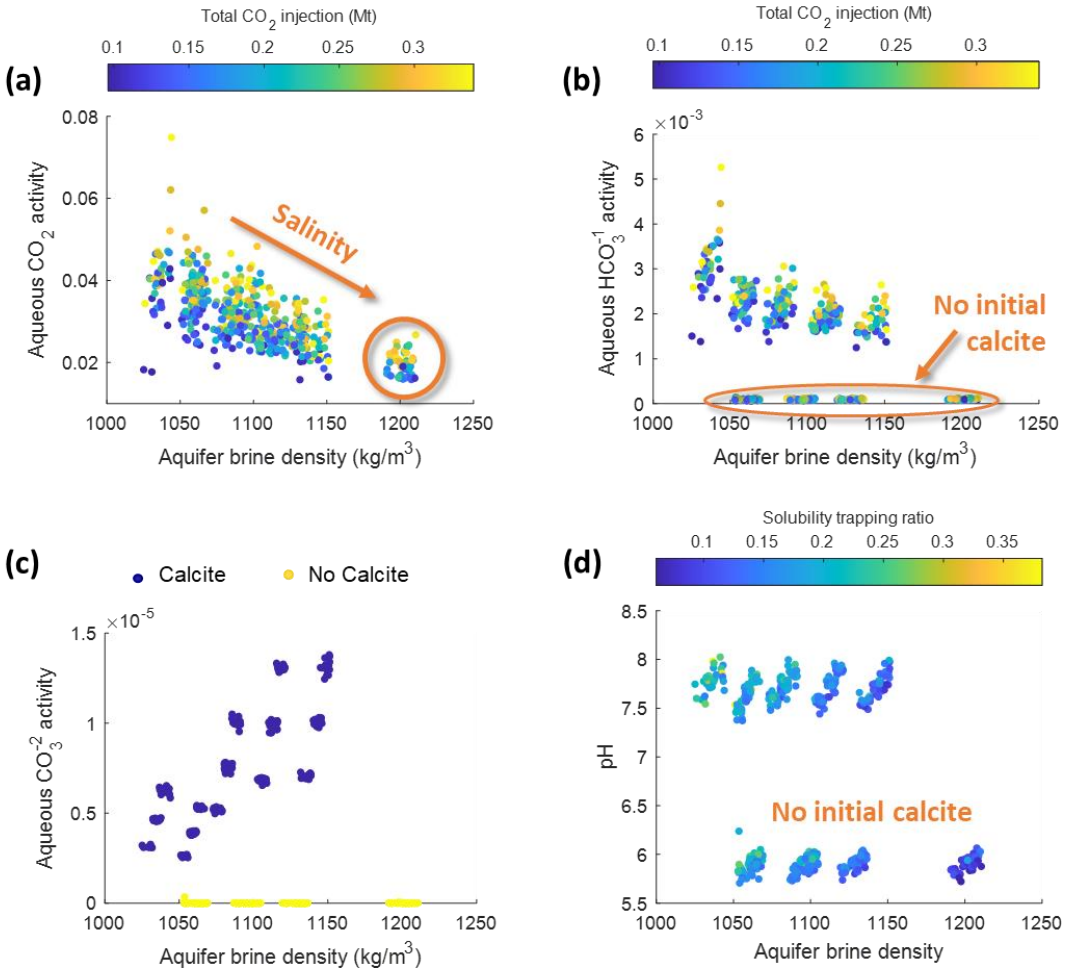

Figure 59. Aquifer brine density after 300 years for all cases scenarios with (a) activity of aqueous CO_2 and total CO_2 injected, (b) activity of aqueous HCO_3^{-1} ions and total CO_2 injected, (c) activity of aqueous CO_3^{-2} ions and initial composition, and (d) pH and solubility trapping ratio.

Figure 59c displays the fluid density behavior with the carbonate ion (CO_3^{-2}) colored by the initial calcite content. Here, CO_3^{-2} activity is positively correlated with brine density, but only when the calcite is initially present in the aqueous phase. The carbonate ion activity depends on calcite dissolution and is related to an increment in Ca^{+2} activity. Due to Ca^{+2}'s larger molecular weight, higher CO_3^{-2} activity is associated with higher brine density. The relationship between the fluid density and the pH is shown in Figure 59d. Again, the pH behavior suggests two main clusters related to the initial calcite content. Within these clusters, various trends are observed explicitly connected with the difference in the initial composition, including additional components such as NaCl and $CaCl_2$. Higher density cases exhibit a lower solubility trapping ratio.

To delve deeper into the CO_2 solubility with time, we evaluated the evolution of the components resulting from CO_2 speciation: CO_2 (aq), $HCO_3^{-1,}$ and CO_3^{-2}. Figure 60 shows these species' average activity as a function of time for all the cases studied. The CO_2 and HCO_3^{-1} activities increase with time due to the larger cumulative CO_2 injected (Figure 60a and Figure 60b) and present similar trends as they are both related by the reaction given in Eq. 55. However, the activity of CO_3^{-2} is not only dependent on the CO_2 injected, but it is also affected by the calcite dissolution and the initial composition. The characteristic trends of different initial compositions are apparent in Figure 60c. Overall, the activity of this ion decreases with time.

Furthermore, the different components' equilibrium in the aqueous phase from CO_2 speciation is highly dependent on the pH (see Figure 58c and Figure 58d for CO_2 and HCO_3^{-1}). At lower pH, the dominant species from CO_2 dissolution is the aqueous CO_2. This explains higher activities given that the chemical system displays a pH declining trend.

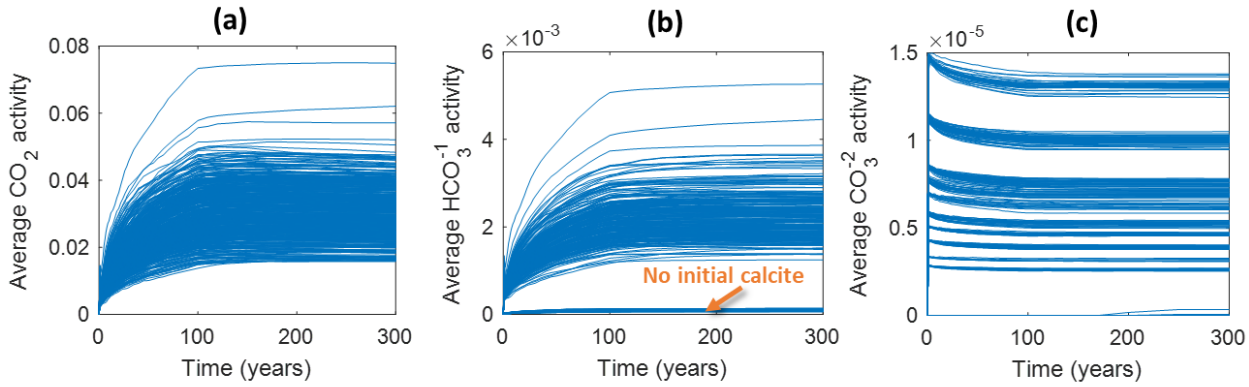

Figure 60. Carbonate species activity for all case scenarios (a) aqueous CO_2 with time, (b) aqueous HCO_3^- with time, and (c) aqueous CO_3^{-2} with time.

In addition, we looked into the relationship of initial composition, in particular, the initial calcite content and the activity of carbonate ions such HCO_3^{-1} and CO_3^{-2}, with the plume dimensions as shown in Figure 61. In general, larger HCO_3^{-1} activity ratios are associated with lower aspect ratios, therefore related to plumes that are laterally deeper into the formation and higher calcite content (Figure 61c). On the other hand, the CO_3^{-2} activity does not show any evident correlation with the plume aspect ratio but exhibits trends determined by the initial fluid composition, and in particular, the calcite content (Figure 61d). This behavior suggests that the initial composition has a role in how the aqueous species interact, while the plume growth is related mostly to the activity of aqueous CO_2 and HCO_3^{-1}, given the additional interactions of CO_3^{-2} with calcite and calcium ions that affect the activity of this ion. The plume growth is related mostly to the activity of aqueous CO_2 and HCO_3^{-1}. However, the additional interactions of CO_3^{-2} with calcite and calcium ions will affect the activity of these ions.

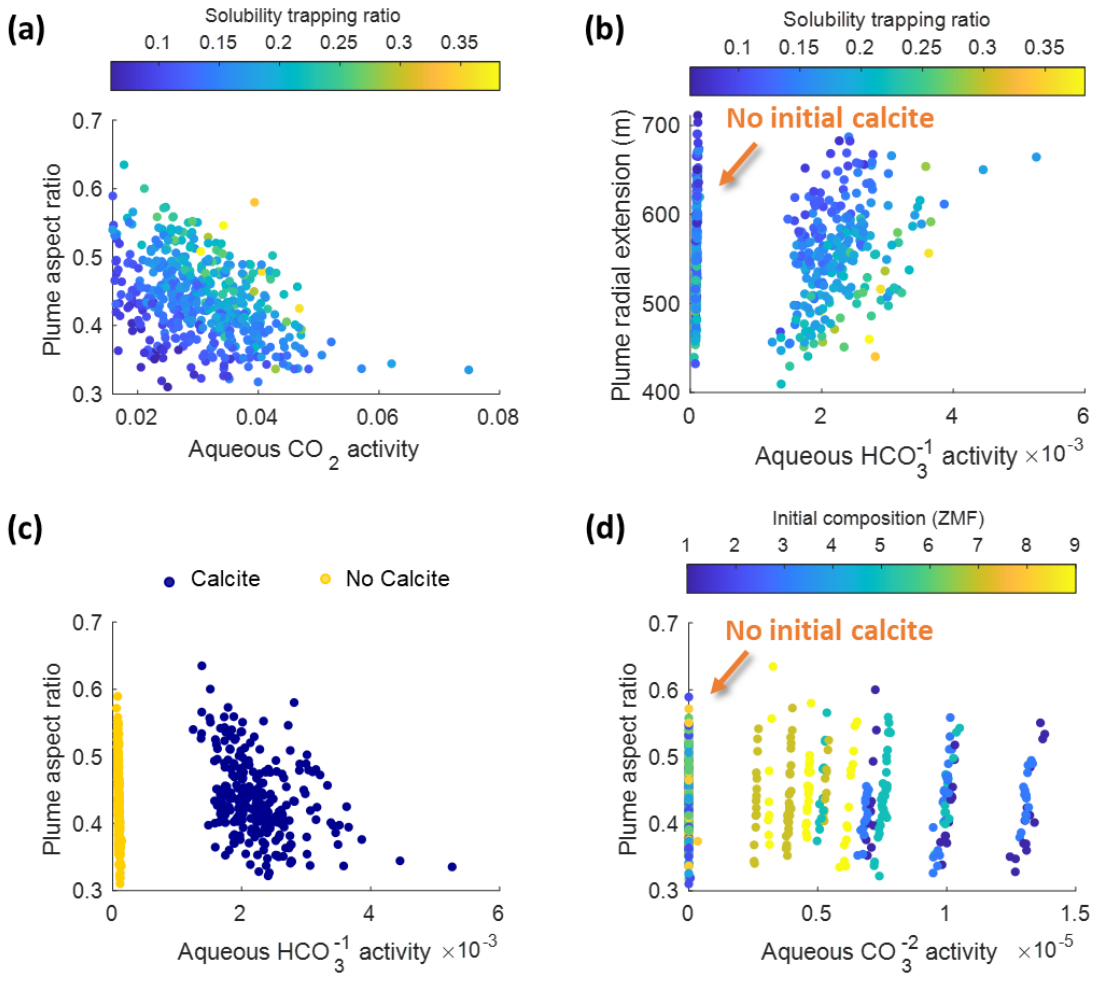

Figure 61. Carbonate species relation with plume dimensions initial calcite content and solubility trapping (a) aqueous CO_2 activity with plume aspect ratio and solubility trapping, (b) HCO_3^{-1} activity with plume radial extension and solubility trapping ratio, (c) HCO_3^{-1} activity with plume aspect ratio and initial calcite content, and (d) CO_3^{-2} activity with plume aspect ratio and initial composition.

4.8.5. Near-Well Monitoring and Average Plume Properties

One of the main challenges in determining an aquifer's storage capacity comes from the lack of information and proper characterization of the fluid properties of existing aquifers with potential for CO_2 storage. In the previous section, we discussed which fluid properties would be useful to monitor the plume dynamics. The next question that arises is, How representative are near-well properties of the plume-average properties? Here, the objective is to detect those changes in fluid properties near and away the injection point, and how they correlate with the plume average

properties. Then, changes in aquifer properties that can be monitored from the well could be used to understand the CO_2 behavior during the injection stages using well-based downhole sensors.

We used two regions for the analysis, namely Region 1 and the Plume-region. Region 1 represents the reservoir closer to the well from 0 to 150 m, and the Plume-region encompasses the aquifer volume that has been contacted by aqueous CO_2. The radial extension of the Plume-region varies by case, as shown previously in Figure 52. We computed the average variation of the fluid properties of interest with depth and time within these regions. For this study, the selected properties include pH, brine density, and various carbonate species' activity.

First, we examined the variations in pH in Region 1 and the Plume-Region. Figure 62 shows the average pH fluctuations with depth and time for selected cases in both regions. On the left, we included the plume shape at the end of 300 years. In general, the average pH can decline up to two units from the original aquifer pH inside the plume-region, and up to 4 units in Region 1 for these simulations' range of conditions. The initial composition of the brine determines the initial pH gradient. The plume pH gradient profile (center) reflects the plume shapes observed on the left. Larger pH drops are observed at depths where the plume grows more in-depth into the reservoir (cases with more considerable radial extension, such as Case 253 and Case 386), and more uniform pH fronts are identified for plumes with more homogeneous growth.

Region 1 gradient profiles do not resemble exactly those in the plume region. However, the profile-change with time and depth provides information about the broader trends inside the plume region. The plume-average pH exhibits more extensive changes above the injection depth (see Figure 62). As the CO_2 plume travels more in-depth into the formation, it also moves upwards, explaining the differences in pH above the injection point when we consider the plume-region. Conversely, near

the well, as CO_2 dissolves into water, the brine becomes denser and generates a downward flow. Thus, the downward flow induces a higher pH reduction below the injection point.

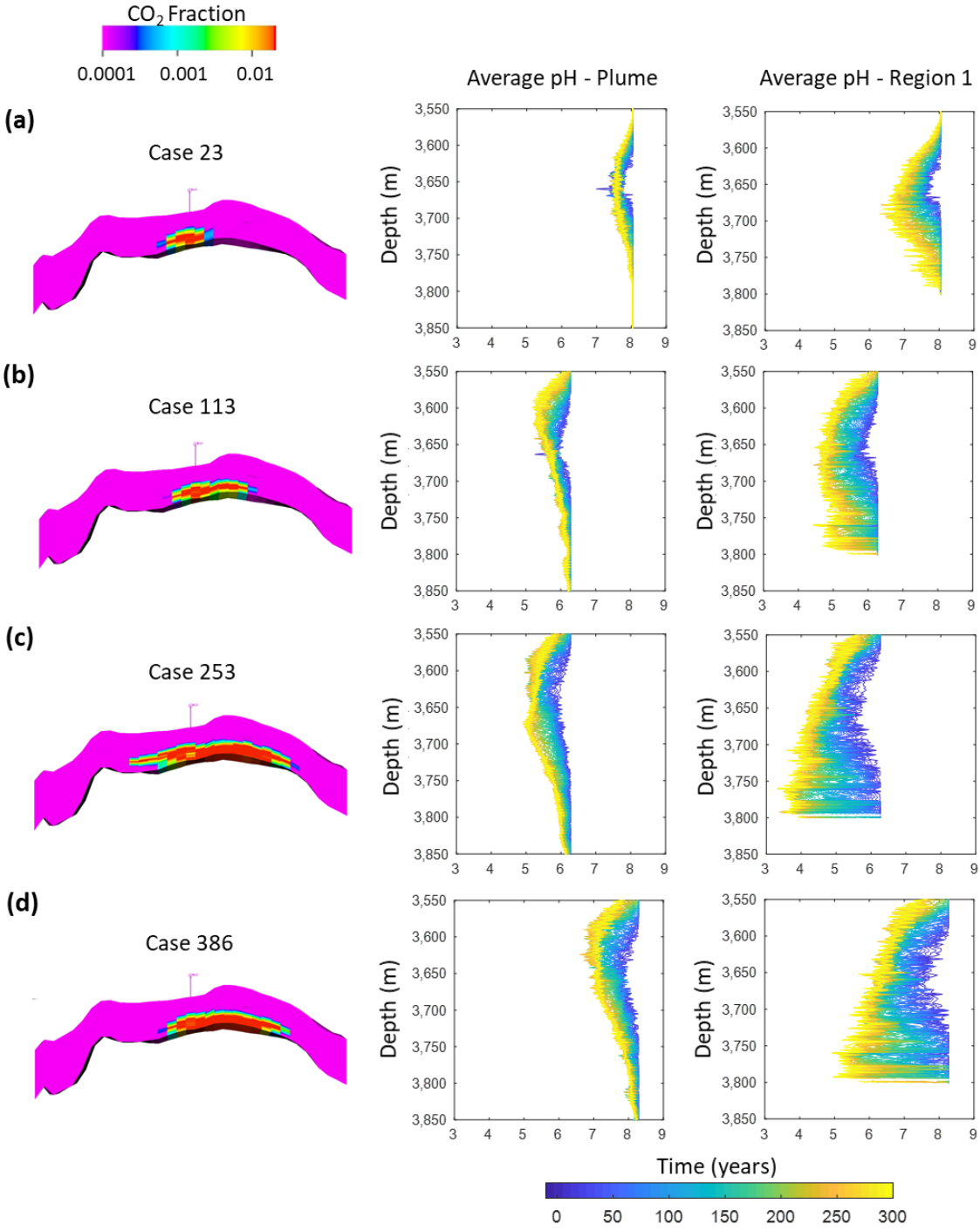

Figure 62. pH gradient evolution for selected case scenarios calculated for both the Plume-region and Region 1 (near the well). On the left, a cross-sectional image of the simulated plume after 100 years of injection is included for each case (a) Case 23, (b) Case 113, (c) Case 253, and (d) Case 386.

Next, we investigated how the near-well and plume-average pH values are correlated. Figure 63 presents cross-plots of the plume-average pH and Region 1 pH for all time and scenarios studied. Figure 63 illustrates the resulting cross-plot. Each data point represents the corresponding near-well and plume-average pH values for a given case at a given time step. As expected, early-time near-well and plume-average pH are well correlated. This is because, before injection, the models assume equilibrated conditions. Here again, two main signatures are apparent attributed to the presence or absence of initial calcite content in the brine. Larger initial pH values were observed in cases with original content of calcite (around 8) compared to cases where no initial calcite was included (around 6). This is an indicator of the role of calcite or similar minerals that can act as buffers during the injection process. As observed, the initial calcite content may affect the pH changes around the injection well and into the reservoir. Similar evidence of pH behavior associated with calcite-pH buffering has been observed in reactive transport simulations of carbonated aquifers (Lagneau et al., 2005). In general, as time progresses, the plume-average pH values deviate from the near-well pH values and become slightly larger.

Another signature observed in some cases is an initial increment in pH (as indicated by the orange arrows in Figure 63), followed by a reduction of pH characterized by the two different slopes previously mentioned. This behavior is apparent irrespective of the presence of initial calcite content. It can be explained by the initial interaction of other salts and ions in the aqueous phase with the injected CO_2. This interaction results from the initial precipitation of salts, and for cases with calcite content, in the initial dissolution of calcite that buffers the pH.

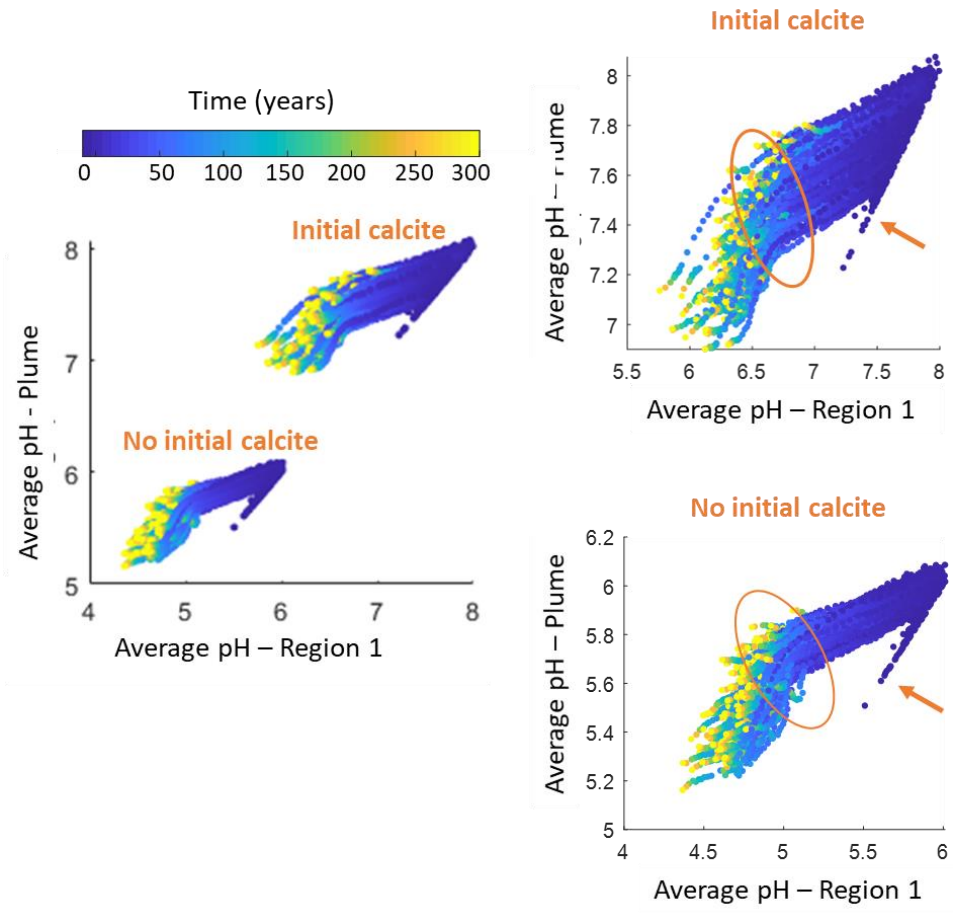

Figure 63. Plume-region pH and Region 1 pH (near-well) relationship for all case scenarios with time.

To explore further the pH relationship, we generated cross-plots of the plume-average pH and Region 1 pH gradients for selected cases, as shown in Figure 64. These cross-plots were created for different time steps and colored by depth. The initial brine pH gives the initial location of the trends. All the cases exhibit similar depth-dependent signatures. The correlations between near-well and plume-average pH improve at shallower depths. Also, wider deviations between the near-well and plume-average pH values are observed for larger plumes and higher injection rates, as in Cases 253 and 386. We also note post-injection progression towards equilibration. Once the injection stops, the correlation between near-well and plume-average pH values improves marginally. Post-injection equilibration happens relatively quicker in the shallower depths.

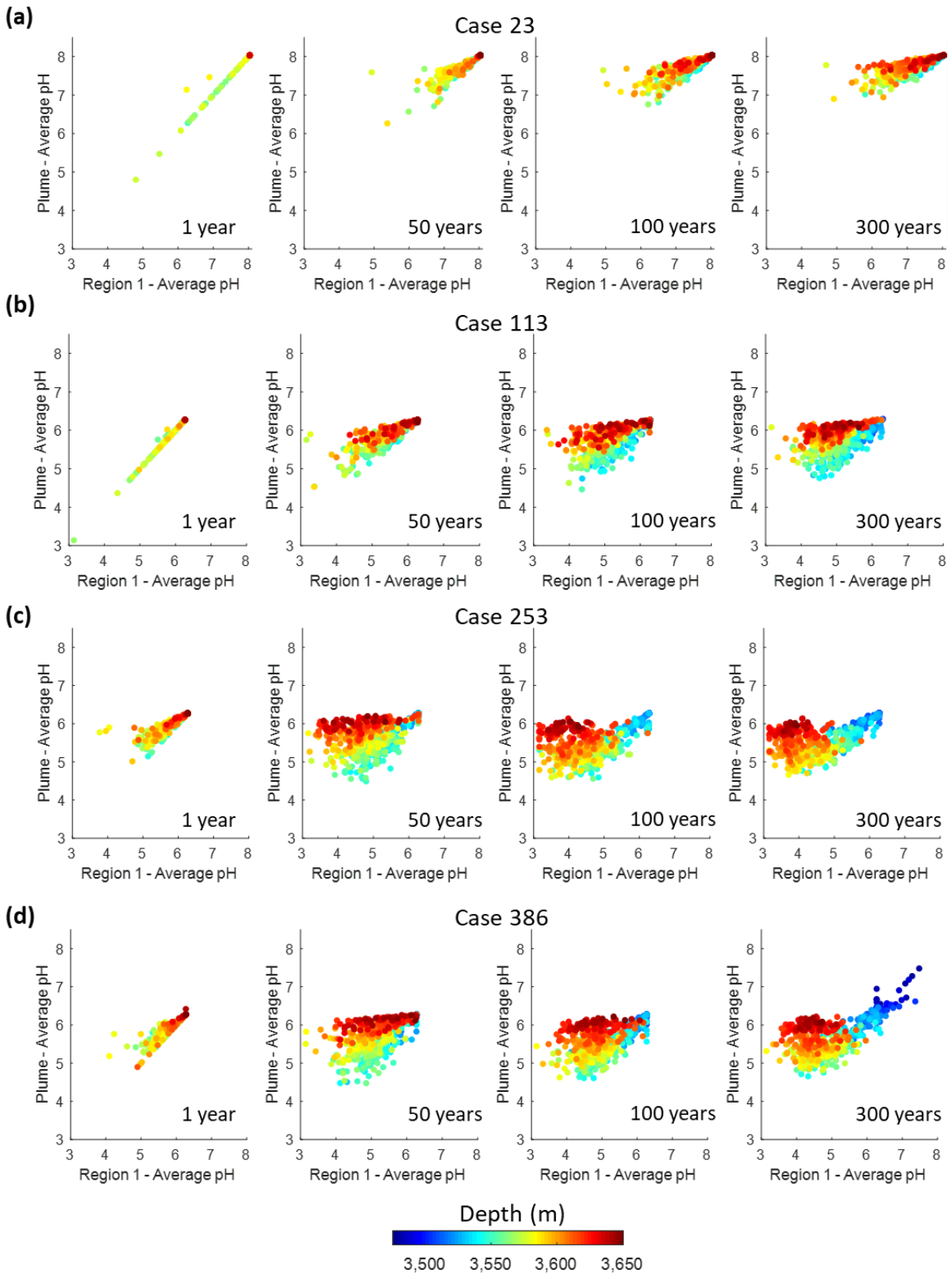

Figure 64. Relationship between the plume pH and Region 1 pH with depth and time for selected cases (a) Case 23, (b) Case 113, (c) Case 253, and (d) Case 386.

Similarly, we analyzed the near-well and plume-average brine density. The brine density in this study is calculated based on pure water density and corrected for the presence of salts and dissolved CO_2, allowing for a more accurate prediction of the density variations. CO_2 tends to increase the brine density. Even small changes in density can affect the dissolution rate of CO_2, as the instability created may induce advective-diffusive mixing and enhanced the CO_2 dissolution.

Figure 65 shows the changes in the near-well and plume-average brine density for selected scenarios with different initial density profiles. Density fluctuations from 2 to 5 units are observed. In general, density increases with time as more CO_2 is injected, and it dissolves into the aqueous phase. The most considerable density variations occur around the injection depth and near the well. In general, broader density alteration is observed for higher injection rates (for example, in Case 253 and 386). Unlike the pH gradients, the density gradient does not reflect the shape of the CO_2 plumes.

We also assessed the speciation of carbonate ions for different cases, including aqueous CO_2 and the bicarbonate ion CO_3^{-2}. Figure 66 presents near-well behavior and the plume-average the activity gradient of CO_2 with time and depth for selected cases. The CO_2 effective concentration (activity) gradient in the plume-region displays similar patterns as the plume shape itself. The effective concentration of aqueous CO2 is mostly correlated to the injected CO_2 (given the initial composition of the brine studied).

For example, cases with higher injection rates such as Cases 253 and 386 show higher variation with depth and reach higher concentrations above the injection point. At the same time, the changes in activity for Case 23 occur closer to the injection point, with lower effective concentrations. Case 23 is characterized by lower injection rates and permeability of the seal formation than other cases (see Appendix, Table A 11). The near-well activity of CO_2 exhibits a more homogeneous growth

for all cases. Overall, the correspondence between near-well and plume-average values for the aqueous phase CO_2 activity appears excellent.

Figure 67 shows the gradient of CO_3^{-2} activity. The effective concentration of the bicarbonate ion presents a dissimilar behavior for many cases due to the variations in initial calcite content that affects the initial presence of CO_3^{-2} with depth. In this case, the activity is a function of both the injection of CO_2 and the brine composition. For cases with initial calcite concentration, the CO_3^{-2} activity decreases with time, especially at depths where the aqueous CO_2 activity increases due to the speciation equilibration (Cases 23 and 386) and is influenced by the brine pH. More extensive ranges of variation are observed in Case 386, where lower pH values are reached, and there is higher CO_2 injection compared with Case 23.

While for cases with no initial calcite, minimal changes in the effective concentration of the bicarbonate ion CO_3^{-2} are observed, and increasing concentration behavior is detected with time (Cases 113 and 253). The difference in speciation of CO_2 in the aqueous phase for cases with or without initial content of calcite highlights the importance of accounting for the presence of relevant minerals to understand not only the CO_2-brine interaction but also the interaction rock-brine that is responsible for precipitation or dissolution of minerals.

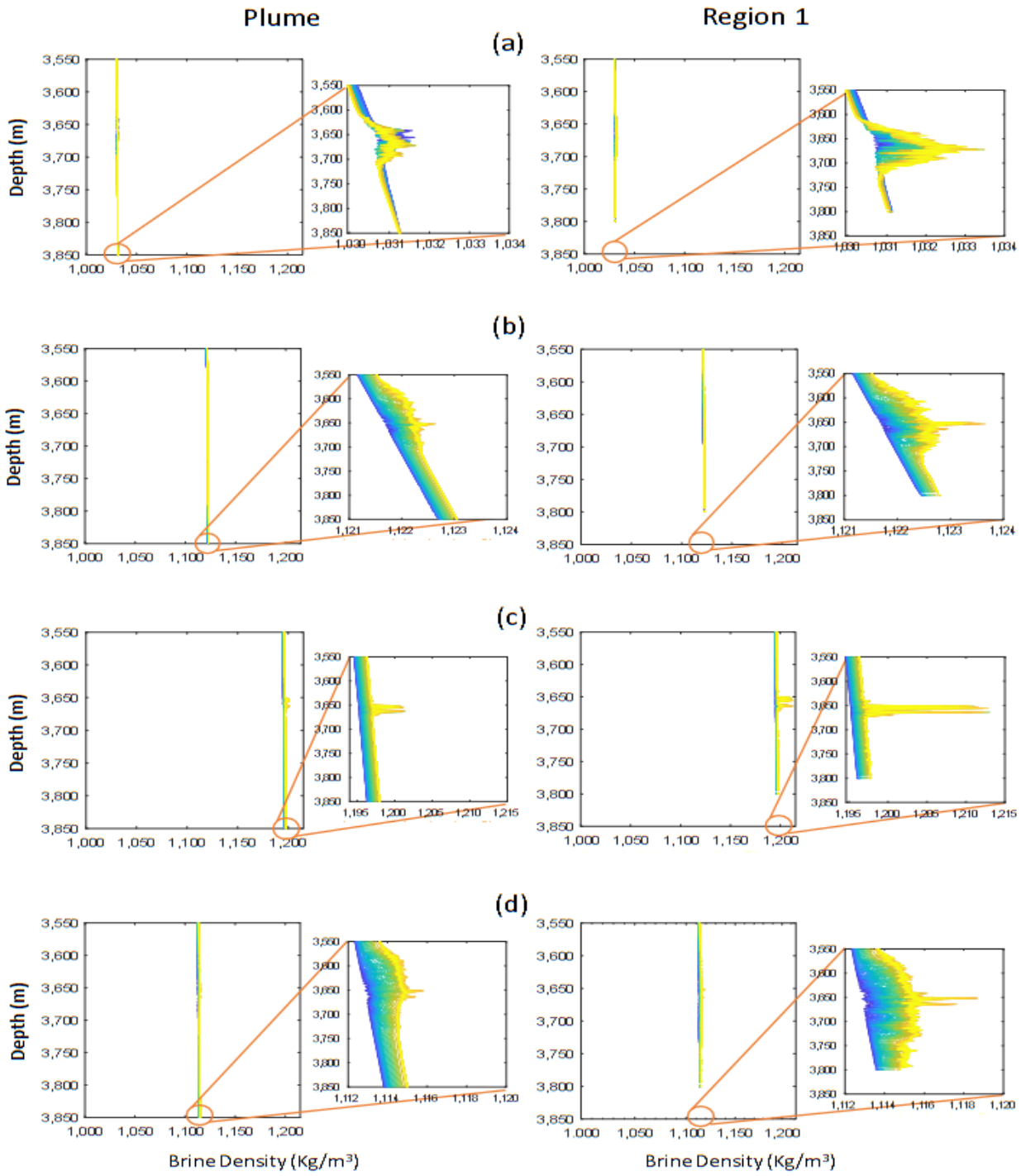

Figure 65. Brine density gradient evolution calculated for the Plume-Region and Region 1 (near the well) for selected cases (a) Case 23, (b) Case 113, (c) Case 253, and (d) Case 386.

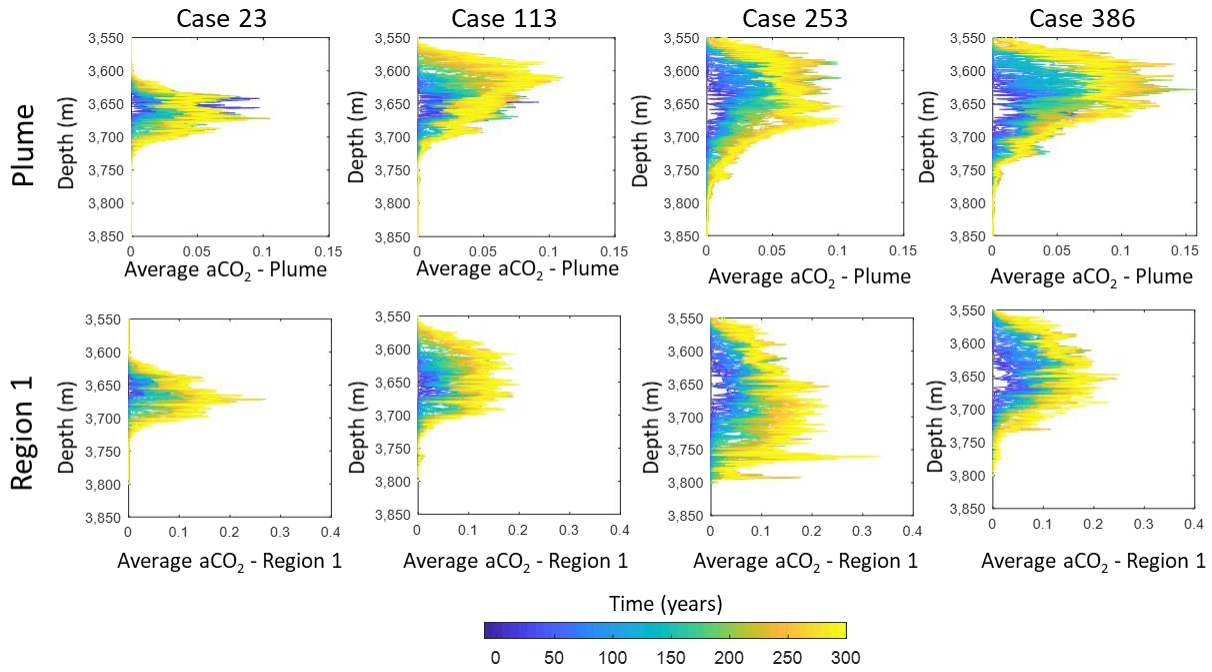

Figure 66. Evolution of the activity in the aqueous phase of CO_2 with time and depth for both the plume region and Region 1 (near-well). Selected case scenarios: Case 23, Case 113, Case 253, and Case 386.

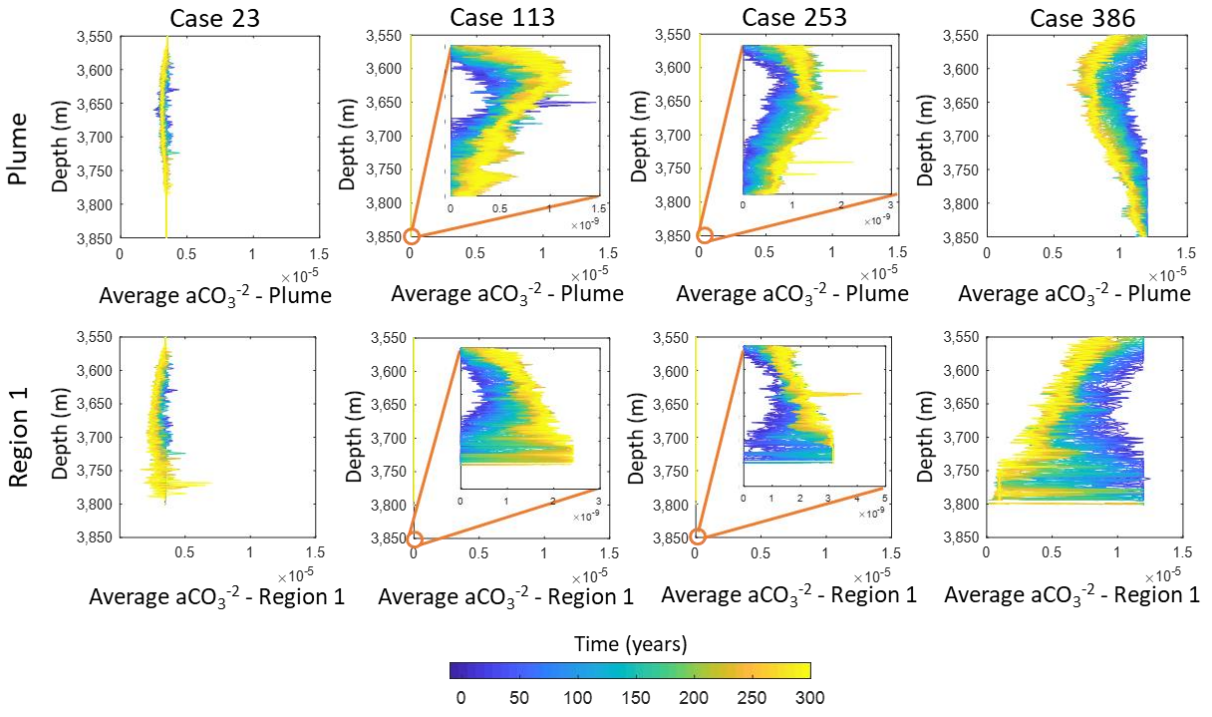

Figure 67. Evolution of the activity in the aqueous phase of CO_3^{-2} with time and depth calculated for both the plume-region and Region 1 (near-well). Selected case scenarios: Case 23, Case 113, Case 253, and Case 386.

4.8.6. Uncertainty and Sensitivity Analysis

We used the design of experiments and simulation results to investigate the relative influence of selected parameters on the plume dynamics and storage mechanisms. Furthermore, we determined the sensitivity of plume characteristics in relation to well-based monitored variables (fluid properties analyzed in the previous section). A description of the methodology, the parameters selected, and the ranges of variation assigned for uncertain parameters for the analysis was presented in section 4.7.4. It is essential to highlight that those ranges of variation selected profoundly influence the correlations presented here.

We first examined the factors affecting different storage mechanisms, namely, mobile supercritical CO_2, structural trapping, residual trapping, and CO_2 dissolved in water (solubility trapping). Figure 68 shows the tornado charts for these variables normalized by the injected CO_2 as a function of the input parameters previously mentioned. We identified an interesting interaction with the storage mechanisms of four types of variables investigated, including the multiphase rock-fluid properties, the aquifer fluid composition, the injection rate, and the porosity.

Multiphase rock-fluid interaction properties, such as relative permeability endpoints, critical saturations, and capillary pressure, impact all trapping mechanisms in different proportions due to the facies characteristics. In particular, CO_2 relative permeability endpoints and capillary pressures of shaly sand appear to negatively affect residual trapping with the opposite effects on the mobile CO_2. Meanwhile, the multiphase rock-fluid interaction properties of sand facies have a significant positive impact on the solubility trapping, and to a lesser extent, on structural trapping. The aquifer fluid composition, in specific, the presence of salts and calcite in the fluid, affects the trapping characteristics. Salts and calcite promote mobile CO_2 strongly, and to a lesser extent, the structural and residual trapping. This behavior can be explained by the inhibition of CO_2 solubility due to

higher salinity, resulting in more CO_2 residing in the supercritical state and, consequently, reducing solubility trapping. In addition to the fluid composition, the injection rate also manifests an inverse relationship with solubility trapping while enhancing supercritical CO_2 mobility. On the other hand, porosity affects mostly structural and solubility trapping. Increasing porosity benefits solubility trapping but restricts structural trapping. The latter is also affected negatively by baffles and permeability stratification. We observed that molecular diffusion has marginal effects on the trapping mechanisms.

We also explored the factors affecting plume geometry. Here, we will discuss the plume characteristics only for the plumes defined based on CO_2 in aqueous and supercritical phases. The features examined include the average height and average radial extension, as presented in the tornado charts in Figure 69. We observed that the injection rate affects the plume dimensions primarily on the radial extension of the plume. The plume radial extension is negatively related to porosity, as more significant accommodation space due to higher porosity retards the movement of CO_2. While the plume radially increases with increasing horizontal permeability. We expect such an impact of horizontal permeability.

Interestingly, molecular diffusion enhances CO_2 dissolved in the aqueous phase to diffuse further away into the aquifer, thus extending the radial dimension. Moreover, facies-dependent rock-fluid interaction parameters impact the plume dimensions, particularly for CO_2 in the supercritical phase, highlighting their role in the free phase's displacement. For instance, the shaly-sands' rock-fluid interaction characteristics have a larger effect on the plume height based on supercritical CO_2. Smaller pore sizes in the shale promote residual trapping. The plume dimensions appear to be mainly controlled by operational constraints with additional effects of permeability anisotropy, permeability values, and porosity.

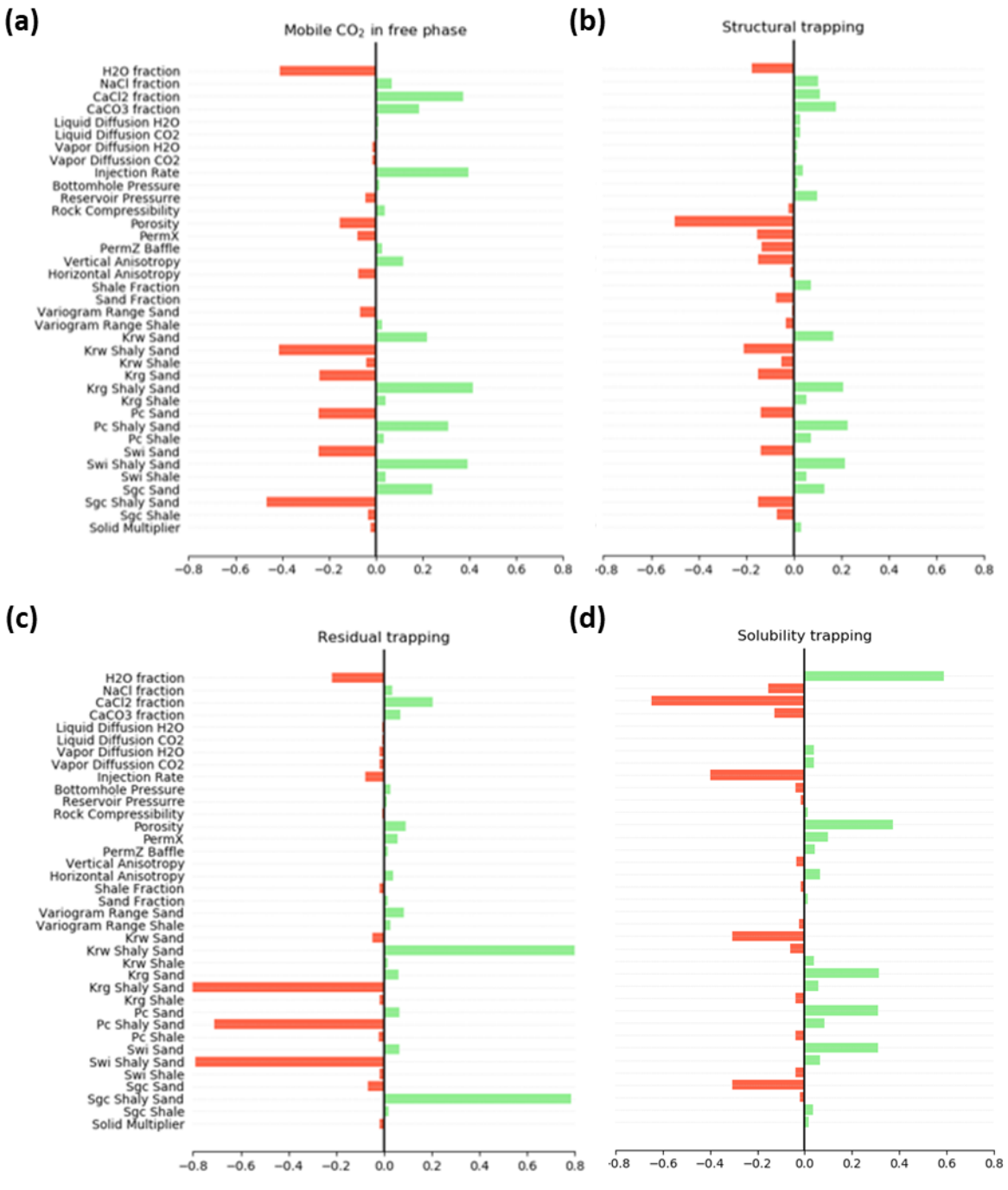

Figure 68. Relative variable influence (a) mobile CO_2 in supercritical free phase ratio, (b) structural trapping ratio, (c) residual trapping ratio, and (d) solubility trapping ratio (CO_2 dissolved in water).

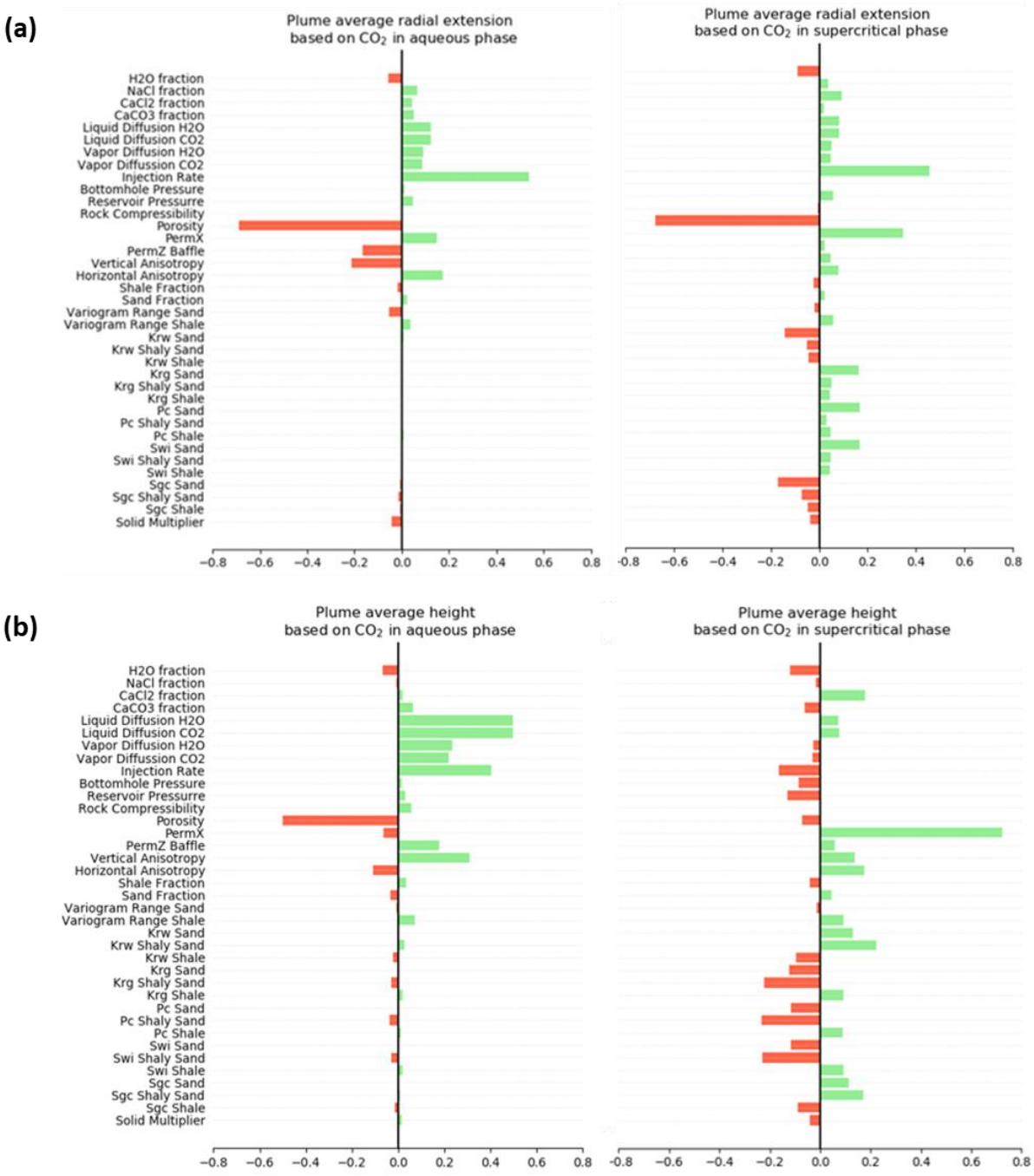

Figure 69. Relative variable influence on plume dimensions based on CO_2 in aqueous and supercritical phase (a) plume aspect ratio, and (b) plume average height.

Once we studied the role of selected parameters on the plume dynamics and storage mechanisms, we continue to explore the relative influence of various fluid properties, from salinity and pH to the effective concentration of ions in aqueous plume dimensions defined based on CO_2 in the supercritical phase. The characteristics examined include average height, average radial extension, and the distribution of the injected CO_2 into different phases and trapping mechanisms, as presented in the heat maps in Figure 70. The heat maps delve into the relative influence of several variables of interest during injection and post-injection periods. It is evident that the relative role of the fluid properties analyzed on the plume dimensions and CO_2 distribution underground varies between the injection and post-injection periods.

Let us discuss the effects on the plume dimensions first. For plume height, the salinity and brine density seem to promote the plume height as they hinder the solubility of CO_2 into the aqueous phase. This effect is also evident based on the plume height's negative correlation with the effective concentration of carbonate ions and the brine pH. Another property affecting the plume height is the CO_2 density. As expected, higher CO_2 density is correlated to shorter plumes in the vertical direction. After injection stops, the brine density and CO_2 speciation influence on the plume height seems to be reduced. This indicates in the post-injection period of the lesser dominance of convective flux and buoyancy-driven flow. Instead, in the post-injection period, the prominence of compositional equilibration via molecular diffusion kicks in.

The plume radial extension appears to be highly dependent on the CO_2 activity in the aqueous phase during the injection period, which is correlated with the total CO_2 injected into the aquifer. Brine salinity and density exhibit some positively correlated to the horizontal plume growth. Once injection stops, we observed a shift in the main parameters influencing the plume growth, with negligible influence from the CO_2 activity. It is now affected to some extent by salinity and the

presence of salts such as $CaCl_2$ (with a larger atomic number), and with a negative influence from the pH.

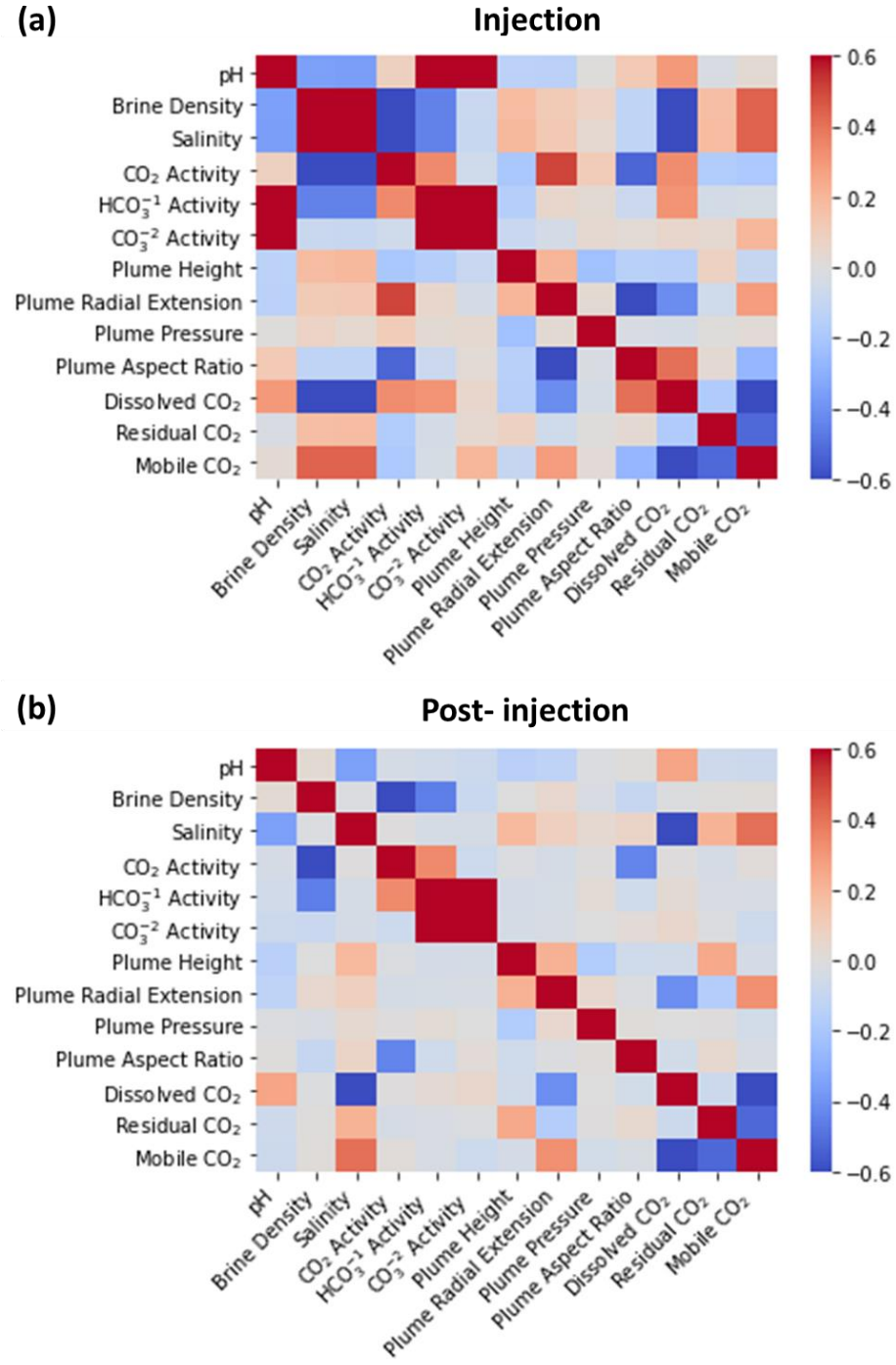

Figure 70**.** Relative influence of fluid properties on plume dimensions and CO_2 distribution into various storage mechanisms underground during (a) injection and (b) post-injection.

Finally, we analyzed the relationship of these fluid properties with the distribution of the injected CO_2 into different phases and trapping mechanisms. Here we considered CO_2 mobile in free-phase, CO_2 dissolved in the aqueous phase, and residual CO_2. To compare the amounts stored in each mechanism, we calculated the ratio of CO_2 in those selected trapping mechanisms concerning the injected CO_2 as described in section 4.8.3. Both salinity and brine density appear to play an important role in all the trapping mechanisms. In particular, higher salinity and brine density values promote CO_2 in free-phase and residually trapped, hindering the CO_2 solubility. This, in turn, is related to the presence of salts and calcite in the aqueous phase. The role of brine density and the effective concentration of various carbonate ions seems to be reduced after injection stops for all cases. On the other hand, the brine pH appears to affect mainly the solubility trapping, with negligible effects on other trapping mechanisms.

4.9. Discussion: Model Advantages and Limitations

The development and implementation pace and success of CO_2 capture and storage technologies depend on predicting, managing, and monitoring changes on the subsurface due to the injection of CO_2. Modeling and simulation of injection, storage, and trapping processes are vital to understanding the behavior and interaction of CO_2 with the minerals and fluids that are part of the aquifer formations.

The CO_2 flow, transport, and storage model presented here is an integrated approach that incorporates different aspects of the process, with realistic geological features, petrophysical properties, and multiphase displacement characteristics that capture the heterogeneous nature of the rocks. Moreover, the physical and chemical models considered include both advection and diffusion as flow drivers, thermodynamics of mutual solubilities between CO_2 and brine, and a

geochemical system that captures the speciation and interaction of CO_2, salts, and calcite in the aqueous phase.

The model can be implemented to evaluate the plume's behavior and different trapping mechanisms via structural, residual, solubility, and mineral trapping. The total residual trapping is quantified based on capillary forces and relative permeability curves related to specific lithologies that determine the displacement of the supercritical phase and the aqueous phase in the formation. Solubility trapping is given by the mutual solubility of the phases and the brine composition. In comparison, estimation of the mineral trapping can be obtained from the precipitation of calcite components. The model also facilitates tracking and monitoring different fluid properties that can predict plume behavior, such as pH, density, and species activities. Considering the variation in the measured properties near the well and the average behavior into the reservoir.

The geochemical system employed is a simplified representation of the interactions at the aqueous phase, given that chemical systems in nature are highly complex. As a result, the mineral trapping predictions are limited by an incomplete description of the pore space's reactions. It would be necessary to include a more detailed mineral composition of the rocks and add mineral-fluid interactions representing the immobilization of CO_2 to improve the model. Furthermore, considerations of physical and chemical processes at the pore-scale would be required, including reactive transport and the effects of mechanical compaction on the pore structure. This implies the coupling of processes at different scales.

Other gaps in our study are related to different physical processes that play a role in sequestration operations. For instance, the hysteretic behavior in relative permeability and capillary pressure curves can affect the CO_2 injection and storage, as both drainage and imbibition processes are expected once the CO_2 is placed in the saline aquifer. Specifically, residual trapping of CO_2 would

be directly impacted, with hysteretic behavior beneficiating rock facies with a more considerable difference in gas residual saturations from drainage to imbibition. For instance, hysteresis in vuggy carbonates will not be that significant compared to the carbonates rich in micro-fissures. The geomechanical influence is another aspect that we have not explored in this study. The carbon sequestration process's integrity and security will strongly depend on the geomechanical-hydrodynamic interaction in the aquifers. Other important aspects would be related to injectivity and well integrity.

4.10. Conclusions

We explored different aspects of CO_2 storage in saline aquifers involving the CO_2 plume dynamics, the storage capacity of varying trapping mechanisms, and monitoring of fluid properties concerning the CO_2 plume characteristics. Our analysis is based on an integrated modeling framework that combines the impact of hydrogeological, petrophysical, and operational constraints. The 3D static model and dynamic simulations used in this study provide a means to analyze the complex interplay of reservoir-dependent geologic parameters with active injection process elements. Among the parameters examined are the facies distribution, aquifer-water composition, heterogeneity and anisotropy of petrophysical properties, transport physics, such as molecular diffusion, and operational variables like injection rate and bottomhole pressure. Moreover, the proposed framework enabled us to ascertain the relative influence of these parameters on plume evolution by analyzing several case scenarios generated based on the Design of Experiments.

We characterized the CO_2 plume based on several property-change metrics. The metrics employed for the definition of the CO_2 plume are based on CO_2 dissolved in the aqueous phase, pH change, presence of CO_2 in a supercritical state, and solid-phase saturation changes due to dissolution

and/or precipitation. The CO_2 in the aqueous phase covers the largest aquifer region surrounding the injection well. Only a limited volume of this region experiences notable changes in pH, while CO_2 in the supercritical phase is typically present in an even smaller aquifer's capacity. Changes in solid-phase saturation occur in the most limited part of the aquifer very close to the injection well, enclosed in the dried-out zone due to the supercritical CO_2.

In terms of the storage mechanism for the scenarios investigated, we observed that 60% of the injected CO_2 within the reservoir exists as a mobile free-phase throughout the injection period. On average, 20% of the injected CO_2 remains stored via residual trapping; however, this percentage varies significantly depending on the lithofacies' relative permeability and capillary pressure curves. The remaining 20% of the injected CO_2 gets sequestered via solubility trapping, which is influenced by porosity, horizontal permeability, water irreducible saturation, capillary pressure of the sand facies, and the initial aquifer water composition (notably, the presence of salts and calcite). Thus, petrophysical and multiphase rock-fluid interaction properties of the facies appear to have a considerable effect on different trapping mechanisms. In solubility trapping, sand facies controlled the storage ratios, while for residual trapping, shaly-sand facies properties prevailed. Meanwhile, the structural trapping represents, on average, 10% of the CO_2 injected.

The plume dimensions appeared to be controlled by several factors. Due to baffles and stratifications, the average lateral propagation of the plume is larger than the vertical dispersion during both injection and post-injection periods. The prevalence of a combination of advective and diffusive driving forces over that of buoyancy triggers this outcome. We also noted that during the post-injection period, the effect of molecular diffusions becomes more apparent. The main parameters affecting the areal expansion of the plume appear to be the horizontal permeability, porosity, and the injection rate. Comparatively, vertical permeability anisotropy and porosity have

the most significant impact on vertical plume height. In general, multiple geometries and growth patterns occur for the CO_2 plume, with plume shape influenced primarily by the total amount of CO_2 injected, the porosity, and the rock-fluid interaction properties of different facies.

Monitoring of the selected fluid properties provided information about the CO_2 movement and plume shape and helped understand the distribution of CO_2 into different trapping mechanisms. For instance, we observed that solubility trapping is correlated to cases with larger pH and lower salinity. At the same time, residual trapping and free-phase CO_2 are favored in higher salinity and brine density cases.

We identified two clusters of pH and CO_2 speciation behavior based on the initial calcite content of the cases studied. The clusters are explained by the buffering of the pH due to the CO_2 interaction with calcite. In both pH clusters, the plume radial extensions are governed by the total CO_2 injection, resulting in larger plumes with larger amounts of CO_2 injected and lower pH. More considerable pH changes are related to higher aqueous CO_2 activity, while the solubility trapping is higher for cases with lower pH changes.

The gradients near the well and in the plume region for both pH and effective concentration of CO_2 in the aqueous phase appear to reflect the shape of the CO_2 plume. Both the injection and post-injection periods can be identified in the pH correlation for these regions. Once injection stops, the correlation slope becomes steeper, and an inflection point is observed for all cases (with and without initial calcite). The initial pH slope (during the injection period) is governed by the CO_2 advection, while the second slope after injection stops is driven by buoyancy and diffusion mechanisms.

On the other hand, the initial fluid composition determines the fluid density and its relationship with the CO_2 solubility and the solid saturation. Cases with higher fluid density exhibit lower solubility trapping ratios. Based on the observations of the fluid properties behavior for cases with and without initial calcite, it is evident that including robust geochemical models that consider the presence of relevant minerals affecting the interaction of the CO_2 with the brine and the rock is vital for an accurate prediction of the amount of CO_2 dissolved.

Chapter 5. Research Contribution

This dissertation contributes to the overall field of multiscale, multiphysics studies in porous media by combining pore-scale network models with experimental data and reservoir scale simulation to investigate the role of pore-scale physical and chemical interactions on various subsurface engineering applications. Three different topics were addressed, namely (1) formation damage due to particle plugging during hydraulic fracturing as a result of proppant crushing and fluid invasion, (2) the evolution of migration pathways due to chemical diagenesis in shales, and (3) plume characterization, storage mechanisms, and well-based monitoring during CO_2 sequestration in saline aquifers.

5.1. Formation Damage at the Matrix-Fracture Interface During Hydraulic-Fracturing: Particle Transport and Plugging

During hydraulic fracturing in shales, formation permeability damage can occur due to particle plugging due to fracturing fluid invasion and proppant crushing. We developed a multiphysics pore-scale plugging simulator integrated with a macroscale fracture simulator to investigate formation permeability damage at the fracture and the rock matrix interface. Fine-scale particles generated from this process can cause further permeability reduction defeating the purpose of hydraulic fracturing. Macroscopic conventional modeling of particle transport in porous media based on classical filtration theory fails to capture the pore space's features such as pore size distribution, the topology of the interconnected pores, and heterogeneity. Our simulations based on flow and transport in pore networks consider all these characteristics at the pore level and incorporate the physics that affect particle-surface interaction.

The integration of pore-networks with the fracture simulator, and the proppant size population balance modeled as a function of stress, provided the necessary tools to quantify the influence of

filtration on permeability reduction during fracturing operations. The simulation results can help planning hydraulic fracturing operations and improve the decision-making process for proppant selection by offering additional information useful to select appropriate concentrations, size, and type. Understanding the proppant and the fracturing fluid interaction with the matrix to delineate the fracturing operations ultimately leads to sustained enhanced permeabilities. Hence, production as the communication between the fracture and the reservoir can be better characterized. Moreover, the workflow can be applied in similar scenarios involving fines or particle deposition due to fluid injection or production in water-disposal operations or asphaltene-deposition processes, when a pore-scale model is coupled with a reservoir-scale simulator incorporating appropriate physics. The computed pressures, fluxes, and changes in the petrophysical properties at the pore space can be upscaled by connecting the pore networks with reservoir scale simulators and incorporating appropriate physics to predict changes at larger scales in the porous media.

5.2. Modeling Chemical Diagenesis at the Pore-Scale: A Study of the Evolution of Migration Pathways in Unconventional Reservoirs

We proposed a pore-scale modeling framework that integrates mineralogical, petrophysical, and chemical data to investigate the role of diagenesis on pore structure changes with time. The pore-scale model has two components, namely diagenetic analysis and reactive transport simulation at the pore-scale. Diagenetic analysis of available samples provides the chemical basis and pore dynamics to understand the main events occurring with significant repercussions on estimating the rock properties. The hybrid 3D pore-networks employed represent the pore structure, incorporating experimental observations on facies dependent pore types and size distributions. Besides, flow simulations help track the changes in the concentration of the mineral components for each pore in the network as a function of advection, diffusion, and chemical reactions.

The pore-scale simulator allowed us to probe the paragenesis and model the evolution of migration pathways in the Woodford Shale. Besides offering key insights about the impact of advective and diffusive processes on the mineral species transport and their interaction with the fluids traveling through the pore space. Understanding the role of diagenesis in rock formations is of interest in studying oil and gas reservoirs because it provides the basis to comprehend the heterogeneous nature of the rock and the evolution of the pore structure. It is vital to properly represent the rock's petrophysical properties that give information on the rock's storage and fluid transport capacity at larger scales. In other words, modeling diagenesis at the pore scale helps to improve the reservoir quality characterization.

5.3. Geological Sequestration of CO_2 in Saline Aquifers: Critical Insights on Plume Dynamics, Storage Efficiency and Monitoring

The CO_2 injection, transport, and storage model presented in our study is an integrated approach that incorporates different aspects of the sequestration process. The model considers advection and diffusion as flow drivers, mutual solubilities between CO_2 and brine, and a geochemical system that captures the speciation and interaction of CO_2 in the aqueous phase. Besides, realistic geological features, petrophysical properties, multiphase displacement characteristics, and operational constraints are included in the model. This investigation provides essential insights that can help unlock the challenges facing the commercial-scale deployment of carbon capture and sequestration (CCS). In particular, in terms of predicting the evolution of injected CO_2 during long-term injection and post-injection periods, apportioning the injected mass across the various trapping mechanisms, and monitoring plume characteristics.

Three main contributions can be highlighted in this study. First, property-based metrics were implemented to generate various plume definitions, including CO_2 dissolved in the aqueous phase,

pH change, presence of CO_2 in a supercritical state, and solid-phase saturation changes due to dissolution and/or precipitation. Next, the investigation of CO_2 storage efficiency employing a novel definition of structural trapping and determining the individual contribution of different trapping mechanisms. Finally, monitoring variations in pH, CO_2 ion activities, and brine density near the well and the plume region to establish which fluid properties reflect the plume front growth.

The diagnostics tools provided improve our understanding of the CO_2 dynamics to help us engineer and optimize subsurface processes, and in turn, be able to increase CO_2 sequestration projects' integrity and security. Besides, the analysis of the storage mechanisms and plume properties helped us identify which parameters have a more significant impact on the CO_2 plume development and mobility, to simplify reservoir-scale models while still reflecting the complex nature of the CO_2 interactions underground and offering insights on the plume evolution. This step could enable the research community to move towards more generalized models that allow project teams to use simulations to optimize sequestration projects' operational aspects.

Appendix

Table A 1. Chemical system components as a combination of available species in the aqueous phase

Component	Species relation
$[Na_T]$	$[Na^+]$
$[Cl_T]$	$[Cl^-]$
$[Mg_T]$	$[Mg^{2+}]$
$[Ca_T]$	$[Ca^{2+}]$
$[C_T]$	$[H_2CO_3] + [CO_3^{-2}] + [HCO_3^-]$
$[Si_T]$	$[H_4SiO_4] + [H_3SiO_4^-] + [H_2SiO_4^{2-}]$
$[Al_T]$	$[Al^{3+}] + [Al(OH)^{2+}] + [Al(OH)_2^+] + [Al(OH)_3] + [Al(OH)_4^-]$
$[H_T]$	$[H^+] - [OH^-] + [H_2CO_3] - [HCO_3^-] - [CO_3^{2-}] + [H_4SiO_4] - [H_3SiO_4^-]$ $-[H_2SiO_4^{2-}] - [Al(OH)^{2+}] - 2[Al(OH)_2^+] - 3[Al(OH)_3] - 4[Al(OH)_4^-]$

Table A 2. Kinetic parameters for mineral reactions at 50 ºC (Nogues et al., 2013).

Parameter	Dolomite	Kaolinite
$log_{10}(k_H)$(mol cm^{-2}s^{-1})	-2.7	-10.8
$log_{10}(k_{OH})$(mol cm^{-2}s^{-1})	0	-15.7
$log_{10}(k_{H2O})$(mol cm^{-2}s^{-1})	-6.82	0
n_H	0.5	0.4
n_{OH}	-	0.3
n_{H2O}	1	-
m	1	0.9

Table A 3. Reaction term for Eq. 23 based on concentration changes due to kinetic reactions for all lumped components in the chemical system

Component	**Reaction term for pore *i***
$[Na_T]$	$\mathrm{A}_{alb,\mathrm{i}}R_{alb,i}$
$[Mg_T]$	$\mathrm{A}_{dol,\mathrm{i}}R_{dol,i}$
$[\mathrm{Ca_T}]$	$\mathrm{A}_{dol,\mathrm{i}}R_{dol,i}$
$[\mathrm{C_T}]$	$2\mathrm{A}_{dol,\mathrm{i}}R_{dol,i}$
$[\mathrm{Si_T}]$	$2\mathrm{A}_{kaol,\mathrm{i}}R_{kaol,i} + 3\mathrm{A}_{alb,\mathrm{i}}R_{alb,i} + 2\mathrm{A}_{anort,\mathrm{i}}R_{anort,i}$
$[\mathrm{Al_T}]$	$2\mathrm{A}_{kaol,\mathrm{i}}R_{kaol,i} + \mathrm{A}_{alb,\mathrm{i}}R_{alb,i} + 2\mathrm{A}_{anort,\mathrm{i}}R_{anort,i}$
$[\mathrm{H_T}]$	$-4\mathrm{A}_{kaol,\mathrm{i}}R_{kaol,i} - 4\mathrm{A}_{alb,\mathrm{i}}R_{alb,i} - 6\mathrm{A}_{anort,\mathrm{i}}R_{anort,i}$

Table A 4. Facies model input data for the base case model.

				Variogram			
Zone	Modeling technique	Facies	Proportion	Major direction, m	Minor direction, m	Vertical, m	Azimuth (°)
1	SIS	Sand	25	350	250	8	-85
		Fine Sand	40	500	400	6	-15
		Shale	35	800	600	6	45
2	SIS	Fine Sand	22	700	600	6	55
		Shale	78	700	600	6	55
4	SIS	Sand	15	350	250	8	-85
		Fine Sand	35	400	300	6	-15
		Shale	50	500	400	6	45
Zone	Modeling technique	Facies	Proportion	Facies body geometry		Major Orientation (°)	
3	OBM	Sand	35	Fluvial channels		50	
		Fine Sand	30	Oxbow lakes		30	
		Shale	35	Background		-	

Table A 5. Porosity model input parameters for the base-case model.

Zone	Facies	Min	Max	Mean	Variogram		
					Major direction, m	Minor direction, m	Vertical, m
1	Sand	0.05	0.25	0.18	400	300	8
	Fine Sand	0.03	0.15	0.1	250	200	5
	Shale	0.03	0.09	0.07	500	400	4
2	Fine Sand	0.03	0.15	0.11	350	250	5
	Shale	0.03	0.09	0.07	500	400	4
3	Sand	0.06	0.28	0.19	500	400	8
	Fine Sand	0.03	0.15	0.1	250	200	5
	Shale	0.03	0.09	0.07	500	400	4
4	Sand	0.05	0.2	0.14	400	300	8
	Fine Sand	0.03	0.14	0.09	250	200	5
	Shale	0.03	0.08	0.06	500	400	4

Table A 6. Permeability model input parameters for the base-case model.

Zone	Facies	Min	Max	Mean	Variogram		
					Major direction, m	Minor direction, m	Vertical, m
1	Sand	0.5	30	6	400	350	6
	Fine Sand	0.1	5	1	200	150	6
	Shale	0.005	0.5	0.1	600	500	4
2	Fine Sand	0.1	5	1	350	250	5
	Shale	0.005	0.5	0.1	600	500	4
3	Sand	0.6	40	7	400	350	6
	Fine Sand	0.1	5	1	200	150	6
	Shale	0.005	0.5	0.1	600	500	4
4	Sand	0.5	20	5	400	350	6
	Fine Sand	0.1	4	0.9	200	150	6
	Shale	0.005	0.4	0.09	600	500	4

Table A 7. Coefficients for the zero-density viscosity calculation (a_i) and the excess viscosity (d_{ij}) (Fenghour et al., 1998)

Zero-density Viscosity		Excess Viscosity	
i	a_i	ij	d_{ij}
0	0.2351	11	0.4071×10^{2}
1	-0.4913	21	0.7198×10^{4}
2	5.2111×10^{-2}	64	0.2412×10^{16}
3	5.3479×10^{-2}	81	0.2971×10^{22}
4	-1.5371×10^{-2}	82	20.1628×10^{22}

Table A 8. Coefficients used to determine the aqueous phase density considering the effects of the electrolytes present in the brine (Zaytsev and Aseyev, 1992).

Component	$b_{0i} \cdot 10^4$	$b_{1i} \cdot 10^6$	$b_{2i} \cdot 10^8$
$CaCl_2$	3,627	0	14
$CaCO_3$	2,625	-665	660
NaCl	3,093.6	68.6	13.8

Table A 9. Nine sets of initial compositions used in the uncertainty analysis.

	Initial component mole fraction				
	H_2O	CO_2	NaCl	$CaCl_2$	$CaCO_3$
Set 1	0.92	0	0.035	0.015	0.03
Set 2	0.935	0	0.035	0.03	0
Set 3	0.94	0	0.03	0.011	0.019
Set 4	0.955	0	0.03	0.015	0
Set 5	0.96	0	0.025	0.007	0.008
Set 6	0.965	0	0.025	0.01	0
Set 7	0.97	0	0.02	0.00425	0.00575
Set 8	0.975	0	0.02	0.005	0
Set 9	0.98	0	0.015	0.0015	0.0035

Table A 10. Fluid mobility reduction due to solid adsorption tables for uncertainty analysis.

Table 1		Table 2		Table 3	
Solid Saturation	Fluid Mobility Multiplier	Solid Saturation	Fluid Mobility Multiplier	Solid Saturation	Fluid Mobility Multiplier
0	1	0	1	0	1
0.1	0.66	0.1	0.9	0.1	0.98
0.3	0.32	0.3	0.7	0.3	0.89
0.5	0.12	0.5	0.5	0.5	0.76
0.7	0.04	0.7	0.3	0.7	0.6
0.9	0.01	0.9	0.1	0.9	0.3
1	0	1	0	1	0

Table A 11. Petrophysical, fluid, and operational parameters for Cases 3, 23, 113, 195, 253, 377, and 386.

Property	Case 3	Case 23	Case 113	Case 195	Case 214	Case 253	Case 377	Case 386
Average porosity, fraction	0.04	0.19	0.18	0.16	0.07	0.05	0.05	0.07
Average permeability in X-direction, mD	0.3	0.36	24.7	12.6	29.9	13.9	26.7	17.3
Average permeability in the seal formation, mD	5×10^{-5}	5×10^{-3}	1.6×10^{-2}	0.22	0.07	1.7×10^{-2}	0.14	6.1×10^{-3}
Permeability vertical anisotropy	0.01	1	0.16	0.64	0.61	0.07	0.31	0.25
Permeability horizontal anisotropy	0.25	0.25	2.66	0.28	1.21	1.4	3.7	2.5
Rock compressibility, 1/bar	2.4×10^{-4}	2.4×10^{-4}	6.7×10^{-5}	1.4×10^{-4}	1.5×10^{-4}	1.3×10^{-4}	6.9×10^{-5}	8.4×10^{-5}
Reservoir pressure, MPa	47.5	46.8	42.8	46.9	35.9	47.1	42.7	43.6
Bottom hole pressure, MPa	60	51	56.5	52.8	59.6	56.6	59.6	55.8
Average injection rate, t/y	1267	1410	2484	1333	1620	4576	3422	3986
CO_2 diffusion coefficient in supercritical phase	5.8×10^{-3}	7.3×10^{-3}	6.5×10^{-3}	5.5×10^{-3}	6.5×10^{-3}	6.5×10^{-3}	6.6×10^{-3}	6.9×10^{-3}
H_2O diffusion coefficient in supercritical phase	2.9×10^{-3}	3.6×10^{-3}	3.2×10^{-3}	2.7×10^{-3}	3.2×10^{-3}	3.2×10^{-3}	3.3×10^{-3}	3.4×10^{-3}
CO_2 liquid diffusion coefficient	4.5×10^{-4}	4.5×10^{-4}	4.5×10^{-4}	3.9×10^{-4}	4.5×10^{-4}	4.5×10^{-4}	3.4×10^{-4}	3.9×10^{-4}
H_2O liquid diffusion coefficient	5.7×10^{-4}	5.7×10^{-4}	5.7×10^{-4}	5.0×10^{-4}	5.7×10^{-4}	5.7×10^{-4}	4.4×10^{-4}	4.9×10^{-4}
Maximum capillary pressure in shale, MPa	4.5	5.8	5.0	4.5	5	5.8	5.8	4.5
Maximum capillary pressure in shaly-sand, MPa	2.2	3.5	2.2	3.5	2.2	2.2	2.2	2.5
Maximum capillary pressure in sand, MPa	0.3	0.3	0.8	0.8	0.8	0.3	0.3	0.8
Residual CO_2 saturation for shale	0.328	0.184	0.271	0.328	0.271	0.184	0.184	0.328
Residual CO_2 saturation for shaly-sand	0.196	0.128	0.196	0.128	0.196	0.196	0.196	0.138
Residual CO_2 saturation for sand	0.035	0.035	0.02	0.02	0.02	0.035	0.035	0.02
Irreducible water saturation for shale	0.32	0.4	0.36	0.32	0.36	0.4	0.4	0.32
Irreducible water saturation for shaly-sand	0.15	0.22	0.15	0.22	0.15	0.18	0.15	0.15
Irreducible water saturation for sand	0.03	0.03	0.08	0.08	0.08	0.03	0.03	0.08
CO_2 rel. permeability at residual water saturation for shale	0.6	0.7	0.65	0.6	0.65	0.7	0.7	0.6
CO_2 rel. permeability at residual water saturation for shaly-sand	0.75	0.85	0.75	0.85	0.75	0.75	0.75	0.8
CO_2 rel. permeability at residual water saturation for sand	0.85	0.85	0.95	0.95	0.95	0.85	0.85	0.95
Water rel. permeability at residual CO_2 saturation for shale	0.6	0.4	0.5	0.6	0.5	0.4	0.4	0.6
Water rel. permeability at residual CO_2 saturation for shaly-sand	0.3	0.2	0.3	0.2	0.3	0.3	0.3	0.25
Water rel. permeability at residual CO_2 saturation for sand	0.7	0.7	0.63	0.63	0.63	0.7	0.7	0.63
Salinity, kppm	57.5	57.5	186.0	57.9	123	289.3	209.8	166.3
Supercritical phase density, Kg/m^3	859	854	822	889	771	853	889	867
Initial $CaCO_3$ mole fraction	0.0035	0.0035	0	0.0035	0.008	0	0.03	0.019
Initial pH	7.7	7.85	6.1	8	7.9	6.1	8.2	8.1

References

Abousleiman, Y., Tran, M., Hoang, S., Bobko, C., Ortega, A., and Ulm, F. J. (2007). Geomechanics field and laboratory characterization of woodford shale: The next gas play. *Proceedings - SPE Annual Technical Conference and Exhibition*, *4*, 2127–2140.

Akrad, O. M., Miskimins, J. L., and Prasad, M. (2011). The effects of fracturing fluids on shale rock mechanical properties and proppant embedment. *SPE Annual Technical Conference and Exhibition*. https://doi.org/10.2118/146658-MS

Al-Khdheeawi, E. A., Vialle, S., Barifcani, A., Sarmadivaleh, M., and Iglauer, S. (2017). Impact of reservoir wettability and heterogeneity on CO_2-plume migration and trapping capacity. *International Journal of Greenhouse Gas Control*, *58*, 142–158. https://doi.org/10.1016/j.ijggc.2017.01.012

Algive, L., Bekri, S., Lerat, O., Nader, F., and Vizika, O. (2009). Reactive pore network modeling technology to evaluate the impact of diagenesis on the petrophysical properties of a rock. *Society of Petroleum Engineers - International Petroleum Technology Conference 2009, IPTC 2009*, *5*, 3452–3461. https://doi.org/10.2523/iptc-14049-ms

Algive, L., Békri, S., Nader, F. H., Lerat, O., and Vizika, O. (2012). Impact of diagenetic alterations on the petrophysical and multiphase flow properties of carbonate rocks using a reactive pore network modeling approach. *Oil & Gas Science and Technology – Revue d'IFP Energies Nouvelles*, *67*(1), 147–160. https://doi.org/10.2516/ogst/2011171

Alramahi, B., and Sundberg, M. I. (2012). Proppant embedment and conductivity of hydraulic fractures in shales. *International Journal of Engineering Science*, *77*, 14–23. https://doi.org/10.1016/j.ijengsci.2013.12.005

Austin, L. G. (1999). A discussion of equations for the analysis of batch grinding data. *Powder Technology*, *106*(1–2), 71–77. https://doi.org/10.1016/S0032-5910(99)00047-9

Babakhani, P., Bridge, J., Doong, R. an, and Phenrat, T. (2017). Continuum-based models and concepts for the transport of nanoparticles in saturated porous media: A state-of-the-science review. *Advances in Colloid and Interface Science*, *246*(June), 75–104. https://doi.org/10.1016/j.cis.2017.06.002

Bachu, S. (2000). Sequestration of CO_2 in geological media: criteria and approach for site selection in response to climate change. *Energy Conversion & Management*, *41*, 953–970.

Bachu, S. (2015). Review of CO_2 storage efficiency in deep saline aquifers. *International Journal of Greenhouse Gas Control*, *40*, 188–202. https://doi.org/10.1016/j.ijggc.2015.01.007

Bachu, S., Bonijoly, D., Bradshaw, J., Burruss, R., Holloway, S., Christensen, N. P., and Mathiassen, O. M. (2007). CO_2 storage capacity estimation: Methodology and gaps. *International Journal of Greenhouse Gas Control*, *1*(4), 430–443. https://doi.org/10.1016/S1750-5836(07)00086-2

Bachu, S., Gunter, W. D., and Perkins, E. H. (1994). Aquifer disposal of CO_2: hydrodynamic and mineral trapping. *Energy Conversion and Management*, *35*(4), 269–279.

Balhoff, M. T., Thompson, K. E., and Hjortsø, M. (2007). Coupling pore-scale networks to continuum-scale models of porous media. *Computers and Geosciences*, *33*(3), 393–410. https://doi.org/10.1016/j.cageo.2006.05.012

Barree and Associates LLC. (2017). GOFHER 3D User manual. Retrieved from https://www.barree.net/gofher.html

Basbug, B., Gumrah, F., and Oz, B. (2005). Simulating the effects of deep saline aquifer properties in CO_2 sequestration. In *6th Canadian International Petroleum Conference, Petroleum Society* (pp. 1–15).

Bauer, D., Goyeau, B., and Gobin, D. (2008). Large particle transport in porous media: effect of pore plugging on the macroscopic transport properties. *Journal of Porous Media*, *11*(4), 343–360.

Baz, H., Noureldin, M., Allinson, W. G., and Cinar, Y. (2016). A field-scale investigation of residual and dissolution trapping of CO_2 in a saline formation in Western Australia. *International Journal of Greenhouse Gas Control*, *46*, 86–99. https://doi.org/10.1016/j.ijggc.2015.12.032

Bazin, B., Bekri, S., Vizika, O., Herzhaft, B., and Aubry, E. (2010). Fracturing in tight gas reservoirs: Application of special-core-analysis methods to investigate formation-damage mechanisms. *SPE Journal*, *15*(4), 975–982. https://doi.org/10.2118/112460-pa

Beaubien, S. E., Jones, D. G., Gal, F., Barkwith, A. K. A. P., Braibant, G., Baubron, J. C., … Strutt, M. H. (2013). Monitoring of near-surface gas geochemistry at the Weyburn, Canada, CO_2-EOR site, 2001-2011. *International Journal of Greenhouse Gas Control*, *16*(1), S236–S262. https://doi.org/10.1016/j.ijggc.2013.01.013

Bedrikovetsky, P., Santos, A., Siqueira, A., Souza, A. L., and Shecaira, F. (2003). A stochastic model for deep bed filtration and well impairment. In *SPE European Formation Damage Conference* (pp. 1–15). The Hague. https://doi.org/10.2523/82230-ms

Bedrikovetsky, P., Siqueira, F. D., Furtado, C., and De Souza, A. L. S. (2010). Quantitative theory for fines migration and formation damage. *Proceedings - SPE International Symposium on Formation Damage Control*, *2*, 1041–1062. https://doi.org/10.2118/128384-ms

Benson, S., and Cook, P. (2005). Undergroung geological storage. In *Carbon Dioxide Capture and Storage* (pp. 195–265).

Benson, S. M., and Cole, D. R. (2008). CO_2 sequestration in deep sedimentary formations. *Elements*, *4*(5), 325–331. https://doi.org/10.2113/gselements.4.5.325

Benson, S. M., Hoversten, M., Gasperikova, E., and Haines, M. (2005). Monitoring protocols and life-cycle costs for geologic storage of carbon dioxide. *Greenhouse Gas Control Technologies*, (510), 1259–1264. https://doi.org/10.1016/B978-008044704-9/50136-1

Berger, G., Lacharpagne, J. C., Velde, B., Beaufort, D., and Lanson, B. (1997). Kinetic constraints on illitization reactions and the effects of organic diagenesis in sandstone/shale sequences. *Applied Geochemistry*, *12*(1), 23–35. https://doi.org/10.1016/S0883-2927(96)00051-0

Bernabé, Y., Mok, U., and Evans, B. (2003). Permeability-porosity relationships in rocks subjected

to various evolution processes. *Pure and Applied Geophysics*, *160*, 2011. https://doi.org/10.1007/978-3-0348-8083-1_9

Berner, R. A. (1980a). Diagenetic chemical processes II : precipitation, dissolution, and authigenic processes. In *Early Diagenesis* (pp. 90–132).

Berner, R. A. (1980b). General theory. In *Early Diagenesis* (pp. 9–14).

Berner, R. A., and Holdren, G. R. (1977). Mechanism of feldspar weathering-II. Observations of feldspars from soils. *Geochimica et Cosmochimica Acta*, *43*, 1173–1186.

Birkholzer, J. T., Zhou, Q., and Tsang, C. (2009). Large-scale impact of CO_2 storage in deep saline aquifers: a sensitivity study on pressure response in stratified systems. *Greenhouse Gas Control*, *3*, 181–194.

Black, J. R., Carroll, S. A., and Haese, R. R. (2015). Rates of mineral dissolution under CO_2 storage conditions. *Chemical Geology*, *399*, 134–144. https://doi.org/10.1016/j.chemgeo.2014.09.020

Blatt, H. (1979). Diagenetic processes in sandstones. *SEPM Special Publication*, *26*, 141–157.

Blunt, M. J., Bijeljic, B., Dong, H., Gharbi, O., Iglauer, S., Mostaghimi, P., … Pentland, C. (2013). Pore-scale imaging and modelling. *Advances in Water Resources*, *51*, 197–216. https://doi.org/10.1016/j.advwatres.2012.03.003

Bradshaw, J., Bachu, S., Bonijoly, D., Burruss, R., Holloway, S., Christensen, N. P., and Mathiassen, O. M. (2007). CO_2 storage capacity estimation: Issues and developedment of standards. *International Journal of Greenhouse Gas Control*, *1*(1), 62–68.

Brennan, S. W. (2016). Integrated characterization of Middle Bakken diagenesis, Williston Basin, North Dakota, U.S.A. *Colorado School of Mines, Master's Thesis*.

Bryant, S. L., King, P. R., and Mellor, D. W. (1993). Network model evaluation of permeability and spatial correlation in a real random sphere packing. *Transport in Porous Media*, *11*(1), 53–70. https://doi.org/10.1007/BF00614635

Budek, A., and Szymczak, P. (2012). Network models of dissolution of porous media. *Physical Review E - Statistical, Nonlinear, and Soft Matter Physics*, *86*(5), 1–16. https://doi.org/10.1103/PhysRevE.86.056318

Burley, S. D., Kantorowicz, J. D., and Waugh, B. (1985). Clastic diagenesis. *Geological Society, London, Special Publications*, *18*(1), 189–226.

Burnside, N. M., and Naylor, M. (2014). Review and implications of relative permeability of CO_2/brine systems and residual trapping of CO2. *International Journal of Greenhouse Gas Control*, *23*, 1–11. https://doi.org/10.1016/j.ijggc.2014.01.013

Cai, Z., Wen, H., Komarneni, S., and Li, L. (2018). Mineralogy controls on reactive transport of Marcellus Shale waters. *Science of the Total Environment*, *630*, 1573–1582. https://doi.org/10.1016/j.scitotenv.2018.02.223

Cao, C., Liao, J., Hou, Z., Wang, G., Feng, W., and Fang, Y. (2020). Parametric uncertainty analysis for CO_2 sequestration based on distance correlation and support vector regression.

Journal of Natural Gas Science and Engineering, *77*(August 2019), 103237. https://doi.org/10.1016/j.jngse.2020.103237

Cardott, B. J. (2013). Woodford Shale: from hydrocarbon source rock to reservoir. In *AAPG Woodford Shale Forum*. Tulsa. OK.

Cardott, Brian J. (2012). Thermal maturity of Woodford Shale gas and oil plays, Oklahoma, USA. *International Journal of Coal Geology*, *103*, 109–119. https://doi.org/10.1016/j.coal.2012.06.004

Chadwick, R. A., Arts, R., Bentham, M., Eiken, O., Holloway, S., Kirby, G. A., … Zweigel, P. (2009). Review of monitoring issues and technologies associated with the long-term underground storage of carbon dioxide. *Geological Society Special Publication*, *313*, 257–275. https://doi.org/10.1144/SP313.15

Chalmers, G. R., Bustin, R. M., and Power, I. M. (2012). Characterization of gas shale pore systems by porosimetry, pycnometry, surface area, and field emission scanning electron microscopy/transmission electron microscopy image analyses: Examples from the Barnett, Woodford, Haynesville, Marcellus, and Doig uni. *AAPG Bulletin*, *96*(6), 1099–1119.

Chilingarian, G. V., and Wolf, K. H. (1988). Ore-related diagenesis - An encyclopedic review. In *Diagenesis I* (pp. 25–470).

Choquette, P. W., and Pray, L. C. (1970). Geologic nomenclature and classification of porosity in sedimentary carbonates. *The American Association of Petroleum Geologists*, *54 (2)*, 207–250.

Civan, F. (2007). Particulate processes in porous media. In *Reservoir Formation Damage* (pp. 191–234). https://doi.org/10.1016/b978-075067738-7/50009-9

Clark, I. (2015). Geochemical reactions. In *Groundwater Geochemistry and Isotopes* (pp. 61–96).

Comer, J. B. (2008). Woodford Shale in Southern Midcontinent, USA-transgressive system tract marine source rocks on an arid passive continental margin with persistent oceanic upwelling. In *AAPG Annual Convention and Exhibition*, San Antonio, TX, Poster, 3 panels.

Craig, J. R., and Vaughan, D. J. (1994). *Paragenesis, formation conditions, and fluid inclusion geothermometry of ores*. *Ore microscopy and ore petrology*.

Cramer, D. D. (2005). Fracture skin: A primary cause of stimulation ineffectiveness in gas wells. *SPE Eastern Regional Meeting*. SPE 96869.

Curtis, C. D. (1983). Geochemistry of porosity enhancement and reduction in clastic sediments. *Geological Society Special Publication*, *12*(1), 113–125. https://doi.org/10.1144/GSL.SP.1983.012.01.12

Curtis, C. D. (1985). Clay mineral precipitation and transformation during burial diagenesis. *Philosophical Transactions of the Royal Society of London, A315*, 91–105.

Dana, E., and Skoczylas, F. (2002). Experimental study of two-phase flow in three sandstones. II. Capillary pressure curve measurement and relative permeability pore space capillary models. *International Journal of Multiphase Flow*, *28*(12), 1965–1981.

https://doi.org/10.1016/S0301-9322(02)00091-5

De Boever, E., Varloteaux, C., Nader, F. H., Foubert, A., Békri, S., Youssef, S., and Rosenberg, E. (2012). Quantification and prediction of the 3D pore network evolution in carbonate reservoir rocks. *Oil and Gas Science and Technology*, *67*(1), 161–178. https://doi.org/10.2516/ogst/2011170

De Silva, G. P. D., Ranjith, P. G., and Perera, M. S. A. (2015). Geochemical aspects of CO_2 sequestration in deep saline aquifers: A review. *Fuel*, *155*, 128–143. https://doi.org/10.1016/j.fuel.2015.03.045

Dees, J. M., and Coulter, G. R. (1986). Fracturing treatment quality control: results of a three-year survey. *SPE Annual Technical Conference and Exhibition, SPE 15512*.

Deng, H., Stauffer, P. H., Dai, Z., Jiao, Z., and Surdam, R. C. (2012). Simulation of industrial-scale CO_2 storage: Multi-scale heterogeneity and its impacts on storage capacity, injectivity and leakage. *International Journal of Greenhouse Gas Control*, *10*, 397–418. https://doi.org/10.1016/j.ijggc.2012.07.003

Deutsch, C. V, and Journel, A. G. (1998). *GSLIB Geostatistical software library and user's guide*.

Diao, Y., Zhu, G., Li, X., Bai, B., Li, J., Wang, Y., … Zhang, B. (2020). Characterizing CO_2 plume migration in multi-layer reservoirs with strong heterogeneity and low permeability using time-lapse 2D VSP technology and numerical simulation. *International Journal of Greenhouse Gas Control*, *92*(October 2019), 102880. https://doi.org/10.1016/j.ijggc.2019.102880

Ding, S., Xi, Y., Jiang, H., and Liu, G. (2018). CO_2 storage capacity estimation in oil reservoirs by solubility and mineral trapping. *Applied Geochemistry*, *89*(September 2017), 121–128. https://doi.org/10.1016/j.apgeochem.2017.12.002

Donaldson, E. C., Baker, B. A., and Carroll, H. B. (1977). Particle transport in sandstones. In *SPE Annual Technical Conference and Exhibition* (Vol. SPE 6905, pp. 1–20). Denver, Colorado. https://doi.org/10.2523/6905-ms

Doughty, C., Benson, S. M., Pruess, K., and Green, C. T. (2001). Capacity Investigation of Brine-Bearing Sands of the Frio Formation for Geologic Sequestration of CO_2. *Proceedings of First National Conference on Carbon Sequestration*, (January), 14–17.

Duenckel, R., Conway, M. W., Eldred, B., and Vincent, M. C. (2011). Proppant diagenesis-integrated analyses provide new insights into origin , occurrence , and implications for proppant performance. *SPE Hydraulic Fracturing Technology Conference*, *SPE-139875*. https://doi.org/10.2118/139875-MS

Elmore, R. D., Heij, G. W., and Wickard, A. K. (2016). Paragenesis of mineralized fractures and diagenesis of prominent North American shales. *The Sedimentary Record*, *14*, 4–10.

Eveline, V. F., Akkutlu, I. Y., and Moridis, G. J. (2017). Numerical simulation of hydraulic fracturing water effects on shale gas permeability alteration. *Transport in Porous Media*, *116*(2), 727–752. https://doi.org/10.1007/s11242-016-0798-4

Ezeakacha, C. P., Salehi, S., and Hayatdavoudi, A. (2017). Experimental study of drilling fluid's

filtration and mud cake evolution in sandstone formations. *Journal of Energy Resources Technology*, *139*(2), 1–8. https://doi.org/10.1115/1.4035425

Fang, Y., Baojun, B., Dazhen, T., Dunn-Norman, S., and Wronkiewicz, D. (2010). Characteristics of CO_2 sequestration in saline aquifers. *Petroleum Science*, *7*(1), 83–92. https://doi.org/10.1007/s12182-010-0010-3

Farah, N., Ding, D. Y., and Wu, Y. S. (2015). Simulation of the impact of fracturing fluid induced formation damage in shale gas reservoirs. *Society of Petroleum Engineers - SPE Reservoir Simulation Symposium 2015*, *2*, 1266–1284. https://doi.org/10.2118/173264-ms

Fatt, I. (1956). The network model of porous media. *Petroleum Transactions, AIME*, *207*(01), 144–181.

Fenghour, A., Wakeham, W. A., and Vesovic, V. (1998). The viscosity of carbon dioxide. *Journal of Physical and Chemical Reference Data*, *27*(1), 31–44. https://doi.org/10.1063/1.556013

Fessenden, J. E., Clegg, S. M., Rahn, T. A., Humphries, S. D., and Baldridge, W. S. (2010). Novel MVA tools to track CO_2 seepage, tested at the ZERT controlled release site in Bozeman, MT. *Environmental Earth Sciences*, *60*(2), 325–334. https://doi.org/10.1007/s12665-010-0489-3

Fitts, C. (2002). Groundwater chemistry. In *Groundwater Science* (pp. 279–338). Elsevier Science.

Flett, M., Gurton, R., and Weir, G. (2007). Heterogeneous saline formations for carbon dioxide disposal: Impact of varying heterogeneity on containment and trapping. *Journal of Petroleum Science and Engineering*, *57*(1–2), 106–118. https://doi.org/10.1016/j.petrol.2006.08.016

Flügel, E. (2013). Diagenesis, porosity and dolomitization. In *Microfacies of Carbonate Rocks* (pp. 267–338). Springer. https://doi.org/978-3-662-08726-8

Freifeld, B. M., Daley, T. M., Hovorka, S. D., Henninges, J., Underschultz, J., and Sharma, S. (2009). Recent advances in well-based monitoring of CO_2 sequestration. *Energy Procedia*, *1*(1), 2277–2284. https://doi.org/10.1016/j.egypro.2009.01.296

Freifeld, B. M., Trautz, R. C., Kharaka, Y. K., Phelps, T. J., Myer, L. R., Hovorka, S. D., and Collins, D. J. (2005). The U-tube: A novel system for acquiring borehole fluid samples from a deep geologic CO_2 sequestration experiment. *Journal of Geophysical Research: Solid Earth*, *110*(10), 1–10. https://doi.org/10.1029/2005JB003735

French, L. B. (2015). Multiscale modeling of particle transport in petroleum reservoirs. *Louisiana State University, Master's Thesis*.

Friedmann, S. J. (2007). *Carbon capture and sequestration technologies: Status and Future Deployment*. Retrieved from https://e-reports-ext.llnl.gov/pdf/353346.pdf

Gardner, R. P., and Austin, L. G. (1962). A chemical engineering treatment of batch grinding. *Proc. 1st European Symposium on Size Reduction*.

Gasda, S. E., Nordbotten, J. M., and Celia, M. A. (2012). Application of simplified models to CO_2 migration and immobilization in large-scale geological systems. *International Journal of Greenhouse Gas Control*, *9*, 72–84. https://doi.org/10.1016/j.ijggc.2012.03.001

Gaus, I. (2010). Role and impact of CO_2-rock interactions during CO_2 storage in sedimentary

rocks. *International Journal of Greenhouse Gas Control*, *4*(1), 73–89. https://doi.org/10.1016/j.ijggc.2009.09.015

Gaus, I., Audigane, P., Andre, L., Lions, J., Jacquemet, N., Durst, P., … Azaroual, M. (2008). Geochemical and solute transport modelling for CO_2 storage, What to expect from it ? *International Journal of Greenhouse Gas Control*, *2*(4), 605–625. https://doi.org/10.1016/j.ijggc.2008.02.011

Gdanski, R., Weaver, J., Slabaugh, B., Walters, H., and Parker, M. (2005). Fracture face damage – it matters. *SPE European Formation Damage Conference, SPE 94649*. https://doi.org/10.2118/94649-MS

Giles, M. R., and Marshall, J. D. (1986). Constraints on the development of secondary porosity in the subsurface : re-evaluation of processes. *Marine and Petroleum Geology*, *3*, 243–255.

Global CCS Institute. (2019). *Global Status of CCS. Targeting Climate Change*. *Status Report*. https://doi.org/10.1007/springerreference_15392

Goldberg, D. S., Takahashi, T., and Slagle, A. L. (2008). Carbon dioxide sequestration in deep-sea basalt. *Proceedings of the National Academy of Sciences of the United States of America*, *105*(29), 9920–9925. https://doi.org/10.1073/pnas.0804397105

Goodman, A., Hakala, A., Bromhal, G., Deel, D., Rodosta, T., Frailey, S., … Guthrie, G. (2011). U.S. DOE methodology for the development of geologic storage potential for carbon dioxide at the national and regional scale. *International Journal of Greenhouse Gas Control*, *5*(4), 952–965. https://doi.org/10.1016/j.ijggc.2011.03.010

Gunter, W. D., Wong, S., Cheel, D. B., and Sjostrom, G. (1998). Large CO_2 sinks: Their role in the mitigation of greenhouse gases from an international, national (Canadian) and provincial (Alberta) perspective. *Applied Energy*, *61*, 209–227. https://doi.org/10.1016/S0306-2619(98)00042-7

Han, J., Wang, J. Y., and Puri, V. (2016). A fully coupled geomechanics and fluid flow model for proppant pack failure and fracture conductivity damage analysis. *Journal of Natural Gas Science and Engineering*, *31*, 546–554. https://doi.org/10.1016/j.jngse.2016.03.034

Hannis, S. D. (2013). Monitoring the geological storage of CO_2. In *Geological Storage of Carbon Dioxide (CO_2): Geoscience, Technologies, Environmental Aspects and Legal Frameworks* (pp. 68–96). Woodhead Publishing Limited. https://doi.org/10.1533/9780857097279.1.68

Harris, P. M., Kendall, C. G. S. C., and Lerchei, I. (1985). Carbonate cementation - A brief review. *SEPM Special Publication*, *36*, 79–95.

Hassanzadeh, H., Pooladi-Darvish, M., and Keith, D. W. (2005). Modelling of convective mixing in CO_2 storage. *Journal of Canadian Petroleum Technology*, *44*(10), 43–51.

Hayes, J. B. (1979). Sanstone diagenesis - The Hole Truth. *SEPM*, *26*, 127–139.

Heidari, P., Li, L., Jin, L., Williams, J. Z., and Brantley, S. L. (2017). A reactive transport model for Marcellus shale weathering. *Geochimica et Cosmochimica Acta*, *217*, 421–440. https://doi.org/10.1016/j.gca.2017.08.011

Herzig, J. P., Leclerc, D. M., and Le Goff, P. L. (1970). Flow of suspensions through porous media— application to deep filtration. *Industrial and Engineering Chemistry*, *62*(5), 8–35. https://doi.org/10.1021/ie50725a003

Hirschfelder, J. O., Byron Bird, R., and Spotz, E. L. (1949). The transport properties of gases and gaseous mixtures II. *Chemical Reviews*, *44*(1), 205–231.

Holloway, S. (1997). An overview of the underground disposal of carbon dioxide. *Energy Conversion and Management*, *38*, 193–198. https://doi.org/10.1016/s0196-8904(96)00268-3

Hossain, M. M., and Rahman, M. K. (2008). Numerical simulation of complex fracture growth during tight reservoir stimulation by hydraulic fracturing. *Journal of Petroleum Science and Engineering*, *60*(2), 86–104. https://doi.org/10.1016/j.petrol.2007.05.007

Hovorka, S. D., Benson, S. M., Doughty, C., Freifeld, B. M., Sakurai, S., Daley, T. M., … Knauss, K. G. (2006). Measuring permanence of CO_2 storage in saline formations: The Frio experiment. *Environmental Geosciences*, *13*(2), 105–121. https://doi.org/10.1306/eg.11210505011

Hurter, S., Labregere, D., and Berge, J. (2007). Simulations for CO_2 injection projects with compositional simulator. *Offshore Europe Conference - Proceedings*, 214–220. https://doi.org/10.2523/108540-ms

Idowu, N. A. (2009). Pore-scale modeling: stochastic network generation and modeling of rate effects in waterflooding. *Imperial College of London, PhD diss.*, (July). Retrieved from http://workspace.imperial.ac.uk/earthscienceandengineering/public/external/Research/PERM/Nasiru Idowu - PhD thesis.pdf

Iglauer, S. (2011). Dissolution trapping of carbon dioxide in reservoir formation brine – A carbon storage mechanism. *Mass Transfer - Advanced Aspects*, 233–262. https://doi.org/10.5772/20206

Imdakm, A. O., and Sahimi, M. (1987). Transport of large particles in flow through porous media. *Physical Review*, *36*(11), 5304–5309.

Imdakm, A. O., and Sahimi, M. (1991). Computer simulation of particle transport processes in flow through porous media. *Chemical Engineering Science*, *46*(8), 1977–1993. https://doi.org/10.1016/0009-2509(91)80158-U

Intergovernmental Panel of Climate Change. (2005). *Carbon dioxide capture and storage*. https://doi.org/10.1016/S0022-3476(75)80125-9

Ison, C. R., and Ives, K. J. (1969). Removal mechanisms in deep bed filtration. *Chemical Engineering Science*, *24*(4), 717–729. https://doi.org/10.1016/0009-2509(69)80064-3

Ives, K. J. (1985). Deep bed filters. In *Mathematical models and design methods in solid-liquid separation* (pp. 90–149). Springer.

Jayasekara, D. W., Ranjith, P. G., Wanniarachchi, W. A. M., and Rathnaweera, T. D. (2020). Understanding the chemico-mineralogical changes of caprock sealing in deep saline CO_2 sequestration environments: A review study. *Journal of Supercritical Fluids*, *161*, 104819. https://doi.org/10.1016/j.supflu.2020.104819

Jenkins, C., Chadwick, A., and Hovorka, S. D. (2015). The state of the art in monitoring and verification - Ten years on. *International Journal of Greenhouse Gas Control*, *40*, 312–349. https://doi.org/10.1016/j.ijggc.2015.05.009

Ji, L., Settari, A., and Sullivan, R. B. (2009). A novel hydraulic fracturing model fully coupled with geomechanics and reservoir simulation. *SPE Journal*, *14*(03), 423–430. https://doi.org/10.2118/110845-PA

Jin, M., Ribeiro, A., Mackay, E., Guimarães, L., and Bagudu, U. (2016). Geochemical modelling of formation damage risk during CO_2 injection in saline aquifers. *Journal of Natural Gas Science and Engineering*, *35*, 703–719. https://doi.org/10.1016/j.jngse.2016.08.030

Johnson, K. S. (1989). Geologic evolution of the Anadarko Basin. *Oklahoma Geological Survey Circular*, *90*, 3–12.

Jones, D. G., Lister, T. R., Smith, D. J., West, J. M., Coombs, P., Gadalia, A., … Lombardi, S. (2011). In Salah gas CO_2 storage JIP: Surface gas and biological monitoring. *Energy Procedia*, *4*, 3566–3573. https://doi.org/10.1016/j.egypro.2011.02.285

Juanes, R., Spiteri, E. J., Orr, F. M., and Blunt, M. J. (2006). Impact of relative permeability hysteresis on geological CO_2 storage. *Water Resources Research*, *42*(12), 1–13. https://doi.org/10.1029/2005WR004806

Karstens, J., Ahmed, W., Berndt, C., and Class, H. (2017). Focused fluid flow and the sub-seabed storage of CO_2: Evaluating the leakage potential of seismic chimney structures for the Sleipner CO_2 storage operation. *Marine and Petroleum Geology*, *88*(2017), 81–93. https://doi.org/10.1016/j.marpetgeo.2017.08.003

Katsube, T. J., and Williamson, M. (1994). Effects of diagenesis on shale nano-pore structure and implications for sealing capacity. *Clay Minerals*, *29*(4), 451–461. https://doi.org/10.1180/claymin.1994.029.4.05

Kim, D., Peters, C. A., and Lindquist, W. B. (2011). Upscaling geochemical reaction rates accompanying acidic CO_2-saturated brine flow in sandstone aquifers. *Water Resources Research*, *47*(1), 1–16. https://doi.org/10.1029/2010WR009472

King, G. E. (2012). Hydraulic fracturing 101: what every representative, environmentalist, regulator, reporter, investor, university researcher, neighbor, and engineer should know about hydraulic fracturing risk. *Journal of Petroleum Technology*, *64*(04), 34–42. https://doi.org/10.2118/0412-0034-jpt

Kirkland, D. W., Denison, R. E., Summers, D. M., Gormly, J. R., Johnson, K. S., and Cardott, B. J. (1992). Geology and organic geochemistry of the Woodford Shale in the Criner Hills and Western Arbuckle Mountains, Oklahoma. *Oklahoma Geological Survey Circular*, *93*, 38–69.

Kopp, A., Class, H., and Helmig, R. (2009a). Investigations on CO_2 storage capacity in saline aquifers-Part 2: Estimation of storage capacity coefficients. *International Journal of Greenhouse Gas Control*, *3*(3), 277–287. https://doi.org/10.1016/j.ijggc.2008.10.001

Kopp, A., Class, H., and Helmig, R. (2009b). Investigations on CO_2 storage capacity in saline aquifers. Part 1. Dimensional analysis of flow processes and reservoir characteristics. *International Journal of Greenhouse Gas Control*, *3*(3), 263–276.

https://doi.org/10.1016/j.ijggc.2008.10.002

Kothamasu, R., Das, P., and Karadkar, P. (2012). Exploring and evaluating eastern hemisphere proppants in fracturing applications. *Proceedings of SPE Saudi Arabia Section Technical Symposium and Exhibition*, 1–10. https://doi.org/10.2118/160858-MS

Krevor, S. C. M., Pini, R., Zuo, L., and Benson, S. M. (2012). Relative permeability and trapping of CO_2 and water in sandstone rocks at reservoir conditions. *Water Resources Research*, *48*(2), 1–16. https://doi.org/10.1029/2011WR010859

Lagneau, V., Pipart, A., and Catalette, H. (2005). Reactive Transport Modeling of CO_2 Sequestration in Deep Saline Aquifers. *Oil and Gas Science and Technology*, *60*(2), 231–247.

Lasaga, A. C. (2014). Transition State Theory. In *Kinetic Theory in the Earth Sciences* (pp. 152–219). https://doi.org/10.5860/choice.36-4499

Laughrey, C. D., and Purrazzella, P. F. (2016). Petroleum Geochemistry and Mudstone Diagenesis of the Woodford Shale Anadarko Basin, USA: An integrated approach: *AAPG Datapages/Search and Discovery Article 90283*.

Le Gallo, Y., Bildstein, O., and Brosse, E. (1998). Coupled reaction-flow modeling of diagenetic changes in reservoir permeability, porosity and mineral compositions. *Journal of Hydrology*, *209*(1–4), 366–388. https://doi.org/10.1016/S0022-1694(98)00183-8

Lengler, U., De Lucia, M., and Kühn, M. (2010). The impact of heterogeneity on the distribution of CO_2: numerical simulation of storage at Ketzin. *International Journal of Greenhouse Gas Control*, (4), 1016–1020.

Li, L. C., Tang, C. A., Li, G., Wang, S. Y., Liang, Z. Z., and Zhang, Y. B. (2012). Numerical simulation of 3D hydraulic fracturing based on an improved flow-stress-damage model and a parallel FEM technique. *Rock Mechanics and Rock Engineering*, *45*(5), 801–818. https://doi.org/10.1007/s00603-012-0252-z

Li, L., Peters, C. A., and Celia, M. A. (2006). Upscaling geochemical reaction rates using pore-scale network modeling. *Advances in Water Resources*, *29*, 1351–1370. https://doi.org/10.1016/j.advwatres.2005.10.011

Li, L., Peters, C. A., and Celia, M. A. (2007). Applicability of averaged concentrations in determining geochemical reaction rates in heterogeneous porous media. *American Journal of Science*, *307*(10), 1146–1166. https://doi.org/10.2475/10.2007.02

Lichtner, P. C. (1996). Continuum formulation of multicomponent-multiphase reactive transport. *Reviews in Mineralogy*, *34*, 1–81.

Loucks, R. G., Dodge, M. M., and Galloway, W. E. (1984). Regional controls on diagenesis and reservoir quality in lower tertiary sandstones along the Texas Gulf Coast. In *Clastic Diagenesis* (pp. 15–45). AAPG.

Loucks, R. G., Reed, R. M., Ruppel, S. C., and Hammes, U. (2012). Spectrum of pore types and networks in mudrocks and a descriptive classification for matrix-related mudrock pores. *AAPG Bulletin*, *96*(6), 1071–1098. https://doi.org/10.1306/08171111061

Lu, W., Guo, H., Chou, I. M., Burruss, R. C., and Li, L. (2013). Determination of diffusion coefficients of carbon dioxide in water between 268 and 473 K in a high-pressure capillary optical cell with in situ Raman spectroscopic measurements. *Geochimica et Cosmochimica Acta*, *115*, 183–204. https://doi.org/10.1016/j.gca.2013.04.010

Mac Dowell, N., Fennell, P. S., Shah, N., and Maitland, G. C. (2017). The role of CO_2 capture and utilization in mitigating climate change. *Nature Climate Change*, *7*(4), 243–249. https://doi.org/10.1038/nclimate3231

Marongiu-Porcu, M., and Economides, M. J. (2008). Economic and physical optimization of hydraulic fracturing. *SPE International Symposium and Exhibition on Formation Damage Control*, *SPE 111793*(February).

Martens, S., Conze, R., De Lucia, M., Henninges, J., Kempka, T., Liebscher, A., … ... (2015). Joint Research Project CO2MAN (CO2MAN Reservoir Management): Continuation of research and development work for CO_2 storage at the Ketzin Pilot site. In *Geological Storage of CO_2 – Long Term Security Aspects* (pp. 1–32).

Matter, J. M., Takahashi, T., and Goldberg, D. (2007). Experimental evaluation of in situ CO_2-water-rock reactions during CO_2 injection in basaltic rocks: Implications for geological CO_2 sequestration. *Geochemistry, Geophysics, Geosystems*, *8*(2). https://doi.org/10.1029/2006GC001427

McDowell-Boyer, L. M., Hunt, J. R., and Sitar, N. (1986). Particle transport through porous media. *Water Resources Research*, *22*(13), 1901–1921.

McGrail, B. P., Schaef, H. T., Ho, A. M., Chien, Y. J., Dooley, J. J., and Davidson, C. L. (2006). Potential for carbon dioxide sequestration in flood basalts. *Journal of Geophysical Research: Solid Earth*, *111*(12), 1–13. https://doi.org/10.1029/2005JB004169

Mehmani, Y., Sun, T., Balhoff, M. T., Eichhubl, P., and Bryant, S. (2012). Multiblock pore-scale modeling and upscaling of reactive transport: application to carbon sequestration. *Transport in Porous Media*, *95*(2), 305–326. https://doi.org/10.1007/s11242-012-0044-7

Meng, X., and Yang, D. (2019). Pore-network modeling of particle dispersion in porous media. *Colloids and Surfaces A: Physicochemical and Engineering Aspects*, *580*(August), 123768. https://doi.org/10.1016/j.colsurfa.2019.123768

Miceli Romero, A., and Philp, R. P. (2012). Organic geochemistry of the Woodford Shale, Southeastern Oklahoma: How variable can shales be? *AAPG Bulletin*, *96*(3), 493–517.

Michael, K., Golab, A., Shulakova, V., Ennis-King, J., Allinson, G., Sharma, S., and Aiken, T. (2010). Geological storage of CO_2 in saline aquifers-A review of the experience from existing storage operations. *International Journal of Greenhouse Gas Control*, *4*(4), 659–667. https://doi.org/10.1016/j.ijggc.2009.12.011

Milliken, K. L. (2003). Late diagenesis and mass transfer in sandstone-shale sequences. *Treatise on Geochemistry*, *7–9*, 159–190. https://doi.org/10.1016/B0-08-043751-6/07091-2

Milliken, K. L., and Day-Stirrat, R. J. (2013). Cementation in mudrocks: brief review with examples from cratonic basin mudrocks. In *Critical Assesment of Shale Resource Plays: AAPG Memoir 103* (pp. 133–150). AAPG.

Miri, R., and Hellevang, H. (2016). Salt precipitation during CO_2 storage-A review. *International Journal of Greenhouse Gas Control*, *51*, 136–147. https://doi.org/10.1016/j.ijggc.2016.05.015

Mohan, K., Scott, K. D., Monson, G. D., and Paul, A. (2013). A systematic approach to understanding well performance in unconventional reservoirs : A Wolfcamp Case study, (August), 12–14.

Moore, C. H., and Wade, W. J. (2013a). *Burial diagenetic environment*. *Developments in Sedimentology* (Vol. 67). https://doi.org/10.1016/B978-0-444-53831-4.00010-0

Moore, C. H., and Wade, W. J. (2013b). The nature and classification of carbonate porosity. In *Developments in Sedimentology* (pp. 51–65). https://doi.org/10.1016/B978-0-444-53831-4.00004-5

Moosavi, S. A., Goshtasbi, K., Kazemzadeh, E., Bakhtiari, H. A., Esfahani, M. R., and Vali, J. (2014). Relationship between porosity and permeability with stress using pore volume compressibility characteristic of reservoir rocks. *Arabian Journal of Geosciences*, *7*(1), 231–239. https://doi.org/10.1007/s12517-012-0760-x

Morel, F., and Hering, J. (1993). *Principles and applications of aquatic chemistry*. John Wiley & Sons.

Newell, P., and Ilgen, A. G. (2019). Overview of geological carbon storage (GCS). *Science of Carbon Storage in Deep Saline Formations*, 1–13. https://doi.org/10.1016/b978-0-12-812752-0.00001-0

Nogues, J. P., Fitts, J. P., Celia, M. A., and Peters, C. A. (2013). Permeability evolution due to dissolution and precipitation of carbonates using reactive transport modeling in pore networks. *Water Resources Research*, *49*(9), 6006–6021. https://doi.org/10.1002/wrcr.20486

Noiriel, C., Steefel, C. I., Yang, L., and Ajo-Franklin, J. (2012). Upscaling calcium carbonate precipitation rates from pore to continuum scale. *Chemical Geology*, *318–319*, 60–74. https://doi.org/10.1016/j.chemgeo.2012.05.014

Nunes, M., Bedrikovetsky, P., Newbery, B., Paiva, R., Furtado, C., and de Souza, A. L. (2010). Theoretical definition of formation damage zone with applications to well stimulation. *Journal of Energy Resources Technology*, *132*(3), 033101. https://doi.org/10.1115/1.4001800

Ochi, J., and Vernoux, J. F. (1995). A two-dimensional network model for simulating permeability decrease during fluid injection into aquifers. In *Groundwater quality: remediation and protection* (pp. 279–287). Prague. https://doi.org/10.1016/0148-9062(95)92345-i

Ojha, S. P., Misra, S., Sinha, A., Dang, S., Tinni, A., Sondergeld, C., and Rai, C. (2017). Relative permeability and residual saturation estimates for organic-rich shale samples from Bakken, Wolfcamp, Eagle ford and Woodford formations. *Proceedings - SPE Annual Technical Conference and Exhibition*.

Okwen, R., Yang, F., and Frailey, S. (2014). Effect of geologic depositional environment on CO_2 storage efficiency. *Energy Procedia*, *63*, 5247–5257. https://doi.org/10.1016/j.egypro.2014.11.556

Øren, P. E., and Bakke, S. (2002). Process based reconstruction of sandstones and prediction of transport properties. *Transport in Porous Media*, *46*(2–3), 311–343. https://doi.org/10.1023/A:1015031122338

Øren, P. E., Bakke, S., and Arntzen, O. J. (1998). Extending predictive capabilities to network models. *SPE Journal*, *3*(4), 324–335. https://doi.org/10.2118/52052-pa

Osholake, T., Wang, J. Y., and Ertekin, T. (2011). Factors affecting hydraulically fractured well performances in the Marcellus shale gas reservoirs. *Society of Petroleum Engineers - SPE Americas Unconventional Gas Conference 2011, UGC 2011*, *135*(March 2013), 391–402. https://doi.org/10.1115/1.4007766

Park, Y. C., Huh, D. G., and Park, C. H. (2013). A sensitivity study of pressure monitoring to detect fluid leakage from geological CO_2 storage site. *Energy Procedia*, *37*, 4207–4214. https://doi.org/10.1016/j.egypro.2013.06.323

Patzek, T. W. (2001). Verification of a complete pore network simulator of drainage and imbibition. *SPE Journal*, *6*(02), 144–156. https://doi.org/10.2118/71310-PA

Patzek, T. W., and Silin, D. B. (2001). Shape factor and hydraulic conductance in noncircular capillaries: i. one-phase creeping flow. *Journal of Colloid and Interface Science*, *236*(2), 295–304. https://doi.org/10.1006/jcis.2000.7413

Payatakes, A. C., Tien, C., and Turian, R. M. (1973). A new model for granular porous media: Part I. Model formulation. *AIChE Journal*, *19*(1), 58–67. https://doi.org/10.1002/aic.690190110

Phan, T. N., Cronk, B. R., Almasoodi, M. M., and Reza, Z. A. (2018). Lithologic and geomechanical control on CO_2 huff-n-puff enhanced oil recovery processes using integrated modeling framework in Wolfcamp. *SPE/AAPG/SEG Unconventional Resources Technology Conference 2018, URTC 2018*. https://doi.org/10.15530/urtec-2018-2901346

Pittman, E. D. (1979). Porosity, diagenesis and productive capability of sandstone reservoirs. *SEPM Special Publication*, *26*, 159–173.

Plasynski, S. I., Litynski, J. T., McIlvried, H. G., Vikara, D. M., and Srivastava, R. D. (2011). The critical role of monitoring, verification, and accounting for geologic carbon dioxide storage projects. *Environmental Geosciences*, *18*(1), 19–34. https://doi.org/10.1306/eg.06231010008

Pommer, M., and Milliken, K. (2015). Pore types and pore-size distributions across thermal maturity, Eagle Ford Formation, Southern Texas. *AAPG Bulletin*, *99*(9), 1713–1744.

Pruess, K., Xu, T., Apps, J., and Garcia, J. (2001). Numerical modeling of aquifer disposal of CO_2. *Society of Petroleum Engineers - SPE/EPA/DOE Exploration and Production Environmental Conference 2001, EPEC 2001*, (1), 1–16. https://doi.org/10.2523/66537-ms

Purcell, W. R. (1949). Capillary pressures - their measurement using mercury and the calculation of permeability therefrom. *Journal of Petroleum Technology*, *1*(2), 39–48. https://doi.org/10.2118/949039-G

Rackley, S. A. (2010). Geological storage. In *Carbon Capture and Storage* (pp. 227–266). https://doi.org/10.1016/b978-1-85617-636-1.00011-0

Rafatian, N., Capsan, J., and Billiton, B. (2014). Petrophysical characterization of the pore space in Permian Wolfcamp rocks, *56*(1), 1–14.

Raoof, A., and Majid Hassanizadeh, S. (2010). A new method for generating pore-network models of porous media. *Transport in Porous Media*, *81*(1), 391–407. https://doi.org/10.1007/s11242-009-9412-3

Raza, A., Gholami, R., Sarmadivaleh, M., Tarom, N., Rezaee, R., Bing, C. H., … Elochukwu, H. (2016). Integrity analysis of CO_2 storage sites concerning geochemical-geomechanical interactions in saline aquifers. *Journal of Natural Gas Science and Engineering*, *36*, 224–240. https://doi.org/10.1016/j.jngse.2016.10.016

Rege, S. D., and Fogler, H. S. (1987). Network model for straining dominated particle entrapment in porous media. *Chemical Engineering Science*, *42*(7), 1553–1564. https://doi.org/10.1016/0009-2509(87)80160-4

Reinicke, A., Rybacki, E., Stanchits, S., Huenges, E., and Dresen, G. (2010). Hydraulic fracturing stimulation techniques and formation damage mechanisms-implications from laboratory testing of tight sandstone-proppant systems. *Chemie Der Erde*, *70*(SUPPL. 3), 107–117. https://doi.org/10.1016/j.chemer.2010.05.016

Rhodes, M. E., Bijeljic, B., and Blunt, M. J. (2008). Pore-to-field simulation of single-phase transport using continuous time random walks. *Advances in Water Resources*, *31*(12), 1527–1539. https://doi.org/10.1016/j.advwatres.2008.04.006

Roberts, J., Heij, G., and Elmore, R. D. (2019). Palaeomagnetic dating of hydrothermal alteration in the Woodford Shale, Oklahoma, USA. *Geological Magazine*, *156*(12), 2043–2052.

Roberts, J. J., Gilfillan, S. M. V., Stalker, L., and Naylor, M. (2017). Geochemical tracers for monitoring offshore CO_2 stores. *International Journal of Greenhouse Gas Control*, *65*(July), 218–234. https://doi.org/10.1016/j.ijggc.2017.07.021

Roberts, J. M., and Elmore., R. D. (2018). A diagenetic study of the Woodford Shale in the Southeastern Anadarko Basin, Oklahoma, USA: Evidence for Hydrothermal Alteration in Mineralized Fractures. *Interpretation*, *6*(1), SC1–SC13.

Rocha, A. C., Murad, M. A., and Le, T. D. (2017). A new model for flow in shale-gas reservoirs including natural and hydraulic fractures. *Computational Geosciences*, *21*(5–6), 1095–1117. https://doi.org/10.1007/s10596-017-9665-9

Rochelle, C. A., Czernichowski-Lauriol, I., and Milodowski, A. E. (2004). The impact of chemical reactions on CO_2 storage in geological formations: A brief review. *Geological Society Special Publication*, *233*, 87–106. https://doi.org/10.1144/GSL.SP.2004.233.01.07

Roded, R., Paredes, X., and Holtzman, R. (2018). Reactive transport under stress: Permeability evolution in deformable porous media. *Earth and Planetary Science Letters*, *493*, 198–207. https://doi.org/10.1016/j.epsl.2018.04.041

Rumpf, B., Nicolaisen, H., Öcal, C., and Maurer, G. (1994). Solubility of carbon dioxide in aqueous solutions of sodium chloride: Experimental results and correlation. *Journal of Solution Chemistry*, *23*(3), 431–448. https://doi.org/10.1007/BF00973113

Sakhaee-Pour, A., and Bryant, S. L. (2015). Pore structure of shale. *Fuel*, *143*, 467–475. https://doi.org/10.1016/j.fuel.2014.11.053

Sakthivadivel, R. (1969). Clogging of a granular porous medium by sediment. *Hydraulic Engineering Laboratory, College of Engineering, University of California.*, 106.

Salehi Mojarad, R., and Settari, A. (2007). Coupled numerical modeling of reservoir flow with formation plugging. *Journal of Canadian Petroleum Technology*, *46*(3), 54–59. https://doi.org/10.2118/2005-061

Sarkarfarshi, M., Malekzadeh, F., Gracie, R., and Dusseault, M. (2014). Parametric sensitivity analysis for CO_2 geosequestration. *International Journal of Greenhouse Gas Control*, *23*, 61–71.

Schmidt, V., and Mcdonald, D. A. (1979a). Texture and recognition of secondary porosity in sandstones. *SEPM Special Publication*, *26*, 209–225.

Schmidt, V., and Mcdonald, D. A. (1979b). The role of secondary porosity in the course of sandstone diagenesis. *SEPM Special Publication*, *26*, 175–207.

Schwartz, M. O. (2020). Can CO_2 sequestration in basalt efficiently reduce greenhouse gas emission? *Environmental Technology (United Kingdom)*, *0*(0), 1–11. https://doi.org/10.1080/09593330.2020.1815859

Shapiro, A. A., and Bedrikovetsky, P. G. (2010). A stochastic theory for deep bed filtration accounting for dispersion and size distributions. *Physica A: Statistical Mechanics and Its Applications*, *389*(13), 2473–2494. https://doi.org/10.1016/j.physa.2010.02.049

Sharma, M. M., and Yortsos, Y. C. (1987). Transport of particulate suspensions in porous media: model formulation. *AIChE Journal*, *33*(10), 1636–1643. https://doi.org/10.1002/aic.690331007

Slatt, R. M., Portas, R., Buckner, N., Abousleiman, Y., O'Brien, N., Tran, M., … Davis, R. (2011). Outcrop-behind outcrop (quarry), multiscale characterization of the Woodford gas shale, Oklahoma. *Shale Reservoirs—Giant Resources for the 21st Century: AAPG Memoir*, *97*, 24. https://doi.org/10.1306/13321481M97441

Slatt, Roger M. (2013). *Geologic controls on reservoir quality*. *Developments in Petroleum Science* (Vol. 61). https://doi.org/10.1016/B978-0-444-56365-1.00006-7

Spycher, N., and Pruess, K. (2005). CO_2-H_2O mixtures in the geological sequestration of CO_2. II. Partitioning in chloride brines at 12-100°C and up to 600 bar. *Geochimica et Cosmochimica Acta*, *69*(13), 3309–3320. https://doi.org/10.1016/j.gca.2005.01.015

Spycher, N., and Pruess, K. (2010). A phase-partitioning model for CO_2-brine mixtures at elevated temperatures and pressures: Application to CO_2-enhanced geothermal systems. *Transport in Porous Media*, *82*(1), 173–196. https://doi.org/10.1007/s11242-009-9425-y

Spycher, N., Pruess, K., and Ennis-King, J. (2003). CO_2-H_2O mixtures in the geological sequestration of CO_2. I. Assessment and calculation of mutual solubilities from 12 to 100°C and up to 600 bar. *Geochimica et Cosmochimica Acta*, *67*(16), 3015–3031. https://doi.org/10.1016/S0016-7037(03)00273-4

Steefel, C., Appelo, C. A. J., Arora, B., Jacques, D., Kalbacher, T., Kolditz, O., … Yeh, G. T. (2015). Reactive transport codes for subsurface environmental simulation. *Computational Geosciences*, *19*(3), 445–478. https://doi.org/10.1007/s10596-014-9443-x

Steefel, C. I. (2008). Geochemical kinetics and transport. In *Kinetics of Water-Rock Interaction* (pp. 545–589). https://doi.org/10.1007/978-0-387-73563-4_11

Steefel, C. I., and MacQuarrie, K. T. B. (1996). Approaches to modeling of reactive transport in porous media. In *Reactive Transport in Porous Media* (pp. 83–129). Mineral Society of America.

Steefel, C. I., Molins, S., and Trebotich, D. (2013). Pore scale processes associated with subsurface CO_2 injection and sequestration. *Reviews in Mineralogy and Geochemistry*, *77*, 259–303. https://doi.org/10.2138/rmg.2013.77.8

Steefel, Carl I., DePaolo, D. J., and Lichtner, P. C. (2005). Reactive transport modeling: an essential tool and a new research approach for the earth sciences. *Earth and Planetary Science Letters*, *240*(3–4), 539–558. https://doi.org/10.1016/j.epsl.2005.09.017

Sun, A. Y., Lu, J., Freifeld, B. M., Hovorka, S. D., and Islam, A. (2016). Using pulse testing for leakage detection in carbon storage reservoirs: A field demonstration. *International Journal of Greenhouse Gas Control*, *46*, 215–227. https://doi.org/10.1016/j.ijggc.2016.01.015

Sun, J., Hu, K., Wong, J., Hall, B., and Schechter, D. (2014). Investigating the effect of improved fracture conductivity on production performance of hydraulic fractured wells through field case studies and numerical simulations. *SPE Hydrocarbon Economics and Evaluation Symposium*, (November), 442–449.

Surdam, A. R. C., Crossey, L. J., Eglinton, G., Durand, B., Pigott, J. D., Raiswell, R., and Berner, R. A. (1985). Organic-inorganic reactions during progressive burial : key to porosity and permeability enhancement and preservation. *Philosophical Transactions of the Royal Society of London. Series A , Mathematical and Physical Sciences*, *315*(1531).

Taku Ide, S., Jessen, K., and Orr, F. M. (2007). Storage of CO_2 in saline aquifers: Effects of gravity, viscous, and capillary forces on amount and timing of trapping. *International Journal of Greenhouse Gas Control*, *1*(4), 481–491. https://doi.org/10.1016/S1750-5836(07)00091-6

Tansey, J., and Balhoff, M. T. (2016). Pore network modeling of reactive transport and dissolution in porous media. *Transport in Porous Media*, *113*(2), 303–327. https://doi.org/10.1007/s11242-016-0695-x

Taylor, T. R., Giles, M. R., Hathon, L. A., Diggs, T. N., Braunsdorf, N. R., Birbiglia, G. V., … Espejo, I. S. (2010). Sandstone diagenesis and reservoir quality prediction : Models, myths, and reality. *AAPG Bulletin*, *94*(8), 1093–1132. https://doi.org/10.1306/04211009123

Terracina, J. M., Turner, J. M., Collins, D. H., and Spillars, S. (2010). Proppant selection and its effect on the results of fracturing treatments performed in shale formations. *SPE Annual Technical Conference and Exhibition*. https://doi.org/10.2118/135502-MS

Thompson, K. E., and Fogler, H. S. (1997). Modeling flow in disordered packed beds from pore-scale fluid mechanics. *AIChE Journal*, *43*(6), 1377–1389. https://doi.org/10.1002/aic.690430602

Todd, A. C., Somerville, J. E., and Scott, G. (1984). The application of depth of formation damage measurements in predicting water injectivity decline. In *SPE International Symposium on Formation Damage Control* (Vol. SPE 12498, pp. 233–244). Bakersfield, CA. https://doi.org/10.2523/12498-ms

Trusler, J. P. M. (2017). Thermophysical properties and phase behavior of fluids for application in carbon capture and storage processes. *Annual Review of Chemical and Biomolecular Engineering*, *8*(1), 381–402. https://doi.org/10.1146/annurev-chembioeng-060816-101426

Tufenkji, N. (2007). Modeling microbial transport in porous media: Traditional approaches and recent developments. *Advances in Water Resources*, *30*(6–7), 1455–1469. https://doi.org/10.1016/j.advwatres.2006.05.014

Vesovic, V., Wakeham, W. A., Olchowy, G. A., Sengers, J. V., Watson, J. T. R., and Millat, J. (1990). The transport properties of carbon dioxide. *Journal of Physical and Chemical Reference Data*, *19*(3), 763–808. https://doi.org/10.1063/1.555875

Walsh, M. P., Bryant, S. L., Schechter, R. S., and Lake, L. W. (1984). Precipitation and dissolution of solids attending flow through porous media. *AIChE Journal*, *30*(2), 317–328. https://doi.org/10.1002/aic.690300222

Wang, Z., and Battiato, I. (2020). Patch-based multiscale algorithm for flow and reactive transport in fracture-microcrack systems in shales. *Water Resources Research*, *56*(2), 1–17. https://doi.org/10.1029/2019WR025960

Weaver, J., Blauch, M., Parker, M., and Todd, B. (1999). Investigation of proppant-pack formation interface and relationship to particulate invasion. *SPE European Formation Damage Conference*, *SPE-54771*.

Weaver, J. D., Parker, M., van Batenburg, D. W., and Nguyen, P. D. (2007). Fracture-related diagenesis may impact conductivity. *SPE Journal*, *12*(03), 272–281. https://doi.org/10.2118/98236-PA

Weir, G. J., White, S. P., and Kissling, W. M. (1996). reservoir storage and containment of greenhouse gases. *Transport in Porous Media*, *23*(1), 37–60.

White, S. P., Allis, R. G., Moore, J., Chidsey, T., Morgan, C., Gwynn, W., and Adams, M. (2005). Simulation of reactive transport of injected CO_2 on the Colorado Plateau, Utah, USA. *Chemical Geology*, *217*(3-4 SPEC. ISS.), 387–405. https://doi.org/10.1016/j.chemgeo.2004.12.020

Wilson, M. D., and Stanton, P. T. (1994). Diagenetic mechanisms of porosity and permeability reduction and enhancement. In *Reservoir quality assessment and prediction in clastic rocks* (pp. 59–118). The Society for Sedimentary Geology.

Wood, J. R. (1994). Chemical diagenesis. In *Reservoir quality assessment and prediction in clastic rocks* (pp. 119–136).

Worden, R. H., and Burley, S. D. (2003). Sandstone diagenesis : the evolution of sand to stone. In *Sandstone Diagenesis: Recent and Ancient* (pp. 3–44).

Wu, Y., Cheng, L., Huang, S., Fang, S., Jia, P., and Rao, X. (2019). An analytical model for

analyzing the impact of fracturing fluid-induced formation damage on rate transient behavior in tight formations. *Journal of Petroleum Science and Engineering*, *179*(March), 513–525. https://doi.org/10.1016/j.petrol.2019.04.090

Würdemann, H., Möller, F., Kühn, M., Heidug, W., Christensen, N. P., Borm, G., and Schilling, F. R. (2010). CO2SINK-From site characterisation and risk assessment to monitoring and verification: One year of operational experience with the field laboratory for CO_2 storage at Ketzin, Germany. *International Journal of Greenhouse Gas Control*, *4*(6), 938–951. https://doi.org/10.1016/j.ijggc.2010.08.010

Xiao, Y., and Jones, G. D. (2006). Reactive transport modeling of carbonate and siliciclastic diagenesis and reservoir quality prediction. *12th Abu Dhabi International Petroleum Exhibition and Conference, ADIPEC 2006: Meeting the Increasing Oil and Gas Demand Through Innovation*, *2*, 757–766. https://doi.org/10.2523/101669-ms

Xu, T., Zheng, L., and Tian, H. (2011). Reactive transport modeling for CO_2 geological sequestration. *Journal of Petroleum Science and Engineering*, *78*(3–4), 765–777. https://doi.org/10.1016/j.petrol.2011.09.005

Xue, Z., Tanase, D., and Watanebe, J. (2006). Estimation of CO_2 Saturation from Time-lapse CO_2 Well Logging in an Onshore Aquifer, Nagaoka, Japan. *Exploration Geophysics*, *37*(1), 19–29.

Yoshida, K., Matubayasi, N., and Nakahara, M. (2008). Self-diffusion coefficients for water and organic solvents at high temperatures along the coexistence curve. *The Journal of Chemical Physics*, *129*(21), 214501. https://doi.org/10.1063/1.3006420

You, Z., Bedrikovetsky, P., Badalyan, A., and Hand, M. (2015). Particle mobilization in porous media: Temperature effects on competing electrostatic and drag forces. *Geophysical Research Letters*, *42*(8), 2852–2860. https://doi.org/10.1002/2015GL063986

Yuan, G., Cao, Y., Gluyas, J., and Jia, Z. (2017). Reactive transport modeling of coupled feldspar dissolution and secondary mineral precipitation and its implication for diagenetic interaction in sandstones. *Geochimica et Cosmochimica Acta*, *207*, 232–255. https://doi.org/10.1016/j.gca.2017.03.022

Zamani, A., and Maini, B. (2009). Flow of dispersed particles through porous media - Deep bed filtration. *Journal of Petroleum Science and Engineering*, *69*(1–2), 71–88. https://doi.org/10.1016/j.petrol.2009.06.016

Zaytsev, I. D., and Aseyev, G. G. (1992). *Properties of aqueous solutions of electrolytes*. Boca Raton, Florida: CRC Press.

Zhang, J., Ouyang, L., Zhu, D., and Hill, A. D. (2015). Experimental and numerical studies of reduced fracture conductivity due to proppant embedment in the shale reservoir. *Journal of Petroleum Science and Engineering*, *130*, 37–45. https://doi.org/10.1016/j.petrol.2015.04.004

Zhang, J., Zhu, D., and Hill, A. D. (2015). A new theoretical method to calculate shale fracture conductivity based on the population balance equation. *Journal of Petroleum Science and Engineering*, *134*, 40–48. https://doi.org/10.1016/j.petrol.2015.07.019

Zhao, H., Liao, X., Chen, Y., and Zhao, X. (2010). Sensitivity analysis of CO_2 sequestration in saline aquifers. *Petroleum Science*, *7*(3), 372–378. https://doi.org/10.1007/s12182-010-0080-2

Zhao, J., Jin, Z., Jin, Z., Hu, Q., Hu, Z., Du, W., … Geng, Y. (2017). Mineral types and organic matters of the Ordovician-Silurian Wufeng and Longmaxi Shale in the Sichuan Basin, China: Implications for pore systems, diagenetic pathways, and reservoir quality in fine-grained sedimentary rocks. *Marine and Petroleum Geology*, *86*, 655–674. https://doi.org/10.1016/j.marpetgeo.2017.06.031